

**Bioapplicable, Nanostructured and Nanocomposite Materials for Catalytic and  
Biosensor Applications**

A Thesis

Submitted to the Faculty

of

Drexel University

by

Alpa C. Patel

in partial fulfillment of the

requirements for the degree

of

Doctor of Philosophy

August 2006

© Copyright 2006  
Alpa C. Patel. All Rights Reserved.

## **Dedications**

This work is dedicated to my parents, Mamta Patel and Chandulal Patel. Their life and the principles they believe in have always been an endless source of inspiration for me. They happily sacrificed many comforts in their life for us (my sister, brother and me) and for our whole family. They have trusted me and given me the freedom to live my life on my own terms, for which I am very grateful.

I hope to live every minute of my life to the fullest and hope to spread joy and happiness to every one I meet on the way.

## Acknowledgments

First, I would like to thank my advisor, Professor Yen Wei, for being the best mentor any one can ask for. His scientific perception and friendship are perhaps only surpassed by his courage in allowing his students to explore the vast scientific landscape, in order to train us to be freethinking independent scientists at the end of the journey. He made me realize that apart from knowing your subject and hard work you need passion and imagination to invent and discover. Without his help and support, I would never be here today.

I would especially like to thank my candidacy examination and/or my dissertation defense committee members, Dr. Sally Solomon, Dr. Jean-Claude Bradley, Dr. Jian-Min Yuan, Dr. Joe Foley and Dr. Reinhard Schweitzer-Stenner for their time and valuable suggestions. I would separately like to acknowledge Dr. Karl Sohlberg my committee chair and Dr. Daniel King for helping with my dissertation. Many thanks are also due to my external committee member, Dr. Huixin He from Rutgers University, for agreeing to be on my committee.

I also would like to express my gratitude to Dr. Shuxi Li for his valuable suggestions that he gathered form years of hands-on experience and which, I would never be able to find in a textbook. I also thank Dr. Solomon Samuel and Aflal Mohamed who helped me with the mechanical testing of my research samples. I thank Dee Breger, Doug Yates, and Dr. Paul Heiney for training me on various microscopic and spectroscopic instruments, Dr. Kevin Owens for training me on the departmental instruments and all the professors and staff in the department for being there for me, and Drexel University for providing me with a great working environment.

I want to acknowledge the various funding organizations, National Institutes of Health, National Science Foundation, Nanotechnology Institute of Southeastern Pennsylvania and the Army Research Lab, because without their support my work at Drexel University would remain just a dream.

I cannot even begin to explain how thankful I am to all the graduate students past and present who have always been there for me. Stephanie Schuster, Kim Kahle, Mozghan Bahadory, William Erb, Guzeliya Korneva, Melissa Mertzman.... the list goes on. Special thanks are due to all the past and present associates and students in Dr. Wei's lab, Dr. Shan Cheng, Dr. Hua Dong, Dr. Houping Yin, Dr. Zhengfei Sun, Dr. Zongtao Zhang, Yi Guo, Andreas Mylonakis, Indraneil Mukherjee, Somang Kim, Charles Bowman, Sudipto Das, Colin Murray and Tom Hughes for the valuable discussions, help and for their awesome company.

Special thanks are due to my friends and roommates who have taken the place of my family in the last five years and given me unconditional love. No matter where I go they will always remain in my heart. Many thanks are due to my pride and joy, my huge family. Starting from my parents and in-laws who have nurtured my very existence with love (Mamta Patel, Chandulal Patel, Debjani Bhattacharyya, Debabrata Bhattacharyya), grandparents who have stayed up nights by my side when I was ill (Mani Patel and Dayalal Patel), siblings (Nilpa Patel and Smith Patel), who are the apple of my eye, and all my wonderful cousins.

Finally, I would like to thank god for giving me the most precious person, my husband, Subhabrata Bhattacharyya. He has loved me unconditionally and stood by my side like a rock. Most importantly, he has given me the space and freedom to flourish.

## Table of Contents

List of Tables .....	xi
List of Schemes .....	xii
List of Figures .....	xiv
List of Symbols .....	xxii
List of Abbreviations .....	xxiii
Abstract .....	xxv
Chapter 1: Introduction to Nanostructured Mesoporous Sol-Gel Silica Materials .....	1
1.1 History and Motivation .....	1
1.2 Fundamentals of Sol-Gel Process .....	5
1.2.1 Inorganic Salt Precursors .....	5
1.2.2 Alkoxide Precursors .....	6
1.3 Methods of Pore Formation in Nanostructured Sol-Gel Materials .....	8
1.3.1 Surfactant Templated Method .....	8
1.3.2 Nonsurfactant Templated Method .....	10
1.4 Immobilization of Nanomaterials in Sol-Gel Materials .....	11
1.5 The Process of Electrospinning Nanofibers .....	14
1.5.1 History of Electrospinning Nanofibers .....	14
1.5.2 Factors Affecting the Process of Electrospinning Nanofibers .....	15
1.5.3 Electrospinning of Sol-gel Composite Fibers .....	19
1.6 Characterization Methods for Porous Materials .....	20
1.6.1 Gas Sorption Measurement .....	21
1.6.2 X-Ray Diffraction (XRD) .....	24
1.6.3 Electron Microscopy .....	25
1.7 Organization of this Dissertation .....	25
1.7 Reference List .....	27
Chapter 2: Sol-Gel Synthesis and Characterization of Silver Nanoparticles in D-Glucose Templated Mesoporous Silica Materials .....	43
2.1 Introduction .....	43
2.1.1 Encapsulation of Metal Nanoparticles in Sol-gel Matrix .....	44
2.1.2 Nonsurfactant Templated Silica Material .....	45
2.2 Experimental Section .....	46
2.2.1 Materials and Reagents .....	46
2.2.2 Synthesis of Glucose Templated Silica Material .....	47
2.2.3 Synthesis of Silver Containing Silica Composites .....	48
2.3 Instrumentation and Characterization .....	49
2.4 Results and Discussions .....	50
2.4.1 Elemental Analysis and X-Ray Mapping .....	50
2.4.2 N <sub>2</sub> Sorption Characterization .....	50
2.4.3 X-Ray Diffraction Characterization .....	53
2.4.4 Transmission Electron Microscopy Characterization .....	54
2.4.5 Optical Characterization .....	54
2.5 Conclusion .....	55

Chapter 3: Fabrication of Organic-Inorganic Hybrid Copolymer Nanofibers via Electrospinning .....	69
3.1 Introduction.....	69
3.2 Experimental Section.....	72
3.2.1 Materials and Reagents .....	72
3.2.2 Synthesis of Trimethoxysilyl Functionalized Polymethacrylate Copolymer (PMCM).....	73
3.2.3 Synthesis of Poly[methyl methacrylate-co-3-(tri-methoxysilyl)propyl methacrylate-silica (PMCM-SiO <sub>2</sub> ) Hybrid Polymer.....	74
3.2.4 Preparation of PMCM Copolymer Electrospinning Solution.....	75
3.2.5 Preparation of PMCM-SiO <sub>2</sub> Copolymer Electrospinning Solution.....	76
3.3 Electrospinning .....	76
3.4 Instrumentation .....	77
3.4.1 Gel Permeation Chromatography (GPC).....	77
3.4.2 Environmental Scanning Electron Microscopy (ESEM).....	77
3.4.3 Fourier Transform Infrared Spectra (FT-IR) .....	77
3.4.4 Differential Scanning Calorimeter (DSC, TA Q100) and Thermogravimetric Analyzer (TGA, TA Q50).....	78
3.5 Results and Discussion .....	78
3.5.1 Properties of PMCM and PMCM-SiO <sub>2</sub> Electrospinning Solution ..	78
3.5.2 Optimization of Properties for Electrospinning Uniform PMCM Copolymer Fibers.....	79
3.5.3 Optimization of Properties for Electrospinning Uniform PMCM-SiO <sub>2</sub> Fibers.....	82
3.6 Characterization of PMCM and PMCM-SiO <sub>2</sub> Fibers .....	84
3.6.1 Fourier Transform Infrared Spectra (FT-IR) .....	84
3.6.2 Thermal Analysis of PMCM and PMCM-SiO <sub>2</sub> Hybrid Fibers.....	86
3.7 Conclusion .....	88
Chapter 4: Use of Organic-Inorganic Hybrid Copolymer Nanofibers for Dental Filler Applications .....	107
4.1 Introduction.....	107
4.1.1 General Background on Dental Composites.....	107
4.1.2 Advantage and Disadvantage of Filler Materials.....	109
4.2 Experimental Section.....	111
4.2.1 Materials and Reagents .....	111
4.2.2 Electrospinning of PMCM-SiO <sub>2</sub> Nanofibers.....	112
4.2.3 Experimental Composite Preparation .....	113
4.2.4 Three Point Bending Test .....	114
4.3 Instrumentation .....	115
4.4 Results and Discussion .....	115
4.4.1 Observation of Fractured Composite Material Surface using ESEM .....	115
4.4.2 Effect of Fiber Mats on Composite Material .....	116
4.4.3 Evaluation of FS and E <sub>y</sub> Values .....	117
4.5 Conclusion .....	119
4.6 Reference List.....	120

Chapter 5: Electrospinning of Porous Silica Nanofibers Containing Silver and Gold Nanoparticles for Catalytic Application .....	132
5.1 Introduction.....	132
5.2 Experimental Section.....	135
5.2.1 Materials and Reagent.....	135
5.2.2 Preparation of Spinning Solution.....	135
5.2.3 Electrospinning .....	137
5.2.4 Testing the Catalytic Activity of Silver Nanoparticles in the Fibers .....	137
5.3 Instrumentation .....	138
5.3.1 Gel Permeation Chromatography (GPC).....	138
5.3.2 Digital Viscometer .....	138
5.3.3 Fourier Transform Infrared Spectrophotometer (FT-IR).....	138
5.3.4 Environmental Scanning Electron Microscopy (ESEM) and Electron Diffraction Spectroscopy (EDX) .....	138
5.3.5 Transmission Electron Microscopy (TEM) .....	139
5.3.6 Thermogravimetric Analyzer (TGA, TA Q50).....	139
5.3.7 X-Ray Diffraction (XRD).....	139
5.3.8 Solid UV Vis Spectroscopy .....	139
5.3.9 Gas Sorption Measurement.....	140
5.4 Results and Discussion .....	140
5.4.1 Effect of PMCM Concentration on Electrospun Nanofibers.....	140
5.4.2 Effect of AgNO <sub>3</sub> Concentration on Electrospun Nanofibers.....	141
5.4.3 Effect of Heat Treatment on Electrospun Nanofibers and Silver Nanoparticles .....	141
5.4.4 Effect of Heat Treatment Time on Electrospun Nanofibers and Silver Nanoparticles .....	144
5.5 Characterization of As-Spun and Heat-Treated Fibers.....	144
5.5.1 Elemental Characterization.....	144
5.5.2 Fourier Transform Infrared Spectra (FT-IR) .....	145
5.5.3 Differential Thermogravimetric Analysis (TGA).....	145
5.5.4 Transmission Electron Microscopy .....	146
5.5.5 Optical Properties of PSFSP .....	147
5.6 Catalytic Activity of Silver Nanoparticles.....	149
5.7 Conclusion .....	150
5.8 Electrospinning of Gold Nanoparticles in Porous Silica Nanofibers.....	150
5.9 Reference List.....	152
Chapter 6: In-Situ Encapsulation of Horseradish Peroxidase in Electrospun Porous Silica Fibers for Potential Biosensor Applications .....	176
6.1 Introduction.....	176
6.2 Experimental Section.....	180
6.2.1 Materials and Reagents .....	180
6.2.2 Preparation of HRP Containing Sol-Gel Electrospinning Solution.....	180
6.2.3 Electrospinning of the Enzyme Containing Sol Gel Mixture .....	182
6.2.4 Activity Assay of Free and Immobilized HRP .....	182
6.3 Characterization of Enzyme Immobilized Electrospun Nanofibers .....	185



6.4 Results and Discussion .....	186
6.4.1 Factors Affecting the Morphology and Diameter of Electrospun Nanofibers.....	186
6.4.2 Infrared Spectroscopy (FT-IR) and Thermogravimetric Analysis (TGA).....	187
6.4.3 Factors Affecting the Mesoporosity of the Electrospun Nanofibers .....	188
6.4.4 Factors Affecting the HRP Activity.....	191
6.4.5 Thermal Stability of Encapsulated HRP Enzymes .....	196
6.4.6 Enzyme Leakage and Reusability of EIMSF.....	197
6.5 Conclusion .....	199
Chapter 7: Electrospinning of Silica Nanofibers Containing CdSe/ZnS Quantum Dots	222
7.1 Introduction.....	222
7.1.1 What are Quantum Dots? (QD) .....	222
7.1.2 Synthesis and Kinds of QD's .....	223
7.1.3 Applications of QD's .....	224
7.1.4 Obtaining Linear Arrays of QD .....	225
7.1.5 Electrospinning .....	226
7.2 Experimental Section.....	227
7.2.1 Materials and Reagents.....	227
7.2.2 Preparation of Electrospinning Solution.....	228
7.2.3 Electrospinning of Silica Nanofibers Containing QD's.....	229
7.2.4 Metal Plate and Rotating Drum Fiber Collector .....	229
7.3 Instrumentation .....	230
7.4 Results and Discussion .....	230
7.4.1 Effect of Silica Precursor on Silica/QD Nanofibers .....	231
7.4.2 Effect of Polymer Additive on Silica/QD Nanofibers .....	232
7.4.3 Effect of QD Size on Silica/QD Nanofibers .....	233
7.4.4 Attempts to Obtain Linear Arrays of QD in Silica Fibers .....	234
7.5 Characterization of Silica/QD Nanofibers.....	235
7.5.1 Environmental Scanning Electron Microscopy (ESEM) and Electron Diffraction Spectroscopy (EDX) .....	235
7.5.2 Fluorescence Emission (FE) .....	235
7.5.3 Fluorescence Microscopy (FM).....	236
7.5.4 Absorption Spectroscopy.....	236
7.5.5 Transmission Electron Microscopy .....	237
7.6 Conclusion .....	237
7.7 Reference List.....	239
Chapter 8: Conclusion and Future Work .....	258
8.1 Formation of Porous Structures in Nanomaterials.....	258
8.2 Electrospinning .....	260
8.3 Products Developed .....	260
8.4 Unique Goals Achieved .....	262
8.5 Future Direction.....	262
Appendix A: Work In Collaboration with Universities and Companies .....	264

Appendix B: Microfabrication of Carbon Nanopipettes for Imaging and Manipulating	
Live Cells .....	290
Vita.....	319

## List of Tables

Table 2-1. Compositions and pore parameters of the silver-silica materials prepared by the reduction of silver nitrate to silver using glucose as a reducing agent. (GTS, glucose templated nonsurfactant silica material). .....	60
Table 3-1. Synthesis of poly[methyl methacrylate-co-3-(tri-methoxysilyl)propyl methacrylate-silica (PMCM-SiO <sub>2</sub> ) hybrid. ....	94
Table 3-2. Solvents employed for electrospinning PMCM co-polymer fibers. Concentration of electrospinning solution and average diameter of the nanofibers.....	95
Table 3-3. The composition of PMCM-SiO <sub>2</sub> electrospinning solution using THF as the solvent and average size of fibers spun at different intervals of time.....	96
Table 3-4. Thermal characteristic of electrospun nanofibers.....	97
Table 4-1. Flexural strength and elastic modulus of PMCM-SiO <sub>2</sub> fiber reinforced BISGMA/TEGDMA dental composites. ....	123
Table 5-1. Sample code and average diameter of silica fibers and silver nanoparticles subjected to various heat treatments. ....	157
Table 5-2. Degradation temperatures and final residue of samples heated up to 700 °C at the rate of 10 °C/min. ....	158
Table 5-3. A comparison of calculated <i>d</i> -spacing ( <i>d</i> <sub>hkl</sub> ) values of silver nanoparticles with that of International Centre for Diffraction Data obtained for silver from JCPDS files (NO. 41-1402).....	159
Table 6-1. Material and activity parameters of free and HRP immobilized mesoporous silica fibers (EIMSF).....	204
Table 7-1. Common types of quantum dots and its important properties.....	244
Table 7-2. Complete specification of quantum dots used for encapsulation in silica nanofibers.....	245
Table A.2-1 Represent the samples produced using various wt% of urea as the nonsurfactant template and various wt% of KMnO <sub>4</sub> as an additive. ....	287

## List of Schemes

Scheme 1-1. Hydrolysis of silicates (e.g., $\text{Na}_2\text{SiO}_3$ ) to $\text{Si}(\text{OH})_4$ under acidic conditions. .	6
Scheme 1-2. Condensation of the hydrolyzed silicates. ....	6
Scheme 1-3. Hydrolysis reaction of TEOS in the presence of water and hydrochloric acid. .....	7
Scheme 1-4. Condensation reaction of TEOS with hydrolyzed TEOS. ....	7
Scheme 1-5. Self-condensation reaction of hydrolyzed TEOS. ....	7
Scheme 1-6. Viscosity in relation to rate of shear and shear stress. ....	16
Scheme 1-7. Represents the amount of gas adsorbed by sample at fixed temperature. ...	21
Scheme 1-8. Represents the amount of gas adsorbed by sample at below critical temperature. ....	21
Scheme 1-9. The Brunauer-Emmett-Teller (BET) gas adsorption equation. ....	23
Scheme 1-10. Bragg equation. ....	24
Scheme 3-1. Synthesis of PMCM. ....	74
Scheme 3-2. Synthesis of PMCM- $\text{SiO}_2$ . ....	75
Scheme 4-1. Molecular structures of dental monomers and initiators. ....	112
Scheme 4-2. Equations used to determine the fracture strength and elastic modulus of dental composite material. ....	114
Scheme 5-1. Schematic representation of porous silica nanofibers containing silver nanoparticles. ....	136
Scheme 5-2. Thermal degradation of PMCM copolymer. ....	142
Scheme 5-3. Thermal condensation of hydrolyzed TEOS. ....	143
Scheme 5-4. Thermal reduction of silver nitrate. ....	143
Scheme 6-1. Fabrication of enzyme encapsulated mesoporous silica nanofibers. ....	181

Scheme 7-1. Fabrication of quantum dot encapsulated silica nanofibers. # PMMA (Mw 350,000). .....	227
Scheme 7-2. Hydrolysis of silica precursor. ....	231
Scheme A.2-1. Reduction of potassium permanganate to manganese dioxide. ....	267

## List of Figures

Figure 1-1. Sol-gel process and their products. ( <a href="http://www.chemat.com/html/solgel.html">www.chemat.com/html/solgel.html</a> ). ...	35
Figure 1-2. Three structure types proposed for silica-surfactant mesophases and the x-ray diffraction patterns: (a) MCM-41 (hexagonal); (b) MCM-48 (cubic); (c) MCM-50 (lamellar). <sup>50,51</sup> .....	36
Figure 1-3. Proposed schematics of the liquid-crystal templating (LCT) mechanism. <sup>22,50</sup> .....	37
Figure 1- 4. Schematic representation of the electrospinning process.....	38
Figure 1-5. Photograph of the electrospinning instrument set-up in our lab. ....	39
Figure 1-6. Taylor cone formed on the tip of the pipette during electrospinning. <sup>86</sup> .....	40
Figure 1-7. IUPAC classification of physisorption isotherms. <sup>48</sup> .....	41
Figure 1-8. IUPAC classification of hysteresis loops. <sup>48</sup> .....	42
Figure 2-1. Representative X-ray energy-dispersive spectra for silver-silica nanocomposites. (a) 0GTS(Ag) does not show any peak for silver; (b) 30GTS(Ag) shows a small peak for silver; (c) 50GTS(Ag) shows a relatively sharper peak for silver.....	61
Figure 2-2. N <sub>2</sub> adsorption-desorption isotherms at -196 °C for control samples (i.e. 0 and 50GTS) and silver-silica composites with different silver content (i.e. 0, 30, 50GTS(Ag) *Samples 20GTS(Ag) show the same trend in results as 30GTS(Ag). ....	62
Figure 2-3. BJH pore size distributions for the control samples (i.e., 0GTS and 50GTS) and for silver-silica composites with different silver contents (i.e., 0, 30, 50GTS(Ag))...	63
Figure 2-4. X- ray diffraction of silver-silica nanocomposites: a) 50GTS(Ag) samples immersed in silver nitrate solution and heat-treated at 300 °C; b) 50GTS(Ag) sample containing silver nanoparticles (not heated); c) 30GTS(Ag) sample containing silver nanoparticles (not heated) and d) control sample Gslid(Ag). ....	64
Figure 2-5. (a) Representative TEM image of mesoporous silver-silica nanocomposites (50GTS(Ag)) along with inserts of electron diffraction patters. The dark spherical spots seen in the micrograph are silver particles and the gray background is the mesoporous silica frame work which clearly shows worm like mesoporous channels; 5(b) TEM image of 30GTS(Ag) sample shows a silica frame work with probable tiny silver particles and electron diffraction pattern of silver nanoparticles. Scale bar 10 nm. ....	65

Figure 2-6. Series of X-ray mapping images of silver-silica nanocomposites containing 50 wt% glucose (i.e., 50GTS(Ag)). (a) As synthesized 50GTS(Ag) sample; (b) oxygen mapping; (c) silicon mapping; (d) silver mapping. Scale bar: 10  $\mu\text{m}$ . ..... 66

Figure 2-7. Solid-state UV-vis reflectance spectrum of mesoporous silver-silica nanocomposites, (a) 0GTS(Ag), (b) 10GTS(Ag), (c) 30GTS(Ag), (d) 40GTS(Ag) and (e) 50GTS(Ag). 0GTS(Ag) and 10GTS(Ag) do not show any maximum absorbance peaks. 30-40GTS(Ag) and 50GTS(Ag) show peaks at 425 and 410 nm respectively. The spectra for all these samples were obtained at a scanning rate of 60 nm/min..... 67

Figure 2-8. Shows the change in color observed in silica nanocomposites. (a) 0GTS samples are transparent because of the absence of silver nanoparticles; (b) 20GTS(Ag) samples are light yellow in color because of the presence of silver nanoparticles in very small amounts and (c) 50GTS(Ag) samples are dark brown in color depicting the presence of high content of silver nanoparticles in the sample. Scale bar 1 cm. .... 68

Figure 3-1. Scanning electron micrographs of fibers spun using PMCM copolymer solution using  $\text{CHCl}_3$  as the solvent with fiber diameter ranging from 1  $\mu\text{m}$  to 4  $\mu\text{m}$ . .... 98

Figure 3-2. Scanning electron micrographs of fibers spun using PMCM copolymer solution using THF as the solvent with fiber diameter ranging from 0.8  $\mu\text{m}$  to 4  $\mu\text{m}$ . .... 99

Figure 3-3. Scanning electron micrographs of fibers spun using PMCM copolymer solution using DMF as the solvent at different concentrations from 2 to 20 wt%, with an electric field of 20 kV and a constant spinning distance of 20 cm. .... 100

Figure 3-4. The size distribution of PMCM copolymer fiber diameter, with DMF as solvent using 6, 12, 20 wt% solutions, with a constant electrical field of 20 kV and a spinning distance of 20 cm. .... 101

Figure 3-5. Comparison of varying PMCM/DMF fiber diameters with respect to electric field and concentration of spinning solution; (6a) spinning distance of 20 cm, concentration of 6 wt% and electric field ranging from 5 to 20 kV; (6b) Spinning distance of 20 cm, concentration of 4 to 20 wt% and electric field of 20 kV..... 102

Figure 3-6. Represents micrograms of PMCM-SiO<sub>2</sub> fibers spun using DMF and THF as solvents. A mixture of 10 wt% PMCM/DMF solution (or PMCM/THF) and hydrolyzed TEOS sol in a (9:1) and (8:2) ratio was used as the spinning solution. The average diameter of the fibers is also noted. .... 103

Figure 3-7. Infrared spectra of fibers: (a) neat PMMA; (b) PMCM; (c) PMCM-SiO<sub>2</sub> (9:1); (d) PMCM-SiO<sub>2</sub> (8:2); (e) Pure SiO<sub>2</sub>..... 104

Figure 3-8. TGA and DTG thermograms of fibers; (a) PMMA ; (b) PMCM; (c) PMCM-SiO<sub>2</sub> (9:1); (d) PMCM-SiO<sub>2</sub> (8:2); (e) Pure SiO<sub>2</sub> (as spun) and (f) Pure SiO<sub>2</sub> (heat-treated to 150 °C for 2 hours before TGA analysis). .... 105

- Figure 3-9. DSC thermogram curves of fibers; (a) neat PMMA; (b) PMCM; (c) PMCM-SiO<sub>2</sub> (9:1); (d) PMCM-SiO<sub>2</sub> (8:2); and (e) Pure SiO<sub>2</sub>. The glass transition of the fibers ( $T_g$ ) is denoted by arrows. .... 106
- Figure 4-1. A flat Teflon<sup>®</sup> sheet and 2 mm x 2 mm, black urethane tape are used to make a mold for fiber reinforced composites. .... 124
- Figure 4-2. Photopolymerized BISGMA/TEGDMA resin dental composite (the gray area) containing one (could be five or eight) layers of fiber mats (represented by the white and black striped line). 2 mm x 2 mm x 25 mm, sized three point bending samples are then cut and polished for studying the FS and  $E_y$  of the sample. .... 125
- Figure 4-3. Schematic representation of the three point bending test. The sample is placed between three points at specific distances as represented above. The white and black striped lines represent the fiber and the gray area represents the BISGMA/TEGDMA composite material. .... 126
- Figure 4-4. PMCM-SiO<sub>2</sub> nanofiber (300 to 400 nm diameter) mats electrospun using a electrospinning solution made up of 10 wt% PMCM/THF copolymer solution and hydrolyzed TEOS sol in a 8:2 mass ratio, respectively. Scale Bar: 5  $\mu$ m. .... 127
- Figure 4-5. Scanning electron micrographs of fractured surface of the three point bending sample. The arrow represents the section of the sample containing the fiber material. The rest of the area is just BISGMA/TEGDMA resin devoid of fiber. Scale bar: 50  $\mu$ m. The inset shows high-resolution micrograph of the fiber/composite, inter penetrated region. Scale bar: 10  $\mu$ m. .... 128
- Figure 4-6. Scanning electron micrographs of fracture surfaces of representative 3 point bending specimen: (a) composite resin with 5 layers of nanofiber fabrics (image taken at the place where the nanofibers were present) Scale bar: 5  $\mu$ m (b) neat resin without nanofibers. Scale bar: 10  $\mu$ m. .... 129
- Figure 4-7a. Flexural strength of the composite resins containing different mass fraction (or layers) of PMCM-SiO<sub>2</sub> nanofiber nonwoven fabrics. Each bar represents the value with standard deviation. .... 130
- Figure 4-7b. Elastic modulus of the composite resins containing different mass fraction ..... 131
- Figure 5-1. ESEM images of non-heat-treated electrospun silica/AgNO<sub>3</sub> nanofibers containing (a) 0 wt% PMCM and 0.06 mol AgNO<sub>3</sub>, (b) 2 wt% PMCM and 0.06 mol AgNO<sub>3</sub>, (c) 6 wt% PMCM and 0.06 mol AgNO<sub>3</sub> and (d) 2 wt% PMCM and 0.1 mol AgNO<sub>3</sub>; and of (e) heat-treated silica fibers (600 °C for 60 min) which were electrospun with a solution containing 2 wt% PMCM and 0.06 mol AgNO<sub>3</sub>. Scale bar: 1  $\mu$ m. .... 160



- Figure 5-2. TEM cross section micrographs of electrospun porous (light features: pores) silica containing silver nanoparticles (dark spherical regions) after thermal treatment (wt% of silver; time of heat treatment; temperature of heat treatment): (a) 10 wt%; 60 min; 400 °C, (b) 10 wt%; 60 min; 600 °C, (c) 10 wt%; 60 min; 800 °C, (d) 10 wt%; 150 min; 400 °C, (e) 20 wt%; 60 min; 400 °C, (f) 10 wt%; 150 min; 600 °C (showing fiber diameters from 100 to 250 nm), and, (g) silica fiber showing homogeneous distribution of silver nanoparticles along the fiber. Scale bar 250 nm. .... 161
- Figure 5-3. Elemental analysis (EDX) of silica fibers electrospun at 20 kV for (a) fibers without any silver content (b) fibers containing 10 wt% of silver nanoparticles after heat treatment. .... 162
- Figure 5-4. Elemental X-ray mapping of fibers containing 10 wt% of silver. (a) ESEM micrograph of heat-treated fibers; (b) oxygen mapping; (c) silicon mapping; (d) silver mapping showing homogeneous distribution of silver nanoparticles. .... 163
- Figure 5-5. Infrared spectra of (a) pure PMCM polymer; (b) pure silica; (c) hydrolyzed TEOS/AgNO<sub>3</sub>/2 wt% PMCM electrospun fibers before heat treatment; (d) silica fibers containing 10 wt% silver nanoparticles heated at 200 °C for 30 min; (e) silica fibers containing 10 wt% silver nanoparticles heated at 600 °C for 30 min. .... 164
- Figure 5-6. Thermogravimetric analysis (TGA) and deconvoluted derivative thermogravimetric (DTG) curves for samples heated at 10 °C/min from 40 °C to 800 °C in air: (a) pure PMCM polymer; (b) PMCM modified silica fibers containing 0.06 mol AgNO<sub>3</sub> before heat treatment; (c) pure SiO<sub>2</sub>. .... 165
- Figure 5-7. (a) White electrospun PMCM modified silica fiber mats containing silver nitrate (AgNO<sub>3</sub>) before heat treatment; (b) golden yellow porous silica fiber mats containing 10 wt% silver nanoparticles after heat treatment at 600 °C for 60 min. Scale bar: 4 cm. .... 166
- Figure 5-8. Optical spectra of porous silica nanofibers containing 10 wt% silver nanoparticles: (a) heat-treated at different temperatures for 30 min and (b) heat-treated for various periods at 400 °C. .... 167
- Figure 5-9. X-ray diffraction patterns for silica fibers containing 10 wt% silver nanoparticles: (a) heat-treated at various temperatures for 30 min and (b) heat-treated for various periods of time at 400 °C. .... 168
- Figure 5-10. Successive UV-visible spectra (taken every 1 min) of methylene blue (MB) dye reduction, using silica nanofibers containing silver nanoparticles as the catalyst and NaBH<sub>4</sub> as the reducing agent. .... 169
- Figure 5-11. Representation of PSFSP. .... 170

- Figure 5-12. ESEM images of non heat-treated electrospun silica/HAuCl<sub>4</sub>.4H<sub>2</sub>O nanofibers containing (a) 0.06 mol HAuCl<sub>4</sub>.4H<sub>2</sub>O (scale bar 10 μm) and (b) 0.1 mol HAuCl<sub>4</sub>.4H<sub>2</sub>O (scale bar 10 μm). ..... 171
- Figure 5-13. ESEM images of heat-treated electrospun silica nanofibers showing (a) precipitation of Au nanoparticles on top of silica fibers (scale bar 5 μm) and (b) high resolution image of Au particles on the silica fiber surface (scale bar 1 μm). ..... 172
- Figure 5-14. Elemental analysis (EDX) of gold nanoparticles present on the heat-treated silica fiber..... 173
- Figure 5-15. TEM cross section micrographs of heat-treated electrospun porous (light features: pores) silica nanofibers, containing gold nanoparticles (dark spherical regions). Low-resolution image (scale bar 0.2 μm) and high-resolution image (scale bar 50 nm). ..... 174
- Figure 5-16. X-ray diffraction patterns for silica fibers containing gold nanoparticles heat-treated at (a) room temperature, (b) 150 °C, (c) 250 °C, (d) 350 °C and (e) 500 °C. .... 175
- Figure 6-1. Enzyme activity assay of template-extracted EIMSF in colorless reagent mixture [phosphate buffer, phenol (PhOH), 4-aminoantipyrine (4-AAP, colorless dye) and H<sub>2</sub>O<sub>2</sub>]. The enzyme present inside the porous fibers converts H<sub>2</sub>O<sub>2</sub> to water in the process converting 4-AAP to quinoneimine (red colored dye). ..... 205
- Figure 6-2. Represents the formation of a colored compound, N-antipyryl-*p*-benzoquinoneimine formed during the HRP catalyzed activity assay, λ<sub>max</sub>=510nm..... 206
- Figure 6-3. Scanning electron micrographs of EIMSF containing, a) 0 wt% glucose (scale bar: 10 μm); b) 20 wt% glucose (scale bar: 10 μm) and c) 40 wt% glucose (scale bar: 1 μm). d) 40 wt% glucose extracted fibers (scale bar: 2 μm). Indent shows the internal surface morphology of the fibers at macroscopic level. .... 207
- Figure 6-4. Fourier transform infrared spectroscopy (FTIR) of EIMSF containing, a) 0 wt% glucose (0EIMSF); b) 20 wt% glucose (20EIMSF) and c) 40 wt% glucose (40EIMSF). d) 40 wt% glucose extracted fibers (washed 40EIMSF). ..... 208
- Figure 6-5a. Thermogravimetric analysis (TGA) profile for glucose, PVA, as fabricated EIMSF and template-extracted EIMSF. .... 209
- Figure 6-5b. Thermogravimetric analysis (TGA) derivative peaks showing maximum degradation temperature for glucose, PVA, as fabricated EIMSF and template-extracted EIMSF..... 210

Figure 6-6a. N <sub>2</sub> adsorption-desorption isotherms at -196 °C for the porous template-extracted fibers synthesized in the presence of 20 and 40 wt% glucose. Control sample is synthesized without adding the template and enzymes. ....	211
Figure 6-6b. The BJH desorption pore size distributions from the N <sub>2</sub> desorption isotherms for the HRP-containing fiber samples synthesized in the presence of 0-40 wt% glucose. ....	212
Figure 6-7. Low-resolution transmission electron micrograph (TEM) of a cluster of template-extracted cross-sectioned 40EIMSF, scale bar: 0.30 μm. High resolution TEM of the same, scale bar; 40 nm. The light features in the micrograph represent interconnected mesopores and channels. ....	213
Figure 6-8a. Effect of the concentration of hydrogen peroxide, [H <sub>2</sub> O <sub>2</sub> ], on the activity of free HRP. ....	214
Figure 6-8b. Effect of the concentration of glucose and [H <sub>2</sub> O <sub>2</sub> ] on the apparent activity of the porous fiber-immobilized HRP. ....	215
Figure 6-8c. Effect of the concentration of glucose on the apparent activity of the fiber-immobilized HRP. The straight lines on the Lineweaver-Burk plots were best-fit using linear regression from which the V <sub>m</sub> and K <sub>m</sub> values were derived. ....	216
Figure 6-9a. Effect of pH on the activity of free HRP. ....	217
Figure 6-9b. Effect of the pH on the activity of fiber-immobilized HRP samples synthesized in the presence of 0-40 wt% glucose. ....	218
Figure 6-9c. Effect of the pH on the activity of free and fiber-immobilized HRP samples synthesized in the presence of 0-40 wt% glucose after normalization. ....	219
Figure 6-10. Thermal stability of free and immobilized HRP. Samples were treated under .....	220
Figure 6-11. Catalytic activity cycle test to determine the efficiency of reusability of enzyme encapsulated fiber samples. ....	221
Figure 7-1. Different sized CdSe/ZnS quantum dots suspended in toluene solution. The same set of materials (CdSe/ZnS) can be used to tune the optical properties of the QD depending on the size of the QD. The blue (Lake Placid Blue) QD have an average diameter of 1.9 nm and the red (Maple Red-Orange) QD's have an average diameter of 5.2 nm. ( <a href="http://www.evidenttech.com/qdot-definition/quantum-dot-introduction.php">http://www.evidenttech.com/qdot-definition/quantum-dot-introduction.php</a> ). ....	246
Figure 7-2. A schematic diagram of the grounded rotating metal cylinder for collecting electrospun nanofibers. ....	247

Figure 7-3. Scanning electron microscopy images of QD encapsulated silica nanofibers fabricated using (a) tetramethyl orthosilicate as the silica precursor (scale bar: 10  $\mu\text{m}$ ) and (b) tetraethyl orthosilicate as the silica precursor (scale bar: 10  $\mu\text{m}$ ). ..... 248

Figure 7-4. A detailed list of the polymer additives and its concentration used to spin silica fibers. <sup>a</sup>The solvent used to dissolve the polymer additive (tetrahydrofuran (THF) and chloroform ( $\text{CHCl}_3$ )), <sup>b</sup>wt% of polymer solution additive and <sup>c</sup>the mass fraction of 15 wt% polymer additive solution to that of hydrolyzed silica sol (silica precursor used is TEOS). For this study, red QD's (0.1 wt% with respect to the final weight of fiber) is added to the silica/PMMA solution before electrospinning. .... 249

Figure 7-5. Scanning electron microscope images of QD encapsulated silica nanofibers fabricated using (a) 0.1 wt% of Lake Placid Blue QD's (scale bar: 10  $\mu\text{m}$ ), (b) 0.05 wt% of Lake Placid Blue QD's (scale bar: 10  $\mu\text{m}$ ) and (c) 0.1% of Maple Red-Orange QD's with respect to the final weight of the fiber (scale bar: 10  $\mu\text{m}$ ). ..... 250

Figure 7-6. Alignment of a) nanoparticles and b) carbon nanotubes during electrospinning and c) mechanical alignment of nanofibers using a rotating metal drum. .... 251

Figure 7-7. a) Irregular, nonwoven fiber mats obtained by collecting the electrospun fibers on grounded flat metal plate (scale bar 10  $\mu\text{m}$ ), b) aligned nanofibers collected using a grounded metal cylinder rotating at 1000 rpm (scale bar 4  $\mu\text{m}$ ) and c) 4500 rpm (scale bar 400 nm). ..... 252

Figure 7-8. Elemental analysis (EDX) of (a) pure CdSe/ZnS quantum dots, (b) pure silica fibers without any QD's and (c) silica fibers containing encapsulated QD's. .... 253

Figure 7-9. Fluorescence emission spectra of (a) pure Maple Red-Orange QD's (620 nm), (b) silica nanofibers containing red QD's (616 nm), (c) pure Lake Placid Blue QD's (490 nm), (d) silica nanofibers containing blue QD's (486 nm) and, (e) pure silica fibers without QD's. .... 254

Figure 7-10. Fluorescence microscopic images of silica nanofibers containing a) Maple Red-Orange QD's and b) Lake Placid Blue QD's (using visible light and UV light at 150x magnification). ..... 255

Figure 7-11. Absorbance spectra of (a) pure Maple Red-Orange QD's (610 nm), (b) silica nanofibers containing red QD's (610 nm), (c) pure Lake Placid Blue QD's (470 nm), (d) silica nanofibers containing blue QD's (468 nm) and (e) pure silica fibers without QD's. .... 256

Figure 7-12. Transmission electron microscopic image of (a) red QD's (size 5.2 nm) in silica fibers collected using a rotating metal cylinder. The arrows point to many more such arrays of QD's. Scale bar: 200 nm. Inset shows a linear array of QD's, scale bar: 10 nm. .... 257

Figure A-1. Pictorial representation of synthesis of enzyme immobilized nonsurfactant templated mesoporous silica samples. The yellow ting comes from the enzyme encapsulated. ....	288
Figure A-2. The final enzyme immobilized sol-gel samples can be used either in the form of discs, particles or powder. The yellow ting seen in the samples is form the encapsulated enzyme. ....	289
Figure B-1. Schematics of atomic force microscopy. ....	311
Figure B-2: Movement of cantilever in the z direction. ( <a href="http://www.nano-lab.com/imagegallery.html">http://www.nano-lab.com/imagegallery.html</a> .) ....	312
Figure B-3. Single walled CNT. ( <a href="http://www.veeco.com/default.asp">http://www.veeco.com/default.asp</a> ).....	313
Figure B-4. Multiwalled CNT. ( <a href="http://www.veeco.com/default.asp">http://www.veeco.com/default.asp</a> ).....	313
Figure B-5. Bamboo shaped CNT. ( <a href="http://www.veeco.com/default.asp">http://www.veeco.com/default.asp</a> ).....	313
Figure B-6a&b. Micrtweezers by Si etching <sup>24</sup> & microsized nut compared to an ant <sup>23</sup> . 314	
Figure B-7. Steps involved in the microfabrication of AFM cantilever. ....	316
Figure B-8. Schematic representation of the cell membrane. ( <a href="http://wsrv.clas.virginia.edu/~rjh9u/humbiol.html">http://wsrv.clas.virginia.edu/~rjh9u/humbiol.html</a> ).....	317
Figure B-9a & b. Cantilever displacement- piezo distance curve <sup>33</sup> .....	318

### List of Symbols

$n^a$	amount of gas adsorbed
D	average particle size
$\Theta$	diffraction angle
$E_y$	elastic modulus
$T_g$	glass transition temperature
$C_p$	heat capacity
$\eta$	viscosity
$ds/dt$	rate of shear
$V_m$	maximal velocity
$K_m$	Michaelis constant
$n_m^a$	monolayer capacity
D	pore size distribution
P	pressure
$P/P_0$	relative pressure
T	temperature
$d$	separation between planes
$\lambda$	wavelength

## List of Abbreviations

0GTS	0 wt% glucose templated silica samples
0GTS(Ag)	0 wt% glucose templated silica samples containing silver
0EIMSF	0 wt% glucose templated enzyme immobilized mesoporous silica fibers
30GTS	30 wt% glucose templated silica samples
30GTS(Ag)	30 wt% glucose templated silica samples containing silver
20EIMSF	20 wt% glucose templated enzyme immobilized mesoporous silica fibers
40EIMSF	40 wt% glucose templated enzyme immobilized mesoporous silica fibers
40EIMSF2	similar to 40EIMSF except for different average fiber diameters
40EIMSF (NoPVA)	similar to 40EIMSF except for absence of PVA
40EIMSF (NoHRP)	similar to 40EIMSF except for the absence of HRP
50GTS	50 wt% glucose templated silica samples
50GTS(Ag)	50 wt% glucose templated silica samples containing silver
AT	Atrazine
BISGMA	2, 20-bis-[4-(methacryloxypropoxy)-phenyl]-propane
BJH	Barrett-Joyner-Halenda
BPO	benzoyl peroxide
BET	Brunauer-Emmett-Teller
CNT	carbon nanotubes
CQ	camphorquinone
DTG	deconvoluted derivative thermogravimetric
DSC	differential scanning calorimeter
DMF	Dimethylformamide
EDX	elemental analysis
ESEM	environmental scanning electron microscope
EIMSF	enzyme encapsulated mesoporous silica fibers
EDTA	ethylenediaminetetraacetic acid
4EDMAB	ethyl-4 (N,N0-dimethylamino) benzoate
EIMSF	enzyme immobilized mesoporous silica fibers
ES30P-10W	gamma high voltage research power supply instrument
FS	flexural strength
FM	fluorescence microscopy
FE	fluorescence emission
FWHM	full width of the peak at half maximum
FT-IR	fourier transform infrared spectra
GPC	gel permeation chromatography
GTS	glucose templated samples
GFP	green fluorescence protein
rGFP	recombinant green fluorescence protein
Gslid(Ag)	samples produced by depositing very thin monolayer of silver

	onto thin glass slides
HPLC	high performance liquid chromatography
HRP	horse radish peroxidase
IUPAC	international union of pure and applied chemistry
LCT	liquid-crystal templating
MB	Methylene blue dye
MSMA	3-(trimethoxysilyl)propyl methacrylate
$\alpha$ - MnO <sub>2</sub>	cryptomelane type I and II
$\delta$ - MnO <sub>2</sub>	Birnessite
$\beta$ - MnO <sub>2</sub>	Pyrolusite
PSD	pore size distributions
PMCM	trimethoxysilyl functionalized polymethacrylate
PS	polystyrene
PSFSP	porous silica nanofibers containing uniformly distributed silver nanoparticles
PMCM-SiO <sub>2</sub>	poly[methyl methacrylate-co-3-(tri-methoxysilyl)propyl methacrylate-silica hybrid
QD	quantum dots
SF10	10 wt% silver nanoparticles containing silica fibers
SF20	20 wt% silver nanoparticles containing silica fibers
SF	surface tension
SEM	scanning electron microscopy
SPR	surface plasmon resonance
TEOS	tetraethylorthosilicate
TMOS	tetramethylorthoxysilicate
TEM	transmission electron microscopy
TGA	thermogravimetric analyzer
TEGDMA	tri (ethylene glycol) dimethacrylate
THF	tetrahydrofuran
UV-vis	ultraviolet and visible
XRD	X-ray diffraction



**Abstract**

Bioapplicable, Nanostructured Materials for Catalytic and Biosensor Applications

Alpa C. Patel

Advisor: Dr. Yen Wei

Novel, nanostructured porous nanocomposites and bioapplicable materials have been successfully developed for catalytic, sensor and reinforcement applications.

Nonsurfactant templated method of pore formation and electrospinning of nanofibers are the two main technologies that have been employed separately and together, to develop novel and potentially commercialize-able products. The porous composite products thus developed take the form of fine particles and nanofiber mats.

For the first time, porous silver nanoparticle/silica composites were synthesized using a simple method of silver nitrate reduction. The glucose template present inside the mesoporous silica material reduces silver nitrate to silver nanoparticles. The particles thus formed are lodged inside the porous silica matrix. The synthesis procedure is very simple, economical, and the samples produced have good catalytic properties.

Organic/inorganic hybrid nanofiber mats were fabricated for the first time using the electrospinning technology. The fiber mats have high surface area and good mechanical properties. These fibers mats are then used in reinforcement applications, by utilizing them as fillers in dental materials. The mechanical properties of dental materials thus produced is seen to improve dramatically with the addition of just a small amount of fiber sample.

An in-situ method was used to produce silver and gold nanoparticles inside porous silica nanofibers via electrospinning. Metal salts used to produce the nanoparticles are mixed with silica and polymer precursors and spun into fibers. The fibers are then

heat-treated to reduce the metal salt into metal nanoparticles. The factors affecting the size and distribution of the nanoparticles inside the porous fibers were studied. The fibers thus produced were then tested for catalytic activity.

Horseradish peroxidase (HRP) enzyme was also encapsulated in porous silica nanofibers via electrospinning. The fibers showed significant enhancement in enzyme activity, which was three orders of magnitude greater than that of the non-templated, conventional microporous silica materials. The factors affecting the enzyme activity, like pH, temperature, etc., was also studied. The response time of the encapsulated enzymes to the external reagents was ~ 2 to 3 seconds, showing high efficiency of the fibers to sensor applications.

Finally, the encapsulation and alignment of quantum dots in silica nanofibers for sensor and telecommunication applications was attempted. MnO<sub>2</sub> and several enzymes encapsulated porous silica samples were also synthesized for universities and companies as part of the ongoing collaborative research work for various catalytic applications.

All the above-mentioned products have high surface area, maintain high enzyme activity, and protect the enzymes and nanoparticles from high temperatures, pH fluctuations and strong chemicals. The morphology, size, porosity, composition of the developed products were studied in detail, via infrared spectroscopy, thermal gravimetric analysis, differential scanning calorimetry, scanning electron microscopy, transmission electron microscopy, X-ray diffraction spectroscopy, etc. Inexpensive raw materials, convenient synthesis method, distinctive structure and physical-chemical properties make the developed products greatly suitable for a wide range of potential applications.



## Chapter 1: Introduction to Nanostructured Mesoporous Sol-Gel Silica Materials

### 1.1 History and Motivation

Nanotechnology and sol-gel process are the two important aspects that form the foundation of this research, which includes the synthesis of mesoporous silica catalyst and biosensors in the form of particles and nanofibers.

According to United States National Nanotechnology Initiative website,<sup>1</sup> “Nanotechnology is defined as the understanding and control of matter at dimensions of roughly 1 to 100 nanometers, where unique phenomena enable novel applications.” The first mention of some of the distinguishing concepts in nanotechnology (but predating use of that name) is often credited to a talk called "There's Plenty of Room at the Bottom", given by physicist Richard Feynman at an American Physical Society meeting at Caltech on December 29, 1959. Feynman described a process by which the ability to manipulate individual atoms and molecules might be developed, using one set of precise tools to build and operate another proportionally smaller set, so on down to the needed scale. The term "nanotechnology" was actually coined by Professor Norio Taniguchi in 1974.<sup>2</sup> In 1980s the basic idea of this definition was promoted by Dr. Eric Drexler, through speeches and various nanotechnology books written by him.<sup>3,4</sup> The actual importance of this technology was realized through the years, due to the tremendous enhancement of applications in all the branches of science, from:

- Nanodrug capsules<sup>5</sup> and nanomanipulators<sup>6,7</sup> in the field of medicine;<sup>8</sup>
- Quantum dots<sup>9</sup> and metal nanoparticles<sup>10</sup> as catalyst<sup>11</sup> in the field of chemistry;

- Nanocircuits<sup>11</sup> and nanofabrication of electronic devices,<sup>12,13</sup> in the field of electronics, to biosensors<sup>14</sup> and decontaminating agents in homeland security division.<sup>15</sup>

The sol-gel process is another aspect that forms the foundation of this thesis work. Sol-gel chemistry is used for making porous glass/ceramic materials. It involves the transition of a system from a liquid (the colloidal "sol") into a solid (the "gel") phase.<sup>16</sup> Sol-gel chemistry is a remarkably versatile approach for fabricating various nanostructured porous materials. It allows the fabrication of materials with a large variety of properties, e.g., ultra-fine porous powders,<sup>17</sup> monolithic ceramics, inorganic membranes, thin film coatings and aerogels. Scientists have used it to produce the world's lightest materials and some of its toughest ceramics. The well documented beginning of sol-gel chemistry can be tracked back to 1956 when Rustom Roy, a graduate student working under Elburt F. Osborn, used sol-gel chemistry to synthesize composites made of tetraethoxide and metal nitrate salts for phase equilibrium studies.<sup>18</sup> He wrote a review that became a classic paper in the field of sol-gel chemistry.<sup>18</sup> Hamilton and Mackenzie in 1960<sup>19</sup> to Biggar and O'Hara in 1969<sup>20</sup> all described variations of the similar process primarily directed towards the preparation of silicate mixtures for phase equilibrium studies. Schott Glass was the first company (in 1959) to have commercialized a sol-gel coating system made mainly from titanium dioxide (TiO<sub>2</sub>) and silica (SiO<sub>2</sub>). An investigation of bulk glass systems by the sol-gel process was also started at Owens-Illinois, Inc. in 1967 by Levene and Thomas.<sup>21</sup> Up to the early 1990s, only microporous sol-gel materials were being synthesized without any conscious efforts to fine-tune the porosity of the sol-gel materials. After which (around 1992), researchers

at Mobil Corporations, produced silica and other metal oxide materials, containing periodic tunable nanoporous structures using a surfactant-templated process, which often required high temperatures and/or high pressures in the synthesis process.<sup>22</sup> This was the first time that the pore size of synthetic porous materials was expanded from micro (< 1.5 nm) to the mesoporous or more generally speaking nanoporous (1.5 to 10 nm) range.

Thus combining nanotechnology and sol-gel chemistry, an innovative strategy for the synthesis of nanostructured sol-gel porous materials, was discovered. From then on, considerable effort has been devoted to developing nanostructured (i.e., structures roughly in the 2-100 nm size range), porous sol-gel materials with a wide range of porosity, morphology and composition.<sup>23-25</sup> The chemical and mechanical properties that influence porosity during and after the synthesis process have also been extensively studied.<sup>26-28</sup> Advanced characterization methods and instruments have been developed, which further supports and drives the research in developing nanostructured, porous sol-gel materials. Sol-gel chemistry has been easily modified to the changing needs of society to produce fine-tuned sol-gel nanostructured porous materials for relevant applications. Some of the important applications range from, 1) thin films for optical coatings, protective and decorative coatings, and electro-optic components;<sup>26</sup> 2) molded macrostructured bulk materials for use as economical lenses and beam splitters,<sup>29,30</sup> 3) ultra fine ceramic powders as abrasives and multicomponent composites for dental and catalytic applications<sup>31</sup> to 4) microfibers for fiber optic sensors and filters.<sup>32-34</sup>

The optical characteristics, large surface area and easy synthesis of the sol-gel materials in various shapes and sizes are some of the properties that attracted a keen interest in studying sol-gel materials for biosensor and catalytic applications.<sup>35,36</sup>

Contributing to this was the need for a reusable and versatile catalyst, as well as a biocompatible device that could be used extensively in health care applications and as biosensors for detecting harmful agents. In the past ten years this study has developed some very interesting materials, which have been coined as “living ceramics” due to the immobilization of active enzymes, cells and proteins in sol-gel materials.<sup>37,38</sup> Even with the above stated advantages, a lot of work has to be done to stabilize the biomolecules and nanoparticles inside these sol-gel materials for them to be reliable and maintain stability for long periods of time, so that these materials could then be produced economically in large scale, for desired applications. Most of the work done on the synthesis of porous sol-gel materials was done using the surfactant technique that required high temperatures and other harsh conditions, which would cause deactivation and decrease in efficiency of the encapsulated biomolecules. In 1998, our group reported a general nonsurfactant templated sol-gel pathway for the formation of porous metal oxide materials, which not only greatly expanded the categories of the template compounds available for the sol-gel synthesis of porous materials but also was biofriendly and mild enough to be used for biomolecular immobilization.<sup>39-42</sup> This invention thus opened a broad spectrum of opportunities for research in exploring and developing state of the art catalysts and biosensors. Further, the federal funding for nanotechnology research and development in the United States, with major focuses on nanocatalyst, and biosensors, has increased from \$116 million in 1997 to an estimated \$ 1.5 billion in 2005 and is expected to increase to \$4 billion in 2007. This amount does not include the private funding from various companies that approximately increases the funding to 2 times the amount.<sup>43</sup> Also at present the actual worldwide business market for

nanotechnology in which nanocatalyst and biosensors holds more than half the share, is at \$30 billion and is projected to increase to \$2.6 trillion in 2014.<sup>44</sup> These data clearly show an urgent need for efficient, economical and environmentally friendly biosensors and catalysts, which would contribute immensely to the further development of humanity.

For the better understanding of the topics discussed in the coming chapters, the sections from here on in this chapter will deal with the brief review of the sol-gel process, templated sol-gel methods, sizes and shapes of sol-gel materials studied till date and finally the electrospinning technique that was used for the synthesis of sol-gel nanofibers in this dissertation. Finally, due to the importance of revealing and verifying the structural properties of synthesized nano-structured porous products, the major characterization techniques used in this research will be briefly discussed.

## **1.2 Fundamentals of Sol-Gel Process**

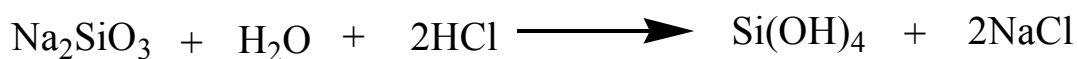
The overall sol-gel process, as the name implies, usually involves two stages as illustrated in Figure 1-1. First, the precursors (usually inorganic salts or organic metal alkoxides) initially undergo hydrolysis and polycondensation to form high molecular weight, yet soluble poly-intermediates called the sol. These intermediates then link together to form a three-dimensional network called a gel. The formation of a gel from both inorganic and organic metal alkoxide precursors will be illustrated in the following section using silica as the primary example.

### **1.2.1 Inorganic Salt Precursors**

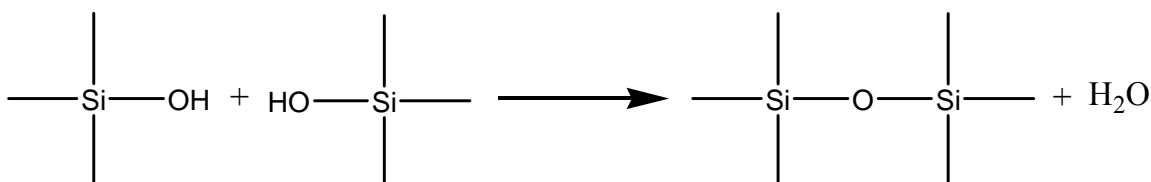
Metal salts that are readily converted to the oxide form by thermal or oxidative decomposition are good candidates for gel formation. Sodium silicates and potassium silicates are two important precursors, which are used for the preparation of porous silica



gels.<sup>45,46</sup> The two steps involved in the chemical reactions are: 1) Hydrolysis of silicates (e.g.,  $\text{Na}_2\text{SiO}_3$ ) to  $\text{Si}(\text{OH})_4$  under acidic conditions, as depicted in a schematic representation (Scheme 1-1), followed by the condensation of the hydrolyzed silicates (Scheme 1-2).<sup>47</sup>



Scheme 1-1. Hydrolysis of silicates (e.g.,  $\text{Na}_2\text{SiO}_3$ ) to  $\text{Si}(\text{OH})_4$  under acidic conditions.

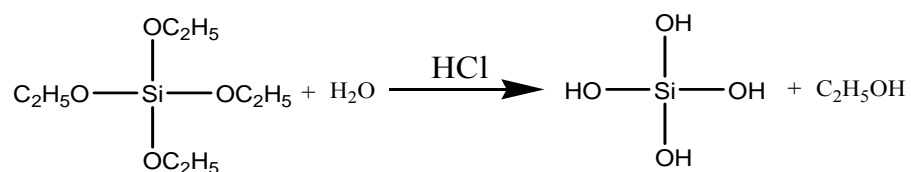


Scheme 1-2. Condensation of the hydrolyzed silicates.

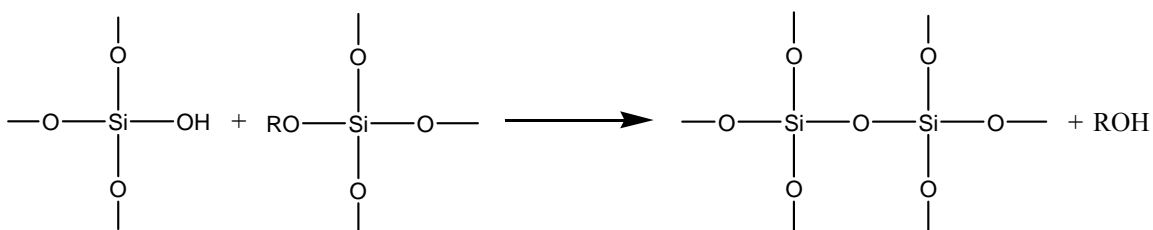
The porosity of the silica gels prepared in this method is affected by the composition of the silicate precursor, temperature, pH, aging and drying conditions, among which pH and the drying condition are the most important ones.<sup>47</sup>

### 1.2.2 Alkoxide Precursors

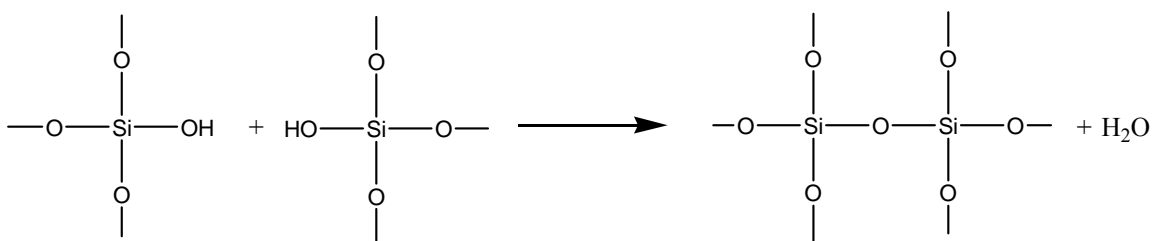
Tetraethylorthosilicate (TEOS), tetramethylorthoxysilicate (TMOS), tetraisopropoxytitanium(IV), tetrapropoxyzirconium(IV) and tributoxyaluminum are some of the alkoxide precursors used in the formation of metal oxides via the sol-gel reactions. TEOS and TMOS are the two main precursors used to synthesize silica due to the controllability of the reaction kinetics. Scheme 1-3 represents the hydrolysis reaction of TEOS in the presence of water and hydrochloric acid. In the next step,  $\text{Si}(\text{OH})_4$  (hydrolyzed form of TEOS) undergoes condensation reaction with the unhydrolyzed TEOS (scheme 1-4) or a self condensation reaction among each other (Scheme 1-5) to finally give rise to silica gel.



Scheme 1-3. Hydrolysis reaction of TEOS in the presence of water and hydrochloric acid.



Scheme 1-4. Condensation reaction of TEOS with hydrolyzed TEOS.



Scheme 1-5. Self-condensation reaction of hydrolyzed TEOS.

The sol-gel materials synthesized using inorganic silicate precursors, as mentioned previously, produce salts, such as NaCl or KCl, as byproducts. These salts are difficult to remove from the silica materials and hence, cause the synthesized silica samples to be impure. In contrast, the gelation reaction of metal alkoxides produces alcohol and water molecules as byproducts that can be readily removed by a simple drying process. Therefore, metal alkoxides are the preferred precursors for the production of porous sol-gel materials with high purity.

### 1.3 Methods of Pore Formation in Nanostructured Sol-Gel Materials

The International Union of Pure and Applied Chemistry (IUPAC) classify porous materials into three main categories,<sup>48</sup> depending on the size of the pores produced:

Microporous	Mesoporous	Macroporous
< 2 nm	2 to 50 nm	> 50 nm

All the synthesized zeolites and the sol-gel materials produced up to year 1990 were microporous (0.7-1.2 nm) in nature.<sup>45,49</sup> No conscious efforts were being made to fine tune the size of pores in the samples. Kresge et al., researchers at Mobil Corporation (in 1992), produced silica and other metal oxide materials containing periodic tunable hexagonal mesoporous structures (1.5 to 10 nm) using a surfactant templating technique.<sup>22,50</sup> From then on, a broad range of pore-forming agents, including various different surfactants and nonsurfactants, as will be mentioned in the coming sections, were tested for formation of different kinds and sizes of pores in sol-gel materials.

#### 1.3.1 Surfactant Templated Method

Alkyltrimethylammonium was the first surfactant to direct the formation of uniform arrangements of hexagonal pores with diameter between 1.5 to 10 nm. The pore size in the samples was controlled by varying the length of the alkyl chains of the template molecules or with the aid of auxiliary organic compounds as additives, spacers and pore fillers.

Figure 1-2 gives the schematic representation of various shapes of pores from hexagonal phase (one-dimensional system of hexagonally arranged cylindrical channels), cubic phase (three-dimensional bicontinuous porous frame structure) to lamellar phase (a

two-dimensional system of layered sheet structure). Other structures with random arrays of pores were also observed.<sup>50,51</sup> The proposed mechanism for the formation of pores using surfactant templating method is called the liquid-crystal templating (LCT) method. “Templating” is a process during which an organic species functions as a central structure, surrounded by inorganic oxide (e.g., silica) framework, as illustrated in Figure 1-3. Here long chain surfactant molecules self-assemble to form various repetitive shapes called micelles that stack up together to finally form liquid crystalline phase. The silicate species or other inorganic species is then deposited between the stacked-up surfactants as seen in Figure 1-3, which then condense to form the inorganic networks. Thus the interaction of the surfactant and silicate species mediates the hexagonal ordering, after which the surfactants are removed by either heating the samples to high temperatures or by solvent extraction to produce porous sol-gel materials. In general, the overall LCT mechanism is directed by two features. One is the dynamics of surfactant molecules to form assemblies, micelle, and ultimately crystalline structure, which functions as template, and the other is the ability of the inorganic oxide to undergo hydrolysis and polycondensation around these crystalline structures to form solid network.<sup>52,53</sup> A wide variety of surfactant molecules with different sizes, shapes, functionalities and charges have been subsequently demonstrated to be able to effectively function as pore structure directing agents. These surfactant molecules are classified into three main groups, depending on their head group chemistry and charges.

- 1) Cationic surfactants:** Here the hydrophilic group carries a positive charge, e.g., tetraalkylammonium salts  $(C_nH_{2n+1})(CH_3)_3NX$ ,  $n = 6, 8, 9, 10, 12, 14, 16, 18, 20, 22$ ;  $X = H, Cl, Br, HSO_4$ ; and  $(C_nH_{2n+1})(C_2H_5)_3N$ ,  $n = 12, 14, 16, 18$ .<sup>54</sup>

- 2) **Anionic surfactants:** The hydrophilic group carries a negative charge, e.g., sulfates<sup>55</sup> ( $C_nH_{2n+1}OSO_3$ ) ( $n = 12, 14, 16, 18$ ), sulfonates<sup>56</sup> ( $C_{16}H_{33}SO_3H$  and  $C_{12}H_{25}C_6H_4SO_3Na$ ), and phosphates<sup>57</sup> ( $C_{12}H_{25}OPO_3H_2$ ,  $C_{14}H_{29}OPO_3K$ ).
- 3) **Neutral surfactants:** The hydrophilic group is not charged, e.g., primary amines ( $C_nH_{2n+1}NH_2$ ) and poly(ethylene oxides) (PEO).<sup>58</sup> Neutral surfactants do not follow the LCT method for pore formation due to the absence of strong electrostatic interactions. Instead they form aggregates due to physical entanglement or hydrogen bonding.<sup>59</sup>

Aluminosilicates and various metal oxides such as titanium oxide, zirconium oxide, vanadium oxide, tungsten oxide, have been used as framework for the formation of pores using the surfactant templated technique. Charged surfactants usually exhibit ordered hexagonal porous structure, while the materials obtained with neutral surfactants sometimes lack long range ordered channel arrangement. The wall thickness, which greatly affects the thermal stability of the material, is controlled by the charge of the surfactant and the formation mechanism. Materials prepared with neutral surfactants usually exhibit a greater wall thickness and furthermore a higher thermal stability than that obtained with ionic surfactants, due to the absence of electrostatic or charge-matching effects.<sup>52,57</sup>

### 1.3.2 Nonsurfactant Templated Method

In the mid 1990s, a novel nonsurfactant templated sol-gel route was invented in our group for the formation of mesoporous silica materials. The templates employed in this method were simple organic compounds, such as glucose, maltose, urea, dibenzoyltartaric acid, and different kinds of readily available artificial sugars.<sup>17,60,61</sup>

Since then, numerous different organic molecules have been studied for use as templates. Unlike the surfactant template method, the nonsurfactant method of pore formation is carried out at room temperature, and the templates are extracted out by simple water extraction. The materials thus produced are mesoporous in nature and have a diameter between 2 to 15 nm. The pore size is controlled by varying the concentration of the templates added into the solution rather than the size of individual template molecules, as is the case in surfactant templates. The materials show high surface area of up to  $\sim 1000 \text{ m}^2 \text{ g}^{-1}$  and large pore volume of up to  $\sim 1.0 \text{ cm}^3 \text{ g}^{-1}$ . The pore structures formed here are not highly ordered and have an interconnected wormlike morphology, which is similar to that of some neutral surfactant templated materials. The actual mechanism of pore formation via nonsurfactant templating sol-gel process is not fully understood. It is proposed that the organic molecules form aggregates, which form interconnected chain assemblies that function as nonsurfactant templates. Several metal oxides, e.g., silica oxide, titanium oxide, zinc phosphate, have been successfully tested using the nonsurfactant templating pathway.<sup>17</sup> In comparison to the surfactant templating technique, the nonsurfactant templating pathway is mild, less expensive, environmentally friendly and biofriendly. The walls of the framework of the nonsurfactant templated samples are thicker ( $\sim 4 \text{ nm}$ ) than the walls in the samples produced using surfactant templates (0.8- 1.5 nm).

#### **1.4 Immobilization of Nanomaterials in Sol-Gel Materials**

In the 1990's, it was realized that nanomaterials (e.g., metal, metal alloys, inorganic nanoparticles, and biomolecules) showed significant advantages for various catalytic and sensor applications. Nanomaterials also showed unique optical, electrical, mechanical and chemical properties, which are quite different from their bulk

counterparts.<sup>62-66</sup> Unfortunately, utilizing these nanomaterials, e.g., biomolecules (enzymes and proteins) and nanoparticles (metal nanoparticles and quantum dots), in their free state as catalysts, was very expensive and disadvantageous, because of their instability in organic chemicals, high temperature, pressure, and the time-consuming methods used to extract them out of the reaction mixtures after use.<sup>67,68</sup> Thus, a broad variety of substrates, e.g., organic polymers and hydrogels, and various encapsulation techniques, like adsorption on solid supports, covalent attachment, and entrapment in polymers, were studied.<sup>69,70</sup> These substrates and techniques showed limited success due to the deformation of the substrates in the reaction mixtures, aggregation of the nanomaterials inside the substrates, thermal instability, limited accessibility of the encapsulated nanomaterials due to the nonporous or microporous nature of the substrate, low surface area, etc. Around this same time, sol-gel materials were being mixed with metal salts and organic dyes at room temperature to obtain colored glass for decorative applications.<sup>71-73</sup> Based on this, further research on using sol-gel materials as a matrix for encapsulating metal nanoparticles, small biomolecules and other nanomaterials was pursued.<sup>74,75</sup> The aim of this study was to obtain uniform, stable distribution of biomolecules or other compounds inside nanoporous sol-gel matrix. This study proved to be successful due to the excellent properties of sol-gel materials including:

- High stability towards chemicals and temperature,
- No photodegradation and, hence, could be used in light induced reaction applications requiring inert substrates,
- Transparent well into the UV range (~250 nm for SiO<sub>2</sub>), and highly suitable for optical applications, and

- Open to a wide variety of chemical modifications.

Many different nanomaterials, such as metal nanoparticles, magnetic nanoparticles, enzymes, proteins, were encapsulated in various sol-gel substrates. The substrates used for these studies were mostly nonporous in nature, which limited the accessibility of the encapsulated nanomaterials to the external reagents.<sup>76,77</sup> The degradation and deactivation rates of the nanomaterials during encapsulation were also very high. Ordered mesoporous molecular sieves synthesized using surfactants showed promise as ideal host matrices for immobilizing nanomaterials, due to its high porosity and surface area. Due to the harsh reaction conditions involved in the hydrothermal synthesis, however (~75 to ~180 °C for several hours to several days), this method was not practical, especially in case of biomolecules, which are extremely sensitive to high temperature. Some attempts made by various research groups to overcome the shortcomings of conventional sol-gel immobilization include substituting the commonly used metal alkoxides, e.g., tetramethylorthosilicate (TMOS) and tetraethylorthosilicate (TEOS), with other sol-gel precursors, using inorganic-organic hybrid host matrices,<sup>78</sup> or stabilizing the nanomaterials before encapsulation by co-immobilizing ligands.

Previous work in our laboratory shows that neutral nonsurfactant organic compounds, such as glucose, fructose, maltose, and glycerol, can be used as pore-forming agents or templates in the synthesis of mesoporous silica materials via the modified sol-gel reactions.<sup>17</sup> This novel synthesis route was further developed for direct immobilization of materials like gold nanoparticles, antibiotics (e.g., vancomycin) and various enzymes (e.g., alkaline phosphatase, acid phosphatase, cytochrome *c*, lipase, heme protein and amyloid  $\beta$  peptide).<sup>41,79,80</sup> In this method the desired biomolecules,



nanoparticles, etc., were added to a mixture of hydrolyzed silica precursor (TMOS or TEOS) and non surfactant template (e.g., glucose) at room temperature. After gelation, the samples were aged, dried and the template was extracted, to finally obtain transparent porous sol-gel bulk samples or powders containing uniformly distributed nanoparticles or biomolecules.

## **1.5 The Process of Electrospinning Nanofibers**

The sol- gel composites mentioned above were further evaluated for potential catalytic and biosensor applications. As the composites are produced in the form of fine powders or as microspheres, recycling or separating the sol-gel composites from reaction mixtures after use become time consuming and expensive. Thus, a method called electrospinning, which was initially used to fabricate polymer nanofibers, was applied for spinning porous sol-gel nanofiber composites. Utilizing this technology, easy extraction of composite fibers from the reaction mixture, as well as further utilization of the fiber composites for catalytic, biosensor, and reinforcement applications, was achieved.

### **1.5.1 History of Electrospinning Nanofibers**

Electrostatic spinning or electrospinning is a process that creates nanofibers through an electrically charged jet of polymer solution or polymer melt. This technology was invented by Formhals in 1934,<sup>81</sup> following which investigations of the process have been carried out by a number of researchers, including Baumgarten (1971),<sup>82</sup> Larrondo and Manley (1981),<sup>83</sup> Reneker, et al. (1996),<sup>84</sup> Wei, et al. (2006)<sup>85</sup>. The electrospinning process, in its simple form, consists of a syringe, which is clamped to an electrically insulated stand, which acts as a support for a blunt capillary pipette. The pipette holds the desired polymer solution, which is to be spun into fibers. A grounded copper plate

covered with aluminum foil acts as a source for the deposition of fibers. A positive voltage is applied to the polymer solution by immersing a copper wire into it. Thus, an electric field is generated between the capillary tube tip containing the polymer solution and the grounded collecting copper plate. The electric field then induces a charge on the surface of the polymer solution, forming a deformed droplet (Taylor cone, Figure 1-6), through which, a charged jet of polymer solution ejects out and is deposited in the form of fibers, as seen in Figure 1-4. A photograph of the electrospinning set up in our laboratory is shown in Figure 1-5. Some of the key points that need to be kept in mind during electrospinning are:

- The solvents present in the spinning solution should evaporate quickly enough for the fiber to retain its integrity when it reaches the collecting target, but not too quickly to allow the fiber to harden before it reaches nanometer range;
- The viscosity and surface tension of the spinning solution must not be too large to prevent the jet from forming, nor be too small to allow the polymer solution to drip from the pipette;
- The power supply should be adequate so as to overcome the viscosity and surface area tension of the polymer solution, to form and sustain the jet from the pipette;
- The grounded plate used to collect fibers should be conductive in nature, and;
- The gap between the tip of the pipette and the grounded plate should not be too close, as this will result in collection of wet fibers.

### **1.5.2 Factors Affecting the Process of Electrospinning Nanofibers**

There are several parameters that influence the morphology of the electrospun fiber, as well as fiber mats. The parameters can be broadly classified into spinning

solution parameters (e.g., molecular weight, solution viscosity, solution conductivity and dielectric effect) and processing condition parameters (e.g., applied voltage, distance, type of collector and surrounding atmospheric conditions).

### 1.5.2.1 Solution Parameters

Viscosity is the measure of resistance to flow. The shear stress  $f$  is the force required to move the plane relative to another that is dependent on a proportionality factor called the coefficient of viscosity,

$$f = \eta \left( \frac{ds}{dt} \right)$$

Scheme 1-6. Viscosity in relation to rate of shear and shear stress.

Where  $\eta$  is viscosity and  $ds/dt$  is the rate of shear.

Two of the important factors that affect the viscosity of the spinning solution are the molecular weight and the concentration of the organic or inorganic polymer solution used to spin fibers.<sup>86-88</sup> Here the molecular weight reflects the length of individual molecular chains. As the molecular weight of the solution increases, the chain entanglement increases and hence, the viscosity increases.<sup>89,90</sup> When the spinning solution leaves the pipette tip during electrospinning, the solution is stretched as it travels towards the grounded metal plate. During the stretching, the large molecular chains present inside the solution entangle among each other and, prevent the spinning solution from breaking up into droplets. The increase in the concentration of the molecules present in the spinning solution also causes greater extent of chain entanglement and, causes increase in viscosity of the solution. As a result, low viscosity or monomeric solutions do not form fibers during electrospinning.

Surface tension (SF) is another property that affects the morphology of the electrospun fibers. SF has the effect of decreasing the surface area per unit mass of a fluid. Here during electrospinning, the solvent present in the spinning solution has a tendency to congregate together, and induce the formation of spherical beads in the fibers. As the viscosity of the solution is increased, the solvent molecules tend to interact with the polymer molecules rather than among each other, hence, reducing the tendency to form beads, thus producing more uniform and smooth fibers.<sup>91</sup>

The conductivity of the spinning solution also plays a role in the morphology of the fibers. The conductivity is increased by addition of small amount of salts or polyelectrolytes into the spinning solution. As the charge of the spinning solution is increased, the repulsion of the charges on the surface of the fibers causes the fibers to extend and hence, causes a decrease in diameter of the collected fibers. The dielectric constant of the solvents used in the spinning solution also plays an important role in fiber diameter. As the dielectric constant of the solvent increases, the diameter of the fibers is found to decrease.<sup>92</sup>

### **1.5.2.2 External Processing Parameters**

Other parameters that affect the electrospinning process and the morphology of the fibers are the external properties that include the applied voltage, the distance between the tip and collector, and feed rate. The applied voltage is one of the crucial properties that affect the size of the fibers. The high voltage induces the required charges in the spinning solution along with the external electric field, which causes an increase in the electrostatic force that overcomes the surface tension of the solution and forms fibers. Research has shown that an approximate voltage of 6 kV is enough to distort the drop of

the spinning solution at the tip of the pipette to form a Taylor Cone during jet initiation.<sup>93</sup> Further increase in voltage causes faster jet formation. If the voltage is increased to 30 kV, the Taylor Cone at the tip of the syringe recedes, due to the increase in speed of fiber formations. The rate at which the solution reaches the tip of the syringe is termed the feed-rate. For a given voltage, there is a corresponding feed rate required for a steady Taylor Cone to be maintained.<sup>93</sup> Thus if the feed rate is not matched to the speed of fiber formation, instability in the fiber formation is noticed, which further causes bead formation. An ideal situation is such that the speed of jet formation matches the feed rate in such a way that the Taylor Cone at the tip of the pipette is not disturbed during the entire electrospinning process.<sup>94,95</sup> Next, the distance between the tip of the pipette and the collecting metal plate needs to be considered. Thick and flat fibers are obtained when the distance of the tip of the pipette is too close to that of the collector. This is because the solvents present in the fiber jet do not have enough time to evaporate, and hence, the fibers are still wet when deposited on the collector, which causes the fibers to blend or stick together.<sup>96</sup> As the spinning distance is increased, the flight time of the jet also increases and the fiber diameter decreases. The morphology of the electrospun fibers is also affected by the surrounding atmosphere, such as the percentage of humidity. The surface of the electrospun fibers tends to form pores if the humidity is above a certain percentage. This could be attributed to the water on top of the fiber surface. As the humidity increases, the pores on the surface of the fibers also increase due to the evaporation of water.<sup>97,98</sup> The type and shape of the fiber collector plays an important role in obtaining fibers in the form of mats, three dimensional scaffolds, etc. The most common method used to collect nanofibers is a flat metal plate, through which films or

mats of nonwoven fibers are obtained. The fibers are also collected on high speed rotating cylindrical collectors, through which aligned and small diameter fibers are obtained. Knife edge disc, wire cage rotating drum, and patterned silicon wafer collector are some of the other examples of fiber collecting device.<sup>99-101</sup>

### **1.5.3 Electrospinning of Sol-gel Composite Fibers**

Metal oxide fibers, e.g., silica and titanium dioxide fibers have been fabricated via a high temperature melt method. In this approach, silicates and metal oxides are heated to a molten state and extruded or drawn into fibers.<sup>102-104</sup> Other techniques involve heating of hydrolyzed metal oxide precursor, such as tetraethylortho silicate (TEOS), to form a viscous solution, which is then drawn into fibers. Three of the main disadvantages of using the above mentioned methods are the application of high temperature, which is not compatible with the encapsulation of nanoparticles and biomaterials, production of large macro-fibers with low surface area, and undesirable mechanical properties.<sup>105,106</sup> An ideal method of obtaining large amounts of sol-gel metal oxide nanofibers at room temperature with easy encapsulation of nanoparticles and biomolecules had to be developed and evaluated. Thus, electrospinning, a method used to spin polymer nanofibers, was modified and used for spinning sol-gel nanofibers. One of the main differences in electrospinning polymer and sol-gel metal oxide fibers is the molecular weight of the spinning solution. As stated in section 1.5, critical values of molecular weight and viscosity are required to produce enough molecular entanglement during electrospinning to obtain polymer nanofibers.<sup>90</sup> On the other hand, sol-gel solutions with limited hydrolysis and condensation are not viscous nor do they have high molecular weight. Thus to obtain sol-gel metal oxide nanofibers, the hydrolyzed sol has to be vacuumed or heated to extract

out solvents and byproducts present in the solution, to increase the viscosity. The entanglement of the hydrolyzed sol-gel solution is induced via hydrogen bonding unlike the physical molecular entanglement produced in polymer solutions. Another important point to consider is that the viscous hydrolyzed sol has a very strong tendency to condense into a gel as seen in Scheme 1-2. This causes the viscous spinning sol to gel in the pipette before forming nanofibers. To counteract this problem, the viscous hydrolyzed sol is cooled to around 0 °C before electrospinning, this causes a decrease in condensation reaction rate and delays gelation. Other methods used to enhance viscosity and hydrogen bonding of the metal oxide spinning solution includes the addition of small amounts of polymer and sugar additives.

The hydrolyzed spinning sol thus produced was further modified by addition of metal salts, nanoparticles and biomolecules and electrospun into composite fibers. Various internal and external electrospinning parameters as explained previously were evaluated to obtain uniform nanofibers. The nanofiber composite fibers were then fine-tuned and evaluated for catalytic, biosensor and dental filler applications.

### **1.6 Characterization Methods for Porous Materials**

Reliable characterization methods are critical in developing efficient porous silica nanoparticle and nanofiber composites. Various structural parameters, such as pore size, pore size distribution, specific surface area, nanofiber diameter, and encapsulated nanoparticles, are some of the important features that need to be evaluated. The techniques used to characterize the samples include gas sorption measurement, small and large angle X-ray diffraction, electron microscopy, infrared, UV-vis and fluorescence spectroscopy.

### 1.6.1 Gas Sorption Measurement

Porous solids tend to adsorb relatively large volumes of condensable gas, due to the large surface area and porosity of the materials. Calculation of the method and amount of gas adsorbed by the material can lead to information on surface area and the pore structure of the sample.<sup>107</sup>

The term “adsorption” was first introduced by Kayser in 1881 to connote the condensation of gases on free surfaces. When a highly dispersed solid is exposed to a gas or vapor of particular pressure in a closed atmosphere, the solid begins to adsorb the gas, resulting in a gradual reduction in the gas pressure at a specific temperature. After some time, the gas pressure becomes constant and the amount of gas adsorbed by the sample can be calculated from the difference in gas pressure by application of gas laws.

The amount of adsorbed gas per gram of solid depends on the equilibrium pressure  $P$ , the temperature  $T$ , and on the nature of the gas and of the sample. For a given gas and sample, the amount of gas adsorbed at a fixed temperature is given by the equation:

$$X = f(P)_{T, \text{gas}, \text{solid}}$$

Scheme 1-7. Represents the amount of gas adsorbed by sample at fixed temperature.

If the gas is below its critical temperature, i.e., if it is in the vapor form, the alternative equation is used:

$$X = f(P/P_0)_{T, \text{gas}, \text{solid}}$$

Scheme 1-8. Represents the amount of gas adsorbed by sample at below critical temperature.



These two equations are expressions of the adsorption isotherm, which can be defined as the relationship between the pressure at which the gas was adsorbed and the equilibrium pressure at constant temperature, used to determine the general pore structure of a porous solid. The adsorption isotherm is usually constructed point-by-point by the aid of a volumetric dosing technique and application of the gas laws.

Though there are tens of thousands of recorded adsorption isotherms, the majority of those isotherms can be grouped into five classes as illustrated in Figure 1-7.<sup>48</sup>

- Type I isotherms are given by microporous solids having relatively small external surfaces, the limiting uptake being governed by the accessible microporous volume rather than by the internal surface area;
- Type II isotherms are obtained with a non-porous or macroporous solid. It demonstrates unrestricted monolayer-multilayer adsorption. The point B labeled in the graph normally means the conversion from monolayer adsorption to multilayer adsorption;
- Type III isotherms are not common. In this case, the adsorbate-adsorbate interaction plays an important role;
- Type IV isotherms have a characteristic hysteresis loop, which is associated with capillary condensation taking place in mesoporous solids. The initial part of the Type IV isotherm is attributed to monolayer-multilayer adsorption since it follows the same path as the corresponding part of a Type II isotherm. Type IV isotherms are given by many mesoporous materials, and;

- Type V isotherms are not common; they are related to the Type III isotherms in that the adsorbate-adsorbate interactions are weak, but is obtained with certain porous adsorbents.

Hysteresis in Type IV isotherms is usually associated with capillary condensation in mesopores structures.<sup>48,108,109</sup> There are four types of hysteresis loops as shown in Figure 1-8:

- H1 loop is always associated with pores with regular shape and narrow size distribution;
- H2 loop is especially difficult to interpret: it was originally attributed to a difference in mechanism between condensation and evaporation processes occurring in pores with narrow necks and wide bodies,<sup>109</sup> but now it is believed that the interconnected network between pores<sup>17,39</sup> also contributes to the H2 loop;
- H3 loop, which does not exhibit any limiting adsorption at high  $P/P_0$ , is observed with aggregates of plate-like particles, and;
- H4 loop is often assigned to narrow slit-like pores.

The Brunauer-Emmett-Teller (BET) gas adsorption method<sup>48</sup> has become the most widely used standard procedure for the determination of the surface area of finely divided and porous materials. The BET equation can be described in the linear form as:

$$\frac{P}{n^a \cdot (P_0 - P)} = \frac{1}{n_m^a \cdot C} + \frac{(C-1) \cdot P}{n_m^a \cdot C \cdot P_0}$$

Scheme 1-9. The Brunauer-Emmett-Teller (BET) gas adsorption equation.

Where,  $n^a$  is the amount of gas adsorbed at a relative pressure  $P/P_0$  and  $n_m^a$  is the monolayer capacity.

### 1.6.2 X-Ray Diffraction (XRD)

X-ray diffraction is one of the cornerstones of twentieth century science.<sup>110</sup> It has been widely used to characterize sol-gel nanoporous materials. X-rays are relatively short wavelength and high energy electromagnetic radiations, generated from a source and focused into a fine beam that is then shone on to a solid sample. Some of the focused X-ray beam is scattered and some adsorbed by the sample leading to a phenomenon called diffraction. It is analogous to a perfectly elastic collision between a photon and an electron. The photon changes direction after colliding with the electron but transfers some of its energy to the electron. The result is that the scattered photon leaves in a new direction but with the same phase and energy as that of the incident photon. Structural information can therefore be deduced from the knowledge of scattering intensity and angle.<sup>111</sup> For example, approximated as the repeating distance in the porous materials, the sum of a pore diameter and a pore wall thickness can be estimated based on the  $d$  spacing calculated from the Bragg equation.

$$n\lambda = 2d \sin \theta$$

Scheme 1-10. Bragg equation.

Where  $\lambda$  is the wavelength,  $d$  is the separation between planes and  $\theta$  is the diffraction angle. In the case of nanoporous materials with regular pore diameter and wall thickness, the  $d$  spacing is the sum of the pore diameter and wall thickness. Using the same X-ray diffraction phenomenon, the size, type and distribution of various metal and metal oxide nanoparticles present inside polymer and silica materials can be evaluated.

### 1.6.3 Electron Microscopy

Electron microscopic observations can provide a straightforward evaluation of pore size, shape and distribution of nanoparticles in the nanoporous materials.<sup>112-114</sup>

Generally, electron microscopes use a beam of highly energetic electrons to examine objects on a very fine scale. This examination can yield the following information:

*Topography*: The surface features of an object or "how it looks", its texture;

*Morphology*: The shape and size of the particles making up the object;

*Composition*: The elements and compounds that the object is composed of, and;

*Crystallographic Information*: How the atoms are arranged in the object.

There are two types of electron microscopes: the transmission electron microscope (TEM) which uses a focused beam of electrons to "see through" the specimen. The scanning electron microscope (SEM), utilizes an electron beam that interacts with the surface of the sample and supplies information on the surface morphology of a sample, unlike TEM, which mainly gives information on the internal characteristics of a sample.

## 1.7 Organization of this Dissertation

Chapter 2 deals with the synthesis and characterization of porous silica material containing silver nanoparticles. Glucose was used as the reducing agent, to reduce silver nitrate to silver nanoparticles. Chapter 3 deals with fabrication of organic-inorganic hybrid nanofiber mats via the electrospinning method. The various factors affecting the morphology and diameter of the fibers were studied. The fibers were also characterized using various spectroscopic and microscopic methods. The fiber mats thus produced were then used as reinforcement materials for preparing dental resin composites, as described in chapter 4. The mechanical properties of the composites were tested. The effect of fiber

content on the fracture strength and elastic modulus of the dental composites was also evaluated. Next porous silica nanofibers containing silver and gold nanoparticle were fabricated as explained in chapter 5. The factors affecting the size and distribution of silver and gold nanoparticles inside the fibers were studied. The fibers thus produced were then tested for catalytic activity. Chapter 6 deals with the encapsulation of enzyme in porous silica nanofibers, using the electrospinning method. The factors affecting the catalytic activity of the encapsulated enzymes were evaluated. Chapter 7 explains the research done to align quantum dots inside silica/polymer composite fibers, for use in telecommunication and sensor applications. A brief conclusion and future work is given in chapter 8. Appendix A represents the work done in encapsulating several enzymes and manganese dioxide, in porous silica materials, as part of the ongoing collaborations with universities and companies. Finally, Appendix B represents the research proposal defended and passed on November 1<sup>st</sup>, 2004, in partial fulfillment of the requirement for the Ph.D. candidacy.

## 1.7 Reference List

1. National Nanotechnology Initiative.  
<http://www.nano.gov/html/facts/whatIsNano.html> . 2006.
2. Taniguchi, N. On the basic concept of nano-technology. Japan society of precision engineering. International Conference Proceeding Engineering Part II. 1978.
3. Drexler. K. E., forwarded by Minsky, M. Engines of creation: the coming era of nanotechnology. Anchor Books Editions, New York. 1986.
4. Drexler. K. E. Nanosystems: molecular machinery, manufacturing, and computation. John Wiley & Sons, Inc., New York. 1992.
5. Song, C., Cui, X., Shi, R., Leng, X., Jiang, Y., Lin, G., Wang, P. Microporous capsules for long-acting drug delivery. Preparation and in vitro drug release evaluation. Zhongguo Shengwu Yixue Gongcheng Xuebao, 10(3), 196-202. 1991.
6. Lim, S. C., Kim, K. S., Lee, I. B., Jeong, S. Y., Cho, S., Yoo, J. E., Lee, Y. H. Nanomanipulator-assisted fabrication and characterization of carbon nanotubes inside scanning electron microscope. Micron, 36(5), 471-476. 2005.
7. Nakayama, Y., Akita, S., Harada, A., Okawa, T. Nanotweezers and nanomanipulators. Daiken Chemical Co., Ltd. Japan. JP1803(2001066460). WO. 2001.
8. Sun, J., Fang, X. Q., Xi, C. Current situation of research on nano-drugs. Yaoxue Fuwu Yu Yanjiu, 3(2), 87-89. 2003.
9. Patel, A. C., Wei, Y. Electrospinning of silica nanofibers containing quantum dots. Abstracts of Papers, 230th American Chemical Society National Meeting, Washington, DC, United States, INOR-158. 2005.
10. Patel, A. C., Li, S., Wei, Y., Wang, C., Zhang, W. Electrospinning of porous silica micro/nanofibers containing silver nanoparticles. Polymer Materials Science Engineering Preprints, 91, 690-691. 2004.
11. Zhou, B., Trevino, H., Wu, Z., Zhou, Z., Liu, C. Reforming nanocatalysts and method of making and using such catalysts. 101241(2006102521). US. 2005.
12. Becerril-Garcia, H. A., Harrison, R. G., Woolley, A. T. Advances in DNA-templated nanofabrication of electronic devices. Abstracts of Joint Regional Meeting of the Northwest and Rocky Mountain Sections of the American Chemical Society, Logan, UT, United States, GEN-200. 2004.
13. Nagahara, L.A., Oden, P.I., Majumdar, A., Carrejo, J.P., Graham, J., Alexander, J. Nanofabrication utilizing the atomic force microscope. Proceedings of SPIE-The International Society for Optical Engineering. 1639(Scanning Probe Microsc.), 171-179. 1992.
14. Patel, A. C., Li, S., Yuan, J. M., Wei, Y. In situ encapsulation of horseradish peroxidase in electrospun porous silica fibers for potential biosensor applications. Nano Letters, 6(5), 1042-1046. 2006.
15. Letant, Sonia E., Hart, Bradley R., Kane, Staci R., Hadi, Masood Z., Shields, Sharon J., Cheng, Tu Chen, Rastogi, Vipin K., Del Eckels, J., Reynolds, John G. Development of a hybrid enzyme-based porous silicon platform for chemical

- warfare agent detection. *Materials Research Society Symposium Proceedings*. 828 (Semiconductor Materials for Sensing), 63-68. 2005.
16. Stein, A., Melde, B. J., Schroden, R. C. Hybrid inorganic-organic meso-porous silicates-nanoscope reactors coming of age. *Advanced Materials*, 12(19), 1403-1419. 2000.
  17. Wei, Y., Xu, J., Dong, H., Dong, J. H., Qiu, K., Jansen-Varnum, S. Preparation and physisorption characterization of glucose-templated mesoporous silica sol-gel materials. *Chemistry of Materials*, 11(8), 2023-2029. 1999.
  18. Roy, D. M., Roy, R. Synthesis and stability of minerals in the system MgO-Al<sub>2</sub>O<sub>3</sub>-SiO<sub>2</sub>-H<sub>2</sub>O. *American Mineralogist*, 40, 147-178. 1955.
  19. Hamilton, D. L., Mackenzie, W. S. Nepheline solid solutions in the system NaAlSiO<sub>4</sub>-KAlSiO<sub>4</sub>-SiO<sub>2</sub>. *Journal of Petrology*, 1, 56-72. 1960.
  20. Biggar, G. M., O'Hara, M. J. Comparison of gel and glass starting materials for phase equilibrium studies. *Mineralogical Magazine and Journal of the Mineralogical Society*, 37(286), 198-205. 1969.
  21. Levene, L., Thomas, I. M. Converting metal-organic compounds to high-purity oxide products. Owens-Illinois, Inc. 69-843777(3640093). US. 1969.
  22. Kresge, C. T., Leonowicz, M. E., Roth, W. J., Vartuli, J. C., Beck, J. S. Ordered mesoporous molecular sieves synthesized by a liquid-crystal template mechanism. *Nature*, 359(6397), 710-712. 1992.
  23. Deshpande, S. B., Potdar, H. S., Kholam, Y., Patil, K. R., Pasricha, R., Jacob, N. E. Room temperature synthesis of mesoporous aggregates of anatase TiO<sub>2</sub> nanoparticles. *Materials Chemistry and Physics*, 97, 207-212. 2006.
  24. Hou, B., Li, Z. J., Xu, Y., Wu, D., Sun, Y. H. Size-controllable barium titanate nanopowder synthesized via one-pot solvothermal route in a mixed solvent. *Journal of Electroceramics*, 16, 127-133. 2006.
  25. Pang, J. B., Qiu, K. Y., Wei, Y. Preparation and characterization of hydroxyapatite microspheres with hollow core and mesoporous shell. *Bioceramics*, 309-311, 65-68. 2006.
  26. Yao, L., Zhu, Y., Qu, D., Du, M., Shen, J., Wang, J. Optical and hydrophobic nano-porous silica thin films with low refractive index. *Proceedings of SPIE-The International Society for Optical Engineering*, 6034, 60340V-1-60340V/7. 2006.
  27. Di, Y., Meng, X., Wang, L., Li, S., Xiao, F. S. Ultralow temperature synthesis of ordered hexagonal smaller supermicroporous silica using semifluorinated surfactants as template. *Langmuir*, 22(7), 3068-3072. 2006.
  28. Kawakami, N., Hirano, T., Fukumoto, Y. Low-temperature sol-gel preparation of low-shrinkage porous silica layers using a supercritical fluid process for porogen removal and structure stabilization. Kabushiki Kaisha Kobe Seiko Sho, Japan. 2004-995234(2005119360). US. 2004.
  29. Nogues, J. L., Howell, R. L. Fabrication of pure silica micro-optics by sol-gel processing. *Proceedings of SPIE-The International Society for Optical Engineering*, 1751(Miniature and Micro-Optics: Fabrication and Systems Applications II), 214-224. 1993.
  30. Takeuchi, T. Manufacture of monolithic quartz glass by sol-gel process. (Seiko Epson Corp., Japan. 88-297691(02145447). JP. 1988.

31. Prencipe, M. Viscoelastic dentifrice composition. (Colgate-Palmolive Co., USA. 92-202397(525913). EP. 1992.
32. Jin, X., Jing, M., Zhou, K., Chi, D., Ge, H., Li, W., Zhuang, Z., Wang, X. The detection of nitrogen dioxide in air with fiber optical sensor based on sol-gel film. *Fenxi Huaxue*, 33(9), 1215-1218. 2005.
33. Xie, W., Sun, Tong., Grattan, K. T., McPolin, D., Basheer, P. A. M., Long, A. E. Fiber optic chemical sensor systems for internal concrete condition monitoring. *Proceedings of SPIE-The International Society for Optical Engineering*, 5502(Second European Workshop on Optical Fibre Sensors, 2004), 334-337. 2004.
34. Sumida, S., Okazaki, S., Ishii, T., Asakura, S., Nakagawa, H., Murayama, H., Kamita, T., Hasegawa, T. Evaluation of a fiber-optic gas sensor prepared by etching method for distributed hydrogen determination. *Chemical Sensors*, 20(Suppl. A), 7-9. 2004.
35. Wei, L., Cui, L. Progress of sol-gel application in biosensors. *Huaxue Chuanganqi*, 23(4), 1-7. 2003.
36. Tang, Y., Cheng, F. Application and development of sol-gel biosensors by immobilization methods. *Zhongnan Minzu Xueyuan Xuebao, Ziran Kexueban*, 19(1), 89-94. 2000.
37. Anon, A. New class of living ceramics developed. *American Ceramic Society Bulletin*, 74(9), 31. 1995.
38. Pope, E. J. A., Braun, K., Van, H. M. Peterson, C. M., Tresco, P., Andrade, J. D. Living ceramics. *Ceramic Transactions 55(Sol-Gel Science and Technology)*, 33-49. 1995.
39. Wei, Y., Dong, H., Xu, J., Wang, C., Feng, Q., Qiu, K. Y., Li, Z. C., Jansen, S. A. Nonsurfactant route to nanoporous phenyl-modified hybrid silica materials. *Series on Chemical Engineering 4(Nanoporous Materials)*, 188-205. 2004.
40. Wei, Y., Dong, H., Xu, J., Feng, Q. Simultaneous immobilization of horseradish peroxidase and glucose oxidase in mesoporous sol-gel host materials. *ChemPhysChem*, 3(9), 802-808. 2002.
41. Wei, Y., Xu, J., Feng, Q., Lin, M., Dong, H., Zhang, W. J., Wang, Ce. A novel method for enzyme immobilization: direct encapsulation of acid phosphatase in nanoporous silica host materials. *Journal of Nanoscience and Nanotechnology*, 1(1), 83-93. 2001.
42. Dong, H., Xu, J., Qiu, K., Jansen-Varnum, S. A., Wei, Y. Synthesis of nonsurfactant-based hybrid mesoporous sol-gel materials. *Book of Abstracts, 219th American Chemical Society National Meeting, San Francisco, CA, OLY-129*. 2000.
43. The National Nanotechnology Coordination Office. Nanotechnology Funding. [http://www.nano.gov/html/funding/home\\_funding.html](http://www.nano.gov/html/funding/home_funding.html). 2006.
44. Genetic Engineering News. Nanotechnology Funding. <http://www.genengnews.com/news/bnitem.aspx?name=1255070>. 2006.
45. Brinker, J. C., Scherer, W. G. *Sol-gel science: The physics and chemistry of sol-gel processing*. Elsevier Science, California. 1990.
46. Aegerter, M. A., Mennig, M. *Sol-gel technologies for glass producers and users*. Kluwer Academic Publications, Massachusetts. 2004.



47. Iler, R. K. *The Chemistry of Silica: Solubility, Polymerization, Colloid and Surface Properties and Biochemistry*. John Wiley & Sons, Inc., New York. 1979.
48. Sing, K. S. W., Everett, D. H., Haul, R. A. W., Moscou, L., Pierotti, R. A., Rouquerol, J., Siemieniewska, T. Reporting physisorption data for gas/solid systems with special reference to the determination of surface area and porosity (Recommendations 1984). *Pure and Applied Chemistry*, 57(4), 603-619. 1985.
49. Skeels, G. W., Breck, D. W. Zeolite chemistry. V - substitution of silicon for aluminum in zeolites via reaction with aqueous fluorosilicate. *Proceedings International Zeolite Conference*, 6th, 87-96. 1984.
50. Beck, J. S., Vartuli, J. C., Roth, W. J., Leonowicz, M. E., Kresge, C. T., Schmitt, K. D., Chu, C. T. W., Olson, D. H., Sheppard, E. W. A new family of mesoporous molecular sieves prepared with liquid crystal templates. *Journal of the American Chemical Society*, 114(27), 10834-10843. 1992.
51. Barton, T. J., Bull, L. M., Klemperer, W. G., Loy, D. A., McEnaney, B., Misono, M., Monson, P. A., Pez, G., Scherer, G. W., Vartuli, J. C., Yaghi, O. M. Tailored porous materials. *Chemistry of Materials*, 11(10), 2633-2656. 1999.
52. Raman, N. K., Anderson, M. T., Brinker, C. J. Template-based approaches to the preparation of amorphous, nanoporous silicas. *Chemistry of Materials*, 8(8), 1682-1701. 1996.
53. Jones, W., Rao, C. N. R., Editors. *Supramolecular Organization and Materials Design*, 446. 2002.
54. Karra, V. R., Moudrakovski, I. L., Sayari, A. Odd-even effect in the synthesis of mesoporous silicate molecular sieves in the presence of alkyl cetyl dimethyl ammonium bromide. *Journal of Porous Materials*, 3(2), 77-82. 1996.
55. Huo, Q., Margolese, D. I., Ciesla, U., Demuth, D. G., Feng, P., Gier, T. E., Sieger, P., Firouzi, A., Chmelka, B. F. Organization of organic molecules with inorganic molecular species into nanocomposite biphasic arrays. *Chemistry of Materials*, 6(8), 1176-1191. 1994.
56. Antonelli, D. M., Ying, J. Y. Synthesis of hexagonally packed mesoporous TiO<sub>2</sub> by a modified sol-gel method. *Angewandte Chemie, International Edition in English*, 34(18), 2014-2017. 1995.
57. Tanev, P. T., Pinnavaia, T. J. A neutral templating route to mesoporous molecular sieves. *Science (Washington, D.C.)*, 267(5199), 865-867. 1995.
58. Bagshaw, S. A., Pinnavaia, T. J. Mesoporous alumina molecular sieves. *Angewandte Chemie, International Edition in English*, 35(10), 1102-1105. 1996.
59. Bagshaw, S. A., Prouzet, E., Pinnavaia, T. J. Templating of mesoporous molecular sieves by nonionic polyethylene oxide surfactants. *Science (Washington, D.C.)*, 269(5228), 1242-1244. 1995.
60. Pang, J. B., Qiu, K. Y., Wei, Y. A novel nonsurfactant pathway to hydrothermally stable mesoporous silica materials. *Microporous and Mesoporous Materials*, 40(1-3), 299-304. 2000.
61. Pang, J. B., Qiu, K. Y., Wei, Y. Preparation of mesoporous silica materials with non-surfactant hydroxy-carboxylic acid compounds as templates via sol-gel process. *Journal of Non-Crystalline Solids*, 283(1-3), 101-108. 2001.

62. Anderson, M. L., Morris, C. A., Stroud, R. M., Merzbacher, C. I., Rolison, D. R. Colloidal gold aerogels: preparation, properties, and characterization. *Langmuir*, 15(3), 674-681. 1999.
63. Pradhan, N., Pal, A., Pal, T. Silver nanoparticle catalyzed reduction of aromatic nitro compounds. *Colloids and Surfaces, A: Physicochemical and Engineering Aspects*, 196(2-3), 247-257. 2002.
64. Jana, N. R., Sau, T. K., Pal, T. Growing small silver particle as redox catalyst. *Journal of Physical Chemistry B*, 103(1), 115-121. 1999.
65. Avnir, D., Braun, S., Lev, O., Ottolenghi, M. Enzymes and other proteins entrapped in sol-gel materials. *Chemistry of Materials*, 6(10), 1605-1614. 1994.
66. Dave, B. C., Czernuszewicz, R. S., Prickril, B. C., Kurtz, D. M., Jr. Resonance raman spectroscopic evidence for the FeS<sub>4</sub> and Fe-O-Fe sites in rubrerythrin from *desulfovibrio vulgaris*. *Biochemistry*, 33(12), 3572-3576. 1994.
67. Canamares, M. V., Garcia-Ramos, J. V., Gomez-Varga, J. D., Domingo, C., Sanchez-Cortes, S. Comparative study of the morphology, aggregation, adherence to glass, and surface-enhanced raman scattering activity of silver nanoparticles prepared by chemical reduction of Ag<sup>+</sup> using citrate and hydroxylamine. *Langmuir*, 21(18), 8546-8553. 2005.
68. Jana, N. R., Sau, T. K., Pal, T. Growing small silver particle as redox catalyst. *Journal of Physical Chemistry B*, 103(1), 115-121. 1999.
69. Schmid, G. Large clusters and colloids. *Metals in the embryonic state. Chemical Reviews (Washington, DC, United States)*, 92(8), 1709-1727. 1992.
70. Lewis, L. N. Chemical catalysis by colloids and clusters. *Chemical Reviews (Washington, DC, United States)*, 93(8), 2693-2730. 1993.
71. Schmidt, U., Schnabel, M., Fuessmann, K., Kaiser, B. Dyeing of silica glass fibers. (Frenzelit-Werke G.m.b.H.und Co.K.-G., Fed. Rep. Ger. 87-3725505(3725505), 5. DE. 1987.
72. Schmidt, U., Schnabel, M., Fussman, K. Thermally stabilized silica glass fibers and textiles, and their manufacture. (Frenzelit-Werke G.m.b.H.und Co.K.-G., Fed. Rep. Ger. 88-112338(301574), 7. EP. 1988.
73. Toki, M., Kanbe, S., Kitabayashi, H., Myashita, S., Takeuchi, T. Manufacture of colored glass. (Seiko Epson Corp., Japan. 86-58675(62216930), 4. JP. 1986.
74. Epifani, M., Giannini, C., Tapfer, L., Vasanelli, L. Sol-gel synthesis and characterization of Ag and Au nanoparticles in SiO<sub>2</sub>, TiO<sub>2</sub>, and ZrO<sub>2</sub> thin films. *Journal of the American Ceramic Society*, 83(10), 2385-2393. 2000.
75. Wang, Y. & Caruso, F. Mesoporous silica spheres as supports for enzyme immobilization and encapsulation. *Chemistry of Materials*, 17, 953-961. 2005.
76. Bronstein, L. M., Polarz, S., Smarsly, B., Antonietti, M. Sub-nanometer noble-metal particle host synthesis in porous silica monoliths. *Advanced Materials (Weinheim, Germany)*, 13(17), 1333-1336. 2001.
77. Gill, I., Ballesteros, A. Encapsulation of biologicals within silicate, siloxane, and hybrid sol-gel polymers: an efficient and generic approach. *Journal of the American Chemical Society*, 120, 8587-8598. 1998.
78. Liu, J., Feng, X., D., Fryxell, G. E., Wang, L. Q., Kim, A. Y., Gong, M. L. Hybrid mesoporous materials with functionalized monolayers. *Advanced Materials (Weinheim, Germany)*, 10(2), 161-165. 1998.

79. Zheng, J. Y., Pang, J. B., Qiu, K. Y., Wei, Y. Synthesis of mesoporous titanium dioxide materials by using a mixture of organic compounds as a non-surfactant template. *Journal of Materials Chemistry*, 11(12), 3367-3372. 2001.
80. Sun, Z., Patel, A. C., Yuan, J. M., Schweitzer-Stenner, R., Wei, Y. A novel method to study aggregation of amyloid b1-42 - a key peptide associated with Alzheimer's disease. *Abstracts of Papers, 231st American Chemical Society National Meeting, Atlanta, GA, United States, INOR-128*. 2006.
81. Formhals, A. Apparatus and process for making artificial threads. 1,975,504. US. 1934.
82. Baumgarten, P. K. Electrostatic spinning of acrylic microfibers. *Journal of Colloid and Interface Science*, 36(1), 71-79. 1971.
83. Larrondo, L., Manley, J. R. Electrostatic fiber spinning from polymer melts. I. experimental observations on fiber formation and properties. *Journal of Polymer Science, Polymer Physics Edition*, 19(6), 909-920. 1981.
84. Reneker, D. H., Chun, I. Nanometer diameter fibers of polymer, produced by electrospinning. *Nanotechnology*, 7(3), 216-223. 1996.
85. Patel, A. C., Li, S., Yuan, J. M., Wei, Y. In situ encapsulation of horseradish peroxidase in electrospun porous silica fibers for potential biosensor applications. *Nano Letters*, 6(5), 1042-1046. 2006.
86. Doshi, J., Reneker, D. H. Electrospinning process and applications of electrospun fibers. *Journal of Electrostatics*, 35(2&3), 151-160. 1995.
87. Zeng, J., Hou, H., Wendorff, J. H., Greiner, A. Processing parameters for electrospun poly(vinyl alcohol) (PVA) nanofibers and photo-mediated crosslinking of modified PVA nanofibers. *Polymer Preprints (American Chemical Society, Division of Polymer Chemistry)*, 44(2), 174-175. 2003.
88. Nyame, V., Dong, H., Jones, W. E., Jr. Systematic study of the physiochemical properties of polymer nanofibers. *Abstracts of Papers, 226th American Chemical Society National Meeting, New York, NY, United States, CHED-208*. 2003.
89. McKee, M. G., Hunley, M. T., Layman, J. M., Long, T. E. Solution rheological behavior and electrospinning of cationic polyelectrolytes. *Macromolecules*, 39(2), 575-583. 2006.
90. Shenoy, S. L., Bates, W. D., Frisch, H. L., Wnek, G. E. Role of chain entanglements on fiber formation during electrospinning of polymer solutions: good solvent, non-specific polymer-polymer interaction limit. *Polymer*, 46(10), 3372-3384. 2005.
91. Fong, H., Chun, I., Reneker, D. H. Beaded nanofibers formed during electrospinning. *Polymer*, 40(16), 4585-4592. 1999.
92. Son, W. K., Youk, J. H., Lee, T. S., Park, W. H. The effects of solution properties and polyelectrolyte on electrospinning of ultrafine poly(ethylene oxide) fibers. *Polymer*, 45(9), 2959-2966. 2004.
93. Tayler GI. *Proceedings of the royal society of london, Series A.*, 280, 383-397. 1964.
94. Yarin, A. L., Koombhongse, S., Reneker, D. H. Taylor cone and jetting from liquid droplets in electrospinning of nanofibers. *Journal of Applied Physics*, 90(9), 4836-4846. 2001.

95. Deitzel, J. M., Kleinmeyer, J. D., Hirvonen, J. K., Beck Tan, N. C. Controlled deposition of electrospun poly(ethylene oxide) fibers. *Polymer*, 42(19), 8163-8170. 2001.
96. Buchko, C. J., Chen, L. C., Shen, Y., Martin, D. C. Processing and microstructural characterization of porous biocompatible protein polymer thin films. *Polymer*, 40(26), 7397-7407. 1999.
97. Casper, C. L., Stephens, J., Chase, B., Rabolt, J. Using humidity and molecular weight to control the surface morphology of electrospun fibers. Abstracts of Papers, 226th American Chemical Society National Meeting, New York, NY, United States, OLY-496. 2003.
98. Casper, C. L., Stephens, J. S., Tassi, N. G., Chase, D. B., Rabolt, J. F. Controlling surface morphology of electrospun polystyrene fibers: effect of humidity and molecular weight in the electrospinning process. *Macromolecules*, 37(2), 573-578. 2004.
99. Bunyan, N., Chen, J., Chen, I., Farboodmanesh, S. Disc electrode for converging and directing electrospun fibers. Abstracts of Papers, 226th American Chemical Society National Meeting, New York, NY, United States, OLY-328. 2003.
100. Baker, S. C., Atkin, N., Gunning, P. A., Granville, N., Wilson, K., Wilson, D., Southgate, J. Characterisation of electrospun polystyrene scaffolds for three-dimensional in vitro biological studies. *Biomaterials*, 27, 3136-3146. 2006.
101. Aussawasathien, D., Dong, J. H., Dai, L. Electrospun polymer nanofiber sensors. *Synthetic Metals*, 154, 37-40. 2005.
102. Rosenflanz, A. Z. Melt spinning method for making amorphous material and fibers with processing to fabricate glass, ceramics and glass-ceramics. (3M Innovative Properties Co., USA. 2002-211684(2004020245). US. 2002.
103. Ceramic fibers or wool. (Gmundner Zementwerke Hans Hatschek A.-G., Austria. 80-4998(368475). AT. 1980.
104. Goto, T. The analysis on the dynamics of the melt spinning of metals using the spinnability of glass. *Sen'i Gakkaishi*, 34(6), T237-T244. 1978.
105. Chatterjee, M., Naskar, M. K., Chakrabarty, P. K., Ganguli, D. Mullite fibre mats by a sol-gel spinning technique. *Journal of Sol-Gel Science and Technology*, 25(2), 169-174. 2002.
106. Jung, K. T., Chu, Y. H., Haam, S., Shul, Y. G. Synthesis of mesoporous silica fiber using spinning method. *Journal of Non-Crystalline Solids*, 298(2,3), 193-201. 2002.
107. Gregg, S. J., Sing, K. S. W. Adsorption, Surface Area and Porosity. 2nd Edition, 303. 1982.
108. Lee, C. K., Chiang, A. S. T., Tsay, C. S. The characterization of porous solids from gas-adsorption measurements. *Key Engineering Materials*, 115, 21-43. 1996.
109. Barrett, E. P., Joyner, L. G., Halenda, P. P. The determination of pore volume and area distributions in porous substances. I. Computations from nitrogen isotherms. *Journal of the American Chemical Society*, 73, 373-380. 1951.
110. Stoeckli, H. F. A generalization of the Dubinin-Radushkevich equation for the filling of heterogeneous micropore systems. *Journal of Colloid and Interface Science*, 59(1), 184-185. 1977.

111. Terasaki, O., Ohsuna, T., Liu, Z., Sakamoto, Y., Garcia-Bennett, A. E. Structural study of meso-porous materials by electron microscopy. *Studies in Surface Science and Catalysis*, 148(Mesoporous Crystals and Related Nano-Structured Materials), 261-288. 2004.
112. Innes, R. W., Fryer, J. R., Stoeckli, H. F. On the correlation between micropore distribution obtained from molecular probes and from high resolution electron microscopy. *Carbon*, 27(1), 71-76. 1989.
113. Sasaki, Y., Kato, H. Nanostructure analysis for applied research on zeolites. *Zeolites*, 21(1), 11-17. 2004.
114. Terasaki, O., Ohsuna, T. Structural study of microporous and mesoporous materials by transmission electron microscopy. *Handbook of Zeolite Science and Technology*, 291-315. 2003.

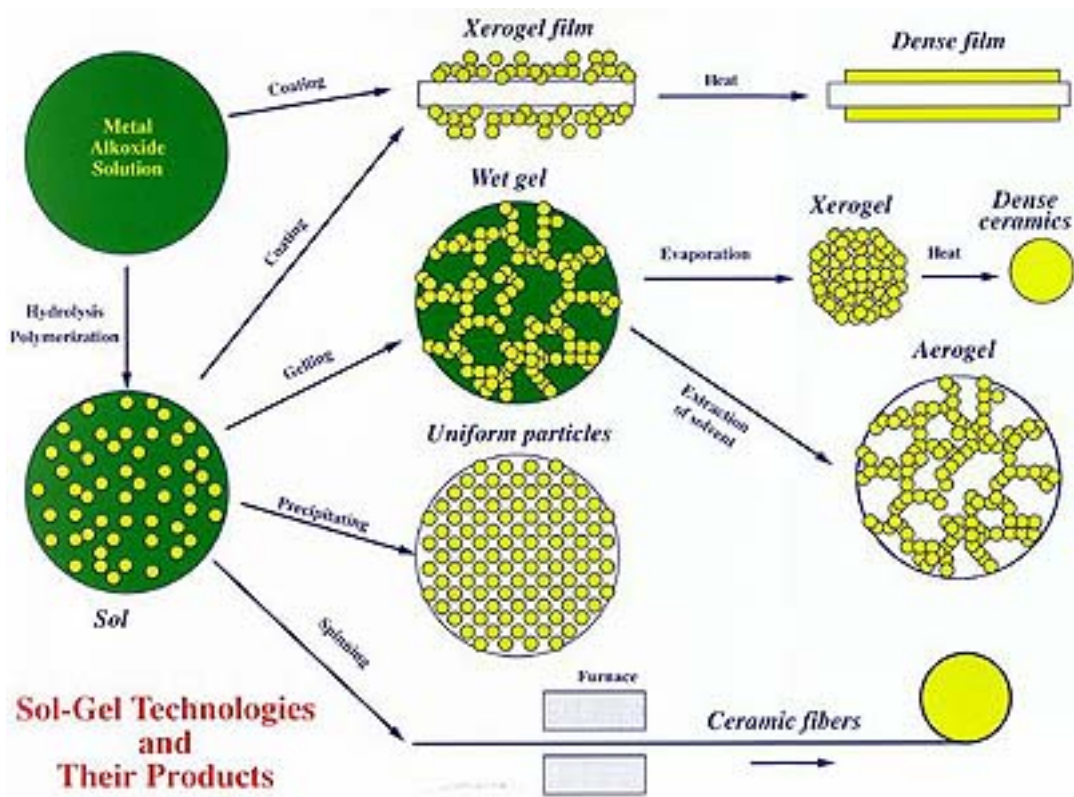


Figure 1-1. Sol-gel process and the products. ([www.chemat.com/html/solgel.html](http://www.chemat.com/html/solgel.html))

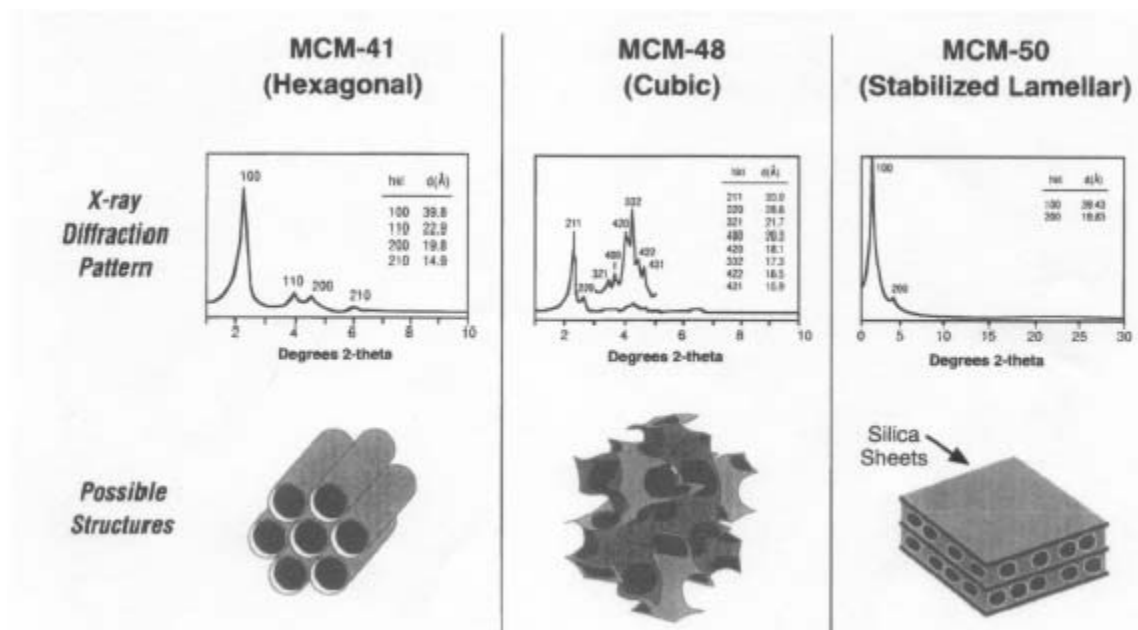


Figure 1-2. Three structure types proposed for silica-surfactant mesophase and the x-ray diffraction patterns: (a) MCM-41 (hexagonal); (b) MCM-48 (cubic); (c) MCM-50 (lamellar).<sup>50,51</sup>

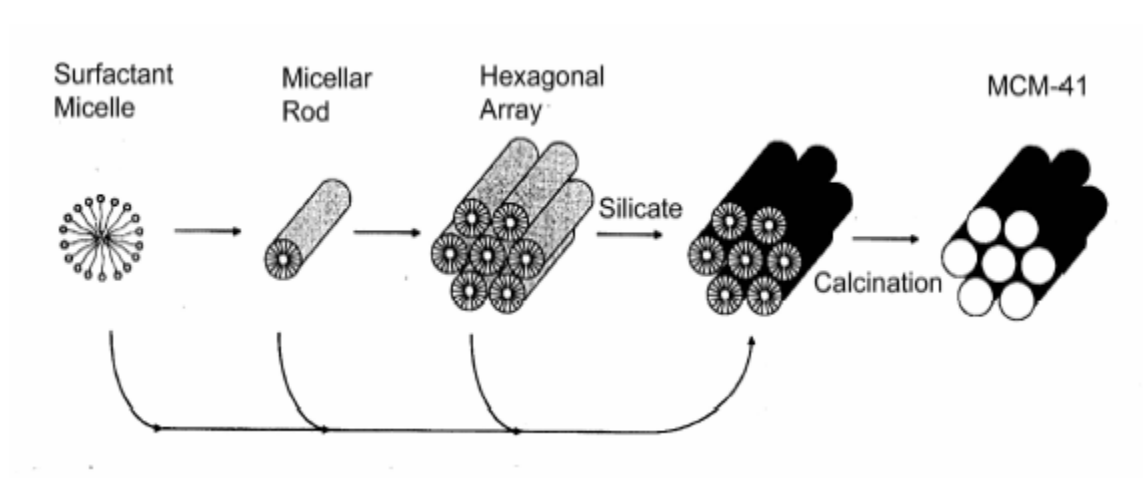


Figure 1-3. Proposed schematics of the liquid-crystal templating (LCT) mechanism.<sup>22,50</sup>



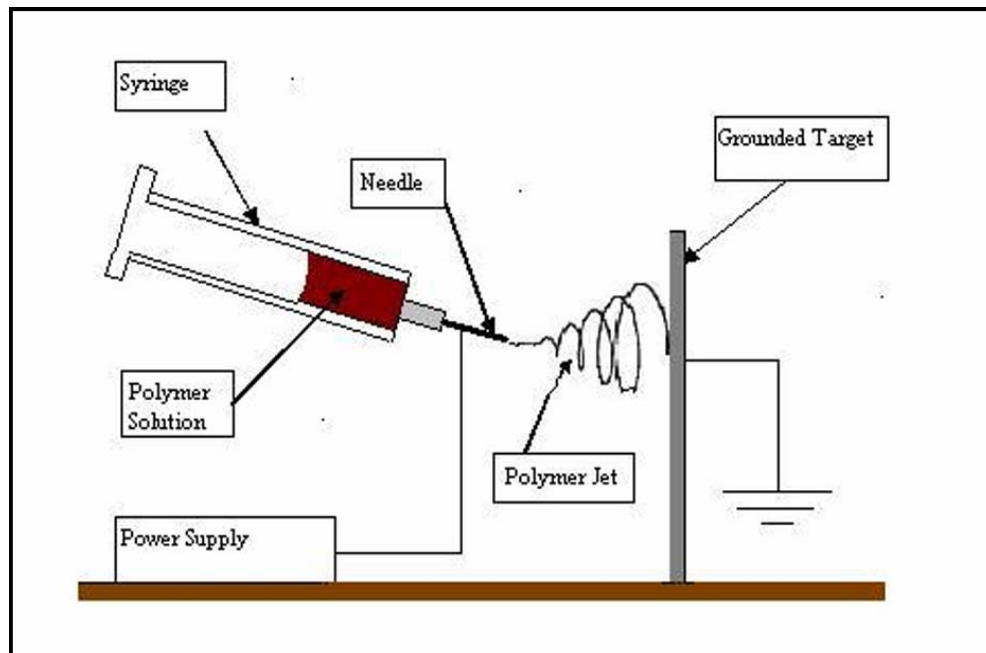


Figure 1- 4. Schematic representation of the electrospinning process.

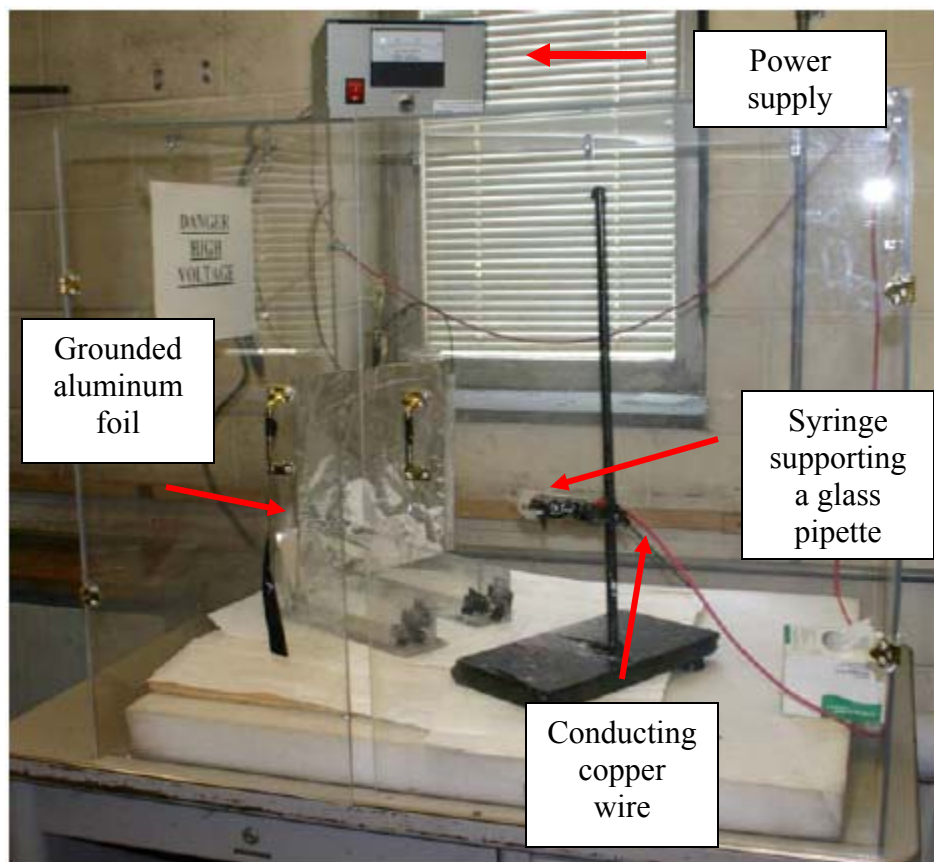


Figure 1-5. Photograph of the electrospinning instrument set-up in our lab.

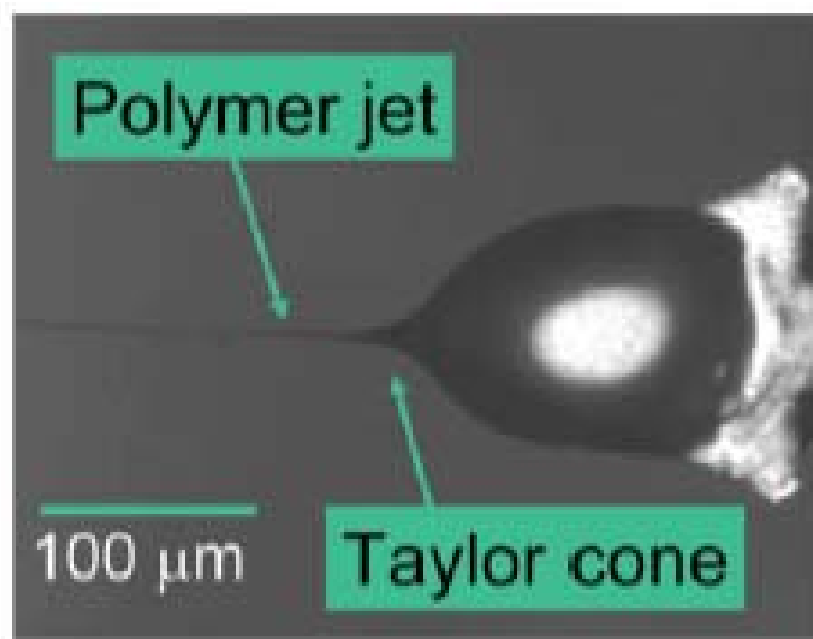


Figure 1-6. Taylor cone formed on the tip of the pipette during electrospinning. <sup>86</sup>

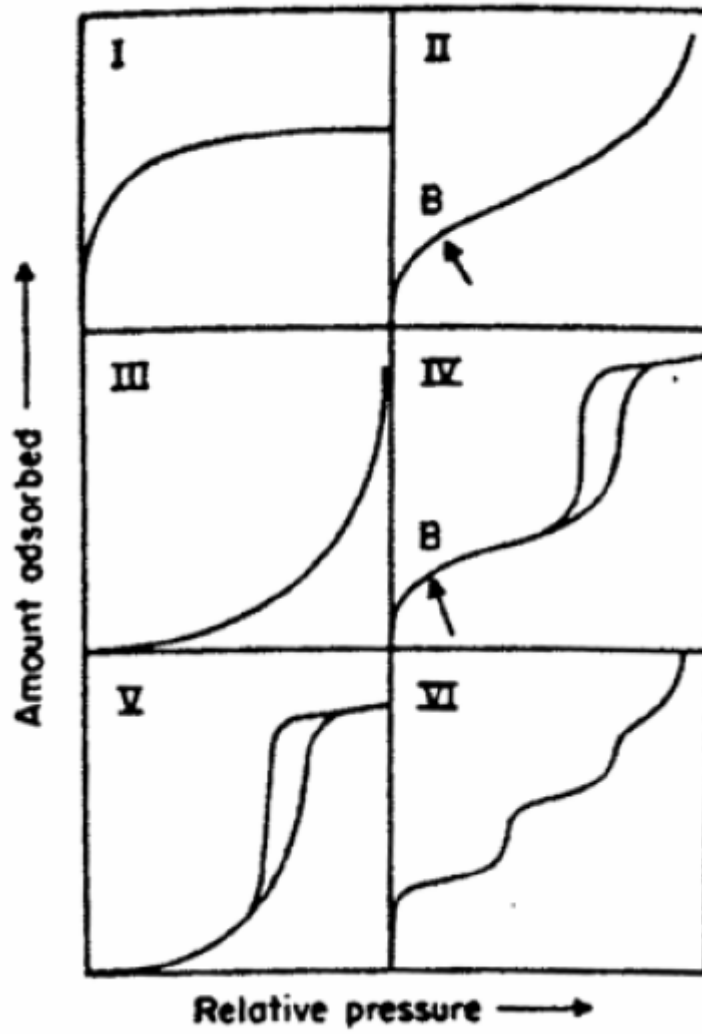


Figure 1-7. IUPAC classification of physisorption isotherms.<sup>48</sup>

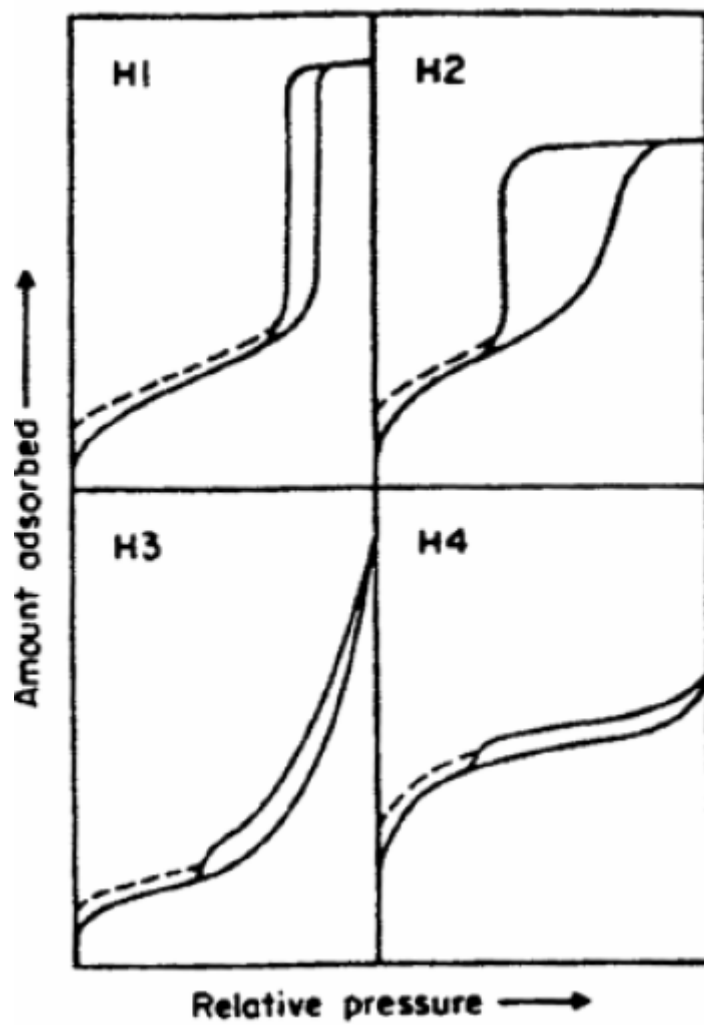


Figure 1-8. IUPAC classification of hysteresis loops.<sup>48</sup>

## Chapter 2: Sol-Gel Synthesis and Characterization of Silver Nanoparticles in D-Glucose Templated Mesoporous Silica Materials

### 2.1 Introduction

Functionalization of mesoporous silica matrix with polymers, metals, semiconductors and metal oxides has received considerable recognition because of their excellent catalytic, optoelectrical, chemical and environmental properties.<sup>1-7</sup> Especially of interest is the doping of sol-gel synthesized silica matrix with metal nanoparticles.<sup>8-13</sup> These metal doped sol-gel materials are used extensively in catalytic,<sup>14-16</sup> optical<sup>5,6</sup> and sensor applications.<sup>17,18</sup>

To increase the efficiency of metal-doped silica matrix for catalytic applications, some of the important properties that are desired include 1) large surface area, 2) ready access of metal nanoparticles to reagents, 3) no leakage of metal nanoparticles from the composite materials, and 4) no metal nanoparticle aggregation or poisoning. To enhance the optical properties of the metal composites, the metal particles present inside the matrix should have uniform size distribution as well as should be dispersed uniformly in the matrix. For the metal composites to act as good sensors, they should demonstrate a visible or electrical change in one of the properties when stimulated by a signal, which could then be detected optically or electronically. For example, Weiping et al.,<sup>19</sup> showed that the silver doped silica material changes color from transparent to different shades of brown depending on the amount of moisture present in the atmosphere, thus acting as a moisture sensory device. Many methods have been thus evaluated for loading metal nanoparticles into the silica matrix for several applications as stated above.

### 2.1.1 Encapsulation of Metal Nanoparticles in Sol-gel Matrix

Some of the important methods, listed according to their decreasing commonality of use, are listed below. 1) Addition of metal salts (nitrate, chloride, and sulfate) directly to the hydrolyzed sol mixtures<sup>20,21</sup> of tetraethyl-orthosilicate (TEOS), tetramethyl-orthosilicate (TMOS), etc., to form gels. The gels thus formed are then subjected to high temperatures to reduce the metal salts to the respective metal nanoparticles. Some of the particles synthesized using this method tend to precipitate out of the silica matrix. This causes a decrease in metal loading, which in turn causes loss in catalytic efficiency. 2) Another method involves soaking of the calcined silica matrix into the metal salt solution for a specific amount of time. The metal salt enters the silica matrix, which then can be reduced to metal nanoparticles by thermal decomposition.<sup>22</sup> The main disadvantage of this method is the uneven distribution of the metal particles as well as the broad distribution of nanoparticle sizes depending on the impregnation of metal salt in the silica matrix. Chemical vapor deposition of metal nanoparticles is also sometimes employed instead of impregnation, as it ensures a better distribution of nanoparticles in the silica matrix. It becomes very difficult however, to maintain a narrow size distribution as the size of the metal particles range from 5 nm to as large as 20 nm. 3) In surfactant replacement method the metal particles replace the surfactants lining the inner walls of the porous silica matrix. The metal particles in this method are deposited by soaking the surfactant containing silica matrix in the metal salt,<sup>23,24</sup> which simply replaces the surfactant. These surfactants are further removed either by chemical treatments or by burning the surfactants by subjecting the samples to high temperatures. 4) The inner walls of the mesoporous silica matrix can also be modified using inorganic moieties, which are

susceptible to metal compounds.<sup>25</sup> In this method, silica precursors such as tetramethylorthosilicate or tetraethylorthosilicate are first modified with long chain organic moieties,<sup>26,27</sup> which are further attached to inorganic moieties containing metal side groups. These compounds are then reduced to metal nanoparticles by calcinations. 5) Even less common is the utilization of metal containing templates, onto which the silica precursor is allowed to condense to form mesoporous materials.<sup>28</sup> Two examples of such substrates are the block copolymer micelle core<sup>29</sup> and micro gels,<sup>30</sup> inside which the nanoparticles are located and which are then used for silica casting. After the metal particles are incorporated into the silica matrix, the templates are burned or extracted out to leave behind silica metal composites. Thus, there has been extensive effort in developing encapsulated nanoparticle materials for catalytic application as stated above. Yet a simple and inexpensive method needs to be developed to encapsulate nanoparticles into the inorganic matrix for the large-scale production of efficient metal catalyst. In this chapter, we report a new and simple method of depositing nanosized silver nanoparticles on the inner walls of the nonsurfactant templated porous silica materials, under relatively mild conditions.

### **2.1.2 Nonsurfactant Templated Silica Material**

Novel low-cost, biocompatible silica (or other metal oxides) materials were synthesized and patented in 1999 by our group.<sup>31</sup> Two of the salient features of this technology are, (1) the room temperature synthesis of the nonsurfactant templated porous inorganic materials and (2) the easy extraction of the nonsurfactant templates from the inorganic matrix using water. The three main steps that go into the formation of the silica materials are the hydrolysis of TEOS using an acid catalyst, addition of non-surfactants



(glucose, fructose, dibenzoyl tartaric acid and urea) into the hydrolyzed solution and finally the formation of silica matrix containing aggregates of nonsurfactants.<sup>32-34</sup>

Glucose was selected in this work as the non-surfactant template for the synthesis of silver-silica composites, due to its multifunctional applications. The glucose template not only acts as a pore-forming agent by producing mesopores with narrow pore size distribution, but also helps control the size of the mesopores depending on the wt% of glucose added into the silica sample. More importantly, when these glucose templated silica samples are immersed in silver nitrate, the glucose present in the silica matrix reduces the silver nitrate to silver metal. The silver metal thus produced is deposited on the inner walls of the pores. The reaction is similar to the silver mirror test, where the silver nitrate is reduced to silver in the presence of glucose. The silver nanoparticles produced in this way have a very narrow-size distribution, and the surface area of the silica metal composites is quite high. The color change that occurs due to the deposition of silver nanoparticles in the silica material varies from light yellow to brown, depending on the wt% of silver nanoparticles in the silica material.

## **2.2 Experimental Section**

The synthesis of silver nanoparticle composites consisted of two main steps. One was the synthesis of glucose templated silica materials with various glucose content, and second is the formation of silver nanoparticles in situ inside the silica matrix via the reduction of silver nitrate to silver.

### **2.2.1 Materials and Reagents**

Tetraethyl orthosilicate (TEOS, 98%) was purchased from Sigma-Aldrich Chemical Co. (Milwaukee, WI). Silver nitrate ( $\text{AgNO}_3$ ), sodium hydroxide (NaOH),

nitric acid ( $\text{HNO}_3$ ), and  $\beta$ -D-glucose ( $\text{C}_6\text{H}_{12}\text{O}_6$ ) were purchased from Fisher Scientific (Fair Lawn, NJ) and ethyl alcohol was supplied by Pharmco Products (Brookfield, CT). All chemicals and reagents were used as received without further purification.

### 2.2.2 Synthesis of Glucose Templated Silica Material

The preparation of mesoporous silica materials followed the similar procedure as reported previously.<sup>35</sup> TEOS was used as the silica precursor, to which water and small amounts of  $\text{HNO}_3$  catalyst were added to facilitate the hydrolysis of TEOS to form a sol. To the resultant TEOS sol, were added various amounts of a 50 wt% glucose aqueous solution. The glucose-containing sol was homogeneous and the sol-gel reactions (i.e., further hydrolysis and polycondensation) proceeded at room temperature. The samples were allowed to dry at room temperature for a few days until dry-transparent and monolithic glucose-containing silica gels were obtained. At high concentrations of glucose, the samples sometimes broke down into smaller but still transparent and crack-free pieces during the drying process. Control samples were also prepared under identical conditions in the absence of glucose template. In a typical procedure, TEOS (0.15 mol/L), ethanol (0.46 mol/L),  $\text{H}_2\text{O}$  (0.35 mol/L), and  $\text{HNO}_3$  (2.0 M, 1.5 mmol/L) were mixed together in a flask at room temperature under agitation. After 15 min, the mixture became homogeneous and the solution was then heated to reflux under  $\text{N}_2$  for 2 hours. Upon cooling to room temperature, the prehydrolyzed TEOS sol thus obtained formed a stock solution ready for the subsequent synthesis. For the preparation of a sample containing 45 wt% glucose, 4.0 g of the prehydrolyzed TEOS sol (containing 10.1 mmol/L of the precursor TEOS initially) was neutralized with 0.32 mL of 0.25 M  $\text{NaOH}(\text{aq})$ , followed by adding a solution of 0.5 g glucose in 0.5 g of distilled water

under stirring. The resultant homogeneous solution was sealed in a cylindrical glass container with paraffin film, which had 10-12 small holes punched with a syringe needle to allow for the evaporation of volatile molecules such as ethanol and water. Upon gelation and drying at room temperature for 3-7 days, a transparent and monolithic disk of glucose-containing silica sample was obtained. Depending on the wt% of glucose added in the sample, the silica materials were labeled as 10GTS to 50GTS for 10 wt% to 50 wt% glucose-templated silica materials, respectively. A control containing 0 wt% of glucose was also synthesized.

### **2.2.3 Synthesis of Silver Containing Silica Composites**

The glucose-containing samples were immersed in a solution of  $\text{AgNO}_3$ , water and ethyl alcohol. The samples broke down into smaller pieces but remained crack free. The silver nitrate diffused inside the silica matrix sample, and the glucose present in the samples reduced the silver nitrate to silver metal, which was deposited on the walls of the mesopores. A change in color from transparent to yellowish brown was observed in the sample containing the silver particles. These silver containing samples were then dried under vacuum for 2 to 3 days. The silver-silica composites thus obtained are denoted as 10GTS(Ag) to 50GTS(Ag) samples depending on the wt% of glucose present in the sample. As a typical procedure for preparing a 50GTS(Ag) sample, 1g of 50GTS sample was immersed in a solution of 10mL of 0.2 M  $\text{AgNO}_3$  and 5mL mixture of ethanol- $\text{H}_2\text{O}$  (1:1 v/v) solution. This suspension was stirred gently for 2 hours and left to stand for an additional 2 hours at room temperature. The samples broke down into smaller but crack free pieces, which were filtered out, washed thoroughly with ethanol and left to dry under

vacuum for 2 to 3 days. Two control samples, 0GTSslid (powdered silver-coated glass slide) and 0GTS(Ag) (0GTS sample immersed in  $\text{AgNO}_3$ ) were also prepared.

### 2.3 Instrumentation and Characterization

The silica samples were characterized using  $\text{N}_2$  sorption via Micromeritics ASAP 2010 (Micromeritics Inc., Norcross, GA) at  $-196^\circ\text{C}$ . All samples were degassed at  $100^\circ\text{C}$  and  $10^{-6}$  Torr overnight prior to  $\text{N}_2$  adsorption-desorption and the surface area, pore diameter and pore volume were calculated using the accompanying software from Micromeritics. Powder X-ray diffraction (XRD) patterns were recorded on a Siemens D500 diffractometer equipped with a rotating anode and using  $\text{Cu K}\alpha$  radiation ( $\lambda = 0.15418$  nm) with scanning rates of  $2^\circ/\text{min}$ . Elemental analysis and X-ray mapping were conducted on an EDX interfaced, Phillips XL-30 environmental scanning electron microscope (ESEM). The instrument was operated at an accelerating voltage of 15 kV, and the samples were deposited on the sample holder with adhesive carbon tape. TEM images of silver-silica nanocomposites were obtained on a Hitachi H-900 HRTEM operated at an accelerating voltage of 300 kV. The TEM samples were prepared by evaporating a suspension of finely powdered sample in ethyl alcohol on a copper grid coated with porous carbon film. Solid-state UV-visible reflectance spectra of the as-synthesized sample were measured on a Perkin Elmer, Model-330 spectrophotometer. The baseline was calibrated with magnesium carbonate. The samples were prepared by spreading a 0.5 mm thick layer of silica-silver composite powder on top of a layer of magnesium carbonate. The sample was then subjected to direct UV-visible light. The spectra were obtained at a scanning rate of 60 nm/min.

## 2.4 Results and Discussions

The composition and the pore parameters of the silver-silica composites are summarized in Table 2-1. After the glucose templated silica samples were immersed in silver nitrate solution for 4 hours, they were washed with water in a Soxhlet apparatus for a span of 2 hours to make sure that all the excess silver nitrate solution present in the GTS(Ag) materials was washed out. The water was also tested for any silver nanoparticles that might have leaked out of the composites during washing. Other than the variation of glucose content in the GTS samples, all other variables, such as the concentration of the silver nitrate solution and the time for which the GTS materials were immersed in the silver nitrate solution, was kept constant.

### 2.4.1 Elemental Analysis and X-Ray Mapping

EDX technique (Figure 2-1) was used to evaluate the silver loading inside the GTS(Ag) materials. The EDX results show an increase in silver content from 6 to 10.6 wt%, with increase in glucose concentration from 30 to 50 wt% in the GTS samples. The amount of silver present in the composites before and after Soxhlet extraction did not vary significantly, suggesting the absence of silver particle leakage from the samples.

### 2.4.2 N<sub>2</sub> Sorption Characterization

Representative nitrogen adsorption-desorption isotherms at -196 °C for the porous silver-silica nanocomposite samples are shown in Figure 2-2. These samples show type-I and type-IV kinds of isotherm.<sup>36,37</sup> The type-I isotherm is produced by adsorption of nitrogen gas on microporous solids. Type-II and III isotherms are produced by non-porous materials the type-IV isotherm is produced by mesoporous materials. A characteristic of the type-IV isotherm is the hysteresis loop. The shape of the loop that the

type-IV isotherm forms varies depending on the surface area of the sample. The two control samples used here are 0GTS and 50GTS. 0GTS sample does not contain either glucose or silver nanoparticles. Control sample 50GTS contains 50 wt% glucose but no silver nanoparticles. These control samples were washed in water to extract out the pore forming glucose template. The samples were dried and then tested for surface area and pore diameter using the BET instruments. The isotherms formed for the template-extracted samples have H2 Hysteresis loops at  $P/P_0$  in the region of  $\sim 0.4-0.7$  nm. The increase in wt% of glucose in the sample increases the surface area of the samples, which further causes the size of the hysteresis loops to range from the smallest in 0GTS materials to the largest in 50GTS. The type of isotherm that 0GTS exhibits is the reversible type I, which is typical for materials with microporous structures. The template-extracted 50GTS materials exhibit a reversible type-IV isotherm. When glucose-containing samples are immersed in silver nitrate solution, silver nanoparticles are formed and the isotherm pattern changes (Figure 2-2). This change occurs when the silver nanoparticles are deposited on the inner walls of the mesopores, causing the surface area of the sample to change. Unlike the decrease in surface area seen when going from 50GTS to 50GTS(Ag), the surface area is seen to increase from 30GTS to 30GTS(Ag) (Table 2-1). The reason for this difference could be attributed to that the silver particles synthesized by the 30GTS(Ag) are smaller than that of 50GTS(Ag). Thus the silver nanoparticles in 30GTS(Ag) line the inner wall of the mesopores, increasing the pore volume and making the mesopores accessible to nitrogen molecules. On the other hand, in the case of 50GTS(Ag) samples the nanoparticles could be blocking the mesopores and

making them inaccessible to nitrogen molecules, thus decreasing the surface area as well as the pore volume of the silica composites.

The Barrett-Joyner-Halenda (BJH) pore size distribution curves derived from desorption branches of the nitrogen isotherms are shown in Figure 2-3. With pore volumes plotted against pore diameter, the curves indicate a relatively narrow size distribution of the mesopores in the range of 3-4 nm for all of the water extracted GTS samples. The 0GTS control sample exhibits a much broader pore size distribution with comparatively lesser number of mesopores similar to data presented in the literature.<sup>38</sup> The water extracted 50GTS control sample, on the other hand, shows a very narrow pore size distribution around 3.4 nm, due to the porosity caused by the glucose templates in the sample. When the 50GTS sample (still containing glucose) is immersed in silver nitrate solution, silver nanoparticles are formed. These particles get lodged inside the mesopores of the sample (i.e., 50GTS(Ag)). The pore-size distribution curve thus drops down considerably to give a much broader curve due to the blocking of some mesopores, hence, obstructing the detection of these pores by the BET instrument. The pore size distribution derived from the H2 hysteresis loop was believed to be associated solely with the data collected from the narrow neck-type mesopores, which are compared to an inkbottle. It is now recognized that the data collected from the hysteresis loop may be influenced by the porous network connections present in the sample.<sup>37</sup> Despite the complexities and a few uncertainties, the nitrogen sorption measurements help in the analyses of porous material. The pore diameter derived from the BHJ method proved to be in favorable agreement with the date obtained from the XRD (Figure 2-4) and TEM (Figure 2-5) analyses.

### 2.4.3 X-Ray Diffraction Characterization

Figure 2-4 represents powder XRD pattern for the control sample (0GTS), silver containing samples (30 and 50GTS(Ag)) and heat-treated 50GTS(Ag) sample. A broad diffraction peak centered at approximately  $23^\circ$  was observed in all of the samples at a high angle range. This broad peak is typical of the amorphous nature of the sol-gel silica samples. A similar type of amorphous peak was also seen in porous silica samples synthesized using cationic and neutral surfactant templates.<sup>36,38</sup> 50GTS(Ag) samples show high angle diffraction crystalline peaks which can be readily indexed according to the crystalline Ag structure as shown in Figure 2-4. The peaks are less intense, as some of the nanoparticles in the sample are not completely formed. When the same 50GTS(Ag) samples were subjected to high temperatures around  $300^\circ\text{C}$ , the peaks for silver became more intense. This is due to the further development of crystalline phase of metallic silver particles. 30GTS(Ag) samples do not show clear high angle diffraction peaks for silver, this again is due to the small size of silver nanoparticles ( $< 5\text{ nm}$ ). This phenomenon can be further explained by comparing the results with a control sample (i.e., Gslid(Ag)), which is produced by depositing a thin monolayer of silver onto a thin glass slide. The XRD diffraction of the control sample did not show any high angle diffraction peaks for silver, similar to the results of 30DTNS(Ag) samples. The reason for this discrepancy is because the concentration of glucose in 30DTNS(Ag) is barely enough to reduce the silver nitrate to silver, and deposit it on the inner walls of the mesoporous samples. When these samples are calcined, the fine silver particles layering the mesoporous walls tend to aggregate and grow in size, giving rise to sharper and intense high angle diffraction peaks, as proved by Mitrikas et al.<sup>39</sup>



#### 2.4.4 Transmission Electron Microscopy Characterization

Glucose not only acts as a reducing agent but also acts as a nonsurfactant templating agent. Hence, the distribution of glucose in the silica matrix governs the way the mesopores are shaped and how the silver nanoparticles are distributed inside the sample. Figure 2-5(a) and (b) shows a bright field TEM micrograph image along with inserts of electron diffraction patterns for 50GTS(Ag) and 30GTS(Ag), respectively. The 50GTS(Ag) TEM picture, shows randomly distributed 3 to 4 nm sized silver nanoparticles embedded in the silica matrix, which complements the results obtained with the other characterization methods. The low resolution TEM micrograph (Figure 2-5(b)) of 30GTS(Ag) does not show any silver particles, this could be due to formation of a thin layer of silver on the inner walls of the pores, rather than the nanoparticles formed in 50GTS(Ag). The distribution of silver particles in the silica matrix was analyzed further by X-ray elemental mapping. Figure 2-6 shows a uniform distribution of oxygen, silicon and silver in the composite sample. Thus, these morphological studies indicate a random but even distribution of silver nanoparticles in the silica matrix.

#### 2.4.5 Optical Characterization

The silver-silica samples vary in color from light yellow to dark brown, depending on the size and concentration of the silver particles in the sample, as seen in Figure 2-8. 30GTS(Ag) samples show a light yellow to orange color, and 50GTS(Ag) samples show a much darker shade of brown. Silver nanoparticles, unlike bulk metals, show unusual optical properties, including light adsorption and scattering. This phenomenon is caused by the surface plasmon resonance (SPR) of the silver nanoparticles. SPR is characteristic of 2-50 nm-size nanoparticles. Electrons from the

particles can oscillate on the particle surface and adsorb electromagnetic radiation from particular energy levels. Particles less than 2 nm do not show this phenomenon because the electrons are present in discrete energy levels.<sup>40</sup> According to Mie theory,<sup>41</sup> small spherical metal nanocrystals should exhibit a single surface plasmon band; whereas anisotropic particles exhibited two to three bands. Recently Jin et al.<sup>42</sup> observed two distinct quadruple plasmon resonances for silver nanoparticles shaped like prisms. The UV-visible spectra for 0 to 50GTS(Ag) samples are depicted in Figure 2-7. The control sample (i.e., 0GTS(Ag)) does not show any plasmon absorbance peaks because of the absence of silver particles in the sample. 10GTS(Ag) samples also shows no peak around 400 nm as the silver particles are not formed. 30-40GTS(Ag) samples show a broad peak around 425nm, and 50GTS(Ag) samples show a much more intense peak at 410 nm, caused due to the silver nanoparticles as previously reported by Maoping et al.<sup>19,43</sup> The plasmon absorbance peaks have a slight tailing near the 600 to 800 nm range, caused due to a broad size distribution of silver nanoparticles (2 to 5 nm).

## **2.5 Conclusion**

A simple process of soaking the glucose templated silica materials in silver nitrate solution leads to the in situ production of silver-silica composites. Thus, the method is compatible for large-scale production of silver-silica composites, required for various catalytic applications. As mentioned before, the wt% of glucose in the sample directly influences the silver loading in the silica matrix. The silver-silica composites show a large pore volume and surface area, along with a narrow size distribution of silver nanoparticles. The detailed characterization of the composites further proves the uniform distribution of silver nanoparticles in the sample.

## 2.6 Reference List

1. Bharathi, S., Nogami, M., Ikeda, S. Layer by layer self-assembly of thin films of metal hexacyanoferrate multilayers. *Langmuir*, 17(24), 7468-7471. 2001.
2. Nogami, M. Sol-gel preparation of non-linear glasses doped with small-sized particles. *Ceramic Transactions 81(Sol-Gel Processing of Advanced Materials)*, 255-261. 1998.
3. Epifani, M., Carlino, E., Blasi, C., Giannini, C., Tapfer, L., Vasanelli, L. Sol-gel processing of Au nanoparticles in bulk 10% B<sub>2</sub>O<sub>3</sub>-90% SiO<sub>2</sub> glass. *Chemistry of Materials*, 13(5), 1533-1539. 2001.
4. Bronstein, L. M., Polarz, S., Smarsly, B., Antonietti, M. Sub-nanometer noble-metal particle host synthesis in porous silica monoliths. *Advanced Materials (Weinheim, Germany)*, 13(17), 1333-1336. 2001.
5. Khushalani, D., Hasenzahl, S., Mann, S. Synthesis of mesoporous silica monoliths with embedded nanoparticles. *Journal of Nanoscience and Nanotechnology*, 1(2), 129-132. 2001.
6. Hayakawa, T., Ono, Y., Nogami, M. Linear and nonlinear optical properties of monodispersed gold clusters in silica glass by sol-gel method. *Proceedings of SPIE-The International Society for Optical Engineering*, 3943(Sol-Gel Optics V), 102-111. 2000.
7. Anderson, M. L., Morris, C. A., Stroud, R. M., Merzbacher, C. I., Rolison, D. R. Colloidal gold aerogels: preparation, properties, and characterization. *Langmuir*, 15(3), 674-681. 1999.
8. Schubert, U. Catalysts made of organic-inorganic hybrid materials. *New Journal of Chemistry*, 18(10), 1049-1058. 1994.
9. Mennig, M., Schmitt, M., Schmidt, H. Synthesis of Ag colloids in sol-gel derived SiO<sub>2</sub> coatings on glass. *Journal of Sol-Gel Science and Technology*, 8(1/2/3), 1035-1042. 1997.
10. Schubert, U., Breitscheidel, B., Buhler, H., Egger, C., Urbaniak, W. Metal complexes in oxidic matrixes. *Materials Research Society Symposium Proceedings*, 271(Better Ceramics through Chemistry V), 621-632. 1992.
11. Mitrikas, G., Trapalis, C. C., Boukos, N., Psycharis, V., Astrakas, L., Kordas, G. Size distribution and EPR of silver nanoparticles in SiO<sub>2</sub> matrix. *Journal of Non-Crystalline Solids*, 224(1), 17-22. 1998.
12. Epifani, M., Giannini, C., Tapfer, L., Vasanelli, L. Sol-gel synthesis and characterization of Ag and Au nanoparticles in SiO<sub>2</sub>, TiO<sub>2</sub>, and ZrO<sub>2</sub> thin films. *Journal of the American Ceramic Society*, 83(10), 2385-2393. 2000.
13. Breitscheidel, B., Zieder, J., Schubert, U. Metal complexes in inorganic matrixes. 7. Nanometer-sized, uniform metal particles in a silica matrix by sol-gel processing of metal complexes. *Chemistry of Materials*, 3(3), 559-566. 1991.
14. Claus, P., Brueckner, A., Mohr, C., Hofmeister, H. Supported gold nanoparticles from quantum dot to mesoscopic size scale: effect of electronic and structural properties on catalytic hydrogenation of conjugated functional groups. *Journal of the American Chemical Society*, 122(46), 11430-11439. 2000.

15. Rath, A., Aceves, E., Mitome, J., Liu, J., Ozkan, U. S., Shore, S. G. Application of  $\{(DMF)_{10}Ln_2[Pd(CN)_4]_3\}$ ... ( $Ln = Y_b, S_m$ ) as lanthanide-palladium catalyst precursors dispersed on sol-gel- $TiO_2$  in the reduction of NO by methane in the presence of oxygen. *Journal of Molecular Catalysis A: Chemical*, 165(1-2), 103-111. 2001.
16. Valden, M., Lai, X., Goodman, D. W. Onset of catalytic activity of gold clusters on titania with the appearance of nonmetallic properties. *Science (Washington, D.C.)*, 281(5383), 1647-1650. 1998.
17. Bharathi, S., Nogami, M. A glucose biosensor based on electrodeposited biocomposites of gold nanoparticles and glucose oxidase enzyme. *The Analyst*, 126(11), 1919-1922. 2001.
18. Lee, Y. H., Farquharson, S., Kwon, H., Shahriari, M., Rainey, P. Sol-gel chemical sensors for surface-enhanced Raman spectroscopy. *Proceedings of SPIE-The International Society for Optical Engineering*, 3537(Electro-Optic, Integrated Optic, and Electronic Technologies for Online Chemical Process Monitoring), 252-260. 1999.
19. Weiping, C., Lide, Z. Synthesis and structural and optical properties of mesoporous silica containing silver nanoparticles. *Journal of Physics: Condensed Matter*, 9(34), 7257-7267. 1997.
20. Sun, T., Ying, J. Y. Synthesis of microporous transition-metal-oxide molecular sieves by a supramolecular templating mechanism. *Nature (London)*, 389(6652), 704-706. 1997.
21. Fryxell, G. E., Liu, J. Designing surface chemistry in mesoporous silica. *Surfactant Science Series 90(Adsorption on Silica Surfaces)*, 665-687. 2000.
22. Mehnert, C. P., Weaver, D. W., Ying, J. Y. Heterogeneous heck catalysis with palladium-grafted molecular sieves. *Journal of the American Chemical Society*, 120(47), 12289-12296. 1998.
23. Yonemitsu, M., Tanaka, Y., Iwamoto, M. Metal Ion-Planted MCM-41. 1. Planting of manganese(II) ion into MCM-41 by a newly developed template-ion exchange method. *Chemistry of Materials*, 9(12), 2679-2681. 1997.
24. Badieli, A. R., Bonneviot, L. Modification of mesoporous silica by direct template ion exchange using cobalt complexes. *Inorganic Chemistry*, 37(16), 4142-4145. 1998.
25. Krocher, O., Koppel, R. A., Froba, M., Baiker, A. Silica hybrid gel catalysts containing group (VIII) transition metal complexes: Preparation, structural, and catalytic properties in the synthesis of N,N-dimethylformamide and methyl formate from supercritical carbon dioxide. *Journal of Catalysis*, 178(1), 284-298. 1998.
26. Moller, K., Bein, T. Internal modification of ordered mesoporous hosts. *Studies in Surface Science and Catalysis*, 117(Mesoporous Molecular Sieves 1998), 53-64. 1998.
27. Shephard, D. S., Zhou, W., Maschmeyer, T., Matters, J. M., Roper, C. L., Parsons, S., Johnson, B. F.G., Duer, M. J. Site-directed surface derivatization of MCM-41: use of high-resolution transmission electron microscopy and molecular recognition for determining the position of functionality within mesoporous materials. *Angewandte Chemie, International Edition*, 37(19), 2719-2723. 1998.

28. Eliseev, A. A., Lukashin, A. V., Soboleva, L. I., Knot'ko, A. V., Khaifets, L. I., Vertegel, A. A., Tret'yakov, Yu. Synthesis of mesoporous silica by using polyvinyl alcohol as template. *Doklady Akademii Nauk*, 372(6), 770-772. 2000.
29. Bronstein, L., Kraemer, E., Berton, B., Burger, C., Foerster, S., Antonietti, M. Successive Use of Amphiphilic Block Copolymers as Nanoreactors and Templates: Preparation of Porous Silica with Metal Nanoparticles. *Chemistry of Materials* 11(6), 1402-1405. 1999.
30. Whilton, N. T., Berton, B., Bronstein, L., Hentze, H. P., Antonietti, M. Organized functionalization of mesoporous silica supports using prefabricated metal-polymer modules. *Advanced Materials (Weinheim, Germany)*, 11(12), 1014-1018. 1999.
31. Wei, Y., Jin, D., Ding, T., Xu, J. Mesoporous materials and methods of making the same. Drexel University, USA. 99-US1116(9936357). WO. 1999.
32. Wei, Y., Dong, H., Xu, J., Feng, Q. Simultaneous immobilization of horseradish peroxidase and glucose oxidase in mesoporous sol-gel host materials. *Chemphyschem. European Journal of Chemical Physics and Physical Chemistry*, 3(9), 802-808. 2002.
33. Pang, J. B., Qiu, K. Y., Wei, Y. A novel nonsurfactant pathway to hydrothermally stable mesoporous silica materials. *Microporous and Mesoporous Materials*, 40(1-3), 299-304. 2000.
34. Pang, J. B., Qiu, K. Y., Wei, Y. Preparation of mesoporous silica materials with non-surfactant hydroxy-carboxylic acid compounds as templates via sol-gel process. *Journal of Non-Crystalline Solids*, 283(1-3), 101-108. 2001.
35. Wei, Y., Xu, J.; Dong, H., Dong, J. H., Qiu, K., Jansen-Varnum, S. A. Preparation and physisorption characterization of glucose-templated mesoporous silica sol-gel materials. *Chemistry of Materials*, 11(8), 2023-2029. 1999.
36. Sing, K.S.W., Everett, D. H., Haul, R. A. W., Moscou, L., Pierotti, R. A., Rouquerol, J., Siemieniewska, T. Reporting physisorption data for gas/solid systems with special reference to the determination of surface area and porosity (Recommendations 1984). *Pure and Applied Chemistry*, 57(4), 603-619. 1985.
37. Lee, C. K., Chiang, A. S. T., Tsay, C. S. The characterization of porous solids from gas-adsorption measurements. *Key Engineering Materials*, 115, 21-43. 1996.
38. Brinker, J. C., Scherer, W. G. *Sol-gel science: The physics and chemistry of sol-gel processing*. Elsevier Science, California. 1990.
39. Mitrikas, G., Trapalis, C. C., Kordas, G. Tailoring the particle size of sol-gel derived silver nanoparticles in SiO<sub>2</sub>. *Journal of Non-Crystalline Solids*, 286(1,2), 41-50. 2001.
40. Cheng, S., Wei, Y., Feng, Q., Qiu, K. Y., Pang, J. B., Jansen, S. A., Yin, R., Ong, K. Facile synthesis of mesoporous gold-silica nanocomposite materials via sol-gel process with nonsurfactant templates. *Chemistry of Materials*, 15(7), 1560-1566. 2003.
41. Mie, G. Contributions to the optics of turbid media, especially colloidal metal solutions. *Annalen der Physik (Weinheim, Germany)*, 25, 377-445. 1908.
42. Jin, R., Cao, Y., Mirkin, C. A., Kelly, K. L., Schatz, G. C., Zheng, J. G. Photoinduced conversion of silver nanospheres to nanoprisms. *Science*, 294(5548), 1901-1903. 2001.

43. Zheng, M., Gu, M., Jin, Y., Jin, G. Optical properties of silver-dispersed PVP thin film. *Materials Research Bulletin* 36(5-6), 853-859. 2001.

Table 2-1. Compositions and pore parameters of the silver-silica materials, prepared by the reduction of silver nitrate to silver, using glucose as a reducing agent. (Glucose templated nonsurfactant silica material (GTS)).

sample code <sup>a</sup>	silver (wt%) <sup>b</sup>		S <sub>BET</sub> <sup>c</sup>	V <sub>PORE</sub> <sup>d</sup>	D <sub>BJH</sub> <sup>e</sup>	micropore volume <sup>f</sup>
	before extraction	after extraction				
0GTS	-----	-----	842	0.2	2.2	120
0GTS(Ag)	0.04	0.0	900	0.2	2.4	100
30GTS	-----	-----	947	0.4	2.6	43
30GTS(Ag)	6.0	5.8	1061	0.5	2.5	130
50GTS	-----	-----	1026	0.7	3.2	-----
50GTS(Ag)	10.6	9.9	791	0.4	2.9	-----

<sup>a</sup>The numerical figures in the sample code denotes the glucose template concentration (wt% of glucose template in the final dry product, excluding the silica and silver content). The sample codes containing the term “Ag” are samples that contain silver nanoparticles (the glucose present in the samples reduced AgNO<sub>3</sub> to silver). <sup>b</sup>Average values of silver present in the silica samples, calculated based on the EDX elemental analysis taken from four different areas of each sample. <sup>c</sup>Surface area and <sup>d</sup>Pore volume of the sample determined by N<sub>2</sub> adsorption-desorption isotherms. <sup>e</sup>Pore size determined from the maxima of the BJH desorption pore size distribution curves with the Halsey equation. <sup>f</sup>Micropore volume determined by the t-plot analysis

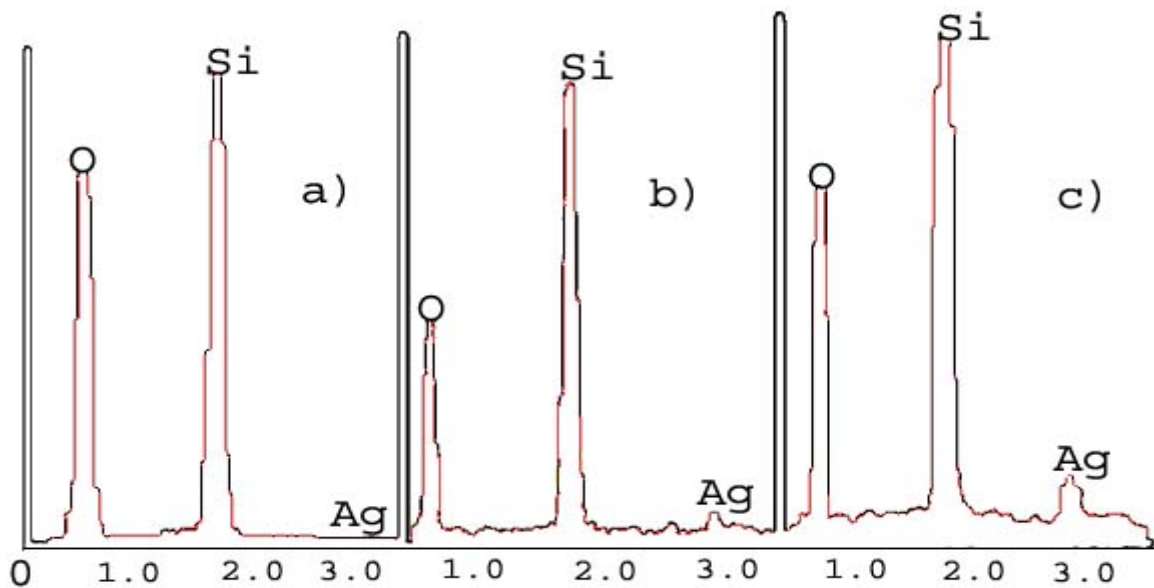


Figure 2-1. Representative X-ray energy-dispersive spectra for silver-silica nanocomposites. (a) 0GTS(Ag) does not show any peak for silver; (b) 30GTS(Ag) shows a small peak for silver; (c) 50GTS(Ag) shows a relatively sharper peak for silver.



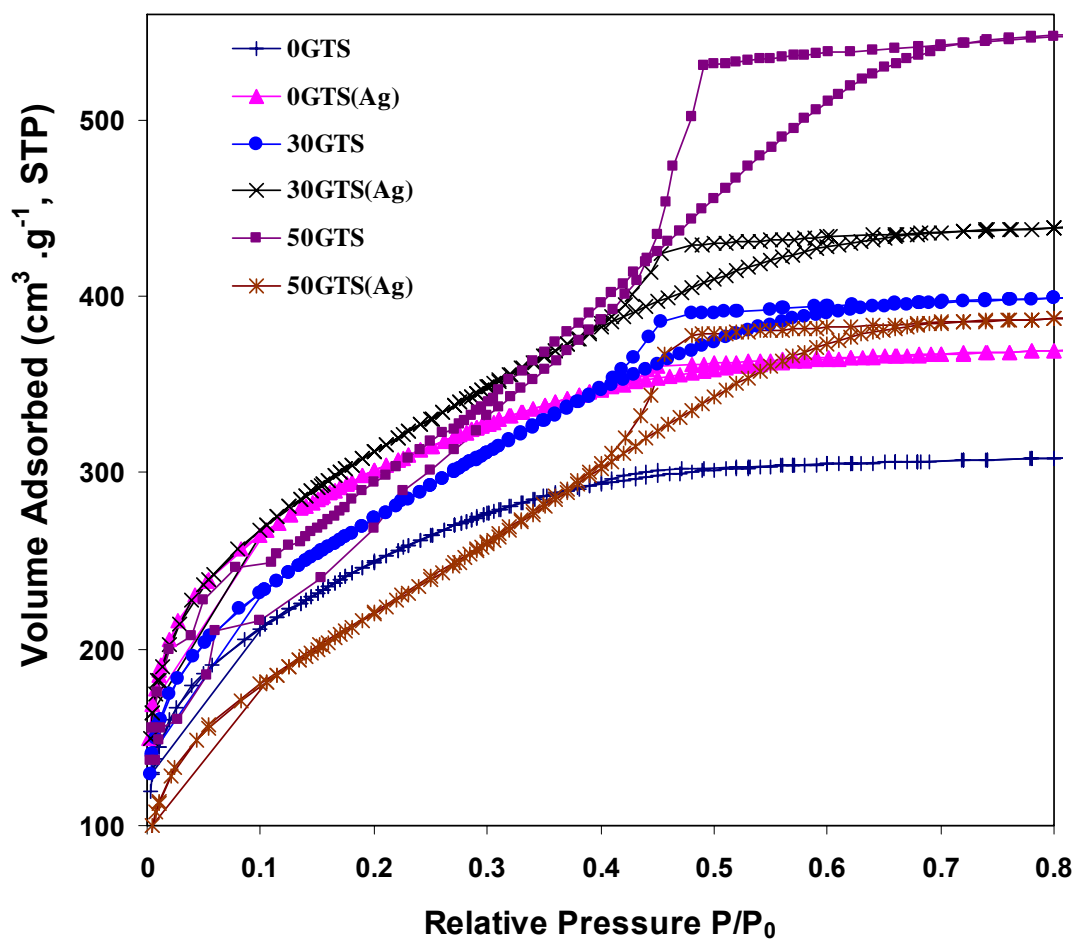


Figure 2-2. N<sub>2</sub> adsorption-desorption isotherms at -196 °C for control samples (i.e., 0 and 50GTS) and silver-silica composites with different silver content (i.e., 0, 30, 50GTS(Ag))  
 \*Samples 20GTS(Ag) show the same trend in results as 30GTS(Ag).

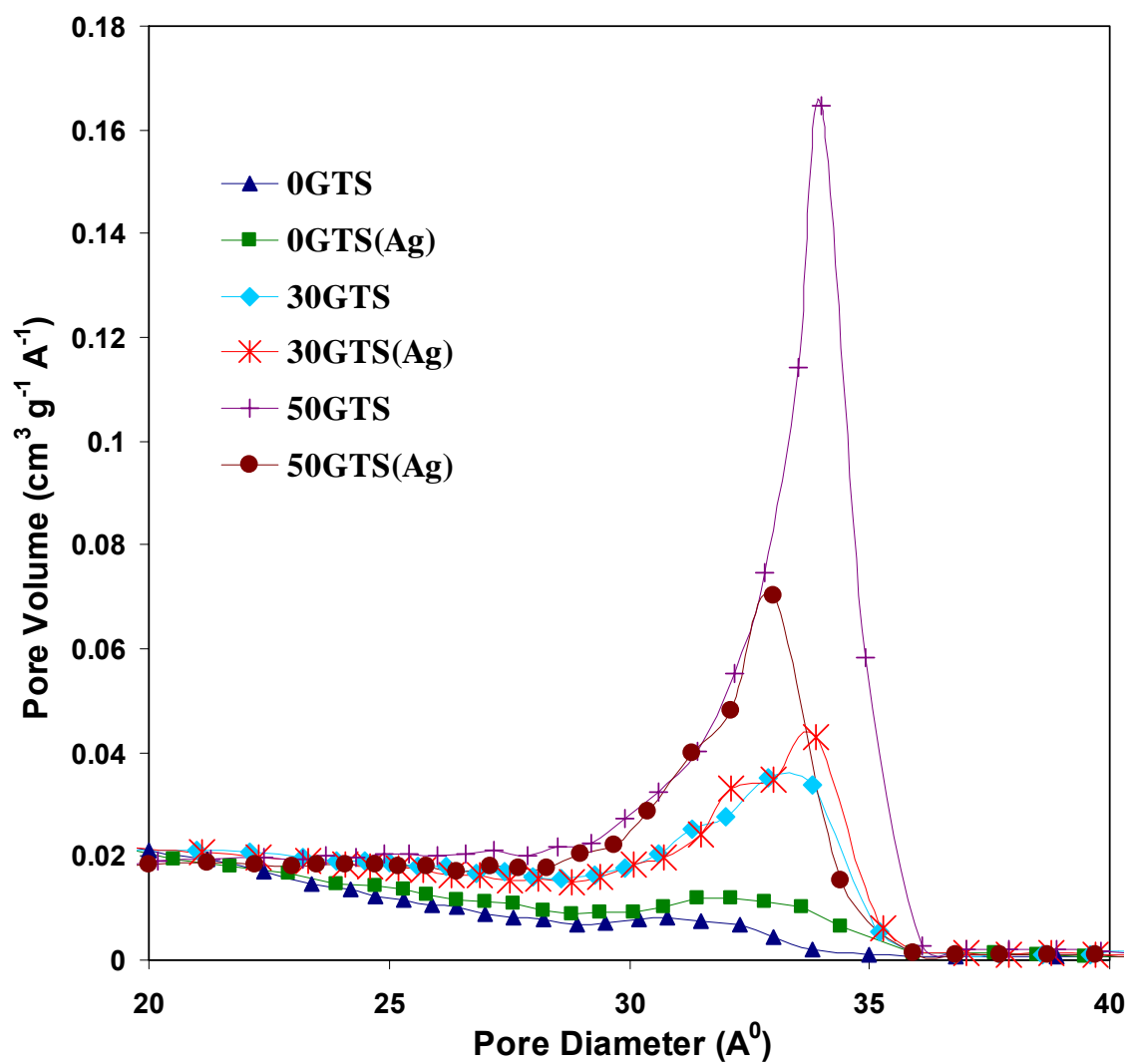


Figure 2-3. BJH pore size distributions for the control samples (i.e., 0GTS and 50GTS) and for silver-silica composites with different silver contents (i.e., 0, 30, 50GTS(Ag)).

\* Samples 20GTS(Ag) show the same trend in results as 30GTS(Ag).

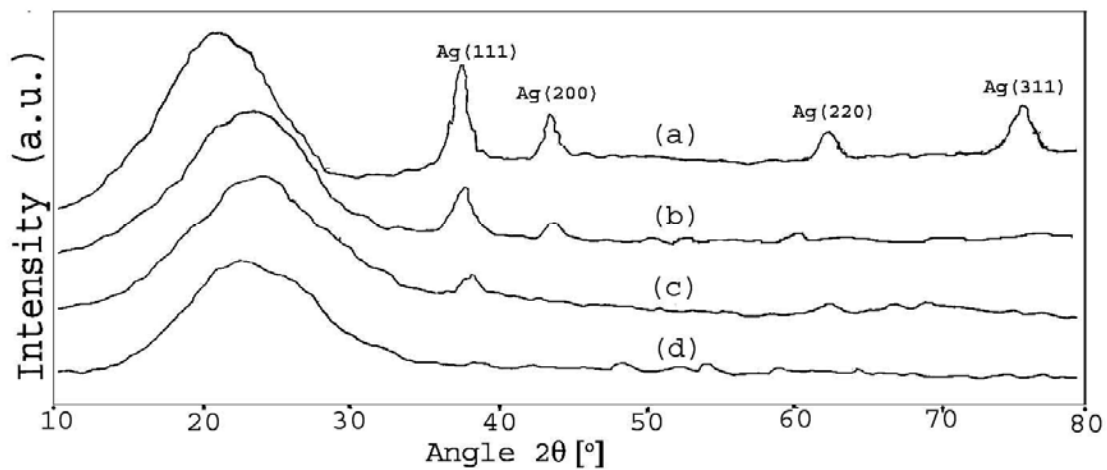


Figure 2-4. X- ray diffraction of silver-silica nanocomposites: a) 50GTS(Ag) samples immersed in silver nitrate solution and heat-treated at 300 °C; b) 50GTS(Ag) sample containing silver nanoparticles (not heated); c) 30GTS(Ag) sample containing silver nanoparticles (not heated) and d) control sample Gslid(Ag).

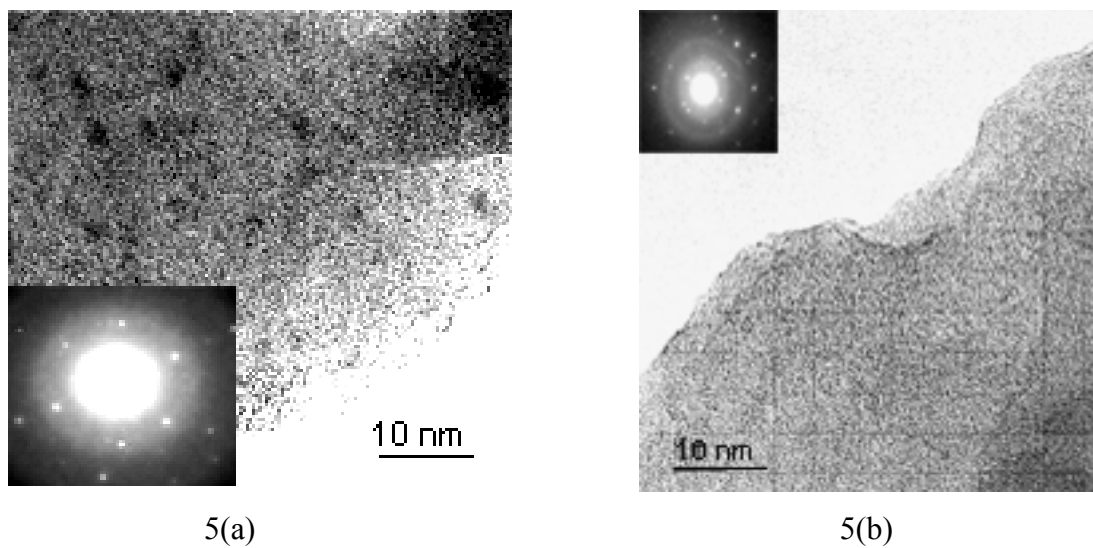


Figure 2-5. (a) Representative TEM image of mesoporous silver-silica nanocomposites (50GTS(Ag)) along with inserts of electron diffraction patterns. The dark spherical spots seen in the micrograph are silver particles, and the gray background is the mesoporous silica frame work, which clearly shows worm-like mesoporous channels; 5(b) TEM image of 30GTS(Ag) sample shows a silica frame work with probable tiny silver particles and electron diffraction pattern of silver nanoparticles. Scale bar 10 nm.

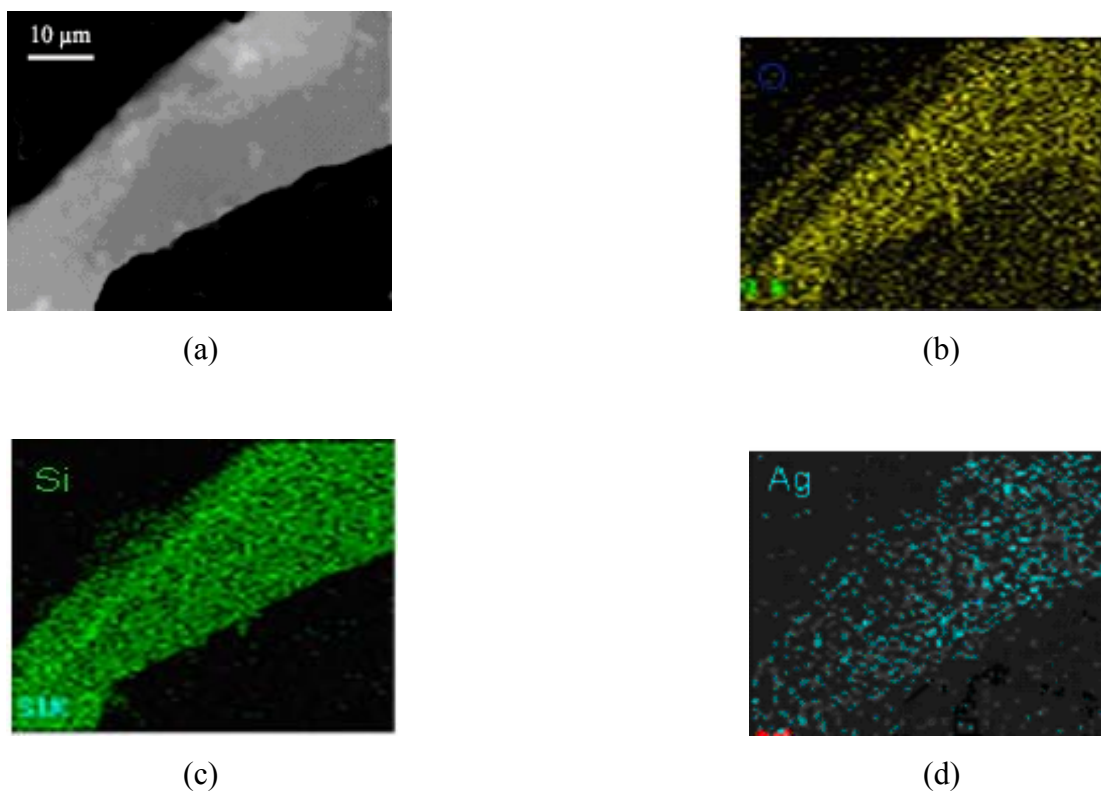


Figure 2-6. Series of X-ray mapping images of silver-silica nanocomposites containing 50 wt% glucose (i.e., 50GTS(Ag)). (a) As synthesized 50GTS(Ag) sample; (b) oxygen mapping; (c) silicon mapping; (d) silver mapping. Scale bar: 10 μm.

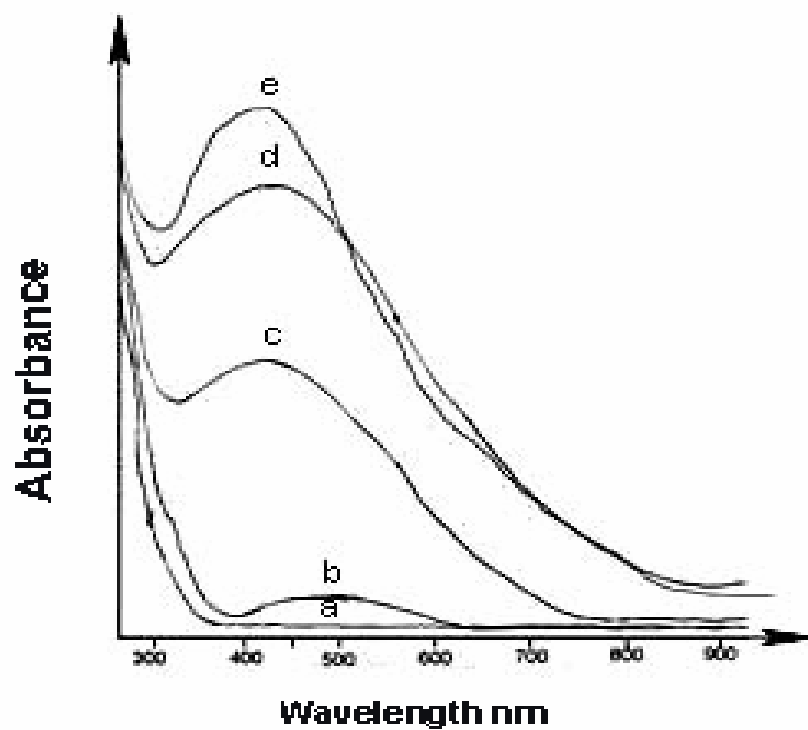


Figure 2-7. Solid-state UV-vis reflectance spectrum of mesoporous silver-silica nanocomposites, (a) 0GTS(Ag), (b) 10GTS(Ag), (c) 30GTS(Ag), (d) 40GTS(Ag) and (e) 50GTS(Ag). 0GTS(Ag) and 10GTS(Ag) do not show any maximum absorbance peaks. 30-40GTS(Ag) and 50GTS(Ag) show peaks at 425 and 410 nm, respectively. The spectra for all these samples were obtained at a scanning rate of 60 nm/min.

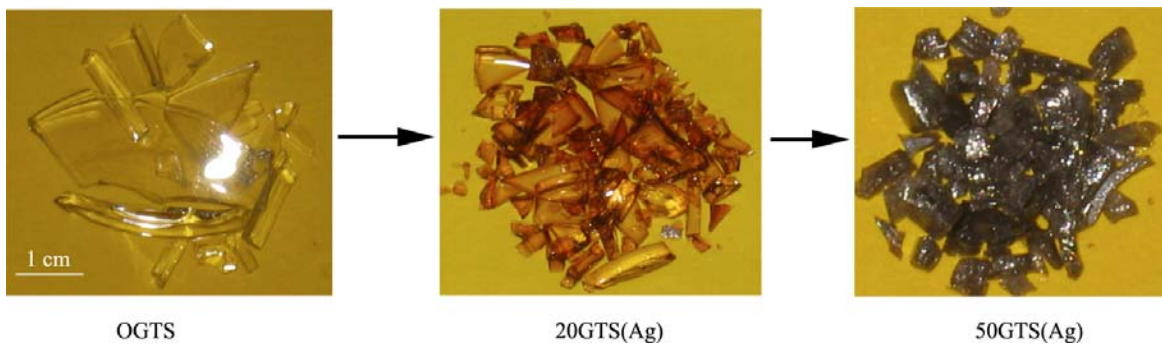


Figure 2-8. Shows the change in color observed in silica nanocomposites. (a) 0GTS samples are transparent because of the absence of silver nanoparticles; (b) 20GTS(Ag) samples are light yellow in color because of the presence of silver nanoparticles in very small amounts and (c) 50GTS(Ag) samples are dark brown in color depicting the presence of high content of silver nanoparticles in the sample. Scale bar 1 cm.

## Chapter 3: Fabrication of Organic-Inorganic Hybrid Copolymer Nanofibers via Electrospinning

### 3.1 Introduction

The boom in the field of nanotechnology has been attributed mainly to the distinct and amazing properties of nanomaterials, such as large surface area, enhanced optical, electrical and mechanical properties.<sup>1-5</sup> Some important nanomaterials that have taken a leading role in the field of material fabrication are nanoparticles, nanospheres, nanotubes, nanofibers.<sup>6-9</sup> As the size of the material shrinks down to the nanoscale range, the properties of the nanomaterial often change considerably from the parent bulk material. Recently, there has been growing interest in the fabrication of nanofibers using various polymers as bulk materials.<sup>10-13</sup> As the diameter of these fibers shrink from submicron size to the nanometer range, various properties such as large surface area, excellent mechanical properties, and enhanced fiber surface sensitivity, emerge.<sup>1,10</sup> Until recently the main techniques used for processing fibers were quite limited and tedious in nature. Some examples of such methods are: 1) fiber drawing,<sup>14</sup> where long individual fibers are drawn one by one manually or mechanically from a polymer melt or viscous solution, thus producing micron sized fibers. Only polymers that are capable of withstanding strong deformations and those which are cohesive enough can be used; 2) template synthesis is another method,<sup>15,16</sup> where porous materials, such as molecular sieves, acid etched silicon wafers, etc., are used as templates for the synthesis of nanotubes. The method is tedious and scale up is not economical; 3) self-assembly<sup>17</sup> is a technique where pre-existing polymer components organize themselves into polymer nanofibers, however the surface morphology and diameter of the fibers produced using this technology is not



uniform. Recently, another method called electrospinning was invented, where continuous fibers can be synthesized in large quantities in a very short time.<sup>18,19</sup>

Electrospinning method for producing nanofibers was popularized by Reneker et al., around 1995.<sup>20</sup> Before this period, electrospinning was used mainly in textile industries. The concept of this technique was developed 60 years back. It was Formulas who obtained a number of patents around 1934 to 1944 discussing the actual fabrication of polymer fibers from polymer solutions, using electrodes to charge the solution and deposit it on an oppositely charged metal collector.<sup>21,22</sup> It was only after 1995, that electrospinning was researched for use in medical<sup>23</sup> and biosensor<sup>24</sup> applications. The electrospinning process can be considered a variation of the electrospray process. When a drop of liquid at the tip of the capillary is subjected to an electrostatic field, it gets distorted into a conical shape and accelerates out as a fine jet of liquid that breaks into fine droplets and is collected on a grounded metal plate.<sup>20,25</sup> If a viscous polymer solution is used instead of a dilute liquid, the accelerating jet from the capillary does not break up into droplets but rather remains as a fiber and is collected on a charged metal collector. There have been many reports on the fabrication of fibers via electrospinning using various polymers, metal oxide solutions.<sup>26,27</sup> Yet relatively few reports have been published dealing with the electrospinning of organic-inorganic hybrid fibers<sup>34,36</sup> and almost none dealing with the processing parameters of these nanofibers. Some of the processing parameters that play an important role in the synthesis of these nanofibers are: a) concentration and viscosity of the polymer solution, which governs the thickness and the uniformity of the fibers; b) accelerating voltage, which when increased or decreased governs the formation of beads in the fiber mats; c) the distance from the tip of the

capillary to that of the collector also governs the length and thickness of the fibers and lastly; d) the ambient parameters, such as solution temperature and humidity, that affect the morphology of the fibers.<sup>20,28</sup>

The applications of the electrospun fibers are innumerable. Reinforcement of composites,<sup>29</sup> filtration membranes,<sup>30</sup> biosensors,<sup>31</sup> biomaterials,<sup>32</sup> military protective clothing,<sup>18</sup> cosmetic masking,<sup>33</sup> etc., are some of the important applications in which extensive research is being conducted, with excellent results for future product commercialization.<sup>34</sup> In addition to these applications, there are other unique applications, which are limited to organic-inorganic hybrid polymer fibers. This new class of materials is based on the combination of organic and inorganic components. They are also called nanocomposites as the inorganic and organic components both are combined together at the nanoscale level. These hybrid fibers have the advantages of both the organic fibers (such as light weight, flexibility and good moldability) and inorganic fibers (such as dynamic strength, heat stability, chemical resistance).<sup>35</sup> The hybrid fibers are expected to be used extensively as scratch and abrasive-resistant hard coatings,<sup>36</sup> as nonlinear optical materials and also as reinforcements in contact lenses, dental materials, plastics and elastomers.<sup>37</sup> Extensive research has been conducted in synthesizing hybrid materials in our laboratory, aiming at utilizing these hybrid materials for applications in developing dental filler composites. Two such synthesized hybrid polymers use 3-(trimethoxysilyl)propyl methacrylate (MSMA) and methyl methacrylate (MMA) as precursors to synthesize trimethoxysilyl functionalized polymethacrylate (PMCM) and poly[methyl methacrylate]-co-3-(tri-methoxysilyl)propyl methacrylate-silica hybrid (PMCM-SiO<sub>2</sub>) materials.<sup>38,39</sup> The PMCM-SiO<sub>2</sub> hybrid polymer has been synthesized by

the sol-gel method, where the organic component is PMCM and the inorganic component is silica. No phase separation between the organic and inorganic components was observed in the PMCM-SiO<sub>2</sub> polymer, due to extensive covalent bonding between them.<sup>40</sup> These hybrid polymers have exceptional thermal mechanical properties and hence, are good reinforcement candidates for dental materials. Thus, the above-mentioned polymer hybrids were synthesized and then used to fabricate nanofibers via the electrospinning technique. The influence of different parameters, such as polymer solution concentration and viscosity, on the morphology of the fibers, was studied. Finally, the hybrid PMCM and PMCM-SiO<sub>2</sub> nanofibers thus formed were then evaluated for use as reinforcements in dental filler applications, as will be explained in the next chapter.

## **3.2 Experimental Section**

The fabrication of hybrid nanofibers involves three main steps. One is the polymer synthesis of the copolymer PMCM. Second is the preparation of the PMCM and PMCM-SiO<sub>2</sub> electrospinning solution, and third is the fabrication of PMCM and PMCM-SiO<sub>2</sub> nanofiber mats.

### **3.2.1 Materials and Reagents**

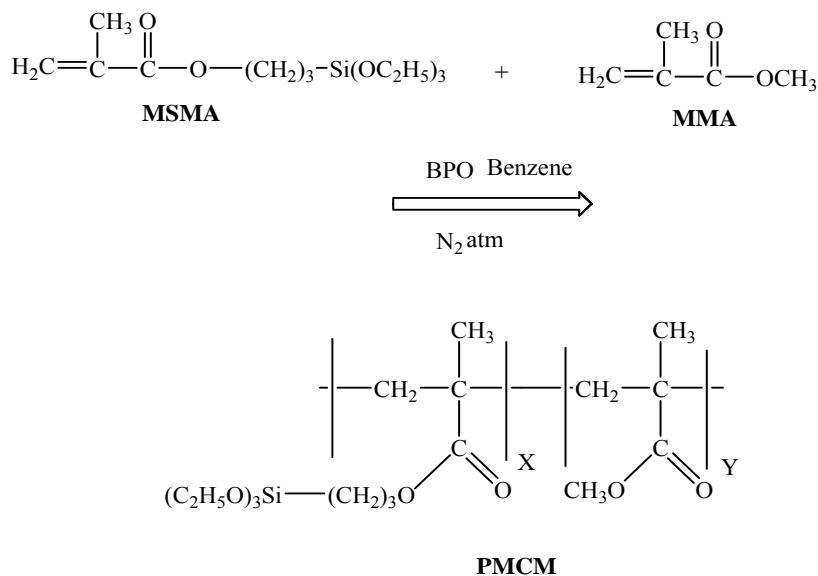
Methyl methacrylate (MMA) monomer, 3-(trimethoxysilyl)propyl methacrylate (MSMA), sodium hydroxide (NaOH), benzoyl peroxide (BPO), anhydrous calcium chloride (CaCl<sub>2</sub>), anhydrous benzene, anhydrous hexane, chloroform (CHCl<sub>3</sub>), tetrahydrofuran (THF) and dimethylformamide (DMF) were all purchased from Sigma-Aldrich Chemical Co. (Milwaukee, WI). MMA was first washed 5 times with equal amounts of 5 wt% NaOH solution to remove the inhibitor. The MMA was then finally

washed with distilled water and dried over anhydrous  $\text{CaCl}_2$  followed by distillation. MSMA was distilled under reduced pressure before use. Benzoyl peroxide (BPO) was purified by re-crystallization in benzene. Anhydrous benzene was also used as the solvent in the PMCM copolymer synthesis. Anhydrous hexane was used to precipitate the PMCM copolymer after synthesis. Solvents, such as chloroform ( $\text{CHCl}_3$ ), tetrahydrofuran (THF), and dimethylformamide (DMF), utilized to dissolve the PMCM copolymer for electrospinning purposes and tetraethyl orthosilicate (TEOS) utilized to synthesize the PMCM- $\text{SiO}_2$  hybrid fibers were also used as received.

### **3.2.2 Synthesis of Trimethoxysilyl Functionalized Polymethacrylate Copolymer (PMCM)**

Scheme 3-1 represents the reaction involved in the synthesis of PMCM. The copolymer was prepared by free radical copolymerization of 3-(trimethoxysilyl)propyl methacrylate (MSMA) with methyl methacrylate (MMA), using BPO as an initiator in benzene at 70 °C. MMA is first washed with sodium hydroxide (NaOH) and distilled water to remove the inhibitor. MMA and MSMA are then purified by distillation under reduced pressure to prevent polymerization. In a typical procedure for the synthesis of PMCM, 27 g of MMA and 7.5 g of MSMA (9:1 mol ratio, respectively) were mixed together in a round bottom flask. 60 ml of anhydrous benzene solvent and 0.1% of BPO (0.03 g) initiator were then added to the monomer mixture. All the steps were carried out as quickly as possible to keep the moisture content to a minimum. The polymerization was conducted at 70 °C under nitrogen for 10 hours. The viscous PMCM polymer thus produced was precipitated out of the reaction mixture using anhydrous hexane. The polymer was re-dissolved and precipitated out using benzene and hexane, respectively, to

wash out any un-reacted monomer. The copolymer was dried at 40 °C under vacuum and in the presence of anhydrous phosphorous pentoxide for three days and finally stored under vacuum in a sealed glass container. The molecular weight of the PMCM copolymer thus obtained was around 85,000 as determined by gel permeation chromatography (GPC).

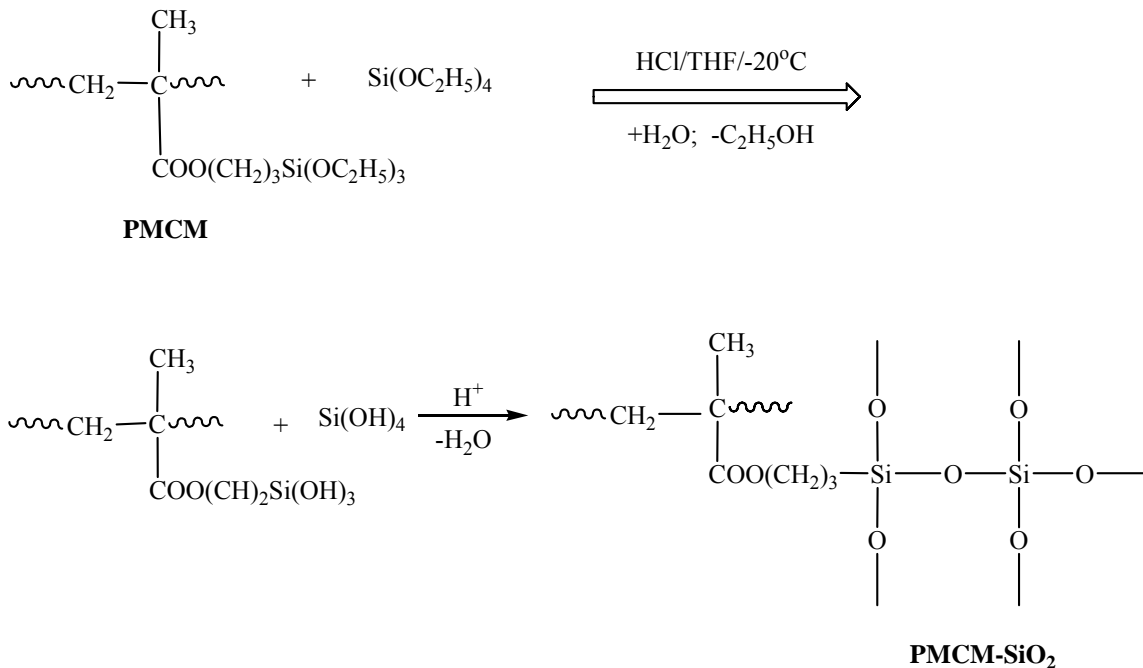


Scheme 3-1. Synthesis of PMCM.

### 3.2.3 Synthesis of Poly[methyl methacrylate]-co-3-(tri-methoxysilyl)propyl methacrylate-silica (PMCM-SiO<sub>2</sub>) Hybrid Polymer

Scheme 3-2 represents the reaction involving the synthesis of PMCM-SiO<sub>2</sub>. Two 10 wt% PMCM copolymer solutions were prepared by dissolving the copolymer in THF and DMF to give solutions A and B, respectively. A hydrolyzed TEOS solution was then prepared by mixing TEOS with THF, water, and 2 M HCl in a molar ratio of 1:3:3:0.01, to give solution C. Next, four solutions of A:C and B:C were prepared by mixing them in 9:1 and 8:2 weight ratios as seen in Table 3-1. In general, 9 g of 10 wt% PMCM/THF

solution is mixed with 1 g of prehydrolyzed TEOS solution dropwise with constant stirring. Covalent bonding between the silanol groups of the hydrolyzed TEOS with those present in the polymer chains of PMCM copolymer (Si-O-Si bond) occurs to give a homogenous and clear hybrid solution.



Scheme 3-2. Synthesis of PMCM-SiO<sub>2</sub>.

### 3.2.4 Preparation of PMCM Copolymer Electrospinning Solution

The copolymer solutions were prepared by dissolving PMCM in HPLC grade chloroform (CHCl<sub>3</sub>), THF and DMF. Different concentrations of the copolymer solutions were prepared and spun into fibers to study the effects of solvents on the morphology of the copolymer fibers, as well as to optimize the fabrication of fibers to the smallest achievable diameter. Table 3-2 gives a detailed list of all the solvents and the concentrations of solutions used for electrospinning. In a typical procedure for the synthesis of 6 wt% PMCM/DMF electrospinning solution, 3 g of PMCM copolymer were

dissolved in 7.8 g of HPLC grade DMF solution. The copolymer solution was constantly stirred at room temperature for 24 hours to obtain a homogeneous solution. Thus, different concentrations of the copolymer solution were prepared for electrospinning.

### **3.2.5 Preparation of PMCM-SiO<sub>2</sub> Copolymer Electrospinning Solution**

As stated under synthesis of PMCM-SiO<sub>2</sub>, two solutions A and B were mixed in a ratio of 9:1 and 8:2 with solution C. The hybrid solution thus prepared was stirred continuously and spun into fibers at different time intervals as specified in Table 3-3.

### **3.3 Electrospinning**

A schematic representation of the electrospinning instrument is shown in Figure 1-4 (Chapter 1). The apparatus consists of a syringe, which is clamped to an electrically insulated stand, which acts as a support for a blunt capillary pipette. The pipette holds the desired polymer solution, which is to be spun into fibers. A grounded copper plate covered with aluminum foil acts as a source for the deposition of fibers. A positive voltage is applied to the polymer solution by immersing a copper wire into it. Thus, an electric field is generated between the capillary tube tip containing the polymer solution and the grounded collecting copper plate. The electric field then induces a charge on the surface of the polymer solution producing a Taylor cone<sup>20,41</sup> through which a charged jet of polymer solution ejects out and is deposited in the form of fibers on the aluminum foil. A gamma high voltage supply ES30P-10W (0-30 kV, 10 Watts, Gamma High Voltage Research, Florida) instrument was used as the power source. The distance between the tip of the capillary tube and the grounded plate was kept constant at around 20 cm. The applied voltage varied from 5 to 20 kV. Ambient temperature was maintained inside the

electrospinning chamber, and care was taken to see that the atmosphere inside the chamber was devoid of humidity.

### **3.4 Instrumentation**

#### **3.4.1 Gel Permeation Chromatography (GPC)**

A Hewlett-Packard HP 1090 liquid chromatograph equipped with a refractive index detector, PLgel column and THF eluent was used to determine the molecular weight of the copolymer. The copolymer was dissolved in THF to obtain a 1% solution, and the instrument was calibrated against secondary polystyrene standards.

#### **3.4.2 Environmental Scanning Electron Microscopy (ESEM)**

The morphology and diameter of the electrospun fibers was analyzed by obtaining micrographs from the field emission environmental scanning electron microscope (Phillips XL-30, ESEM). Approximately 1 cm x 1 cm square pieces of fiber mats were mounted on top of sample holders using conducting carbon tape. The samples were then sputter coated with a monolayer of platinum. The sputter-coated fibers were then exposed to a voltage of 20 kV. The average diameter of the fibers was determined by measuring 100 random fibers from micrographs using UTHSCSA ImageTool 3.0.

#### **3.4.3 Fourier Transform Infrared Spectra (FT-IR)**

Infrared spectra of PMCM and PMCM-SiO<sub>2</sub> fibers were analyzed by an attenuated FT-IR Perkin-Elmer, Model-1600 spectrophotometer. Each spectrum was acquired by accumulation of 50 scans with the resolution of 4 cm<sup>-1</sup>.



#### **3.4.4 Differential Scanning Calorimeter (DSC,TA Q100) and Thermogravimetric Analyzer (TGA, TA Q50)**

3 mg of electrospun fibers were sealed in aluminum sample pans for DSC analysis. The analysis was conducted under dry nitrogen at a heating rate of 20 °C/min from 10 to 300 °C. The TGA analysis was performed in air using 20 mg of the sample placed in an open platinum pan over a temperature range of 25 to 600 °C at a heating rate of 20 °C/min.

### **3.5 Results and Discussion**

#### **3.5.1 Properties of PMCM and PMCM-SiO<sub>2</sub> Electrospinning Solution**

Various concentrations of copolymer PMCM solutions using several solvents were prepared for electrospinning. The solutions were all homogenous in nature, and the molecular weight of the PMCM polymer was relatively high enough to withstand the break down of the solution to droplets, thus producing long and non-woven fiber mats. The PMCM-SiO<sub>2</sub> hybrid solution prepared for electrospinning was also homogenous in nature, and the PMCM-SiO<sub>2</sub> hybrid fibers produced showed uniform distribution of PMCM polymer chains inside the silica matrix. The reason for the uniform distribution could be due to the rapid formation of covalent bonds between the PMCM polymer and the hydrolyzed TEOS during spinning. Since the hydrolysis of TEOS is carried out using an acid catalyst (HCl), as explained in the experimental section, the silicates formed in the PMCM-SiO<sub>2</sub> fibers are mostly linear rather than branched (which is the case when using base catalyst). Large domains of silicate aggregates are thus avoided in the PMCM-SiO<sub>2</sub> fibers and hence, no phase separation is noticed.<sup>38,39</sup>

### **3.5.2 Optimization of Properties for Electrospinning Uniform PMCM Copolymer Fibers**

#### **3.5.2.1 Effect of Solvents on PMCM Copolymer Fibers**

PMCM copolymer was electrospun using three different solvents. Table 3-2 gives the type of solvents used as well as the size of the fibers obtained for each polymer/solvent pair. The morphology and the size of the fibers were seen to vary considerably, with solvent. A detailed explanation of the effect of solvents is given below.

##### **Chloroform (CHCl<sub>3</sub>)**

Bongnitzki et al.,<sup>10</sup> in 2001, were among the first researchers to study the factors involved in the formation of nanostructures on electrospun nanofibers. In 2002 Megelski et al.<sup>25</sup> reported the formation of pores on polystyrene (PS) nanofibers, spun using CHCl<sub>3</sub> solvent. They stated that the high volatility, boiling point and vapor pressure of CHCl<sub>3</sub> played an important role in the formation of pores. The PMCM nanofibers that were spun using CHCl<sub>3</sub> solvent also showed similar porous morphology as seen in Figure 3-1. The surface of the fibers showed large number of pores, with the size of the pores varying considerably from 100 nm to 200 nm. The PMCM/CHCl<sub>3</sub> solution was found to dry out at the tip of the pipette during electrospinning, causing the tip to clog and require cleaning every few minutes. The diameter of the fibers was also seen to increase with increase in concentration of polymer solution. Thus increasing the concentration of the PMCM/CHCl<sub>3</sub> solution from 6 and 12 wt% caused the diameter of the fibers to increase from 1 to 4 μm.

**Tetrahydrofuran (THF)**

As the vapor pressure of THF is not as high as  $\text{CHCl}_3$ , the fibers synthesized using THF solvent did not contain any pores on the surface, and therefore, the fibers were smooth and cylindrical in nature, as seen in Figure 3-2. When the concentration of the polymer solutions was increased from 6 to 12 wt%, the diameter of the fibers also increased from 800 nm to 4  $\mu\text{m}$ , respectively.

**Dimethylformamide (DMF)**

The PMCM copolymer formed a homogenous solution when dissolved in DMF. The fibers produced in this case were smooth and cylindrical, with the diameter of the fibers much smaller than that obtained in the case of PMCM/THF and PMCM/ $\text{CHCl}_3$  solution. Thus, due to the formation of uniform and small diameter fibers, DMF was used as the standard solvent for the further optimization of the PMCM nanofibers.

**3.5.2.2 Effect of Concentration on PMCM Copolymer Fibers**

Deitzel et al.<sup>42</sup> demonstrated that viscosity and surface tension play an important role in determining the size of the fibers. When the concentration or viscosity of the electrospinning polymer solution was lower than a certain limit, drops were formed. As the concentration of the solution increased, the drops slowly gave rise to nanofibers. With further increase in concentration of spinning solution, the diameter of the fibers also increased, to finally produce larger ( $\mu\text{m}$  to cm size) fibers. Thus, the concentration of the PMCM solution (PMCM/DMF) was found to have a significant influence on the final size distribution of the fibers. It was noted that PMCM/DMF solutions with concentration below 3 wt% produced only droplets. This was due to the lack of polymer entanglement

and evaporation of DMF during electrospinning, causing the deposition of drops on the collecting plate rather than fibers. At concentrations between 3 to 5 wt%, a combination of fibers and droplets were produced. With further increase in concentration from 5 to 20 wt%, pure fibers without any beads or droplets were formed. Figure 3-3 represents the morphology and diameter of the fibers formed using several concentrations of PMCM/DMF spinning solution (4 to 20 wt% solutions). For 21 to 23 wt% solutions, extremely thick fibers were obtained. The fibers did not easily break off from the tip of the pipette, causing the fibers to oscillate in the electric field, and when they gained enough mass, they dropped on to the collecting plate. Electrospinning for solutions higher than 23% did not give any fibers as the viscosity was extremely high. It became increasingly difficult for the solution to flow and reach the tip of the pipette. The distribution of fiber diameters at 6, 12, and 20 wt% concentrations (PMCM/DMF) are shown in Figure 3-4. It was observed that the concentration of the PMCM copolymer solution is directly proportional to the diameter of the fibers. 6 wt% solutions produced fibers with diameters as small as 32 nm with no bead formation, and 20 wt% solutions produced fibers as large as 2.3  $\mu\text{m}$ .

### **3.5.2.3 Effect of Voltage and Spinning Distance on PMCM Copolymer Fibers**

The charge transport between the tip of the pipette containing the spinning solution to that of the grounded copper plate is carried out by the flow of polymer fibers. Thus, an increase in the electrospinning current reflects an increase in the mass flow rate from the capillary tube to the collector. An actual initiation of the PMCM/DMF solution jet took place at about 5 kV. As the voltage was increased from 5 kV to 20 kV, the flow rate of the spinning solution in the pipette also increased. The morphology and diameter

of the fibers did not vary significantly with the voltage. Only a small increase in diameter of the nanofibers was noticed upon increasing 5 to 20 kV. At voltages above 20 kV, there was no further change in the diameter of the fibers. Figure 3-5 further explains the effect of electrospinning voltage and concentration of spinning solution on the average diameter of the fibers. It was noted that the concentration of the polymer solution apparently has more effect on the diameter of the fibers than the electric field. When the distance between the tip of the pipette and the grounded metal plate was below 5 cm, wet and beaded fibers were formed. Increasing the distance to 20 cm produced uniform and smooth fibers. Thus optimum properties, such as voltage, type of solvent, and concentration, were studied to obtain smooth, uniform and small diameter fibers.

### **3.5.3 Optimization of Properties for Electrospinning Uniform PMCM-SiO<sub>2</sub> Fibers**

#### **3.5.3.1. Effect of Solvent on PMCM-SiO<sub>2</sub> Fibers**

As stated in the experimental section, PMCM-SiO<sub>2</sub> fibers were electrospun by mixing a PMCM polymer solution (either PMCM/DMF or PMCM/THF) with hydrolyzed TEOS sol in a 9:1 (or 8:1) ratio, respectively. All these reactions are performed at room temperature and at low-viscosity to facilitate good miscibility and uniformity between the organic components and the hydrolyzed sol. In order to prevent phase separation of organic (PMCM) and inorganic components (SiO<sub>2</sub>) from occurring, however the components should interact mechanically and chemically at the molecular level. In the PMCM-SiO<sub>2</sub> polymer fiber formation, covalent bonding between the silanol groups of the hydrolyzed TEOS with those present in the polymer chains of PMCM copolymer (Si-O-Si bond) is seen to occur, as seen in Scheme 3-2.

**Dimethylformamide (DMF)**

The common chemical interaction that occur between the organic and inorganic components include hydrogen bonding<sup>43,44</sup> and aromatic and ionic interaction.<sup>45</sup> Recently, Ogoshi et al.<sup>46</sup> reported the use of amphiphilic solvents, such as DMF, as compatibilizer that forms hydrogen bonds between the amide group of the DMF solvent and that of the silanol moieties of the hydrolyzed TEOS.

DMF was first used to dissolve PMCM polymer and then hydrolyzed TEOS sol was mixed into it. All the basic parameters, such as the distance between the tip of the pipette to the collector and the voltage, were kept constant at 20 cm and 20 kV, respectively. The fibers spun using DMF were thick and had a very broad size distribution. The reason for this was the presence of water in the added hydrolyzed TEOS sol, which could not evaporate completely during spinning of the fibers and hence, caused the deposition of wet and thick fibers. Another reason could be the rapid formation of covalent bonds induced by DMF causing the spinning solution to thicken, which made it difficult for the hybrid solution to maintain a continuous drop at the tip of the pipette, and eventually the hybrid solution turned into a gel.

**Tetrahydrofuran (THF)**

The synthesis of PMCM-SiO<sub>2</sub> hybrid fibers using THF as a solvent produced smaller diameter fibers compared to the DMF solvent. The formation of covalent bonds between the silanol groups of PMCM polymer and the hydrolyzed TEOS was relatively slow, which prevented the thickening of the spinning solution and hence, caused easy formation of fibers. The basic parameters, such as spinning distance and voltage, were

kept constant. Two different ratios of PMCM solution : hydrolyzed TEOS (9:1 and 8:2) were prepared as previously stated in the experimental section 3.2.5. The hybrid solutions of PMCM-SiO<sub>2</sub> thus prepared were spun at different time points as seen in Figure 3-6. The (9:1 and 8:2) hybrid fibers were fabricated in 3 sets each, at 24-hour intervals of each run until the solution finally condensed completely to form a gel. Figure 3-6 shows micrograms of hybrid fibers spun using DMF and THF (9:1 and 8:2 ratio hybrid fibers at 24 hour intervals).

### **3.5.3.2 Effect of Hydrolyzed TEOS and Spinning Time Interval on PMCM-SiO<sub>2</sub> Fibers**

With increase in prehydrolyzed TEOS solution and spinning time interval, the water content and covalent bonding (between the silanol groups of PMCM polymer and the hydrolyzed TEOS) in the spinning solution was also seen to increase. This caused the spinning solution to become viscous and, caused the production of large diameter fibers (Figure 3-6).

## **3.6 Characterization of PMCM and PMCM-SiO<sub>2</sub> Fibers**

### **3.6.1 Fourier Transform Infrared Spectra (FT-IR)**

Figure 3-7 represents the infrared spectra for polymethylmethacrylate (PMMA), PMCM copolymer, SiO<sub>2</sub> and PMCM-SiO<sub>2</sub> hybrid fibers (9:1 and 8:2 (PMCM: Hydrolyzed TEOS)). PMCM copolymer and PMCM-SiO<sub>2</sub> hybrid fibers showed distinct infrared adsorption peaks for the PMMA functional groups and silica structure. The IR peaks were well resolved, and can be used to investigate the development of material structure with increase in silica content. Figure 3-7 shows the spectrum for pure PMMA fiber. The (C=O) functional group for PMMA fiber is represented by the distinct peak at

1740  $\text{cm}^{-1}$ . The pure  $\text{SiO}_2$  fiber spectra (Figure 3-7) shows characteristic peaks at 795, 950 and 1081  $\text{cm}^{-1}$  that are all assigned to (Si-O) vibrations. Some broad peaks around 2800-3000  $\text{cm}^{-1}$  and 1400-1800  $\text{cm}^{-1}$  are also seen for ( $-\text{OCH}_2\text{CH}_3$ ,  $\text{CH}_3$  and  $\text{CH}_2$ ), which represents the unhydrolyzed TEOS structure. The broad band seen around 3390  $\text{cm}^{-1}$  is a result from the intra- and intermolecular hydrogen bonds of the silanol groups. Figure 3-7 represents the spectrum for the PMCM copolymer, in which peaks at around 1730  $\text{cm}^{-1}$  for (C=O), 1458-1450  $\text{cm}^{-1}$  for ( $\text{CH}_2$ -bending), 1088  $\text{cm}^{-1}$  for (Si-O-C bending) and 486  $\text{cm}^{-1}$  for (Si-O-C antisymmetric band) are noticed.<sup>38,39</sup>

Figure 3-7 also shows the spectra for 9:1 and 8:2 PMCM- $\text{SiO}_2$  fibers respectively. Absorption peaks for (Si-O-Si) asymmetric stretching at 1081  $\text{cm}^{-1}$  can be seen more clearly in 8:2 hybrid fibers compared to that of 9:1 hybrid fibers. This peak is caused by the asymmetric stretching of the (Si-O-Si) bonds in the sol-gel process of hydrolyzed TEOS and is due to the covalent bond formation between the organic polymer and the inorganic precursor. The absorption peak of (Si-OH) at 948  $\text{cm}^{-1}$  represents the hydrolyzed TEOS groups that sometimes escape condensation. (C=O) peaks which comes from the MMA and MSMA units of the PMCM copolymer are also seen in 9:1 hybrid fiber (Figure 3-7). A clear shift in dominance from PMCM peaks to silica peaks is seen going from 9:1 to 8:2 PMCM- $\text{SiO}_2$  fibers (Figure 3-7).

To further, prove that the PMCM polymer and hydrolyzed TEOS are covalently bonded to each other in the PMCM- $\text{SiO}_2$  fibers (rather than by hydrogen or ionic bonding), solvent extraction of PMCM- $\text{SiO}_2$  fibers in THF was conducted. Huang et al.<sup>47</sup> showed that, during solvent extraction, the weak hydrogen or ionic bonds between polymer and silica tend to dissolve the polymer completely, leaving behind silica



particles. If the bonding is strong (covalent bonding) and the interaction of PMCM and silica is at the nanoscale level, no polymer is dissolved during extraction. In case of 9:1 PMCM-SiO<sub>2</sub> hybrid fibers, 90 wt% of the sample remained unchanged after extraction in THF for 2 days, suggesting nanoscale interaction of PMCM copolymer with the silica groups.

### **3.6.2 Thermal Analysis of PMCM and PMCM-SiO<sub>2</sub> Hybrid Fibers**

#### **3.6.2.1 Differential Thermogravimetric Analysis (TGA)**

Figure 3-8 represents results of the differential thermogravimetric analysis (TGA) of neat SiO<sub>2</sub>, neat PMMA, PMCM copolymer and PMCM-SiO<sub>2</sub> hybrid fibers in air. The degradation temperatures for the samples are all slightly lower than the literature values, as the samples for this experiment were characterized as synthesized and none was tempered by heat treatment. The hybrid fibers are further categorized depending on the silica content present in the fibers. The deconvoluted derivative thermogravimetric (DTG) curves of the fibers have been shown in the Figure 3-8 inset. Furthermore, degradation temperatures, experimental and calculated residue values (which represent the final silica content of the fibers after complete burning of the polymer present in the fibers) were tabulated in Table 3-4. There is a slight discrepancy noticed between the calculated and experimental values obtained for the silica residue in all the fibers, which could be explained via the TGA curves of the pure silica fibers represented by curves (Figure 3-8e) and (Figure 3-8f) of Figure 3-8. They represent the curves that were obtained for as-spun pure silica fibers and heat-treated silica nanofibers (150 °C for 2 hours). Curve (Figure 3-8e), shows a slight degradation compared to curve (Figure 3-8f), which is caused due to the self-condensation reaction of the silanol groups. Curve (Figure

3-8f), does not show any such degradation, as all the silanol groups are degraded in the heat treatment procedure conducted before the actual TGA experiment.

A single degradation stage curve was formed for pure PMMA fibers at around 288 °C (Figure 3-8a). No significant change in the thermal behavior was noticed among the pure PMMA and PMCM copolymer fibers. Increase in degradation temperature of the hybrid fibers from 310 °C in PMCM fibers to 371 °C in PMCM-SiO<sub>2</sub> fibers (8:1) is noticed (Table 3-4). This increase in thermal stability of the fibers with increase in silica content can be attributed to the greater increase in the cross linking between the PMCM chains, via the hydrolysis and condensation of the hydrolyzed TEOS precursor.<sup>48-50</sup>

### 3.6.2.2 Differential Scanning Calorimeter (DSC)

All the fibers starting from neat PMMA to PMCM-SiO<sub>2</sub> hybrids were analyzed as shown in Figure 3-9 by DSC to determine the glass transition temperature ( $T_g$  is the temperature when the mechanical properties of a material changes from rubber (elastic) to that of glass (brittle)). From the established concepts in the field of nanocomposites by Huang et al.<sup>47</sup> it is proposed that as the content of the filler (silica) in the sample (PMCM and PMCM-SiO<sub>2</sub>) increases, the  $T_g$  peak becomes broader and also shifts to a higher value. The  $C_p$  (heat capacity) also has been noticed to decrease with increase in the filler content. Huang, et al.<sup>47</sup> also observed the broadening and eventually the disappearance of  $T_g$  as the content of SiO<sub>2</sub> was increased.

The DSC curves for the PMCM-SiO<sub>2</sub> fibers also showed similar trends. Pure SiO<sub>2</sub> fibers as seen in Figure 3-9 did not show any  $T_g$ , nor any endothermic curve. This was due to extremely high decomposition temperatures of SiO<sub>2</sub> (>1000 °C), due to the ridged Si-O-Si bonds. On the other hand, PMMA and PMCM fibers showed a single  $T_g$  at

around 124 °C and 104 °C, respectively (Figure 3-9). Considerable broadening of the curves, due to the increase in the content of silica was observed in going from PMMA all the way to SiO<sub>2</sub> fibers (Figure 3-9). Comparison of the DSC results in (9:1) and (8:2) PMCM-SiO<sub>2</sub> fibers produced interesting results. (8:2) PMCM-SiO<sub>2</sub> fibers produced two T<sub>g</sub>'s, at 108 °C and 245 °C, compared to the single T<sub>g</sub> at 106 °C observed in (9:1) PMCM-SiO<sub>2</sub> fibers. The increase and broadening of the first T<sub>g</sub> temperature curve from 106 °C in (9:1) PMCM-SiO<sub>2</sub> fibers to 108 °C in (8:2) PMCM-SiO<sub>2</sub> fibers was due to the increased content of inorganic precursor (silica). The presence of two T<sub>g</sub> in the (8:2) PMCM-SiO<sub>2</sub> fibers could be due to phase separation between the polymer and the inorganic content of the fibers, which was previously observed by Huang et al.<sup>47</sup> in the hybrid samples with higher silica content. It can thus be concluded that, with the increase in content of silica in the hybrid fibers, the onset of T<sub>g</sub>, broadening of the T<sub>g</sub> curves and the chance of phase separation, increases.<sup>48-50</sup>

### 3.7 Conclusion

Fiber mats of hybrid composites containing different silica content were fabricated via the combination of sol-gel and electrospinning methods. The processing parameters on the morphology of the PMCM and the PMCM-SiO<sub>2</sub> fibers have been explored. A strong influence of the solvent, concentration and silica content on the electrospinning of fibers was noticed. The applied voltage and the spinning distance also influenced the diameter and morphology of the fibers to some extent. After the parameters for the fabrication of the fibers were set, the chemical and thermal properties of the hybrid fibers were analyzed. The rapid formation of covalent bonds between the polymer and the silica content in the PMCM-SiO<sub>2</sub> fibers prevents phase separation from

occurring. The thermal analysis of the fibers using TGA and DSC further proved the absence of phase separation and the presence of covalent bonds between the organic-inorganic components in the fibers. The PMCM-SiO<sub>2</sub> fiber mats showed better thermal stability compared to PMCM fibers. This is because the PMCM-SiO<sub>2</sub> fiber mats not only contain properties of polymer fibers (such as flexibility and elasticity), but also contain inorganic properties (resistance to strong chemicals and thermal stability) contributed by the silica content of the fibers. The hybrid fiber mats thus produced could then be utilized as fillers, to increase the mechanical properties of products such as dental materials, ballistic materials and protective surface coatings.

### 3.8 Reference List

1. Huang, Z. M., Zhang, Y. Z., Kotaki, M., Ramakrishna, S. A review on polymer nanofibers by electrospinning and their applications in nanocomposites. *Composites Science and Technology*, 63(15), 2223-2253. 2003.
2. Epifani, M., Carlino, E., Blasi, C., Giannini, C., Tapfer, L., Vasanelli, L. Sol-gel processing of Au nanoparticles in bulk 10% B<sub>2</sub>O<sub>3</sub>-90% SiO<sub>2</sub> glass. *Chemistry of Materials*, 13(5), 1533-1539. 2001.
3. Bronstein, L. M., Polarz, S., Smarsly, B., Antonietti, M. Sub-nanometer noble-metal particle host synthesis in porous silica monoliths. *Advanced Materials (Weinheim, Germany)*, 13(17), 1333-1336. 2001.
4. Hayakawa, T., Ono, Y., Nogami, M. Linear and nonlinear optical properties of monodispersed gold clusters in silica glass by sol-gel method. *Proceedings of SPIE-The International Society for Optical Engineering*, 3943(Sol-Gel Optics V), 102-111. 2000.
5. Khushalani, D., Hasenzahl, S., Mann, S. Synthesis of mesoporous silica monoliths with embedded nanoparticles. *Journal of Nanoscience and Nanotechnology*, 1(2), 129-132. 2001.
6. Nalwa, H. S. *Handbook of nanostructured materials and nanotechnology*, volume 3: electrical properties. Academic Press, Massachusetts, 597. 2000.
7. Nalwa, H. S. *Handbook of nanostructured materials and nanotechnology*, volume 1: synthesis and processing. Academic Press, Massachusetts, 645. 2000.
8. Nalwa, H. S. *Handbook of nanostructured materials and nanotechnology*, volume 4: optical properties. Academic Press, Massachusetts, 681. 2000.
9. Nalwa, H. S. *Handbook of nanostructured materials and nanotechnology*, volume 5: organics, polymers, and biological materials. Academic Press, Massachusetts, 783. 2000.
10. Bognitzki, M., Czado, W., Frese, Thomas., Schaper, A., Hellwig, M., Steinhart, M., Greiner, A., Wendroff, J. H. Nanostructured fibers via electrospinning. *Advanced Materials (Weinheim, Germany)*, 13(1), 70-72. 2001.
11. Reneker, D. H., Chun, I. Nanometer diameter fibers of polymer, produced by electrospinning. *Nanotechnology*, 7(3), 216-223. 1996.
12. Al. Shehri, H., Smith, D. J., Hansen, L. M., Reneker, D. Preservation of enzymes in electrospun nanofibers. *Technical Papers - American Chemical Society, Rubber Division, Spring Technical Meeting*, 163rd, San Francisco, CA, United States, 670-698. 2003.
13. Aryal, S., Dharmaraj, N., Bhattarai, S. R., Khil, M. S., Kim, H. Y. Deposition of gold nanoparticles on electrospun MgTiO<sub>3</sub> ceramic nanofibers. *Journal of Nanoscience and Nanotechnology*, 6, 510-513 (2006).
14. Dees, J. R., Spruiell, J. E. Structure development during melt spinning of linear polyethylene fibers. *Journal of Applied Polymer Science*, 18(4), 1053-1078. 1974.
15. Martin, C. R. Membrane-based synthesis of nanomaterials. *Chemistry of Materials*, 8(8), 1739-1746. 1996.

16. Feng, L., Li, S., Li, H., Zhai, J., Song, Y., Jiang, L., Zhu, D. Super hydrophobic surface of aligned polyacrylonitrile nanofibers. *Angewandte Chemie, International Edition*, 41(7), 1221-1223. 2002.
17. Whitesides, G. M., Grzybowski, B. Self-assembly at all scales. *Science*, 295(5564), 2418-2421. 2002.
18. Gibson, P., Schreuder-Gibson, H., Pentheny, C. Electrospinning technology: direct application of tailorable ultrathin membranes. *Journal of Coated Fabrics*, 28(July), 63-72. 1998.
19. Reneker, D. H., Chun, I. Nanometer diameter fibers of polymer, produced by electrospinning. *Nanotechnology*, 7(3), 216-223. 1996.
20. Doshi, J., Reneker, D. H. Electrospinning process and applications of electrospun fibers. *Journal of Electrostatics*, 35(2&3), 151-160. 1995.
21. Formhals, A. Apparatus for producing artificial filaments from material such as cellulose acetate. 1975504. US. 1934.
22. Formhals, A. Apparatus and process for making artificial threads. 364780. GB. 1934.
23. Badami, A. S., Kreke, M. R., Thompson, M. S., Riffle, J. S., Goldstein, A. S. Effect of fiber diameter on spreading, proliferation, and differentiation of osteoblastic cells on electrospun poly(lactic acid) substrates. *Biomaterials*, 27, 596-606. 2006.
24. Aussawasathien, D., Dong, J. H., Dai, L. Electrospun polymer nanofiber sensors. *Synthetic Metals*, 154, 37-40. 2005.
25. Megelski, S., Stephens, J. S., Chase, D. B., Rabolt, J. F. Micro- and nanostructure surface morphology on electrospun polymer fibers. *Macromolecules*, 35(22), 8456-8466. 2002.
26. Azad, A. M., Matthews, T., Swary, J. Processing and characterization of electrospun Y<sub>2</sub>O<sub>3</sub>-stabilized ZrO<sub>2</sub> (YSZ) and Gd<sub>2</sub>O<sub>3</sub>-doped CeO<sub>2</sub> (GDC) nanofibers. *Materials Science and Engineering B-Solid State Materials for Advanced Technology*, 123, 252-258. 2005.
27. Azad, A. M. Fabrication of yttria-stabilized zirconia nanofibers by electrospinning. *Materials Letters*, 60, 67-72. 2006.
28. Buer, A., Ugbohue, S. C., Warner, S. B. Electrospinning and properties of some nanofibers. *Textile Research Journal*, 71(4), 323-328. 2001.
29. Kojima, Y., Usuki, A., Kawasumi, M., Okada, A., Kurauchi, Toshio., Kamigaito, O. Synthesis of nylon 6-clay hybrid by montmorillonite intercalated with ε-caprolactam. *Journal of Polymer Science, Part A: Polymer Chemistry*, 31(4), 983-986. 1993.
30. Chung, H. Y. Polymer, polymer microfiber, polymer nanofiber and applications including filter structures. Donaldson Company, Inc. USA. 2001-US24948(2002020668), 92. WO. 2001.
31. Patel, A. C., Li, S., Yuan, J. M., Wei, Y. In situ encapsulation of horseradish peroxidase in electrospun porous silica fibers for potential biosensor applications. *Nano Letters*, 6(5), 1042-1046. 2006.
32. Chu, B. Biodegradable and/or bioabsorbable fibrous articles and methods for using the articles for medical applications. 2001-859007(2002173213), 29. US. 2001.

33. Smith, D., Reneker, D., Kataphinan, W., Dabney, S. Electrospun skin masks and uses thereof. (University of Akron, USA. 2000-US27775(2001026610), 14. WO. 2000.
34. Jayaraman, K., Kotaki, M., Zhang, Y., Mo, X., Ramakrishna, S. Recent advances in polymer nanofibers. *Journal of Nanoscience and Nanotechnology*, 4(1-2), 52-65. 2004.
35. Shao, C., Kim, H., Yong G. J., Ding, B., Lee, D. R., Park, S. J. Fiber mats of poly(vinyl alcohol)/silica composite via electrospinning. *Materials Letters*, 57(9-10), 1579-1584. 2003.
36. Wen, J., Vasudevan, V. J., Wilkes, G. L. Abrasion resistant inorganic/organic coating materials prepared by the sol-gel method. *Journal of Sol-Gel Science and Technology*, 5(2), 115-126. 1995.
37. Huang, Z. M., Ramakrishna, S. Modeling inelastic and strength properties of textile laminates: an unified approach. *Composites Science and Technology*, 63(3-4), 445-466. 2003.
38. Wei, Y., Yang, D., Tang, L. Synthesis, characterization, and properties of new polystyrene-silica hybrid sol-gel materials. *Journal of Materials Research*, 8(5), 1143-1152. 1993.
39. Wei, Y., Jin, D., Yang, C., Kels, M. C., Qiu, K. Y. Organic-inorganic hybrid materials. Relations of thermal and mechanical properties with structures. *Materials Science & Engineering, C: Biomimetic Materials, Sensors and Systems*, C6(2,3), 91-98. 1998.
40. Wei, Y., Jin, D., Brennan, D. J., Rivera, D. N., Zhuang, Q., DiNardo, N. J., Qiu, K. Atomic force microscopy study of organic-inorganic hybrid Mmaterials. *Chemistry of Materials*, 10(3), 769-772. 1998.
41. Tayler GI. *Proceedings of the royal society of london, Series A.* 280, 383-397. 1964.
42. Deitzel, J. M., Kleinmeyer, J., Harris, D., Beck Tan, N. C. The effect of processing variables on the morphology of electrospun nanofibers and textiles. *Polymer*, 42(1), 261-272. 2000.
43. Chujo, Y., Saegusa, T. Organic polymer hybrids with silica gel formed by means of the sol-gel method. *Advances in Polymer Science 100 (Macromol.: Synth., Order Adv. Prop.)*, 11-29. 1992.
44. Chujo, Y., Matsuki, H., Kure, S., Saegusa, T., Yazawa, T. Control of pore size of porous silica by means of pyrolysis of an organic-inorganic polymer hybrid. *Journal of the Chemical Society, Chemical Communications*, (5), 635-636. 1994.
45. Tamaki, R., Chujo, Y. Synthesis of polystyrene and silica gel polymer hybrids utilizing ionic interactions. *Chemistry of Materials*, 11(7), 1719-1726. 1999.
46. Ogoshi, T., Chujo, Y. Synthesis of organic-inorganic polymer hybrids utilizing amphiphilic solvent as a compatibilizer. *Bull. Chem. Soc. Jpn*, 76, 1865-1871. 2003.
47. Huang, Z. H., Qiu, K. Y., The effects of interactions on the properties of acrylic polymers/silica hybrid materials prepared by the in situ sol-gel process. *Polymer*, 38(3), 521-526. 1997.

48. Chan, C. K., Peng, S. L., Chu, I. M., Ni, S. C. Effects of heat treatment on the properties of poly(methyl methacrylate)/silica hybrid materials prepared by sol-gel process. *Polymer*, 42(9), 4189-4196. 2001.
49. Lipatov, Y. Physical chemistry of filled polymers. Rubber and Plastics Research Association, Shrewsbury, England, 304. 1977.
50. Wang, Y. T., Chang, T. C., Hong, Y. S., Chen, H. B. Effect of the interfacial structure on the thermal stability of poly(methyl methacrylate)-silica hybrids. *Thermochimica Acta*, 397(1-2), 219-226. 2003.



Table 3-1. Synthesis of poly[methyl methacrylate]-co-3-(tri-methoxysilyl)propyl methacrylate-silica (PMCM-SiO<sub>2</sub>) hybrid.

C		
	9:1	8:2
	wt ratio	wt ratio
A	A:C	A:C
B	B:C	B:C

A represents 10 wt% PMCM/THF solution; B represents 10 wt% PMCM/DMF solution and C represents the hydrolyzed TEOS solution.

Table 3-2. Solvents employed for electrospinning PMCM copolymer fibers. (Includes concentration of electrospinning solution and average diameter of the nanofibers).

solvent	concentration wt%	diameter of fibers Nm
CHCl <sub>3</sub>	6.0	1000
	12.0	4000
THF	6.0	800
	12.0	4000
DMF	6.0	32-75
	12.0	50-470
	20.0	680-2300

Table 3-3. The composition of PMCM-SiO<sub>2</sub> electrospinning solution using THF as the solvent and average size of fibers spun at different intervals of time.

A / C (v/v)	average diameter of fibers nm		
	set 1 <sup>a</sup> immediately	set 2 <sup>b</sup> after 24 hour	set 3 <sup>c</sup> after 48 hour
9:1	310	497	1421
8:2	426	1016	1566

A represents 10 wt% of PMCM solution in THF, C represents prehydrolyzed TEOS sol.  
<sup>a</sup>Electrospinning solution (PMCM solution : hydrolyzed TEOS sol) spun immediately after mixing.  
<sup>b</sup>Electrospinning solution (PMCM solution : hydrolyzed TEOS sol) spun 24 hours after mixing.  
<sup>c</sup>Electrospinning solution (PMCM solution : hydrolyzed TEOS sol) spun 48 hours after mixing.

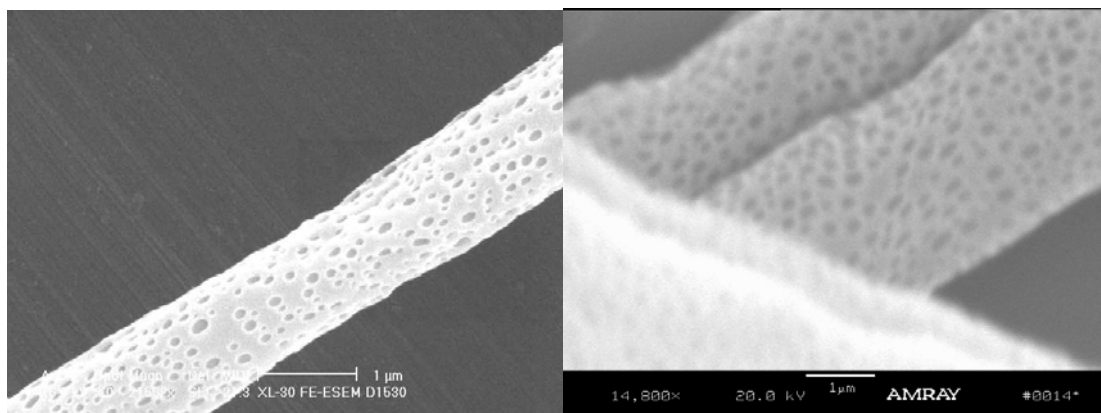
Table 3-4. Thermal characteristics of electrospun nanofibers.

sample ID <sup>a</sup>	(T <sub>g</sub> ) <sup>d</sup>	degradation temperature (Max peak) <sup>e</sup>	SiO <sub>2</sub> (wt%) <sup>f</sup> calculated	SiO <sub>2</sub> (wt%) <sup>g</sup> experimental
PMMA	124	288	0	0
PMCM	104	311	4	3.5
PMCM-SiO <sub>2</sub> (9:1)	110	366	25	24
PMCM-SiO <sub>2</sub> (8:2)	115	371	36	32
Pure SiO <sub>2</sub> (untreated) <sup>b</sup>	-----	-----	100	91
Pure SiO <sub>2</sub> (heat-treated) <sup>c</sup>	-----	-----	100	100

<sup>a</sup>Electrospun nanofibers that were subjected to heat treatment from 25 to 600 °C at the rate of 20 °C/min in air. <sup>b</sup>as-spun silica nanofibers. <sup>c</sup>Electrospun silica nanofibers heated to 150 °C for 2 hours before TGA analysis. <sup>d</sup>Glass transition temperature of nanofibers.

<sup>e</sup>Degradation temperature of electrospun nanofibers determined using TGA.

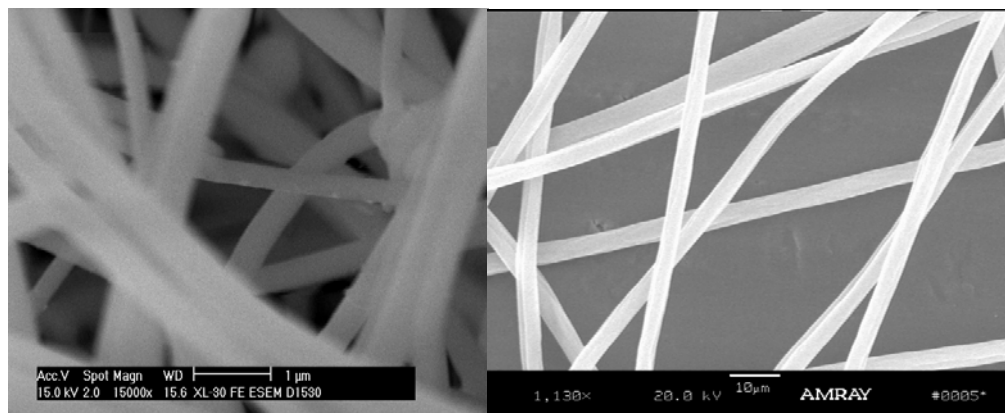
<sup>f</sup>Theoretical wt% of silica content present in the electrospun nanofibers. <sup>g</sup>Experimental wt% of silica content present in electrospun nanofibers determined using TGA.



1a

1b

Figure 3-1. Scanning electron micrographs of fibers spun using PMCM copolymer solution using  $\text{CHCl}_3$  as the solvent with fiber diameter ranging from  $1\mu\text{m}$  to  $4\mu\text{m}$ . (1a) 6 wt% solution and (1b) 12 wt% solution. Scale bar  $1\mu\text{m}$ .



2a

2b

Figure 3-2. Scanning electron micrographs of fibers spun using PMCM copolymer solution using THF as the solvent with fiber diameter ranging from 0.8 μm to 4 μm (2a) 6 wt% solution and (2b) 12 wt% solution. Scale bar: 10 μm.

wt% of PMCM polymer solution	scanning electron micrograph	fiber diameter nm
2%		
4%		AV: 90 Max:201 Min:70
6%		AV: 55 Max:75 Min:32
12%		AV: 187 Max:470 Min:50
20%		AV: 1499 Max:2300 Min:680

Figure 3-3. Scanning electron micrographs of fibers spun using PMCM copolymer solution using DMF as the solvent at different concentrations from 2 to 20 wt%, with an electric field of 20 kV and a constant spinning distance of 20 cm.

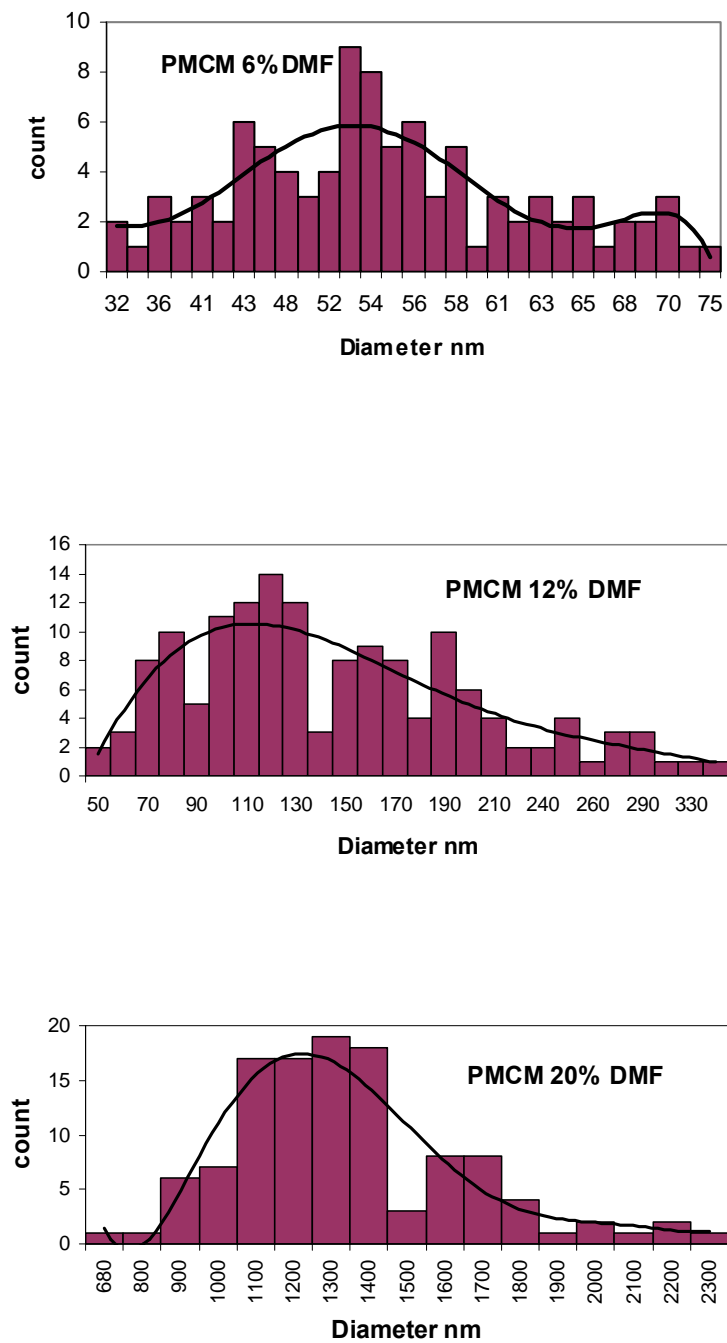
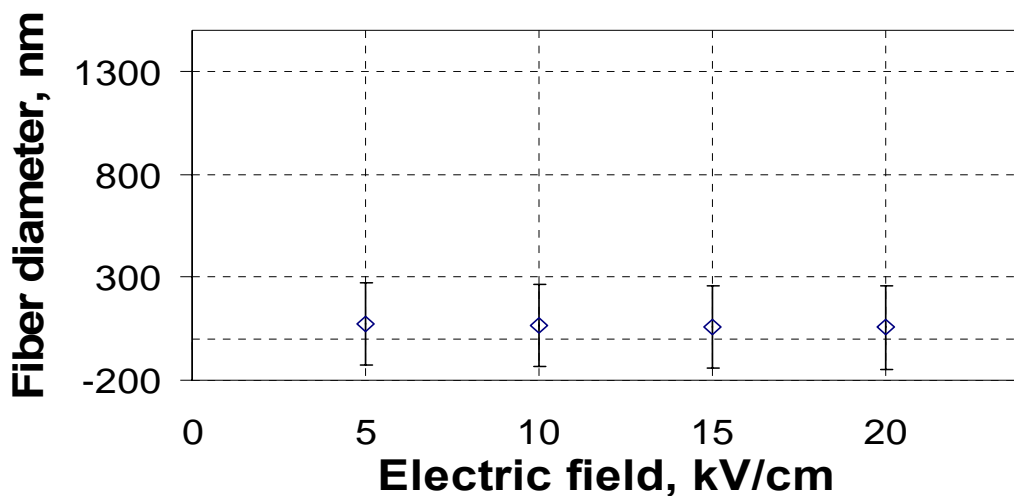
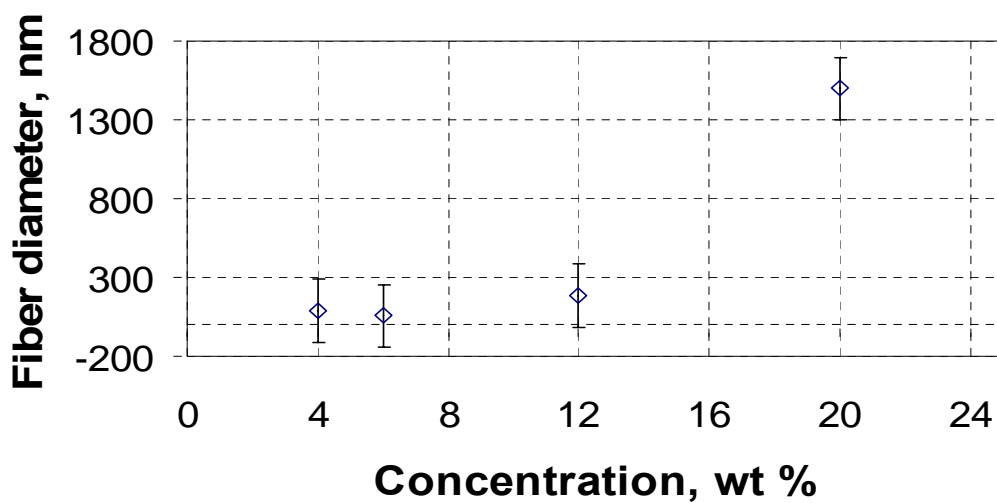


Figure 3-4. The size distribution of PMCM copolymer fiber diameter, with DMF as solvent using 6, 12, 20 wt% solutions, with a constant electrical field of 20 kV and a spinning distance of 20 cm.





(a)



(b)

Figure 3-5. Comparison of varying PMCM/DMF fiber diameters with respect to electric field and concentration of spinning solution; (5a) spinning distance of 20 cm, concentration of 6 wt% and electric field ranging from 5 to 20 kV; (5b) Spinning distance of 20 cm, concentration of 4 to 20 wt% and electric field of 20 kV.

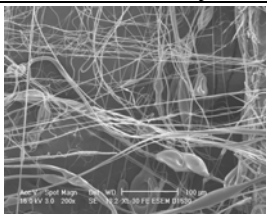
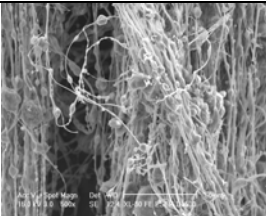
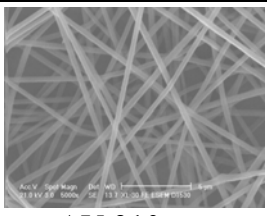
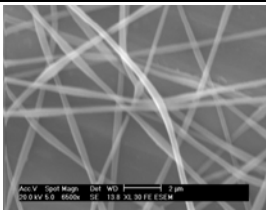
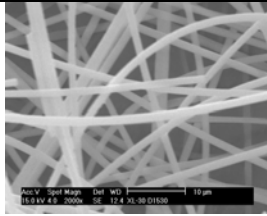
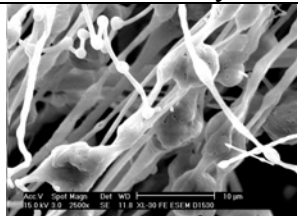
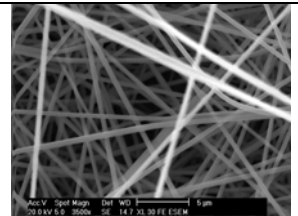
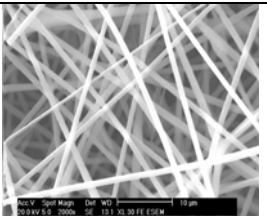
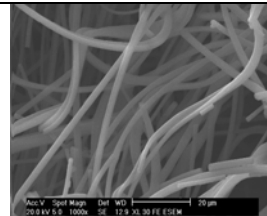
(9:1) (PMCM solution : Hydrolyzed TEOS sol)			
spin time interval	immediately	after 24 hours	after 48 hours
PMCM-SiO <sub>2</sub> /DMF	 AV: 670 nm	 AV: 2340 nm	gel
PMCM-SiO <sub>2</sub> /THF	 AV: 310 nm	 AV: 497 nm	 AV: 1421 nm
(8:2) (PMCM solution : Hydrolyzed TEOS sol)			
spin time interval	immediately	after 24 hours	after 48 hours
PMCM-SiO <sub>2</sub> /DMF	 AV: 3450 nm	gel	gel
PMCM-SiO <sub>2</sub> /THF	 AV: 426 nm	 AV: 1016 nm	 AV: 1566 nm

Figure 3-6. Micrograms of PMCM-SiO<sub>2</sub> fibers spun using DMF and THF as solvents. A mixture of 10 wt% PMCM/DMF solution (or PMCM/THF) and hydrolyzed TEOS sol in a (9:1) and (8:2) ratio was used as the spinning solution. The average diameter of the fibers is also noted.

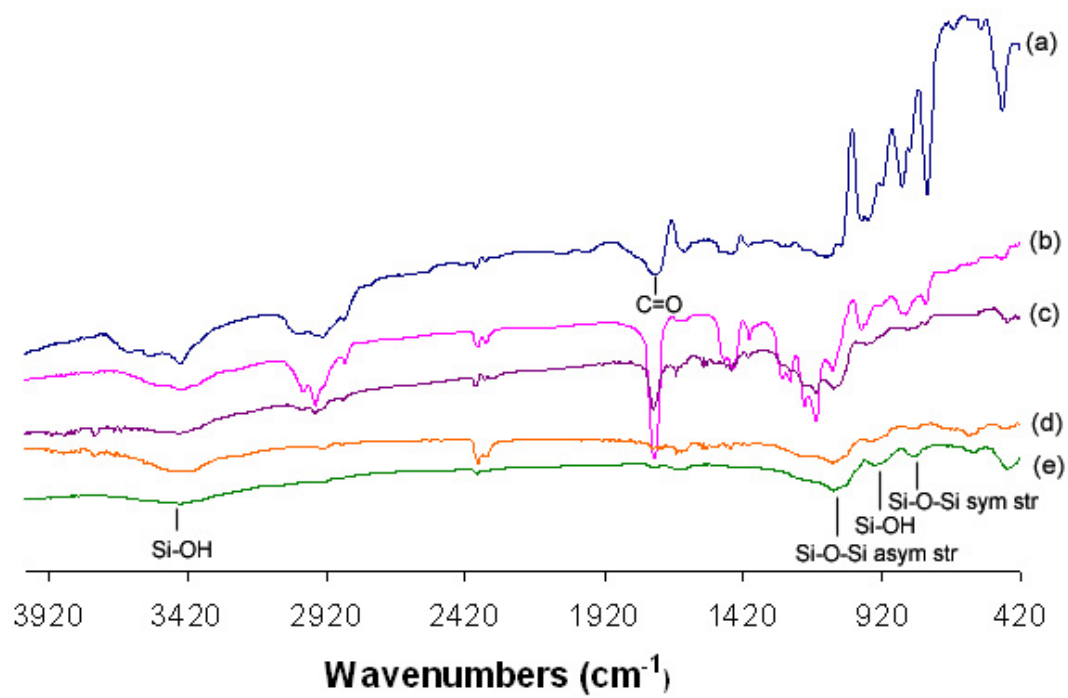


Figure 3-7. Infrared spectra of fibers: (a) neat PMMA; (b) PMCM; (c) PMCM-SiO<sub>2</sub> (9:1); (d) PMCM-SiO<sub>2</sub> (8:2); (e) Pure SiO<sub>2</sub>.

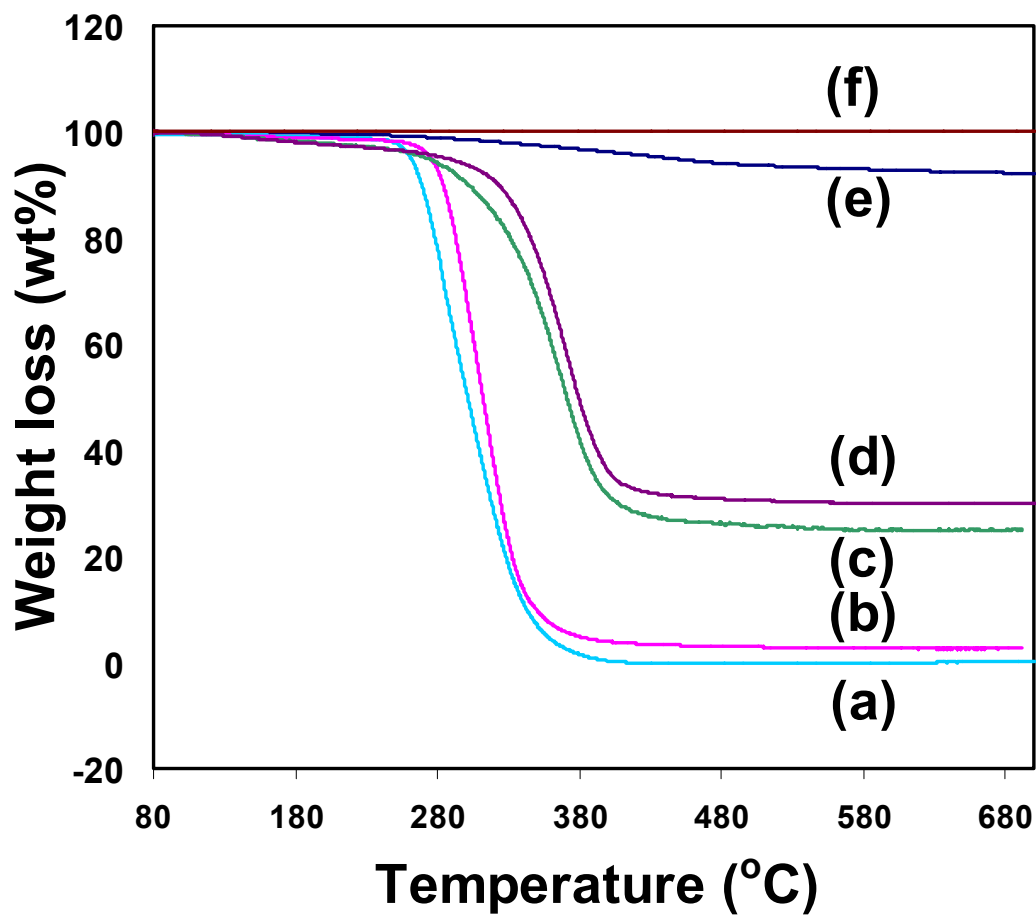


Figure 3-8. TGA and DTG thermograms of fibers; (a) PMMA ; (b) PMCM; (c) PMCM-SiO<sub>2</sub> (9:1); (d) PMCM-SiO<sub>2</sub> (8:2); (e) Pure SiO<sub>2</sub> (as spun) and (f) Pure SiO<sub>2</sub> (heat-treated to 150 °C for 2 hours before TGA analysis).

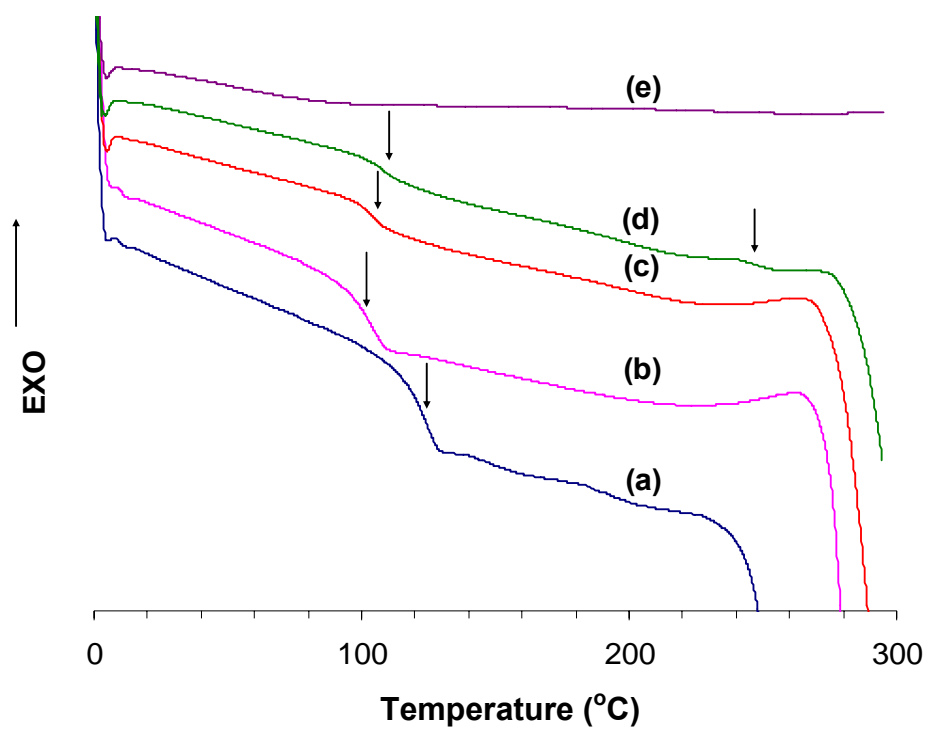


Figure 3-9. DSC thermogram curves of fibers; (a) neat PMMA; (b) PMCM; (c) PMCM-SiO<sub>2</sub> (9:1); (d) PMCM-SiO<sub>2</sub> (8:2); and (e) Pure SiO<sub>2</sub>. The glass transition of the fibers (T<sub>g</sub>) is denoted by arrows.

## **Chapter 4: Use of Organic-Inorganic Hybrid Copolymer Nanofibers for Dental Filler Applications**

### **4.1 Introduction**

In this section, general background on dental restoration materials, their use and advancement will be described. A comparison of available dental materials for dental restorative applications is made. The results on utilizing various types of dental composites as dental restoration materials are reviewed. The key features of an ideal dental restoration material are analyzed and a method to obtain good dental composites using electrospun hybrid fibers as filler is researched.

#### **4.1.1 General Background on Dental Composites**

One of the most common and expensive health problems faced by humankind is the deterioration of dentition caused by accidents or infections (teeth cavities). Use of dental amalgam as dental fillers has been one of the important breakthroughs, which has remained unchanged for the past 160 years.<sup>1,2</sup> Even with research directed towards replacing dental amalgam with better materials, it remains a popular material for use in posterior teeth repairs. Unfortunately, amalgam fillers had their share of disadvantages, such as corrosive and high thermal conductivity,<sup>2</sup> dark metallic gray appearance, which was not esthetically pleasing, and higher teeth sensitivity to galvanic currents and temperature increase caused by mechanical friction during food grinding. Due to these disadvantages, better and safer alternatives had to be researched.

Thus, replacements, including dental silicates and porcelain,<sup>3</sup> were introduced with limited success due to lack of stiffness, edge strength, erosion in the mouth and irritation of pulpal tissues surrounding teeth.<sup>2-4</sup> Dental composites were then introduced

as replacements for amalgams about 40 years ago.<sup>5,6</sup> A dental composite is usually made up of the polymer resin matrix, pure inorganic reinforced fillers and interfacial coupling agents. Methacrylate resin matrix containing silanized glass and ceramics are some common examples.<sup>7-9</sup> These materials presented opportunities never before equaled in modern dentistry, and have been widely accepted by the professionals to replace traditional 'dental amalgams', alleviating both safety and cosmetic concerns. Some advantages of dental composites are their aesthetics, elimination of galvanic currents, thermal conductivity, tensile strength and toughness.<sup>4,8</sup> The resin matrix is usually cured (hardened) by photoinitiated free radical polymerization. The monomer 2, 2-bis-[4-(methacryloxypropoxy)-phenyl]-propane (BISGMA) is one of the most commonly used base monomers, which was introduced by Bowen in 1962.<sup>5</sup> BISGMA is a very viscous, honey-like liquid and its advantages include reduced coefficient of thermal expansion, increased hardness and wear resistance. To improve the handling qualities, a low viscosity diluent monomer, such as tri (ethylene glycol) dimethacrylate (TEGDMA), is added to thin the resin.<sup>6</sup> In the BISGMA/TEGDMA system, BISGMA functions to limit polymerization shrinkage and enhance resin reactivity, while TEGDMA provides for increased methacrylate double bond conversions.<sup>10,11</sup> Only one drawback of using a diluent is that it causes decrease in strength and adsorption of water in the final cured material.<sup>12-14</sup> Introducing fillers into resins further reduces volume shrinkage, increases the mechanical properties of composite materials depending on volume fraction, size and shape of fillers,<sup>15</sup> causing a further increase in elastic modulus, hardness and compressive yield strength of the final dental composite.<sup>16</sup>

#### 4.1.2 Advantage and Disadvantage of Filler Materials

Different types of filler materials have been tested. Some of the most common fillers that have been used are silicates, glasses and glass-ceramics. The diverse shapes and size of the fillers used vary from spherical nanoparticles, irregularly shaped particles, fibers, whiskers, etc.<sup>6,9,15,17</sup> Spherically fused silica was used by Bowen et al. due to its similar refractive index with resin.<sup>18-20</sup> Gander et al.<sup>21</sup> introduced quartz particles and Rossi et al.<sup>22</sup> further improved the quality by using finer grain sizes to obtain better finish. Boyd<sup>23</sup> and Dietz et al.<sup>24</sup> recommended low-thermal-expansion fillers.

Investigations of the composite materials carried out over longer periods, however, were considerably less successful. Specifically, after 12–18 months of service, the degree of wear or loss of anatomical form was shown to be extensive.<sup>25-27</sup> Further investigations into reasons for failure revealed that, among other reasons, the inorganic filler particle was a major contributor.<sup>28,29</sup> Ironically, the inorganic filler, which had been added to the resin to fortify the material, was actually responsible, at least in part, for its demise.

During function, masticatory stresses were transmitted through the bolus of food and onto the surface of the particles projecting from the dental material surface. Since the particles were considerably harder than the resin matrix in which they were embedded, much of the stress was transmitted through the particle and into the resin itself. Wherever the submerged portion of the particle was angulated or irregular in shape, the stress concentrations became excessively high. Such a condition tended to generate small cracks around the particle, thereby weakening the matrix locally.

Around 1999, Xu et al. were among a few scientists who tried using short silica whiskers and other inorganic fibers as fillers. They showed that fibers contribute in a



much better way to the mechanical properties of the dental composites compared to particles, due to the ease with which fibers propagated the stress induced on the composite along the fiber length, rather than transferring it to the matrix and thus avoiding fractures.<sup>9,20,30,31</sup> Apart from avoiding fractures in the matrix, the nanofibers are also flexible and have high surface area, which means better attachment to the resin. The network of fibers can also physically bind well with the matrix and hence, will not slide out of the composite matrix, as do particles. The sol-gel silica fibers containing silanol groups on the surface of the fibers have also proven to have better interaction with the resin.<sup>32,33</sup> Krause et al.<sup>34</sup> reported the use of silane-treated glass fibers to reinforce BISGMA/TEGDMA resin, which caused 50% increase in tensile and compressive strengths compared to using particles.

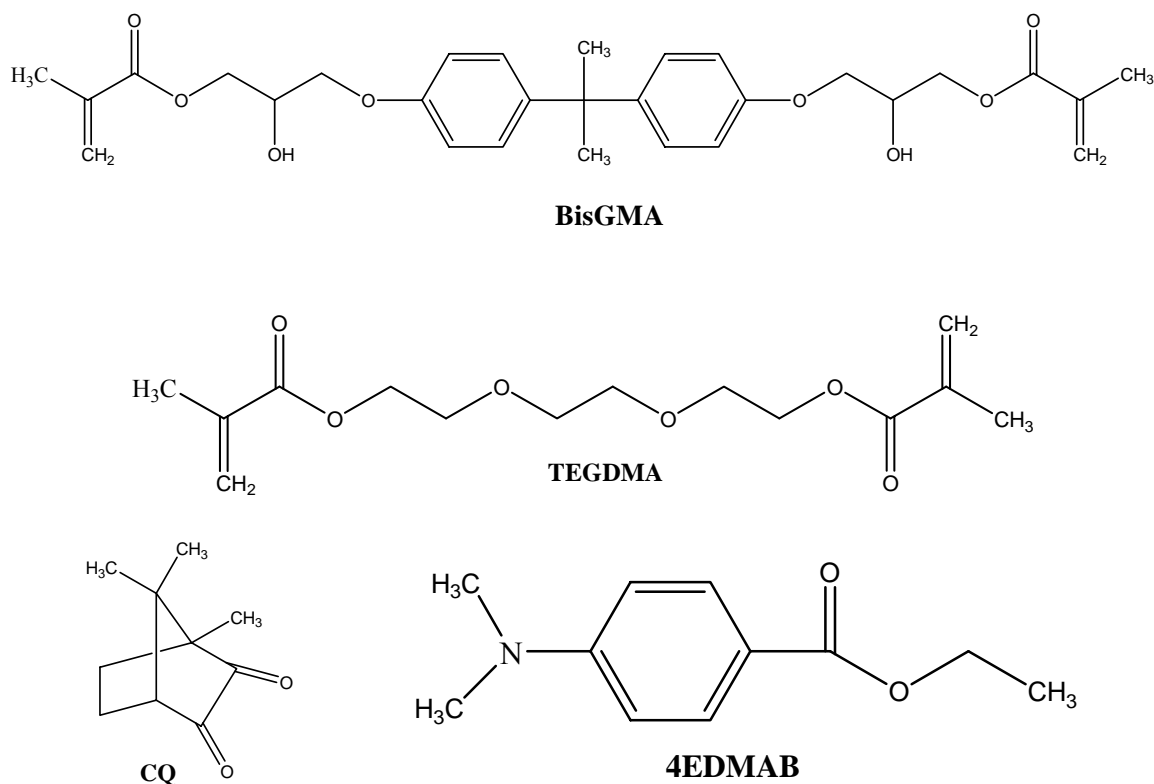
Extensive research is being done in our lab to develop new types of dental materials.<sup>35-38</sup> Research is also being conducted to study the thermal stability, density, and hardness of polymethacrylate-inorganic oxide hybrid materials (PMCM-SiO<sub>2</sub>) by investigating the relationship of polymer molecular weight, organic-inorganic composition and the thermal history of these materials in relation to utilizing the materials for dental applications.<sup>33,39-42</sup> Increasing the silica content of the polymer hybrid increases the hardness and density of the material. From the extensive research done in our group on these new hybrid polymer materials, it is clear that these materials have the properties of both organic polymers and inorganic materials and have a good potential in dental applications. Recently, Fong et al.<sup>31</sup> presented some work on using electrospun nylon fibers as filler with very promising results. In chapter 3, detailed research on electrospinning PMCM-SiO<sub>2</sub> fibers and studies of the various properties that affect the

morphology and diameter of the fibers were explained. Electrospinning is a very simple technique used to fabricate polymer nanofibers. Various organic and inorganic polymer materials have been used to spin fibers.<sup>43-46</sup> In this chapter, electrospun PMCM-SiO<sub>2</sub> fibers containing 25 wt% silica were added into BISGMA/TEGDMA resin, which was photocured into the final composite material. The fracture strength and elastic modulus of the fiber-filled composite materials and pure BISGMA/TEGDMA control samples (no fibers) were then analyzed.

## **4.2 Experimental Section**

### **4.2.1 Materials and Reagents**

PMCM-SiO<sub>2</sub> nanofibers were synthesized as explained in chapter 3. Methyl methacrylate (MMA), 3-(trimethoxysilyl)propyl methacrylate (MSMA), tetraethyl orthosilicate (TEOS), sodium hydroxide (NaOH), benzoyl peroxide (BPO), anhydrous benzene and hexane were all purchased from Sigma-Aldrich Chemical Co. (Milwaukee, WI). BISGMA and TEGDMA monomers (Scheme 4-1) that form the composite matrix, camphorquinone (CQ) and co-initiator ethyl-4 (N,N0-dimethylamino) benzoate (4EDMAB), which initiates photopolymerization (Scheme 4-1), were all purchased from Aldrich Chemical Co. All materials were used as received without further purification. A 2 mm x 2 mm roll of urethane foam tape and a 10 cm x 10 cm square Teflon<sup>®</sup> sheet, with a thickness of 0.5 cm, were purchased from 3M (Minnesota, USA) for the construction of a mold to produce the final dental composite test sample.



Scheme 4-1. Molecular structures of dental monomers and initiators.

#### 4.2.2 Electrospinning of PMCM-SiO<sub>2</sub> Nanofibers

Trimethoxysilyl functionalized polymethacrylate copolymer (PMCM) is the starting material for the synthesis of PMCM-SiO<sub>2</sub> hybrid fibers. A detailed procedure on synthesizing PMCM copolymer, preparing the PMCM-SiO<sub>2</sub> spinning solution and formation of PMCM-SiO<sub>2</sub> nanofiber mats is explained under the experimental section of chapter 3. In short a 10 wt% of PMCM copolymer solution prepared using THF as the solvent was mixed with a hydrolyzed TEOS solution in an 8:2 weight ratio. The solution thus prepared was then used to electrospin PMCM-SiO<sub>2</sub> fibers. A grounded copper plate covered with aluminum foil placed at a distance of 20 cm from the tip of the pipette acted as a source for the deposition of fibers.<sup>46,47</sup> The nonwoven fabric thus formed had 25 wt%

silica content with respect to the final weight of the fiber. The collected nonwoven fiber mat was then peeled off from the aluminum foil. The fabric thus collected was about 15 cm wide and 20 cm long, with a compressed thickness of about 30  $\mu\text{m}$ .

#### **4.2.3 Experimental Composite Preparation**

The peeled electrospun fabric was heat-treated at 100  $^{\circ}\text{C}$  in a vacuum oven for 5 hours, to remove any remaining solvent or moisture and to drive the sol-gel reactions to completion. 6 cm x 6 cm square fiber mats were then cut from the fabric sheets. The final dental composite material containing the PMCM-SiO<sub>2</sub> fiber mats was prepared in a mold (Figure 4-1), which was constructed on top of a 0.5cm thick Teflon<sup>®</sup> sheet, placed on a calibrated and leveled table. 2mm thick urethane foam tape formed the boarder of the 6 cm x 6 cm x 2 mm mold (Figure 4-1).

A dental resin monomer mixture of BISGMA/TEGDMA in 50/50 mass fraction was mixed together in a beaker. This solution was activated with the photo initiator CQ at mass fraction of 0.2% and the co-initiator 4EDMAB at a mass fraction of 0.8%.

Ultrasonic vibration (2510 Branson, USA) was employed to mix the light curable resin and remove any trapped air bubbles. A certain amount of the resin mixture was then placed inside the mold (on top of the Teflon<sup>®</sup> sheet). Layers of heat-treated and weighed fiber mats were then immersed into the resin. Within an hour, the fibers soaked up some amount of resin and swelled, after which more resin was added into the mold and the entire mold was placed inside the ultrasonic bath to remove any entrapped air. A thin glass slide was then placed on top of the mold to obtain an airtight composite mixture. The resin fiber mixture was then polymerized using a light-curing gun, for five minutes. The cured composite was then removed from the mold and allowed to stand overnight at

room temperature. The composite material thus formed was polished very carefully with a 2400 grid silicon carbide paper in a longitudinal direction. After which 2 mm x 2 mm x 25 mm size samples were cut using a diamond blade saw and polished one last time to obtain dental composite test samples (Figure 4-2). The mass fraction of each layer of nanofiber was approximately 0.5% with respect to the weight of the test sample.

#### 4.2.4 Three-Point Bending Test

Figure 4-3 represents a schematic drawing of a three-point bending test material, which was tested for flexural strength (FS) and elastic modulus ( $E_y$ ). It should be noted that, in the preparation of the 3-point bending specimen, one layer of fabric contributed approximately to 0.5% (mass fraction) of hybrid fibers, with respect to the composite resin. The final dimensions of the specimens were measured again and recorded. The specimens were fractured in a three-point bending jig with a 25-mm span on a computer-controlled Universal Testing Machine (model 8872, Instron Corp., Canton, MA) at a cross-head speed of 0.5 mm/min to record stress-strain curves. Calculations were made using the following equations<sup>31</sup>:

$$FS = 3P_1L/2WT_1^2$$

$$E_y = (P_1/d)(L^3/4WT_1^3)$$

Scheme 4-2. Equations used to determine the fracture strength and elastic modulus of dental composite material.

Where  $P_1$  is the load at fracture,  $L$  is the distance between two supports (which was set to be 20 mm),  $W$  is the width of the specimen,  $T_1$  is the thickness of the specimen, and  $d$  is the deflection, in millimeters, at load  $P_1$ .

### 4.3 Instrumentation

A Universal Testing Machine was used to conduct the three-point bend test to evaluate the FS and  $E_y$  of the samples. The samples were loaded on the instrument and a crosshead speed of 0.5 mm/min was used. The distance between the support beams of the three-point test jig was 20 mm. A field emission environmental scanning electron microscope (Phillips XL-30, ESEM) was used to study the selected fracture surfaces of the 3-point bending specimens for fracture origins (e.g., air bubbles, nanofiber agglomerates) and crack-fiber interactions (e.g., fracture of nanofiber, nanofiber pullout). Prior to SEM observations, the samples were sputter coated with a monolayer of platinum to allow for better electrical conduction and better resolution.

### 4.4 Results and Discussion

Table 4-1 gives a detailed description of the sample types that were analyzed using the three-point bending test. Three sets of (ten samples in each set) composite samples, containing one, five and eight layers of PMCM-SiO<sub>2</sub> fibers were prepared. A blank control composite material without fibers was also prepared for comparison.

#### 4.4.1 Observation of Fractured Composite Material Surface using ESEM

Figure 4-4 shows the SEM image of a PMCM-SiO<sub>2</sub> fiber sample. The average diameter of the fibers ranged from 300 to 400 nm. After the electrospun nanofibers were heat-treated, immersed and completely soaked in the mixture of activated BISGMA/TEGDMA monomers, the fabric swelled up. This process converted the PMCM-SiO<sub>2</sub> nanofibers from the dry and dense nonwoven fabric to the scaffold-like, completely soaked framework. After the photopolymerization, the resin completely covered the fibers and interpenetrated it completely. The nanofibers inside the composites

were randomly distributed with no clear alignment. The embedded nanofibers tended to break instead of pull/out during the 3-point bending test, suggesting good bonding between the nanofibers and BISGMA/TEGDMA matrix (Figure 4-5). Thus, it can be assumed that the interface between the matrix and the fibers was very strong and there were no empty spaces between the surface of the fibers and the composite material. The fracture surface of the composite material was devoid of any holes, which further proved that there was no pull out of fibers from the composite at breaking point. The fibers were seen to break close to the surface, which implied that the fibers absorbed the stress during breaking, and hence, contributed in reinforcing the composite material. Figures 4-6a and 4-6b are used to study and compare the morphology of the fractured surface of the composite materials containing fibers with that of the neat resin. The direction of the crack propagation during the 3-point bending test was approximately from top to bottom in each micrograph. The fracture surface of the nanofiber-reinforced composite resin (Figure 4-6a) was very rough, while the fracture surface of the neat resin (Figure 4-6b) was much smoother. Meanwhile, the neat resin sample had relatively large fracture steps, indicating little resistance to the applied force. The nanofibers deflected the crack during force application, and when the crack finally broke away from the nanofibers, numerous fracture lines and steps were created in the fracture surface, suggesting energy consumption during breaking.

#### **4.4.2 Effect of Fiber Mats on Composite Material**

Each layer of fabric contributed to 0.5% (mass fraction) of PMCM-SiO<sub>2</sub> nanofibers in the composite resin. Thus, one, five and eight layers of fabrics represented the mass fractions of 0.5, 2.5 and 4 wt% of nanofibers, with respect to composite resin,

respectively. Figures 4-7a and 4-7b compare the FS and  $E_y$  of zero, one, five and eight layer fibers containing composite materials obtained by taking the mean value of ten measurements, with the error bar showing a standard deviation. From Figure 4-7, it is clear that with increase in amounts of PMCM-SiO<sub>2</sub> fibers in the composite, the FS and  $E_y$  modulus of the materials also increase. The FS and  $E_y$  of the neat resin (mean  $\pm$  standard deviation) were  $110 \pm 9$  and  $2200 \pm 70$  MPa, respectively. For one-layer fiber composites, which represent 0.5 wt% nanofiber filler composites, the FS and  $E_y$  increased only very slightly to  $140 \pm 10$  and  $2250 \pm 50$  MPa, respectively. When the mass fraction of fibers increased to 2.5% (5 layers of fibers), the FS and  $E_y$  increased further to  $200 \pm 20$  and  $2600 \pm 70$  MPa, respectively. Finally, when the mass fraction of the fibers increased to 4.0%, the FS and  $E_y$  increased to  $280 \pm 10$  and  $2800 \pm 150$  MPa, respectively. From neat resin to one layer (0.5%) fiber composite material, FS improved by 25%, but  $E_y$  did not improve at all. Increasing the mass fraction of fibers in the composite sample to 2.5 wt%, the FS and  $E_y$  were seen to increase by 63 and 18%, respectively. Finally with the addition of 4% of fibers (8 layers), the FS and  $E_y$  of the composite improved by 70% and 27% in relation to neat resin (Figure 4-7).

#### **4.4.3 Evaluation of FS and $E_y$ Values**

As seen in Figure 4-7b, the  $E_y$  of the samples were not as significantly improved as were the FS. Two reasons for this discrepancy can be suggested. First, the mechanical properties of the PMCM-SiO<sub>2</sub> nanofiber mats influenced the final properties of the composite materials. The presence of silica in the fibers causes the fibers to become more brittle, which might be the cause of low  $E_y$ . Further studies on varying the amount of silica content in the fibers, and analyzing the effect of silica on the final properties of the



composite material is needed. Another reason for this discrepancy could be the fact, that even though there is good interpenetration of the composite material between the fiber mats, the composite material present between the layers (Figure 4-5) is still devoid of any fibers and hence, behaves as neat resin. Thus, the improvements of the mechanical properties of the composites might be limited at the interface between the nanofibers and the matrix.

One suggested reason for the increase in the FS of the samples (Figure 4-7a), with increase in wt% of fibers are the strong bond between the nanofibers and the resin (Figure 4-4), which caused the nanofibers to break, rather than pull out of the sample and hence, increase the strength of the composite. Thus, the strength of the matrix could be potentially tailored with the toughness, by controlling the nanofiber/matrix interfacial strength. Finally, although in this study electrospun PMCM-SiO<sub>2</sub> nanofibers were embedded in the BISGMA/TEGDMA resins in the form of layers of nonwoven fabric stripes, the actual dental application might require the fabric to be cut into much smaller pieces in order to mix well with the dental monomers, and to make an applicable dental paste. This would only enhance the properties of the composite material, due to strong interactions of the surface on the nanofibers with that of the resin. Nevertheless, since relatively small amounts (e.g., 4.0% mass fraction) of nanofibers could effectively increase the overall mechanical properties of the dental restorative composite resins, the PMCM-SiO<sub>2</sub> nanofibers might have a bright future as reinforcing filler materials in the dental restorative composite applications.

#### 4.5 Conclusion

The main objective of this research was to study the reinforcement properties of electrospun PMCM-SiO<sub>2</sub> fibers as filler material on BISGMA/TEGDMA dental restorative matrix. The ordinary textile fibers available in the market today are about one-twelfth the size of the PMCM-SiO<sub>2</sub> fibers. The small diameter of the PMCM-SiO<sub>2</sub> nanofibers provided a high ratio of surface area to volume, which enhanced the intermolecular bonding between the PMCM-SiO<sub>2</sub> nanofiber and the matrix of BISGMA/TEGDMA resin, and further resulted in good interfacial properties of the composite resins. With increase in mass fraction of fibers in the composite material from 0.5 to 4%, an increase in FS was noticed. A small increase in E<sub>y</sub> was also noticed. Further methods, such as changing the silica content of the fibers, and varying the mass fraction of the fibers, modifying the surface morphology of the fibers, could further improve the properties of the dental restorative materials.

#### 4.6 Reference List

1. Dickerson, W. G. Decay under amalgams and under diagnosing. *Oral Health*, 89(3), 55. 1999.
2. Dickson, G. Physical and chemical properties and wear. *Journal of Dental Research*, 58(5), 1535-1543. 1979.
3. Steenbock, P. Process of manufacturing vitreous cement. 04-213723(771184). US. 1904.
4. Skinner, E. W., Phillips, R. W. *The science of dental materials*, 5th ed. Saunders Publishers, FL, 636. 1960.
5. Bowen, R. L. Acrylic esters of bisphenol A diglycidyl ether. U.S. Dept. of Commerce. 3179623, 4. US. 1961.
6. Mabie, C. P., Menis, D. L. Microporous glassy fillers for dental composites. *Journal of Biomedical Materials Research*, 12(4), 435-472. 1978.
7. Ferracane, J. L., Mitchem, J. C. Properties of posterior composite: results of round robin testing for a specification. *Dental Materials: Official Publication of the Academy of Dental Materials*, 10(2), 92-99. 1994.
8. Jordan, R. E., Suzuki, M. Posterior composite restorations. Where and how they work best. *Journal of the American Dental Association*, 122(11), 30-37. 1991.
9. Xu, H. H., Martin, T. A., Antonucci, J. M., Eichmiller, F. C. Ceramic whisker reinforcement of dental resin composites. *Journal of dental research*, 78(2), 706-712. 1999.
10. Antonucci, J. M., Stansbury, J. W. Molecularly designed dental polymers. *Desk Reference of Functional Polymers*, 719-738. 1997.
11. Reed, B. B., Choi, K., Dickens, S. H., Stansbury, J. W. Effect of resin composition on kinetics of dimethacrylate photopolymerization. *Polymer Preprints (American Chemical Society, Division of Polymer Chemistry)*, 38(2), 108-109. 1997.
12. Dulik, D., Bernier, R. & Brauer, G. M. Effect of diluent monomer on the physical properties of bis-GMA-based composites. *Journal of Dental Research*, 60(6), 983-989. 1981.
13. Stanley, H. R., Bowen, R. L., Folio, J. Compatibility of various materials with oral tissues. II: Pulp responses to composite ingredients. *Journal of Dental Research*, 58(5), 1507-1517. 1979.
14. Bowen, R. L. Compatibility of various materials with oral tissues. I: The components in composite restorations. *Journal of Dental Research*, 58(5), 1493-1503. 1979.
15. Cross, M., Douglas, W. H., Fields, R. P. The relationship between filler loading and particle size distribution in composite resin technology. *Journal of Dental Research*, 62(7), 850-852. 1983.
16. Nielsen, L. E., Landel, R. F. *Mechanical properties of polymers and composites* second edition. *Textile Research Journal*, 64(11), 696. 1994.

17. Xu, H. H. K., Ostertag, C. P., Fuller, E. R., Braun, L. M., Lloyd, I. K. Fracture resistance of SiC-fiber-reinforced Si<sub>3</sub>N<sub>4</sub> composites at ambient and elevated temperatures. *Journal of the American Ceramic Society*, 78(3), 698-704. 1995.
18. Bowen, R. L. Dental inserts containing silicon dioxide-containing glass particles and adhesives. (American Dental Association Health Foundation, USA. 86-862706(4744759), 9. US. 1986.
19. Bowen, R. L. Composite dental material. (American Dental Association, USA. 78-940597(4215033), 12. US. 1978.
20. Bowen, R. L. Effect of particle shape and size distribution in a reinforced polymer. *Journal of the American Dental Association*, 69, 481-495. 1964.
21. Gander, R. J. Dental restorative cement compositions. (Johnson and Johnson). 72-223284(3835090), 9. US. 1972.
22. Rossi, C. J. Dental filling compositions. (Lee Pharmaceuticals). 71-2164668(2164668), 13. DE. 1971.
23. Boyd, R. N. Dental filling composition of a coefficient of thermal expansion approximating that of natural tooth enamel. (Dentsply International Inc.). 66-535727(3503128), 4. US. 1966.
24. Dietz, E. D. Tooth filling and facing composition comprising a radiopaque glass. (Owens-Illinois, Inc. USA. 72-247293(3911581), 5. US. 1972.
25. Leinfelder, K. F., Sluder, T. B., Sockwell, C. L., Strickland, W. D., Wall, J. T. Clinical evaluation of composite resins as anterior and posterior restorative materials. *The Journal of Prosthetic Dentistry*, 33(4), 407-416. 1975.
26. Phillips, R. W., Avery, D. R., Mehra, R., Swartz, M. L., McCune, R. J. Observations on a composite resin for class II restorations: two-year report. *The Journal of Prosthetic Dentistry*, 28(2), 164-169. 1972.
27. Phillips, R. W., Avery, D. R., Mehra, R., Swartz, M. L. McCune, R. J. Observations on a composite resin for Class II restorations: three-year report. *The Journal of Prosthetic Dentistry*, 30(6), 891-897. 1973.
28. Kusy, R. P., Leinfelder, K. F. Pattern of wear in posterior composite restorations. *Journal of Dental Research*, 56(5), 544. 1977.
29. Abell, A. K., Leinfelder, K. F., Turner, D. T. Microscopic observations of the wear of a tooth restorative composite in vivo. *Journal of Biomedical Materials Research*, 17(3), 501-507. 1983.
30. Xu, H. H. K., Eichmiller, F. C., Giuseppetti, A. A. Reinforcement of a self-setting calcium phosphate cement with different fibers. *Journal of Biomedical Materials Research*, 52(1), 107-114. 2000.
31. Fong, H. Electrospun nylon 6 nanofiber reinforced BIS-GMA/TEGDMA dental restorative composite resins. *Polymer*, 45(7), 2427-2432. 2004.
32. Randklev, R. M. Radiopaque, low visual opacity dental composites containing nonvitreous microparticles. (Minnesota Mining and Manufacturing Co., USA. 84-602114(4503169), 12. US. 1984.
33. Wei, Y., Yang, D., Bakthavatchalam, R. Thermal stability and hardness of new polyacrylate-silica hybrid sol-gel materials. *Materials Letters*, 13(4-5), 261-266. 1992.

34. Krause, W. R., Park, S. H., Straup, R. A. Mechanical properties of BIS-GMA resin short glass fiber composites. *Journal of Biomedical Materials Research*, 23(10), 1195-1211. 1989.
35. Praveen, S., Boberick, K., Mylonakis, A., Mukherjee, I., Kim, S., Li, Shuxi, Baran, G., Wei, Y. A new class of materials for potential use as flowable dental composites. Abstracts, 38th Middle Atlantic Regional Meeting of the American Chemical Society, Hershey, PA, United States, MRM-350. 2006.
36. Praveen, S., Chao, M. C., Patel, A. C., Guo, Y., Li, S., Baran, G. R., Wei, Y. Mesoporous SBA-15 materials as potential fillers for dental composites. Abstracts of Papers, 231st ACS National Meeting, Atlanta, GA, United States, INOR-454. 2006.
37. Praveen, S., Sun, Z., Xu, J., Ranade, R., Patel, A. C., Baran, G. R., Wei, Y. Effect of mesoporous fillers on the compression and aging properties of experimental dental composites. Abstracts of Papers, 230th ACS National Meeting, Washington, DC, United States, OLY-102. 2005.
38. Praveen, S., Li, S., Boberick, K., Davis, J., Zuckman, B., Baran, G., Wei, Y. Novel organic-inorganic hybrid reactive adhesives for potential dental applications. Abstracts of Papers, 230th ACS National Meeting, Washington, DC, United States, MSE-005. 2005.
39. Wei, Y., Jin, D., Xu, J., Baran, G., Qiu, K. Y. Mechanical properties of interface-free polyacrylate-silica hybrid sol-gel materials for potential dental applications. *Polymers for Advanced Technologies*, 12(6), 361-368. 2001.
40. Wei, Y., Jin, D., Ding, T., Xu, J. Mesoporous materials and methods of making the same. (Drexel University, USA. 99-US1116(9936357), 79. WO. 1999.
41. Wei, Y., Jin, D., Yang, C., Kels, M. C., Qiu, K. Y. Organic-inorganic hybrid materials. Relations of thermal and mechanical properties with structures. *Materials Science & Engineering, C: Biomimetic Materials, Sensors and Systems*, C6(2,3), 91-98. 1998.
42. Wei, Y., Jin, D., Wei, G., Yang, D., Xu, J. Novel organic-inorganic chemical hybrid fillers for dental composite materials. *Journal of Applied Polymer Science*, 70(9), 1689-1699. 1998.
43. Doshi, J., Reneker, D. H. Electrospinning process and applications of electrospun fibers. *Journal of Electrostatics* 35(2&3), 151-160. 1995.
44. Fong, H., Chun, I., Reneker, D. H. Beaded nanofibers formed during electrospinning. *Polymer*, 40(16), 4585-4592. 1999.
45. Reneker, D. H., Chun, I. Nanometer diameter fibers of polymer, produced by electrospinning. *Nanotechnology*, 7(3), 216-223. 1996.
46. Reneker, D. H., Yarin, A. L., Fong, H., Koombhongse, S. Bending instability of electrically charged liquid jets of polymer solutions in electrospinning. *Journal of Applied Physics*, 87(9, Pt. 1), 4531-4547. 2000.
47. Tayler G.I. Proceedings of the royal society of London, Series A. 280, 383-397. 1964.

Table 4-1. Flexural strength and elastic modulus of PMCM-SiO<sub>2</sub> fiber reinforced BISGMA/TEGDMA dental composites.

PMCM-SiO <sub>2</sub> nanofiber mass fraction <sup>a</sup>	number of PMCM- SiO <sub>2</sub> fiber layers <sup>b</sup>	FS <sup>c</sup> MPa	E <sub>y</sub> <sup>d</sup> MPa
0%	0	110 ± 9	2200 ± 70
0.5%	1	140 ± 10	2250 ± 50
2.5%	5	200 ± 20	2600 ± 70
4%	8	280 ± 10	2800 ± 150

<sup>a</sup>Mass fraction of PMCM-SiO<sub>2</sub> nanofibers present in each three-point bending test sample (2 mm x 2 mm x 25 mm); <sup>b</sup>each layer of fiber present in the three-point bend test makes up for 0.5% mass fraction of the three point bending sample; <sup>c</sup>average flexural strength value with standard deviation obtained by analyzing ten three-point bending samples and <sup>d</sup>average elastic modulus value with standard deviation obtained by analyzing ten, three-point bending samples.

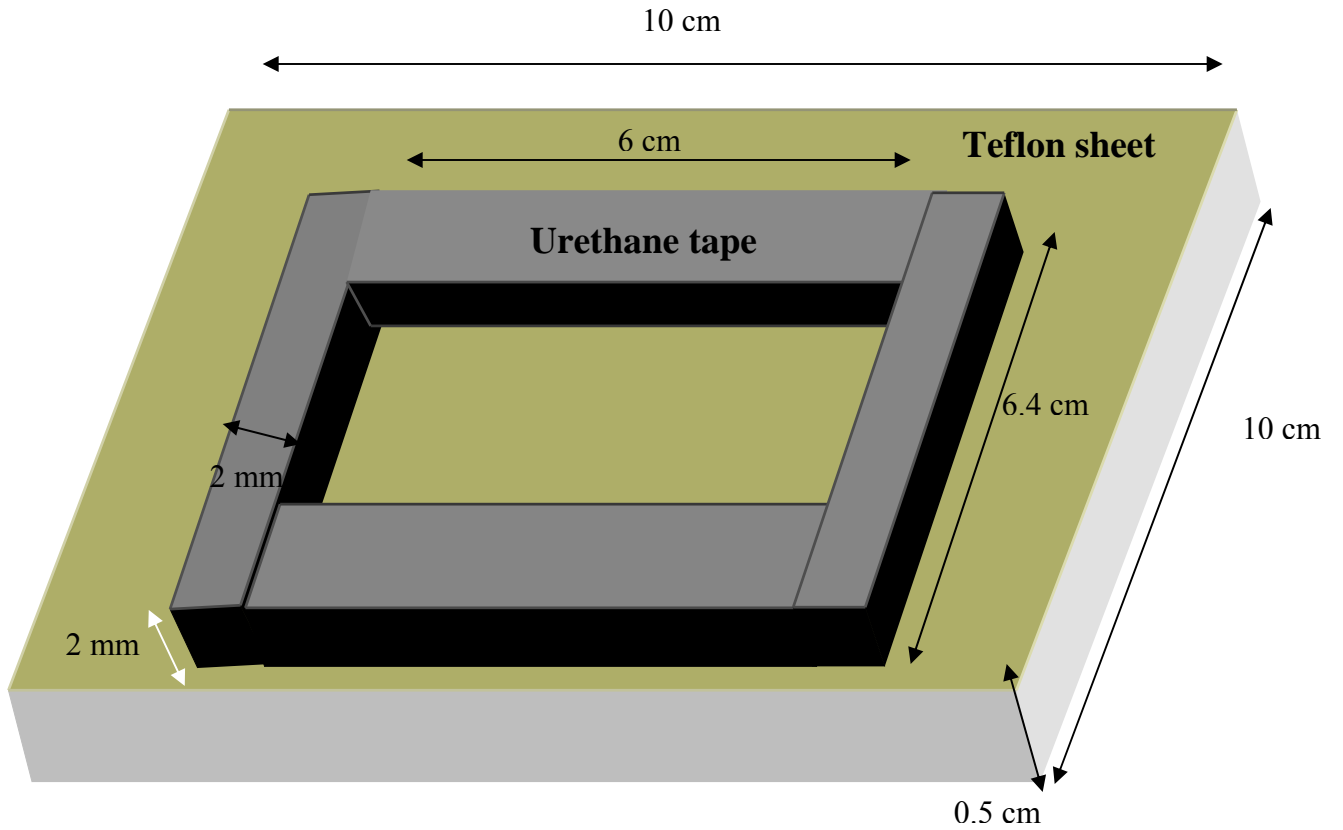


Figure 4-1. A flat Teflon<sup>®</sup> sheet and 2 mm x 2 mm, black urethane tape are used to make a mold for fiber reinforced composites.

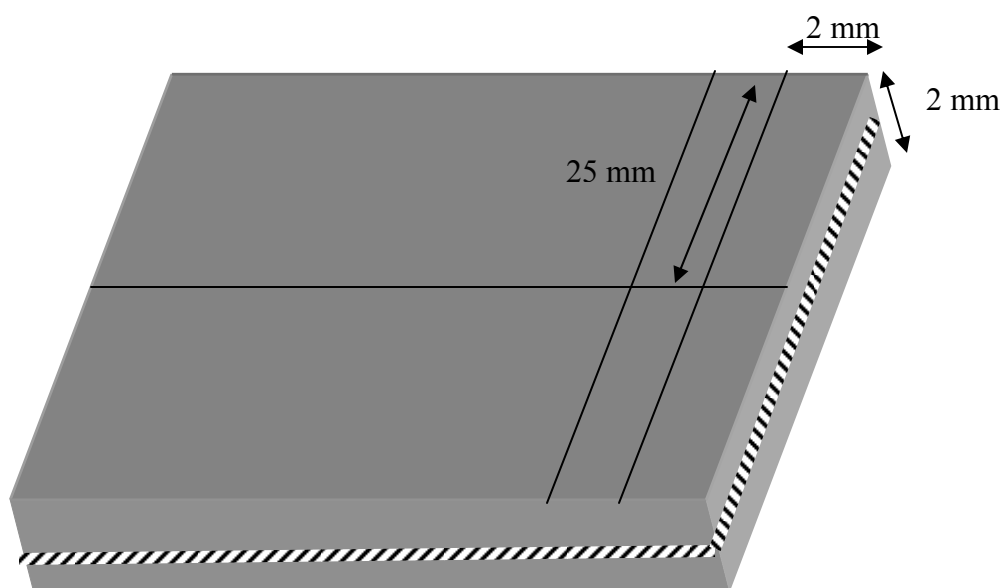


Figure 4-2. Photopolymerized BISGMA/TEGDMA resin dental composite (the gray area) containing one (could be five or eight) layers of fiber mats (represented by the white and black striped line). 2 mm x 2 mm x 25 mm-sized three-point bending samples are then cut and polished for studying the FS and  $E_y$  of the sample.



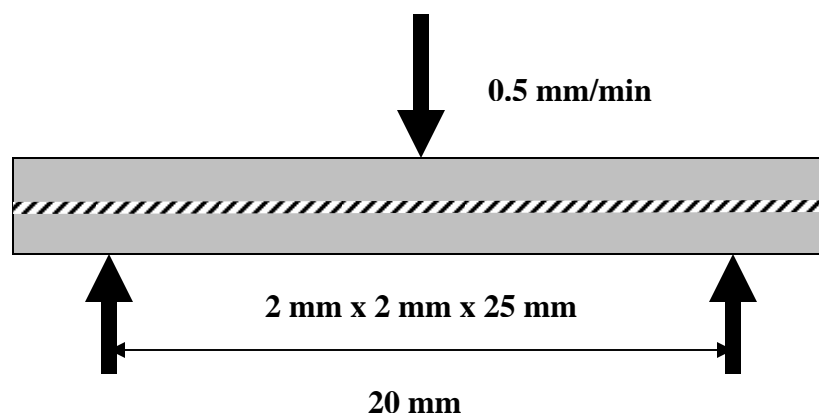


Figure 4-3. Schematic representation of the three-point bending test. The sample is placed between three points at specific distances as represented above. The white and black striped lines represent the fiber and the gray area represents the BISGMA/TEGDMA composite material.

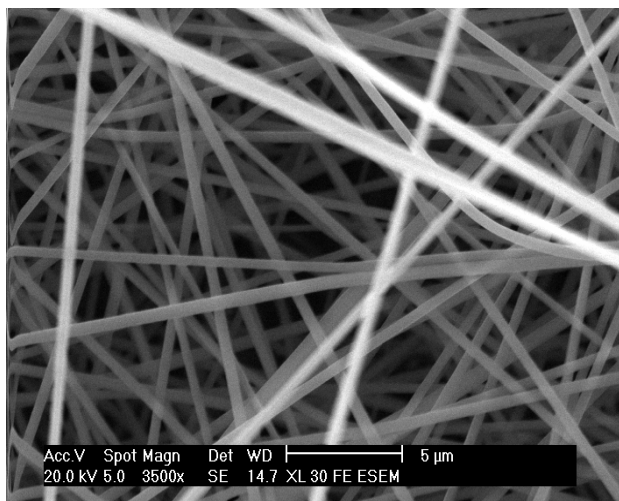


Figure 4-4. PMCM-SiO<sub>2</sub> nanofiber (300 to 400 nm diameter) mats electrospun using an electrospinning solution made up of 10 wt% PMCM/THF copolymer solution and hydrolyzed TEOS sol in a 8:2 mass ratio, respectively. Scale Bar: 5 μm.

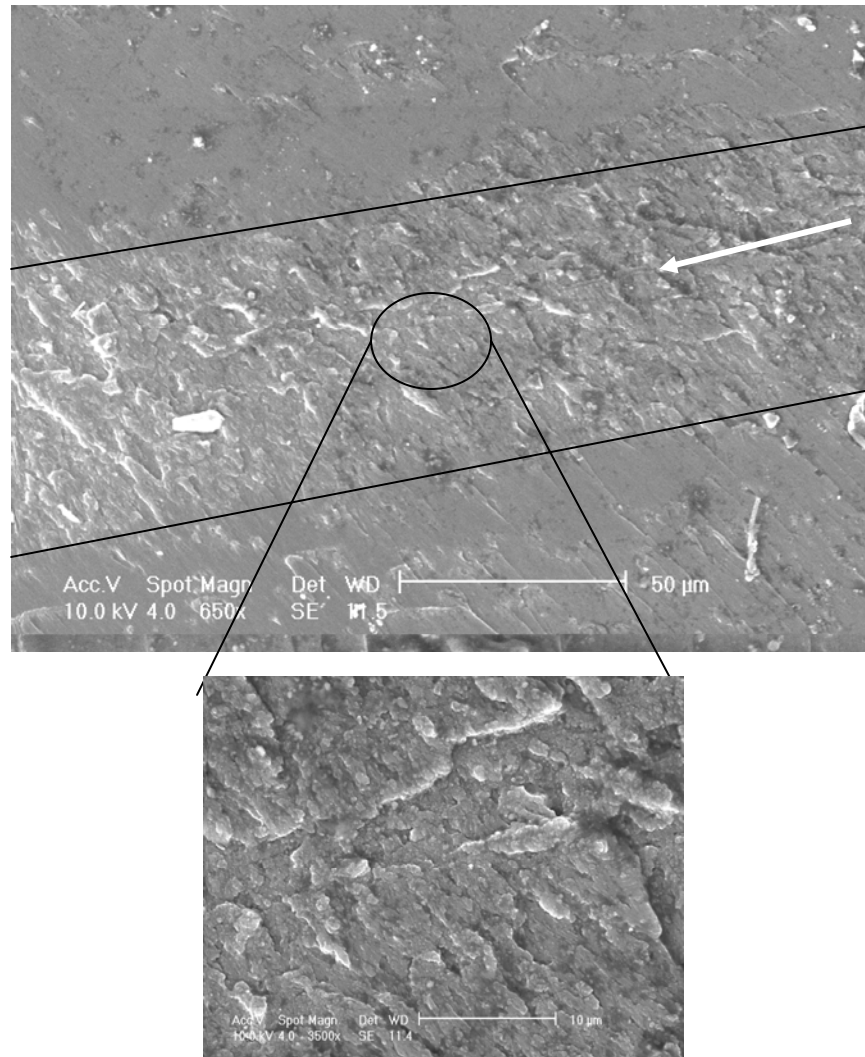
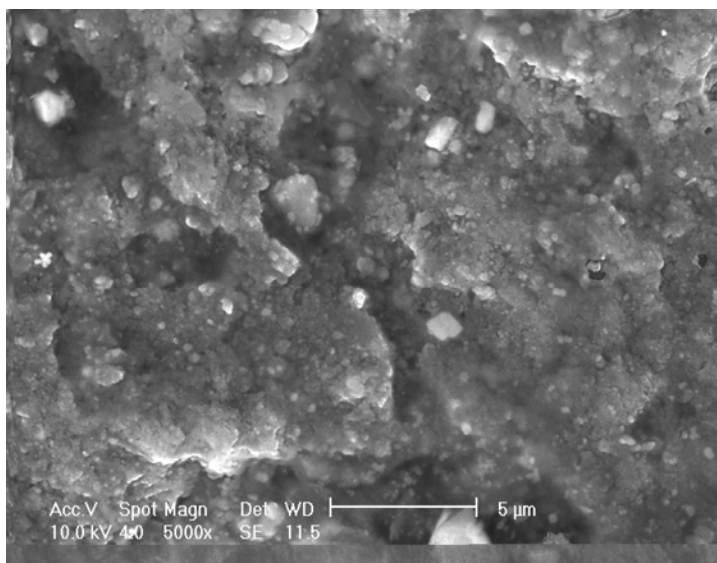
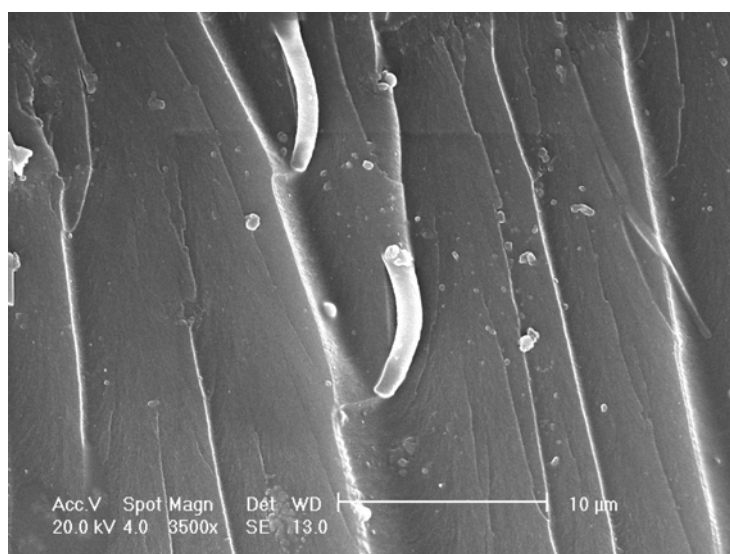


Figure 4-5. Scanning electron micrographs of fractured surface of the three-point bending sample. The arrow represents the section of the sample containing the fiber material. The rest of the area is just BISGMA/TEGDMA resin devoid of fiber. Scale bar: 50 µm. The inset shows high-resolution micrograph of the fiber/composite, interpenetrated region. Scale bar: 10 µm.



(6a)



(6b)

Figure 4-6. Scanning electron micrographs of fracture surfaces of representative 3-point bending specimen: (a) composite resin with 5 layers of nanofiber fabrics (image taken at the place where the nanofibers were present). Scale bar: 5  $\mu\text{m}$ . (b) Neat resin without nanofibers. Scale bar: 10  $\mu\text{m}$ .

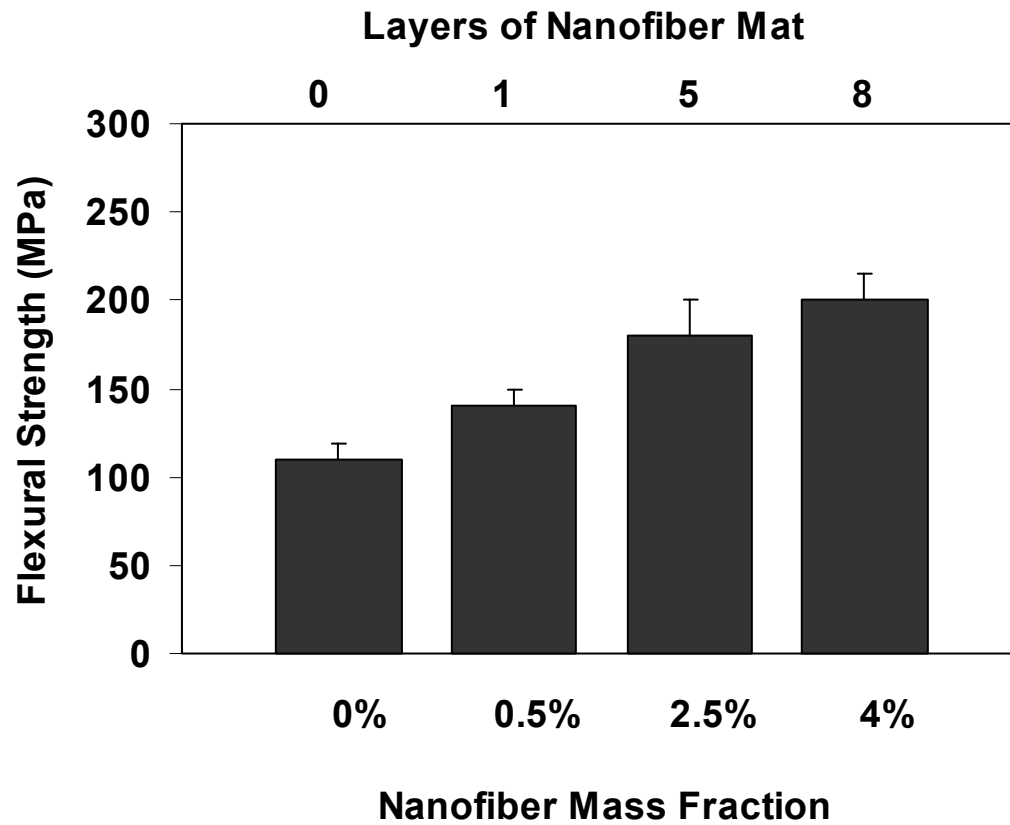


Figure 4-7a. Flexural strength of the composite resins containing different mass fraction (or layers) of PMCM-SiO<sub>2</sub> nanofiber nonwoven fabrics. Each bar represents the value with standard deviation.

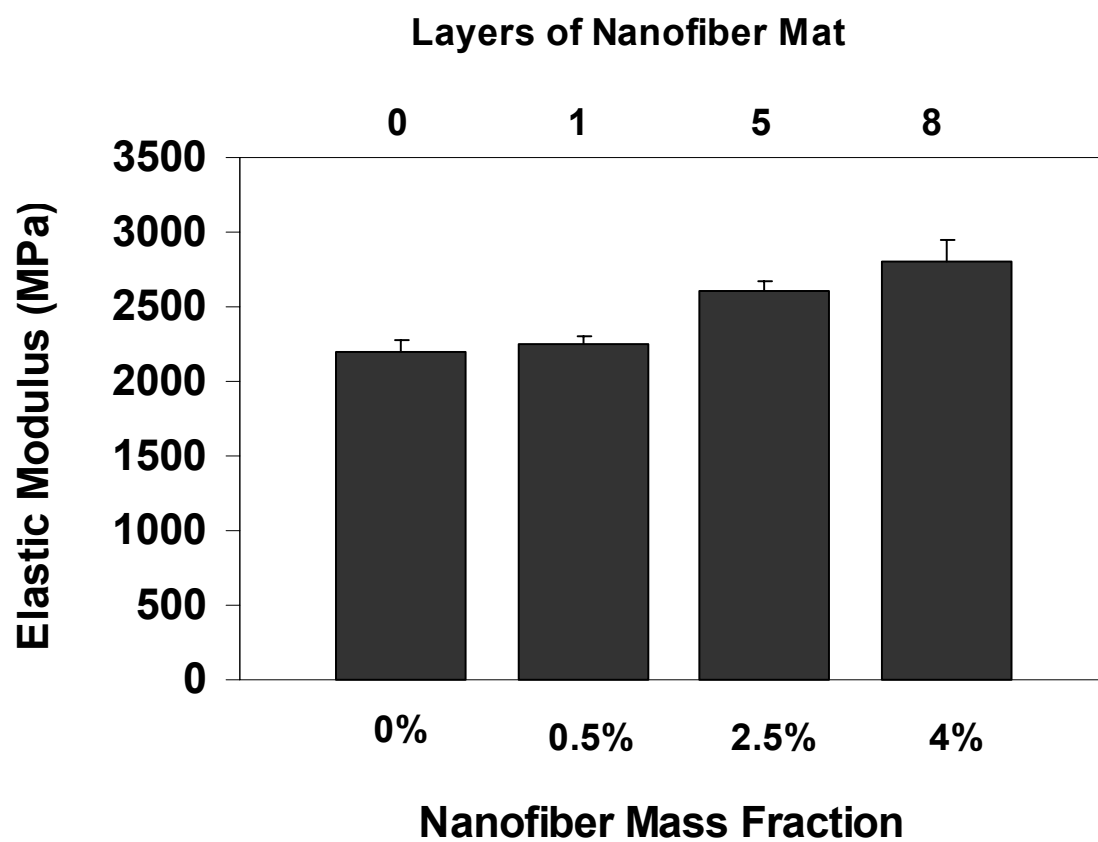


Figure 4-7b. Elastic modulus of the composite resins containing different mass fraction (or layers) of PMCM-SiO<sub>2</sub> nanofiber nonwoven fabrics. Each bar represents the value with standard deviation.

## Chapter 5: Electrospinning of Porous Silica Nanofibers Containing Silver and Gold Nanoparticles for Catalytic Application

### 5.1 Introduction

During the last decade, metal nanoparticles have found a niche in various fields of science, ranging from chemistry to physics, and biotechnology.<sup>1-4</sup> Because of their optical,<sup>5-7</sup> electrical<sup>8-10</sup> and catalytic properties,<sup>5,11-13</sup> metal nanoparticles have been exploited for unique applications as sensors,<sup>14</sup> optical switches,<sup>15</sup> biological markers,<sup>16</sup> nanoelectronic devices<sup>17</sup> and catalysts<sup>12</sup> for many chemical and biological reactions. Among the important chemical reactions which, they demonstrate to have high catalytic activity are hydrogenation, hydroformylation, carbonylation, etc.<sup>18-21</sup> Due to their tendency to aggregation, deactivation and poisoning, however, the metal nanoparticles have proven undesirable for large scale use.<sup>22</sup> Thus, research efforts have been made to protect the particles by stabilizing them in colloidal solutions containing surfactants and by forming complexes with polymer ligands.<sup>23,24</sup> Though the particles have been stabilized successfully using these techniques, the metal composites thus formed do not show good catalytic activity, due to the restricted access of these particles to external reagents.<sup>24</sup> Therefore, to utilize metal nanoparticles for various catalytic applications in the most efficient way, it is necessary to explore novel techniques of metal particle stabilization.

The nanoscale dispersion of metal nanoparticles in polymers,<sup>25,26</sup> silicates<sup>27</sup> and metal oxide<sup>28</sup> substrates, on the other hand, have attracted great interest because of their stability, reusability and good catalytic properties.<sup>29-31</sup> Various metals, such as gold, platinum, palladium, and silver,<sup>12,28</sup> have been encapsulated using a variety of methods

including chemical vapor deposition<sup>12</sup> and reduction of metal salts by thermal,<sup>6</sup> chemical<sup>32</sup> or UV light<sup>1</sup> treatment. The substrates used for metal particle encapsulations range from metal oxides<sup>28,33</sup> to organically modified silicates<sup>27</sup> polymers shaped as thin films,<sup>8,25</sup> spheres,<sup>34,35</sup> fibers,<sup>32,36</sup> and dendrimers.<sup>26</sup> For metal nanocomposites to perform as good catalysts, they should possess three important characteristics: 1) the substrate should have high surface area,<sup>11,33,37</sup> 2) the nanoparticles present inside the substrate should be easily accessible to various chemical reagents,<sup>37</sup> and 3) the size and distribution of the nanoparticles inside the substrate should be uniform.<sup>28</sup>

Electrospinning is a widely employed method in recent years to produce polymer nanofiber mats with high surface area,<sup>32,36,38-44</sup> which could be used as metal supporting substrates for catalytic applications.<sup>32,44-48</sup> Some of the obstacles that have to be overcome in order to utilize this technique for metal nanoparticle encapsulation and for catalytic applications include aggregation of nanoparticles, poisoning of surface stabilized particles and limited resistance of the polymer fibers to strong organic solvents and high temperature.

To address the above-mentioned problems, we have developed a facile method that combines sol-gel processing with electrospinning to prepare porous silica nanofibers containing uniformly distributed silver nanoparticles (PSFSP). The unique features that make PSFSP an ideal candidate for catalytic applications include 1) high sensitivity and reactivity of porous silica nanofibers because of large surface area (average fiber diameter of 100 nm, fiber length of up to 10 cm and surface area of 600 m<sup>2</sup> g<sup>-1</sup>), 2) resistance to high temperature and strong solvents making the catalytic fibers usable and reusable under harsh conditions, 3) easy control of size and density of metal nanoparticles



in the fibers, and 4) the freedom to encapsulate various kinds of nanoparticles, including gold, palladium, and quantum dots.

Tetraethylorthosilicate (TEOS), trimethoxysilyl functionalized polymethacrylate copolymer (PMCM) and silver nitrate ( $\text{AgNO}_3$ ) are the main precursors used to synthesize porous silica nanofibers containing silver nanoparticles. A viscous solution is prepared containing the above-mentioned precursors and then spun into fibers. It has been well established in chapter 3 that the sol-gel reactions between the hydrolyzed inorganic precursor TEOS and the copolymer precursor PMCM could produce organic vinyl polymer - inorganic silica hybrid nanofibers, in which the polymer chains are uniformly distributed and covalently bonded to silica network.<sup>49-51</sup> The PMCM- $\text{SiO}_2/\text{AgNO}_3$  nanofibers thus produced are then heat-treated to reduce  $\text{AgNO}_3$  to silver nanoparticles, and pyrolyze the PMCM- $\text{SiO}_2$  component of the nanofibers to porous silica fibers. Various electron microscopic and spectroscopic characterizations were performed to study the effects of concentration of  $\text{AgNO}_3$  and PMCM on the morphology of the silica fiber and the effect of heat treatment on the production of silver nanoparticles. The catalytic efficiency of the silver nanoparticles encapsulated inside porous silica fibers was evaluated in a silver catalyzed reduction of methylene blue dye (MB) by sodium borohydride ( $\text{NaBH}_4$ ) under nitrogen. The reaction is thermodynamically favorable, and the color change from blue in its oxidized state to colorless in its reduced state can be easily detected using a simple UV-vis spectroscopy method.<sup>52,53</sup> It should be noted that substituting silver nitrate with another metal salt, e.g., hydrogen tetrachloro-aurate tetrahydrate ( $\text{HAuCl}_4 \cdot 4\text{H}_2\text{O}$ ), will lead to the production of gold nanoparticles, rather than silver nanoparticles, during heat treatment.

## 5.2 Experimental Section

The synthesis of porous silica nanofibers containing silver nanoparticles (PSFSP) involves three main steps. One is the basic synthesis of PMCM copolymer; second is the electrospinning of PMCM/hydrolyzed TEOS/AgNO<sub>3</sub> solution into nanofibers, and third is the heat treatment of the electrospun fibers to obtain uniformly distributed silver nanoparticles in porous silica fibers.

### 5.2.1 Materials and Reagent

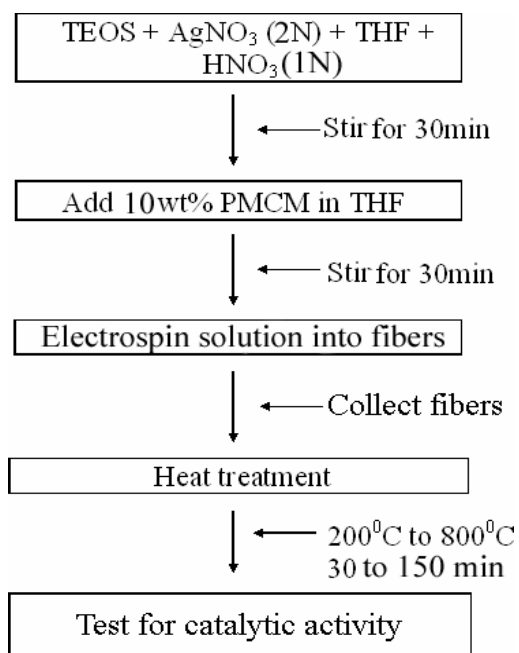
Tetraethylorthosilicate (TEOS, 98%), silver nitrate (AgNO<sub>3</sub>, 2 N solution in water), hydrogen tetrachloro-aurate tetrahydrate (HAuCl<sub>4</sub>.4H<sub>2</sub>O, 2 N solution in water), nitric acid (HNO<sub>3</sub>, 1 N solution in water), reagent grade tetrahydrofuran (THF, 99.9%) and sodium borohydride (NaBH<sub>4</sub>, 99.9%) were all purchased from Sigma-Aldrich Chemical Co. and used as received. Methyl methacrylate (MMA) monomer, 3-(trimethoxysilyl)propyl methacrylate (MSMA), sodium hydroxide (NaOH), benzoyl peroxide (BPO), anhydrous calcium chloride (CaCl<sub>2</sub>), anhydrous benzene, and anhydrous hexane were also purchased from Sigma-Aldrich Chemical Co. and used to synthesize the trimethoxysilyl functionalized methacrylate copolymer (PMCM) following the previously reported procedure by Wei et al.<sup>54,55</sup> A detailed procedure for the synthesis of PMCM copolymer is also given in the experimental section of chapter 3.

### 5.2.2 Preparation of Spinning Solution

Scheme 5-1 shows the important steps involved in the fabrication of PSFSP. PMCM copolymer was first synthesized, according to the procedure explained in the experimental section of chapter 3. Scheme 3-1 represents the reaction involved in the

synthesis of PMCM. The molecular weight of the PMCM copolymer obtained was around 85,000 as determined by gel permeation chromatography (GPC).

The first step was the preparation of silicate/AgNO<sub>3</sub> sol. Thus, TEOS was mixed with THF and then a mixture of 2N AgNO<sub>3</sub> and 1N HNO<sub>3</sub> was added dropwise at two different [TEOS]: [THF]: [HNO<sub>3</sub>, 1N]: [AgNO<sub>3</sub>, 2 N] molar ratios of 1:2:0.05:0.06 and 1:2:0.05:0.1 with constant stirring for 30 min at room temperature. The water required for hydrolysis of TEOS was obtained from the dilute AgNO<sub>3</sub> solution used in the preparation of the sol. Next, 10 wt% PMCM solution in THF was added dropwise to the hydrolyzed TEOS/AgNO<sub>3</sub> sol with constant stirring to obtain a transparent homogeneous solution with a viscosity of around 60 to 70 cP and a final PMCM content of 2 to 4 wt%, with respect to the wt% of silica.



Scheme 5-1. Schematic representation of porous silica nanofibers containing silver nanoparticles.

### 5.2.3 Electrospinning

The spinning solution prepared as above was collected in a pipette with a tip opening of approximately 0.5 mm. An electric field of 20 kV (Gamma High Voltage Research D-ES30) was then applied by dipping a charged copper wire directly into the spinning solution. A grounded aluminum plate placed at a distance of 20 cm from the tip of the pipette was used as a fiber-collecting device. Under the electric field, a droplet suspended from the tip of the pipette acted as the feed source, from which a charged jet of hydrolyzed TEOS/AgNO<sub>3</sub>/PMCM sol solution was ejected out in the form of nanofibers. The two sets of PMCM-modified fibers containing 0.06 and 0.1 mol/L AgNO<sub>3</sub> with respect to 1 mol/L TEOS thus collected were then subjected to varying heat treatments in air. This caused the hydrolyzed TEOS to reduce to silica, the PMCM polymer to degrade, and the AgNO<sub>3</sub> salt present in the fibers to reduce to silver nanoparticles, finally producing porous silica fibers containing approximately 10 wt% (0.06 mol/L AgNO<sub>3</sub>) and 20 wt% (0.1 mol/L AgNO<sub>3</sub>) silver nanoparticles.

### 5.2.4 Testing the Catalytic Activity of Silver Nanoparticles in the Fibers

The catalytic activity of the silver nanoparticles in the fibers was analyzed following the published procedure.<sup>29,56</sup> In a typical procedure, a certain amount of silica fibers containing 10 wt% silver nanoparticles was homogeneously dispersed into a MB dye solution in water (2 mL, 0.01 mol/L), followed by injecting aqueous NaBH<sub>4</sub> (1 mL, 0.1 mol/L) rapidly under constant stirring. The blue color of the mixture gradually disappeared, indicating the silver-catalyzed reduction of the dye. The rate and time of color disappearance, as indicative of catalytic activity of silver particles, was monitored with UV-vis spectrophotometer.

## **5.3 Instrumentation**

### **5.3.1 Gel Permeation Chromatography (GPC)**

A Hewlett-Packard HP 1090 liquid chromatograph, equipped with a refractive index detector, PLgel column and THF eluent was used to determine the molecular weight of the synthesized PMCM copolymer. The copolymer was dissolved in THF to obtain a 1% solution, and the instrument was calibrated against secondary polystyrene standards.

### **5.3.2 Digital Viscometer**

Brookfield Instruments model DV-II+ was used to determine the viscosity of the spinning solution

### **5.3.3 Fourier Transform Infrared Spectrophotometer (FT-IR)**

An FT-IR, Perkin-Elmer, Model-1600 spectrophotometer was used to analyze the as-spun hybrid fibers containing  $\text{AgNO}_3$ , as well as the heat-treated fibers made of silica and silver nanoparticles. The fiber samples were measured in the form of KBr powder-pressed pellets under ambient conditions. Each spectrum was acquired by accumulation of 50 scans with the resolution of  $4 \text{ cm}^{-1}$ .

### **5.3.4 Environmental Scanning Electron Microscopy (ESEM) and Electron**

#### **Diffraction Spectroscopy (EDX)**

Measurement of the diameter of the electrospun nanofibers and elemental analysis was conducted by obtaining micrographs from the field emission environmental scanning electron microscope (Phillips XL-30 ESEM) equipped with an energy dispersive X-ray analyzer (EDX). Approximately  $1 \times 1 \text{ cm}$  square pieces of fiber mats were mounted on top of sample holders using conducting carbon tape. The samples were then sputter

coated with a monolayer of platinum. The sputter-coated fibers were then exposed to a voltage of 20 kV. The average diameter of the fibers was determined by measuring 100 random fibers from micrographs using UTHSCSA ImageTool 3.0.

### **5.3.5 Transmission Electron Microscopy (TEM)**

A transmission electron microscope (TEM, JEOL 2000FX) operated at the accelerating voltage of 300 kV, was used to study the internal morphology of the PSFSP. The samples for TEM micrographs were prepared by embedding the fibers into a resin and microtoming the resin into 100 nm thick cross sections. The morphology of the fibers and the size and distribution of silver particles present inside the fibers were evaluated.

### **5.3.6 Thermogravimetric Analyzer (TGA, TA Q50)**

TGA analysis was performed in air over a temperature range of 40 to 800 °C at a heating rate of 20 °C/min. During the heat treatment, degradation of PMCM polymer and formation of silver nanoparticles take place.

### **5.3.7 X-Ray Diffraction (XRD)**

The as-spun fibers and heat-treated fiber square mats (2 x 2 cm) were used to study the size and distribution of silver nanoparticles via the large angle X-ray diffraction (XRD, Siemens D-500, copper  $K\alpha$  -radiation ( $\lambda = 1.542 \text{ \AA}$ ) size of 0.4 x 8 mm generated by a 1.35 KW Cu X-ray tube). The diffracted intensity was recorded using a 2°/sec - 2  $\theta$  step from 10° to 90° for each scan.

### **5.3.8 Solid UV-Vis Spectroscopy**

Solid-state UV-visible reflectance spectra of the as-spun fibers and heat-treated fibers are measured with a Perkin Elmer, Model-330 spectrophotometer, at a wavelength between 200 to 800  $\text{cm}^{-1}$ .

### 5.3.9 Gas Sorption Measurement

N<sub>2</sub> sorption characterization of the as-spun and heat-treated fibers was, conducted on a Micromeritics ASAP 2010 surface area and pore size analyzer (Micromeritics Inc., Norcross, GA) at -196 °C. All samples were degassed at 100 °C and 10<sup>-6</sup> Torr overnight prior to N<sub>2</sub> adsorption-desorption, and the surface area, pore diameter and pore volume were calculated using the accompanying software from Micromeritics.

## 5.4 Results and Discussion

Figure 5-11 summarizes the formation of PSFSP in a simple schematic representation. All the fibers studied and analyzed were synthesized using similar electrospinning parameters, as stated in the experimental section (i.e., pipette tip diameter of 0.5 mm; voltage of 20 kV; fiber collecting distance of 20 cm). Approximately 10 ESEM micrographs were taken randomly from different regions of a 20 x 20 cm square silica fiber mat, and the average fiber diameter (Table 5-1) of 100 silica fibers from each sample was then measured using UTHSCSA ImageTool 3.0.

### 5.4.1 Effect of PMCM Concentration on Electrospun Nanofibers

Figures 5-1a, 5-1b and 5-1c show fibers containing 0, 2 and 6 wt% of PMCM polymer with respect to the weight of silica, respectively. Silica fibers spun without any PMCM showed beaded morphology, due to the low molecular weight and low viscosity of the sol-gel silicates in the spinning solution (10 cP). On the other hand, the long molecular chains of the PMCM copolymer when added to the spinning solution tend to get entangled with the smaller silica sol molecules forming covalent bonds, via the cross-condensation of the silanol groups (i.e., Si-OH) present in both TEOS and PMCM.<sup>55</sup> The silica fibers spun with 2 wt% PMCM show a uniform morphology with average diameter

of around  $180 \pm 10$  nm (Table 5-1). As the wt% of PMCM is increased from 2 to 6 wt%, the viscosity of the spinning solution also increased from 40 to 60 cP, which in turn increased the diameter of the fibers from  $180 \pm 10$  nm to  $290 \pm 10$  nm. The increase in diameter of fibers with viscosity has been noticed previously in many electrospun polymer fibers.<sup>47</sup> It has to be noted that all silica fibers studied from here on contain 2 wt% of PMCM (with respect to silica), unless stated otherwise.

#### **5.4.2 Effect of AgNO<sub>3</sub> Concentration on Electrospun Nanofibers**

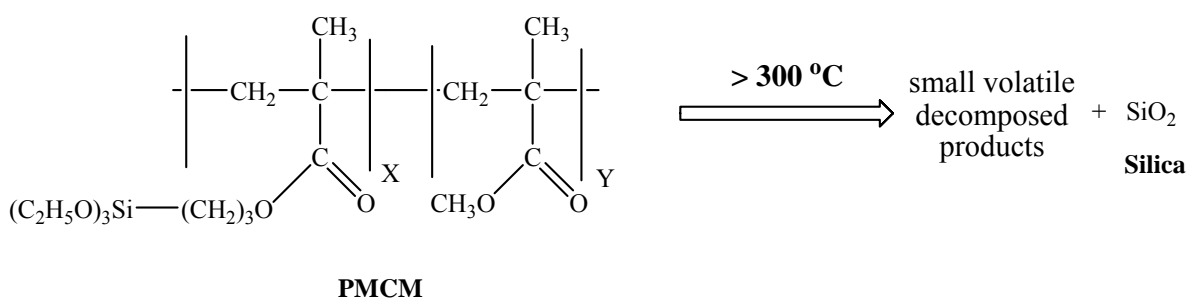
The amount of AgNO<sub>3</sub> added to the spinning silica solution also plays a role in governing the morphology of the fibers. Increasing the amount of AgNO<sub>3</sub> from 0.06 mol/L (10 wt% silver) to 0.1 mol/L (20 wt% silver) in the spinning solution caused the fibers to stick together, as well as caused an increase in the diameter of the spun fibers (Table 5-1, Figures 5-1d and 5-2e). This surface morphology change could be attributed to the localized charge effects on the surface of the fibers, as well as slow evaporation of water from the fibers causing the wet fibers to stick together during electrospinning.<sup>32,36,38</sup> All silica fibers discussed from here on contain 10 wt% silver (0.06 mol/L AgNO<sub>3</sub>) with respect to silica, unless stated otherwise. Thus, a narrow size distribution of the diameter of the silica fibers with smooth morphology can be obtained by regulating the amount of PMCM (2 wt%) and AgNO<sub>3</sub> (0.06 mol/L) added into the spinning solution.

#### **5.4.3 Effect of Heat Treatment on Electrospun Nanofibers and Silver Nanoparticles**

The electrospun hybrid fibers are subjected to varying temperatures and times from 200 °C to 600 °C for 60 to 150 min as seen in Table 5-1. The fibers undergo three different chemical and morphological changes:



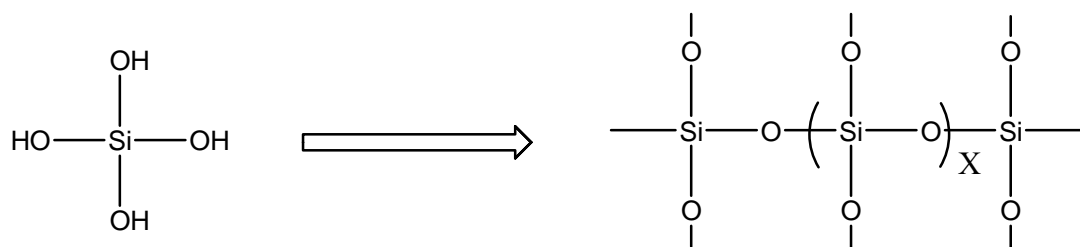
**I:** The degradation temperature for pure PMCM polymer is found to be around 300 °C. Thus, as the fibers are heated above 300 °C, the PMCM binder present inside the fibers starts degrading, and at around 500 °C the degradation of PMCM is complete, leaving behind pure porous silica fibers as seen in scheme 5-2. The degradation causes the fibers to become porous in nature and, enhances the catalytic efficiency of the fibers by increasing the surface area of the fibers. The porous structures left behind in the silica fibers after the complete degradation of the PMCM copolymer are partially occupied by the growing<sup>57</sup> silver nanoparticles in the fibers. The particles eventually stop growing when they encounter the rigid silica walls of the fibers.



Scheme 5-2. Thermal degradation of PMCM copolymer.

**II:** As the fibers are subjected to higher temperatures, the partially condensed silica present in the fibers is forced to complete condensation<sup>58</sup> (Scheme 5-3). This causes the release of small molecules such as ethanol and water from the fibers causing the fibers to shrink a little (Table 5-1). A comparison between the as-spun and heat-treated fibers, reveal that the average diameter of heat-treated fibers decreases only slightly (Table 5-1). Unlike polymer fibers, which show major shrinkage and degradation at high temperature, the rigid network of highly branched inorganic silica chains in the silica

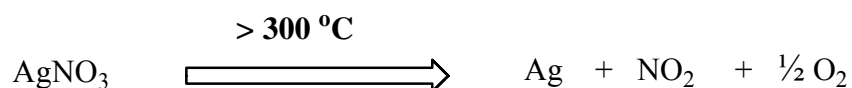
fibers causes the fibers to retain their shape and prevents major shrinkage. The heat treatment also makes the fibers highly resistant to strong acids and corrosive chemicals.



Hydrolyzed TEOS

Scheme 5-3. Thermal condensation of hydrolyzed TEOS.

**III:** During fiber heat treatment,  $\text{AgNO}_3$  present in the as-spun fibers is reduced to Ag nanoparticles (Scheme 5-4). The size of the nanoparticles increases slightly with increase in temperature, which is caused by Ostwald ripening. This occurs when silver ions flock together and form crystals. Some of these crystals grow larger, at the expense of smaller crystals, with increase in temperature and finally form nanoparticles. The size of the nanoparticles reach a maximum limit, when it comes in contact with the ridge silica walls of the fibers, which further prevent the agglomeration of the silver nanoparticles with the surrounding particles. Thus, the size of the silver particles is not only dependent on the heat treatment of the silica fibers, but also the average diameter of the pores produced by the degradation of PMCM copolymer.



Scheme 5-4. Thermal reduction of silver nitrate.

#### **5.4.4 Effect of Heat Treatment Time on Electrospun Nanofibers and Silver Nanoparticles**

As seen in Table 5-1 along with temperature variation, the time span of heat treatment also was varied, from 60 to 150 min. The degradation of PMCM binder and condensation of silica are only slightly affected by the time span of heat treatment. The silver nanoparticles on the other hand are dependent both on the time and on the temperature of heat treatment.

#### **5.5 Characterization of As-Spun and Heat-Treated Fibers**

The as-spun and heat-treated fibers were analyzed for surface morphology, fiber diameter and surface area, using various elemental and optical analysis instruments. The surface area and porosity of the fibers were analyzed with the Micromeritics ASAP 2010 instrument. As anticipated, degradation of PMCM polymer inside the fibers during heat treatment lead to the increase in surface area from  $11 \text{ m}^2 \text{ g}^{-1}$  for non heat-treated fibers to  $600 \text{ m}^2 \text{ g}^{-1}$  for heat-treated fibers. The TEM micrograph images (Figure 5-2) of the heat-treated silica fibers clearly show a homogeneous distribution of silver nanoparticles inside the porous silica fibers.

##### **5.5.1 Elemental Characterization**

The wt% of silver in the heat-treated silica fibers, which was experimentally determined via the EDX (Figures 5-3) and X-ray mapping technique (Figure 5-4), was found to be around 9 wt%. This value is close to the actual stoichiometric value of silver (10 wt%) calculated from the electrospinning solution (hydrolyzed TEOS/(0.06 mol/L)AgNO<sub>3</sub>/2 wt% PMCM) mixture (Table 5-1). The EDX spectrum for blank samples (fibers containing 0 wt% silver) shows no peak for silver (Figure 5-3a). Heat-treated

fibers containing silver nanoparticles on the other hand, as seen in Figure 5-3b, show a sharp peak for silver. The distribution of the silver particles, as seen in Figure 5-4, is also studied using the X-ray mapping technique. A series of X-ray mapping images of silicon, oxygen and silver for heat-treated fibers show an evenly distributed silver content at the macroscopic level.

### 5.5.2 Fourier Transform Infrared Spectra (FT-IR)

Figure 5-5 shows FT-IR data for as-spun and heat-treated fibers. The characteristic peaks for pure PMCM copolymer (Figure 5-5) are at  $1730\text{ cm}^{-1}$  (C=O),  $1458\text{--}1450\text{ cm}^{-1}$  (CH<sub>2</sub>-bending),  $1088\text{ cm}^{-1}$  (Si-O-C bending) and  $486\text{ cm}^{-1}$  (Si-O-C antisymmetric band)<sup>59</sup>. Characteristic peaks for pure silica powder (Figure 5-5) are at  $900\text{ cm}^{-1}$  (Si-OH) and  $795\text{ cm}^{-1}$ ,  $950\text{ cm}^{-1}$  and  $1081\text{ cm}^{-1}$  (Si-O-vibrations)<sup>59</sup>. Characteristic (Si-O) and (Si-OH) peaks are also seen for as-spun fibers (Figure 5-5) and heat-treated fibers (Figure 5-5 and Figure 5-5). The heat-treated silica fibers show a gradual decrease in Si-OH peaks at  $900\text{ cm}^{-1}$  and an increase in Si-O peak at  $1081\text{ cm}^{-1}$  caused by the forced condensation of hydrolyzed TEOS (Si-OH) to silica (Si-O-Si) during heat treatment. As the as-spun fibers (Figure 5-5) have only trace amounts of PMCM copolymer, the characteristic (C=O) peak for PMCM is not clearly visible.

### 5.5.3 Differential Thermogravimetric Analysis (TGA)

Figure 5-6 shows differential thermogravimetric analysis (TGA) curves for pure PMCM copolymer, pure silica powder and as-spun fibers. All the samples are heated in air from room temperature to  $700\text{ }^{\circ}\text{C}$  at the rate of  $10\text{ }^{\circ}\text{C}/\text{min}$ . The deconvoluted derivative thermogravimetric (DTG) curves of the fibers are also shown in Figure 5-6. Furthermore, degradation temperatures, experimental and calculated silica residue values

(which represent the final silica content of the fibers after complete burning of PMCM binder and formation of nanoparticles) are tabulated in Table 5-2. Due to high resistance of silica to temperatures up to 1000 °C, no degradation of any kind is noticed in pure silica TGA curve (Figure 5-6). A single degradation curve at around 300 °C is noticed for pure PMCM copolymer (Figure 5-6)<sup>60</sup>, with 2 wt% silica residue. A broad degradation curve is noticed for as-spun fibers (Figure 5-6),<sup>61</sup> caused by moisture, reduction of silver nitrate to silver nanoparticles, and degradation of trace PMCM copolymer present in the silica fibers.

#### **5.5.4 Transmission Electron Microscopy**

The TEM micrograph images (Figure 5-2) of the heat-treated silica fibers clearly show a homogeneous distribution of silver nanoparticles inside the porous silica fibers. In order to optimize the catalytic efficiency of the silver nanoparticles present in the porous silica fibers, a controlled and reproducible size distribution along with high density of silver nanoparticles has to be achieved. Thus, the factors affecting the size of the silver nanoparticles must be evaluated. Table 5-1 lists the size of the silver nanoparticles, which were obtained by measuring 20 silver nanoparticles from each sample via the TEM micrographs (Figure 5-2). The size of the silver nanoparticles present in the heat-treated silica fibers (Figures 5-2a, 5-2b and 5-2c; 250-nm diameter silica fibers; 0.06 mol/L AgNO<sub>3</sub>; heated for 60 min) was seen to increase with increase in temperature from 400 °C to 600 °C. Further increase in temperature of the fibers to 800 °C did not cause any sharp increase in the size of the silver nanoparticles. Similarly, when the time for which the fibers were heated (5-2a and 5-2d; 250 nm diameter silica fibers; 0.06 mol/L AgNO<sub>3</sub>; heated at 400 °C) was increased from 60 to 150 min, an increase in the size of the silver

nanoparticles was noticed. This effect of temperature and time on the size of the silver nanoparticles is due to the Ostwald ripening phenomenon, as explained previously.<sup>62</sup> Figures 5-2a and 2e show TEM micrographs of heat-treated (250-nm diameter silica fibers; heated at 400 °C for 60 min) silica fibers, electrospun using 0.06 and 0.1 mol/L AgNO<sub>3</sub>, respectively. The increase in concentration of AgNO<sub>3</sub> from 0.06 to 0.1 mol/L leads to an increase in number and size of silver nanoparticles.<sup>32</sup> Similarly, with the increase in diameter of silica fibers from 100 to 250 nm, the average size of the silver nanoparticles also increased (Figure 5-2f; 0.06 mol/L AgNO<sub>3</sub>, heated at 600 °C for 150 min).

### 5.5.5 Optical Properties of PSFSP

The optical properties of heat-treated silica fibers were studied to evaluate further the distribution and size of silver nanoparticles in the fibers. Before heat treatment, the PMCM-modified silica fiber mats containing 0.06 mol/L of AgNO<sub>3</sub> were white in color. Upon heating, these fiber mats changed to a light golden yellow color as seen in Figure 5-7, owing to the surface plasma resonance (SPR) of the silver nanoparticles produced in the silica fibers during heat treatment. SPR is a characteristic feature of metal nanoparticles between the sizes of 2–50 nm.<sup>28,52</sup> Here the electrons freely oscillate on the metal particle surface and absorb electromagnetic radiation from particular energy levels. Particles less than 2 nm, on the other hand, do not show this phenomenon due to the presence of electrons in discrete energy levels.<sup>28,52</sup>

Figure 5-8a shows UV spectra of heat-treated silica fibers, which exhibit well-defined plasmon peaks indicating a narrow size distribution of silver nanoparticles. The fibers heated up to 200 °C for 30 min do not show any plasmon peaks due to the

incomplete formation of silver nanoparticles in the sample. On the other hand, samples heated up to 400 and 600 °C for 30 min, show sharp spectral bands for silver at around 406 and 410 nm, respectively. The shift in wavelength seen in fibers at higher temperature is due to the increase in size of silver nanoparticles. Similarly, Figure 5-8b shows UV spectra of fiber samples heated to 400 °C for 30, 90 and 150 min. As the time of heat treatment is increased, the plasmon peak shifts to higher wavelength, due to the increase in size of the silver nanoparticles.<sup>6,28,57</sup>

Figure 5-9 shows XRD spectra for silica fibers heat-treated to various temperatures and time. The diffuse reflection peaks at  $2\theta$  value of  $20^\circ$  observed in all the samples are indicative of the amorphous nature of sol-gel silica materials.<sup>58</sup> The peaks at  $2\theta$  values of  $38.2$ ,  $44.5$ ,  $64.6$ , and  $77.5^\circ$  correspond to the (111), (200), (220) and (311) crystal planes of silver particles.<sup>63</sup> The calculated  $d$ -spacing (Table 5-3) of the silver particles were found to be consistent with the International Centre for Diffraction Data (Table 5-3) obtained from JCPDS files (NO. 41-1402), indicating that the silver nanoparticles have cubic symmetry. Apart from measuring the size of silver nanoparticles via TEM micrographs, the average size of the silver nanoparticles (Table 5-1) was also calculated using Brigg's and Sherrer's equation ( $D = 0.9\lambda / \text{FWHM} \cos\theta$ ;  $D$  is the average particle size in Å; FWHM is the full width of the peak at half maximum and  $\theta$  the diffraction angle).<sup>27</sup> In all, samples heated to 300 °C did not show any peaks for silver, indicating that the silver ions were not yet converted to silver nanoparticles. As the samples were heated to higher temperatures and for longer time, the peaks for silver crystals appeared and increased in intensity.

## 5.6 Catalytic Activity of Silver Nanoparticles

Silver nanoparticles have been studied as a catalyst in reduction reactions of nitrophenols, nitroanilines and various dyes, such as methylene blue (MB) and fluorescein.<sup>29-31</sup> Reduction of MB by NaBH<sub>4</sub> is used as a standard for determining the catalytic activity of the silver nanoparticles encapsulated in the porous silica fibers. In agreement with previous results, the reduction of MB, if it occurs at all, is insignificant in the absence of silver particles.<sup>29,64,65</sup> In the solution containing silver particles, however, the reduction of the dyes by NaBH<sub>4</sub> is completed within 2 to 20 minutes. The choice of MB dye for testing the catalytic activity of the PSFSP is based on two factors: 1) the dye changes from blue to colorless when reduced, thus giving a sharp visible color, change and 2) the absorbance maximum ( $\lambda_{\max}$ ) for MB is around 665 nm, which does not interfere with the  $\lambda_{\max}$  of silver nanoparticles, which is around 420 nm.<sup>52</sup> The preliminary catalytic testing for PSFSP was carried out by reduction of 2 mL of MB (0.01 mol/L) in water, using 0.10 g silica fibers containing approximately 10 wt% silver nanoparticles as catalyst and 1 mL of NaBH<sub>4</sub> (0.1 mol/L) as the reducing agent. The progression of the catalytic reduction of MB can be easily followed (Figure 5-10) by the change in optical density at the  $\lambda_{\max}$  of 665 nm (oxidized form of MB). Evidently, the absorbance at  $\lambda_{\max}$  of MB gradually decreases with the reaction time, which is indicative of the reduction of MB from blue to colorless. As expected, the catalytic reduction of MB proceeded successfully, and no deactivation or poisoning of the catalyst was observed. The band at 420 nm (which comes from the silver nanoparticles present inside the fibers) was not very prominent at the initial stages of the reaction, but as the reduction of MB proceeded, the band at 665 nm (oxidized form of MB) disappeared, and the band at 410 nm (silver



nanoparticles present inside the fibers) became prominent. The induction period of 1 min seen at the initial stage of the reaction, could be due to the time required for the dye to enter the porous network of the silica fibers and come in direct contact with the silver nanoparticles. The entire reduction reaction experiment was conducted under nitrogen, to avoid obtaining false results due to the reduction of MB via oxygen.<sup>65</sup> A blank test containing a mixture of MB dye plus NaBH<sub>4</sub> reducing agent, with pure silica fibers containing no silver particles did not show any reduction or color change for more than 24 hours.

### **5.7 Conclusion**

In this study, novel catalytic silica nanofibers containing silver nanoparticles have been successfully synthesized via a simple electrospinning method. The density and size of the silver nanoparticles present in the fibers can be readily controlled by varying the diameter of the electrospun fibers, concentration of silver nitrate salt and heat treatment conditions. The silver nanoparticles in the silica fibers exhibited good catalytic properties, based on the results obtained from the silver-catalyzed reduction of MB dye.

### **5.8 Electrospinning of Gold Nanoparticles in Porous Silica Nanofibers**

Gold nanoparticles were synthesized inside porous silica nanofibers using the exact same procedure utilized for silver nanoparticles. The only difference in the preparation of the spinning solution was the addition of hydrogen tetrachloro-aurate tetrahydrate salt (HAuCl<sub>4</sub>·4H<sub>2</sub>O) solution instead of AgNO<sub>3</sub>. In a typical procedure, TEOS was mixed with THF and then a mixture of 2 N HAuCl<sub>4</sub>·4H<sub>2</sub>O and 1 N HNO<sub>3</sub> was added dropwise at two different [TEOS]: [THF]: [HNO<sub>3</sub>, 1N]: [HAuCl<sub>4</sub>·4H<sub>2</sub>O, 2 N] molar ratios of 1:2:0.05:0.06 and 1:2:0.05:0.1 with constant stirring for 30 min at room

temperature. The water required for hydrolysis of TEOS was obtained from the dilute  $\text{HAuCl}_4 \cdot 4\text{H}_2\text{O}$  solution used in the preparation of the sol. Next, 10 wt% PMCM solution in THF was added dropwise to the hydrolyzed TEOS /  $\text{HAuCl}_4 \cdot 4\text{H}_2\text{O}$  sol with constant stirring to obtain a transparent homogeneous solution with a viscosity of around 60 to 70 cP and a final PMCM content of 2 to 4 wt%, with respect to the wt% of silica. The solution thus prepared was then used to spin fibers using the specifications given under the experimental section for electrospinning porous silica nanofibers containing silver nanoparticles. Figure 5-12 represents a micrograph of the electrospun nanofibers. The two sets of fibers containing 0.06 and 0.1 mol/L of  $\text{HAuCl}_4 \cdot 4\text{H}_2\text{O}$  thus electrospun are then heat-treated to 500 °C. After heat treatment, the fibers changed from white to pinkish red in color. This was due to the reduction of  $\text{HAuCl}_4 \cdot 4\text{H}_2\text{O}$  to pure gold nanoparticles inside the silica fibers. The polymer additive (PMCM) also degraded leaving behind porous silica fibers. The fibers that contained 0.1 mol/L of  $\text{HAuCl}_4 \cdot 4\text{H}_2\text{O}$  salt when heat-treated reduced the salt to gold particles, some of which precipitated out of the fibers in the form of discs, cylinders and spheres as seen in Figure 5-13. Elemental analysis of the precipitated particles (Figure 5-14) represents a sharp peak for Au. TEM analysis of the fibers was also conducted using the same specifications that were followed for silver, wherein the fibers are cross-sectioned using a microtome. The TEM micrograph of silica nanofibers containing gold particles is clearly seen in Figure 5-15. Finally, XRD was used to analyze the distribution and size of Au particles. Figure 5-16 shows the XRD pattern of fibers heat-treated up to 500 °C. This clearly showed an increase in particle size with heat treatment.

## 5.9 Reference List

1. Henglein, A. Colloidal silver nanoparticles: photochemical preparation and interaction with O<sub>2</sub>, CCl<sub>4</sub>, and some metal ions. *Chemistry of Materials*, 10, 444-450. 1998.
2. Mostafavi, M., Marignier, J. L., Amblard, J., Belloni, J. Nucleation dynamics of silver aggregates. Simulation of photographic development processes. *Radiation Physics and Chemistry*, 34(4), 605-617. 1989.
3. Mallin, M. P., Murphy, C. J. Solution-phase synthesis of sub-10 nm Au-Ag alloy nanoparticles. *Nano Letters*, 2(11), 1235-1237. 2002.
4. Pastoriza-Santos, I., Liz-Marzan, L. M. Synthesis of silver nanoprisms in DMF. *Nano Letters*, 2(8), 903-905. 2002.
5. Moller, K., Bein, T. Inclusion chemistry in periodic mesoporous hosts. *Chemistry of Materials*, 10(10), 2950-2963. 1998.
6. Shi, H., Zhang, L., Cai, W. Composition modulation of optical absorption in Ag<sub>x</sub>Au<sub>1-x</sub> alloy nanocrystals in situ formed within pores of mesoporous silica. *Journal of Applied Physics*, 87(3), 1572-1574. 2000.
7. Powers, K. W., Hench, L. L. The effect of pore size on metal cluster formation in silica sol gel monoliths. *Ceramic Transactions*, 101(Surface-Active Processes in Materials), 253-266. 2000.
8. Bharathi, S., Nogami, M., Ikeda, S. Layer by layer self-assembly of thin films of metal hexacyanoferrate multilayers. *Langmuir*, 17(24), 7468-7471. 2001.
9. Hayakawa, T., Ono, Y., Nogami, M. Linear and nonlinear optical properties of monodispersed gold clusters in silica glass by sol-gel method. *Proceedings of SPIE-The International Society for Optical Engineering*, 3943(Sol-Gel Optics V), 102-111. 2000.
10. Anderson, M. L., Morris, C. A., Stroud, R. M., Merzbacher, C. I., Rolison, D. R. Colloidal gold aerogels: preparation, properties, and characterization. *Langmuir*, 15(3), 674-681. 1999.
11. Ying, J. Y., Mehnert, C. P., Wong, M. S. Synthesis and applications of supramolecular-templated mesoporous materials. *Angewandte Chemie, International Edition*, 38(1/2), 56-77. 1999.
12. Mehnert, C. P., Weaver, D. W., Ying, J. Y. Heterogeneous heck catalysis with palladium-grafted molecular sieves. *Journal of the American Chemical Society*, 120(47), 12289-12296. 1998.
13. Morey, M. S., Bryan, J. D., Schwarz, S., Stucky, G. D. Pore surface functionalization of MCM-48 mesoporous silica with tungsten and molybdenum metal centers: perspectives on catalytic peroxide activation. *Chemistry of Materials*, 12(11), 3435-3444. 2000.
14. Whetten, R. L., Shafiqullin, M. N., Khoury, J. T., Schaaff, T.G. Vezmar, I., Alvarez, M. M., Wilkinson, A. Crystal structures of molecular gold nanocrystal arrays. *Accounts of Chemical Research*, 32(5), 397-406. 1999.

15. Francois, L., Mostafavi, M., Belloni, J., Delouis, J. F., Delaire, J., Feneyrou, P. Optical limitation induced by gold clusters. 1. size effect. *Journal of Physical Chemistry B*, 104(26), 6133-6137. 2000.
16. Glynou, K., Ioannou, P. C., Christopoulos, T. K., Syriopoulou, V. Oligonucleotide-functionalized gold nanoparticles as probes in a dry-reagent strip biosensor for DNA analysis by hybridization. *Analytical Chemistry*, 75(16), 4155-4160. 2003.
17. Greenwood, N. N., Earnshaw, A. *Chemistry of the Elements*, 2nd Edition. Butterworth-Heinemann Publishers. Oxford. 1997.
18. Pradhan, N., Pal, A., Pal, T. Silver nanoparticle catalyzed reduction of aromatic nitro compounds. *Colloids and Surfaces, A: Physicochemical and Engineering Aspects*, 196(2-3), 247-257. 2002.
19. Zaera, F., Gellman, A. J., Somorjai, G. A. Surface science studies of catalysis: classification of reactions. *Accounts of Chemical Research*, 19(1), 24-31. 1986.
20. Fendler, J. H. Atomic and molecular clusters in membrane mimetic chemistry. *Chemical Reviews (Washington, DC, United States)*, 87(5), 877-899. 1987.
21. Hercules, D. M., Proctor, A., Houalla, M. Quantitative analysis of mixed oxidation states in supported catalysts. *Accounts of Chemical Research*, 27(12), 387-393. 1994.
22. Canameres, M. V., Garcia-Ramos, J. V., Gomez-Varga, J. D., Domingo, C., Sanchez-Cortes, S. Comparative study of the morphology, aggregation, adherence to glass, and surface-enhanced raman scattering activity of silver nanoparticles prepared by chemical reduction of Ag<sup>+</sup> using citrate and hydroxylamine. *Langmuir*, 21(18), 8546-8553. 2005.
23. Schmid, G. Large clusters and colloids. *Metals in the embryonic state. Chemical Reviews (Washington, DC, United States)*, 92(8), 1709-1727. 1992.
24. Lewis, L. N. Chemical catalysis by colloids and clusters. *Chemical Reviews (Washington, DC, United States)*, 93(8), 2693-2730. 1993.
25. Zheng, M., Gu, M., Jin, Y., Jin, G. Optical properties of silver-dispersed PVP thin film. *Materials Research Bulletin*, 36, 853-859. 2001.
26. Li, L., Cao, X., Yu, F., Yao, Z., Xie, Y. G1 dendrimers-mediated evolution of silver nanostructures from nanoparticles to solid spheres. *Journal of Colloid and Interface Science*, 261(2), 366-371. 2003.
27. Chakrabarti, K., Whang, C. M. Silver doped ORMOSIL - an investigation on structural and physical properties. *Materials Science & Engineering, B: Solid-State Materials for Advanced Technology*, B88(1), 26-34. 2002.
28. Epifani, M., Giannini, C., Tapfer, L., Vasanelli, L. Sol-gel synthesis and characterization of Ag and Au nanoparticles in SiO<sub>2</sub>, TiO<sub>2</sub>, and ZrO<sub>2</sub> thin films. *Journal of the American Ceramic Society*, 83(10), 2385-2393. 2000.
29. Pal, T., De, S., Jana, N. R., Pradhan, N., Mandal, R., Pal, A., Beezer, A. E., Mitchell, J. C. Organized media as redox catalysts. *Langmuir*, 14(17), 4724-4730. 1998.
30. Kundu, S., Mandal, M., Ghosh, S. K., Pal, T. Photochemical deposition of SERS active silver nanoparticles on silica gel and their application as catalysts for the reduction of aromatic nitro compounds. *Journal of Colloid and Interface Science* 272(1), 134-144. 2004.

31. Pradhan, N., Pal, A., Pal, T. Silver nanoparticle catalyzed reduction of aromatic nitro compounds. *Colloids and Surfaces, A: Physicochemical and Engineering Aspects*, 196(2-3), 247-257. 2002.
32. Demir, M. M., Gulgun, M. A., Menciloglu, Y. Z., Erman, B., Abramchuk, S. S., Makhaeva, E. E., Khokhlov, A. R., Matveeva, V. G., Sulman, M. G. Palladium nanoparticles by electrospinning from poly(acrylonitrile-co-acrylic acid)-PdCl<sub>2</sub> solutions. Relations between preparation conditions, particle size, and catalytic activity. *Macromolecules*, 37(5), 1787-1792. 2004.
33. Khushalani, D., Hasenzahl, S., Mann, S. Synthesis of mesoporous silica monoliths with embedded nanoparticles. *Journal of Nanoscience and Nanotechnology*, 1(2), 129-132. 2001.
34. Jiang, T., Chen, W., Zhao, F., Liu, Y., Wang, R., Du, H., Zhang, T. Preparation of porous spherical MgCl<sub>2</sub>/SiO<sub>2</sub> complex support as precursor for catalytic propylene polymerization. *Journal of Applied Polymer Science*, 98(3), 1296-1299. 2005.
35. Lin, K. J., Chen, L. J., Prasad, M. R., Cheng, C. Y. Core-shell synthesis of a novel, spherical, meso porous silica/platinum nanocomposites: Pt/PVP@MCM-41. *Advanced Materials (Weinheim, Germany)*, 16(20), 1845-1849. 2004.
36. Huang, Z. M., Zhang, Y. Z., Kotaki, M., Ramakrishna, S. A review on polymer nanofibers by electrospinning and their applications in nanocomposites. *Composites Science and Technology*, 63, 2223-2253. 2003.
37. Bronstein, L. M., Polarz, S., Smarsly, B., Antonietti, M. Sub-nanometer noble-metal particle host synthesis in porous silica monoliths. *Advanced Materials (Weinheim, Germany)*, 13(17), 1333-1336. 2001.
38. Dai, H., Gong, J., Kim, H., Lee, D. A novel method for preparing ultra-fine alumina-borate oxide fibres via an electrospinning technique. *Nanotechnology* 13(5), 674-677. 2002.
39. Desai, K., Sung, C. Electrospinning nanofibers of PANI/PMMA blends. *Materials Research Society Symposium Proceedings*, 736(Electronics on Unconventional Substrates--Electrotexiles and Giant-Area Flexible Circuits), 121-126. 2002.
40. Hou, H., Reneker, D. H. Carbon nanotubes on carbon nanofibers: A novel structure based on electrospun polymer nanofibers. *Advanced Materials (Weinheim, Germany)*, 16(1), 69-73. 2004.
41. Kataphinan, W., Teye-Mensah, R., Evans, E. A., Ramsier, R. D., Smith, D. J., Reneker, D. H. High temperature electrospun fibers and rare-earth modification. *Polymeric Materials Science and Engineering*, 88, 282-283. 2003.
42. Madhugiri, S., Zhou, W., Ferraris, J. P., Balkus, K. J. Electrospun mesoporous molecular sieve fibers. *Microporous and Mesoporous Materials*, 63(1-3), 75-84. 2003.
43. Madhugiri, S., Sun, B., Smirniotis, P. G., Ferraris, J. P., Balkus, K. J. Electrospun mesoporous titanium dioxide fibers. *Microporous and Mesoporous Materials*, 69(1-2), 77-83. 2004.
44. Wang, C., Li, Z. Y., Li, D., Yang, Q. B., Hong, Y. Preparation and stability of the nanochains consisting of copper nanoparticles and PVA nanofiber. *International Journal of Nanoscience*, 1(5 & 6), 471-476. 2002.

45. An, L., Wang, Y. Development and application of nanofiber technology. *Dangdai Shiyu Shihua*, 10(1), 41-45. 2002.
46. Dai, L. Polymer nanostructures. *Encyclopedia of Nanoscience and Nanotechnology*, 8, 763-790. 2004.
47. Ramakrishna, S. *An Introduction to Electrospinning and Nanofibers*. World Scientific Publishing Company. Singapore. 2005.
48. Yang, Q.B., Li, D. M., Hong, Y. L., Li, Z. Y., Wang, C., Qiu, S. L., Wei, Y. Preparation and characterization of a pan nanofibre containing ag nanoparticles via electrospinning. *Synthetic Metals*, 137(1-3), 973-974. 2003.
49. Wei, Y., Bakthavatchalam, R., Whitecar, C. K. Synthesis of new organic-inorganic hybrid glasses. *Chemistry of Materials*, 2(4), 337-339. 1990.
50. Wei, Y., Yang, D., Bakthavatchalam, R. Thermal stability and hardness of new polyacrylate-silica hybrid sol-gel materials. *Materials Letters*, 13(4-5), 261-266. 1992.
51. Wei, Y., Wang, W., Yang, D., Tang, L. Synthesis of Water-Soluble Polyacrylics Modified Silica Sol-Gel Materials. *Chemistry of Materials*, 6(10), 1737-1741. 1994.
52. Jana, N. R., Sau, T. K., Pal, T. Growing small silver particle as redox catalyst. *Journal of Physical Chemistry B*, 103(1), 115-121. 1999.
53. Jiang, Z. J., Liu, C. Y., Sun, L. W. Catalytic properties of silver nanoparticles supported on silica spheres. *Journal of Physical Chemistry B*, 109(5), 1730-1735. 2005.
54. Wei, Y., Jin, D., Yang, C., Kels, M. C., Qiu, K. Y. Organic-inorganic hybrid materials. Relations of thermal and mechanical properties with structures. *Materials Science & Engineering, C: Biomimetic Materials, Sensors and Systems* C6(2,3), 91-98. 1998.
55. Wei, Y., Feng, Q., Xu, J., Dong, H., Qiu, K. Y., Jansen, S. A., Yin, R., Ong, K. K. Polymethacrylate-silica hybrid nanoporous materials: A bridge between inorganic and polymeric molecular sieves. *Advanced Materials (Weinheim, Germany)*, 12, 1448-1450. 2000.
56. Jana, N. R., Pal, T. Redox catalytic property of still-growing and final palladium particles: A comparative study. *Langmuir*, 15(10), 3458-3463. 1999.
57. Ritzer, B., Villegas, M. A., Fernandez Navarro, J. M. Influence of temperature and time on the stability of silver in silica sol-gel glasses. *Journal of Sol-Gel Science and Technology*, 8(1/2/3), 917-921. 1997.
58. Choi, S. S., Lee, S. G., Im, S. S., Kim, S. H., Joo, Y. L. Silica nanofibers from electrospinning/sol-gel process. *Journal of Materials Science Letters*, 22(12), 891-893. 2003.
59. Huang, Z. H., Qiu, K. Y. The effects of interactions on the properties of acrylic polymers/silica hybrid materials prepared by the in situ sol-gel process. *Polymer*, 38(3), 521-526. 1997.
60. Chan, C. K., Peng, S. L., Chu, I. M., Ni, S. C. Effects of heat treatment on the properties of poly(methyl methacrylate)/silica hybrid materials prepared by sol-gel process. *Polymer*, 42(9), 4189-4196. 2001.

61. Chan, C. K., Peng, S. L., Chu, I. M., Ni, S. C. Effects of heat treatment on the properties of poly(methyl methacrylate)/silica hybrid materials prepared by sol-gel process. *Polymer*, 42(9), 4189-4196. 2001.
62. Sun, Y., Mayers, B., Herricks, T., Xia, Y. Polyol synthesis of uniform silver nanowires: A plausible growth mechanism and the supporting evidence. *Nano Letters*, 3(7), 955-960. 2003.
63. Mitrikas, G., Trapalis, C. C., Kordas, G. Tailoring the particle size of sol-gel derived silver nanoparticles in SiO<sub>2</sub>. *Journal of Non-Crystalline Solids*, 286(1,2), 41-50. 2001.
64. Pal, T., Sau, T. K., Jana, N. R. Silver hydrosol, organosol, and reverse micelle-stabilized sol - a comparative study. *Journal of Colloid and Interface Science* 202(1), 30-36. 1998.
65. Pal, T., Sau, T. K., Jana, N. R. Reversible formation and dissolution of silver nanoparticles in aqueous surfactant media. *Langmuir*, 13(6), 1481-1485. 1997.

Table 5-1. Sample code and average diameter of silica fibers and silver nanoparticles subjected to various heat treatments.

temperature <sup>a</sup> °C	time <sup>a</sup> min	average diameter SF10 <sup>b</sup>			average diameter SF20 <sup>b</sup>		
		silica fibers <sup>c</sup> nm	silver nanoparticles nm		silica fibers <sup>c</sup> nm	silver nanoparticles nm	
			TEM <sup>d</sup>	XRD <sup>e</sup>		TEM <sup>d</sup>	XRD <sup>e</sup>
30	-	180 ± 10	-	-	290 ± 10	-	-
200	30	175 ± 15	-	-	290 ± 30	-	-
	60	174 ± 17	-	-	280 ± 10	-	-
	150	170 ± 17	-	-	280 ± 20	-	-
400	30	150 ± 20	-	-	265 ± 10	-	-
	60	150 ± 12	9	8.5	258 ± 17	12	11
	150	135 ± 15	12	11	250 ± 15	15	14.5
600	30	130 ± 17	10	11	252 ± 10	15	14
	60	100 ± 17	15	14	252 ± 30	20	18.5
	150	100 ± 20	20	19	248 ± 25	25	21

<sup>a</sup>Various temperature and times used to heat treat PMCM modified electrospun silica fibers. <sup>b</sup>Average diameter of heat-treated silica nanofibers SF10 and SF20 containing 10 wt% silver nanoparticles and 20 wt% silver nanoparticles, respectively. <sup>c</sup>Average diameter (mean± standard deviation) of SF10 and SF20 obtained by measuring 100 fibers of a single sample from ESEM micrographs after heat treatment. <sup>d</sup>Average diameter of silver nanoparticles present in SF10 and SF20 obtained by measuring 20 nanoparticles from TEM micrographs. <sup>e</sup>Diameter of silver nanoparticles in SF10 and SF20 obtained from the Bragg's and Sherrer's equation calculated using the XRD graph.



Table 5-2. Degradation temperatures and final residue of samples heated up to 700 °C at the rate of 10 °C/min.

sample	Degradation temperature °C	SiO <sub>2</sub> (wt%) calculated	SiO <sub>2</sub> by TGA (wt%)
pure SiO <sub>2</sub>	no degradation seen	100	100
PMCM binder	309	2	3
*SF10	269 and 300	78	73

\*silica fibers containing 10 wt% of silver nanoparticles.

Table 5-3. A comparison of calculated  $d$ -spacing ( $d_{hkl}$ ) values of silver nanoparticles with that of International Centre for Diffraction Data obtained for silver from JCPDS files (NO. 41-1402).

$(hkl)^a$	calculated $d_{hkl}^b$	$d_{hkl}$ from JCPDS files <sup>c</sup>
(111)	0.2356	0.2359
(200)	0.2036	0.2043
(220)	0.1444	0.1445
(311)	0.1231	0.1231

<sup>a</sup>Cubic crystal lattice planes of silver nanoparticles. <sup>b</sup>Calculated  $d$ -spacing (interplanar spacing in Å) of silver particles ( $\lambda = 2d \sin \theta$ ) present inside silica fibers. <sup>c</sup>International centre for diffraction data obtained for silver from JCPDS files (NO. 41-1402).

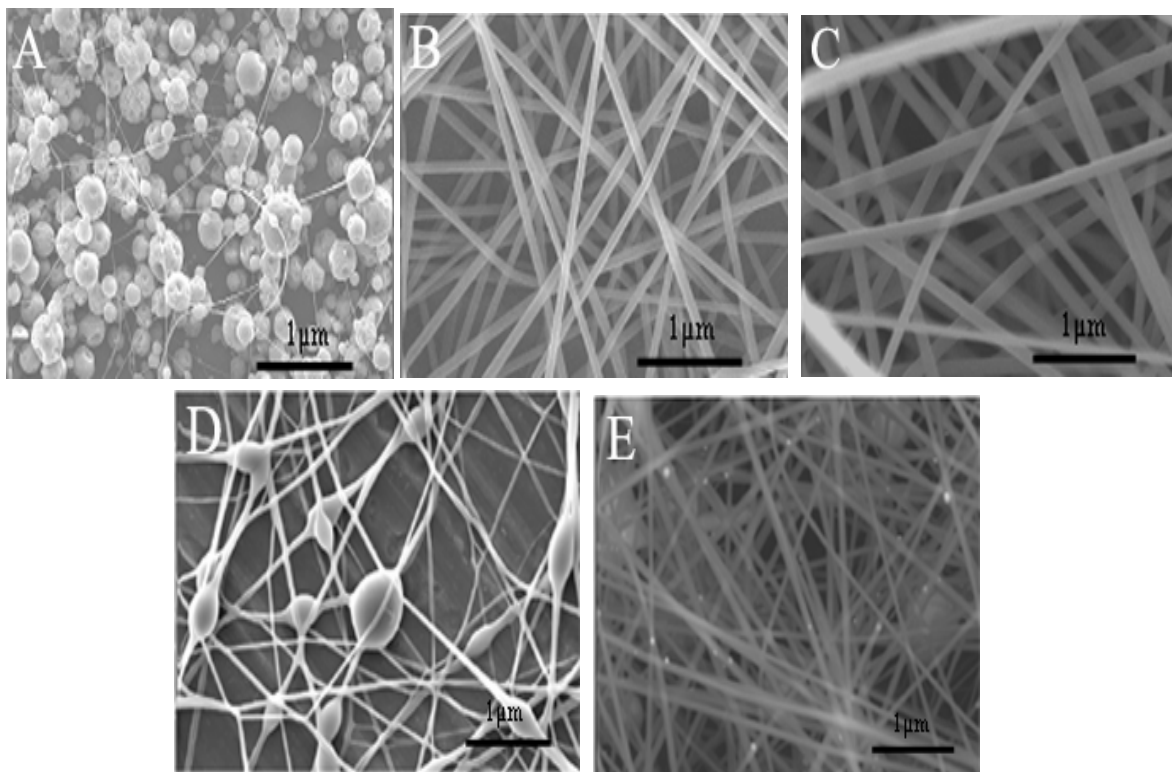


Figure 5-1. ESEM images of non-heat-treated electrospun silica/AgNO<sub>3</sub> nanofibers containing (a) 0 wt% PMCM and 0.06 mol/L AgNO<sub>3</sub>, (b) 2 wt% PMCM and 0.06 mol/L AgNO<sub>3</sub>, (c) 6 wt% PMCM and 0.06 mol/L AgNO<sub>3</sub> and (d) 2 wt% PMCM and 0.1 mol/L AgNO<sub>3</sub>; and of (e) heat-treated silica fibers (600 °C for 60 min) that were electrospun with a solution containing 2 wt% PMCM and 0.06 mol/L AgNO<sub>3</sub>. Scale bar: 1 μm.

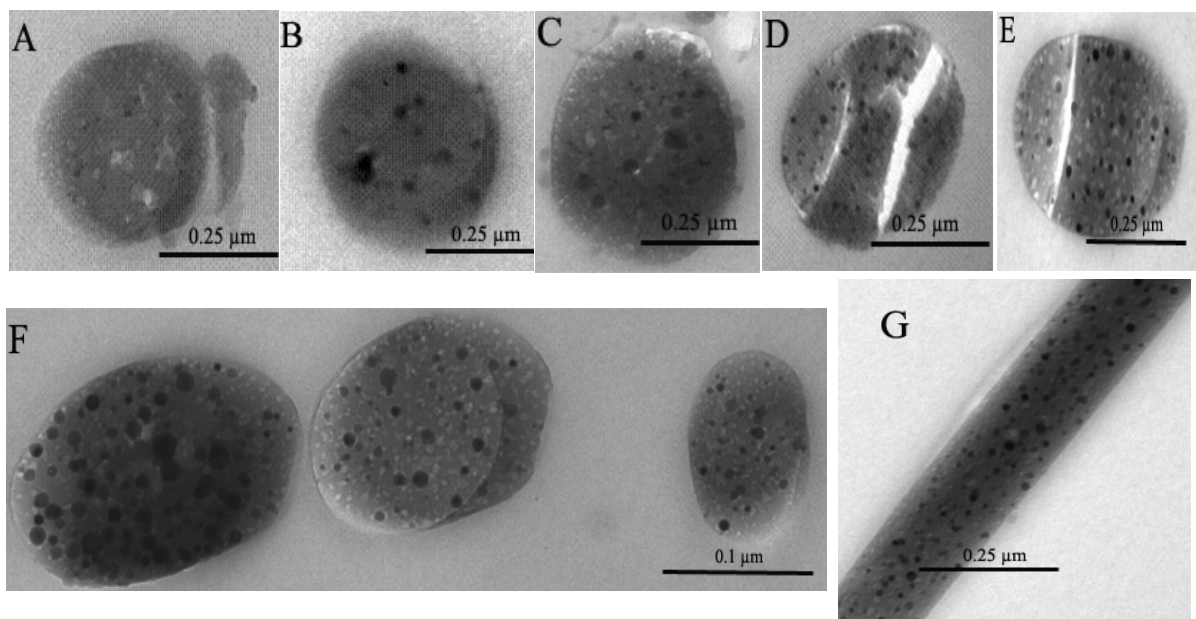


Figure 5-2. TEM cross-section micrographs of electrospun porous (light features: pores) silica-containing silver nanoparticles (dark spherical regions) after thermal treatment (wt% of silver; time of heat treatment; temperature of heat treatment): (a) 10 wt%, 60 min, 400 °C, (b) 10 wt%, 60 min, 600 °C, (c) 10 wt%, 60 min, 800 °C, (d) 10 wt%, 150 min, 400 °C, (e) 20 wt%, 60 min, 400 °C, (f) 10 wt%, 150 min, 600 °C (showing fiber diameters from 100 to 250 nm), and, (g) silica fiber showing homogeneous distribution of silver nanoparticles along the fiber. Scale bar 250 nm.

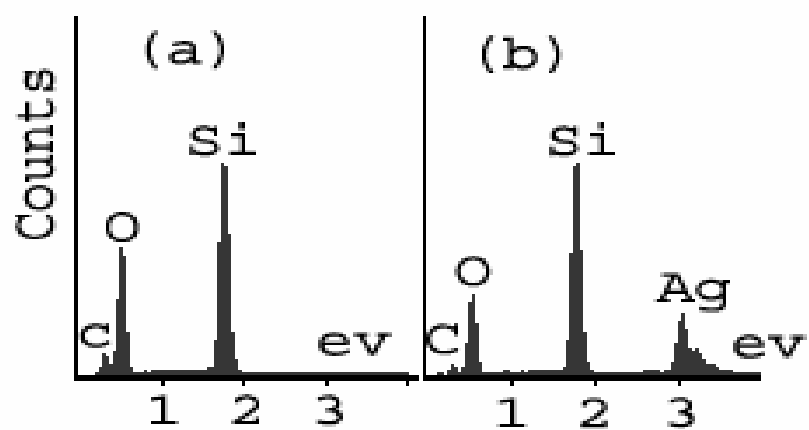


Figure 5-3. Elemental analysis (EDX) of silica fibers electrospun at 20 kV for (a) fibers without any silver content and (b) fibers containing 10 wt% of silver nanoparticles after heat treatment.

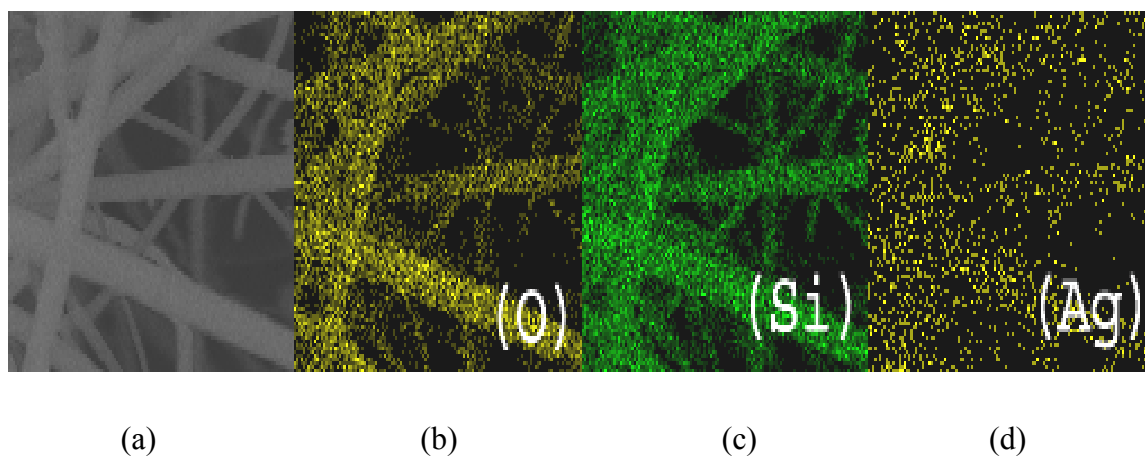


Figure 5-4. Elemental X-ray mapping of fibers containing 10 wt% of silver. (a) ESEM micrograph of heat-treated fibers; (b) oxygen mapping; (c) silicon mapping; (d) silver mapping showing homogeneous distribution of silver nanoparticles.

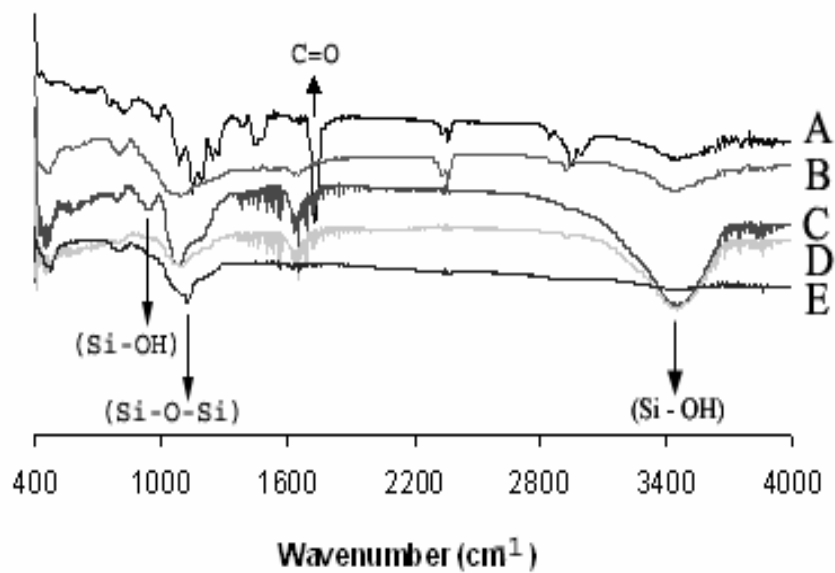


Figure 5-5. Infrared spectra of (a) pure PMCM polymer; (b) pure silica; (c) hydrolyzed TEOS/AgNO<sub>3</sub>/2 wt% PMCM electrospun fibers before heat treatment; (d) silica fibers containing 10 wt% silver nanoparticles heated at 200 °C for 30 min; (e) silica fibers containing 10 wt% silver nanoparticles heated at 600 °C for 30 min.

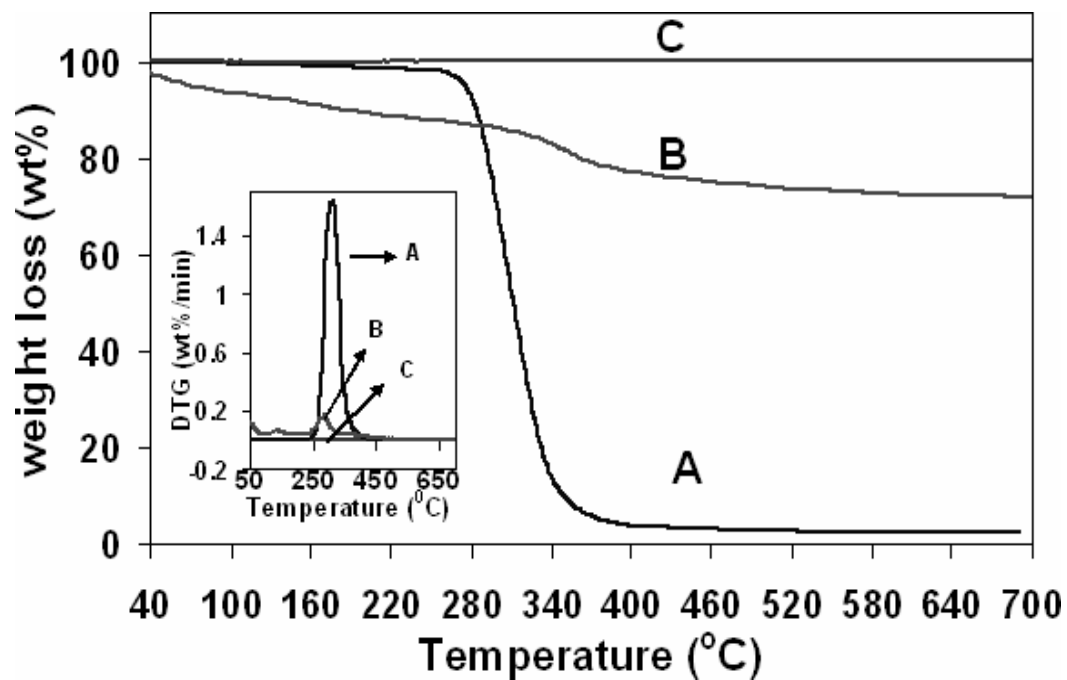


Figure 5-6. Thermogravimetric analysis (TGA) and deconvoluted derivative thermogravimetric (DTG) curves (inset) for samples heated at 10 °C/min from 40 °C to 800 °C in air: (a) pure PMCM polymer; (b) PMCM modified silica fibers containing 0.06 mol/L AgNO<sub>3</sub> before heat treatment; (c) pure SiO<sub>2</sub>.



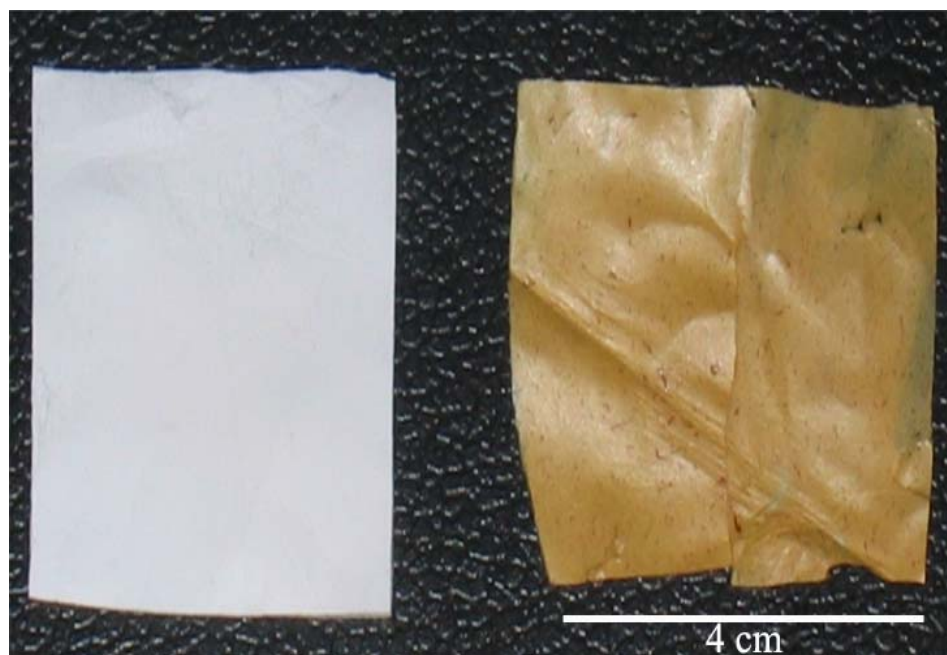


Figure 5-7. (a) White electrospun PMCM-modified silica fiber mats containing silver nitrate ( $\text{AgNO}_3$ ) before heat treatment; (b) golden yellow porous silica fiber mats containing 10 wt% silver nanoparticles after heat treatment at 600 °C for 60 min. Scale bar: 4 cm.

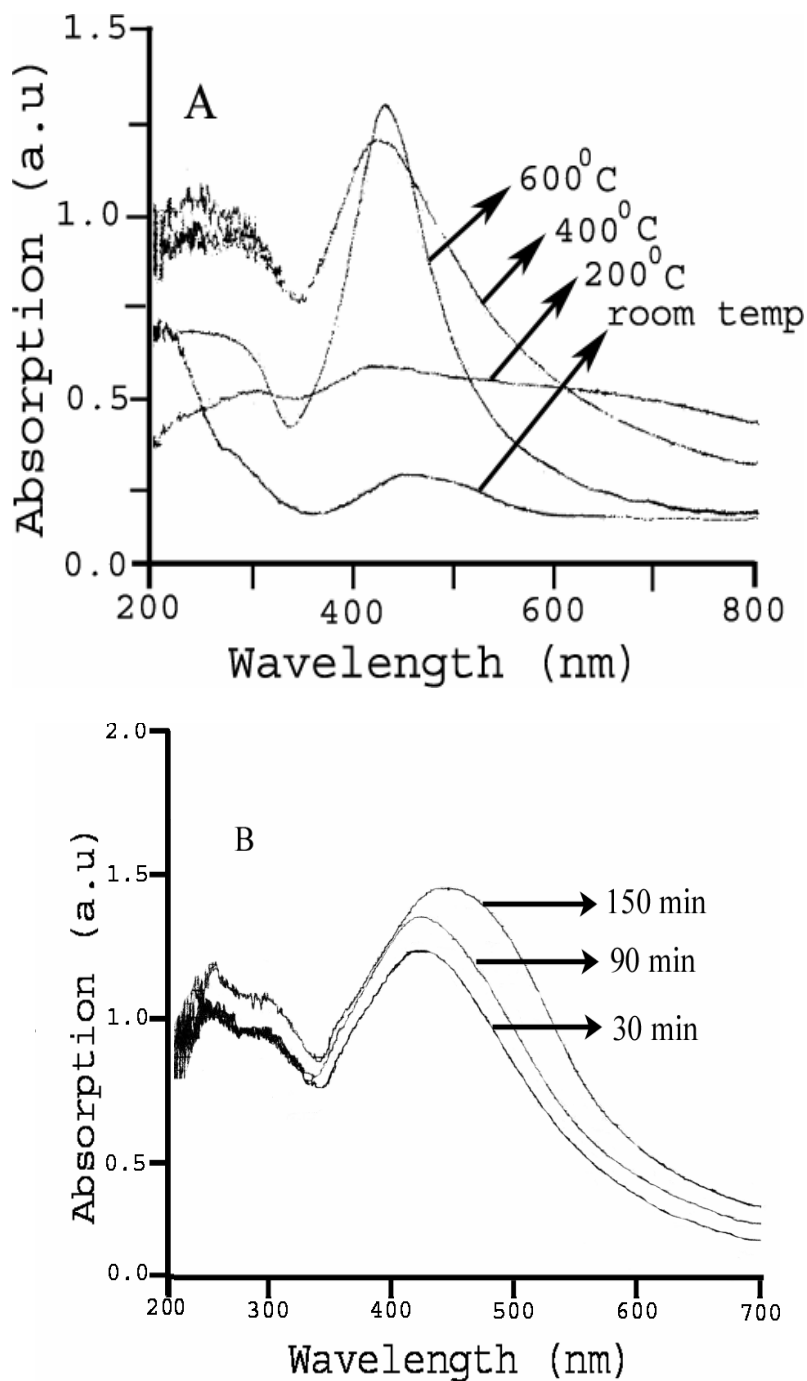


Figure 5-8. Optical spectra of porous silica nanofibers containing 10 wt% silver nanoparticles: (a) heat-treated at different temperatures for 30 min and (b) heat-treated for various periods at 400 °C.

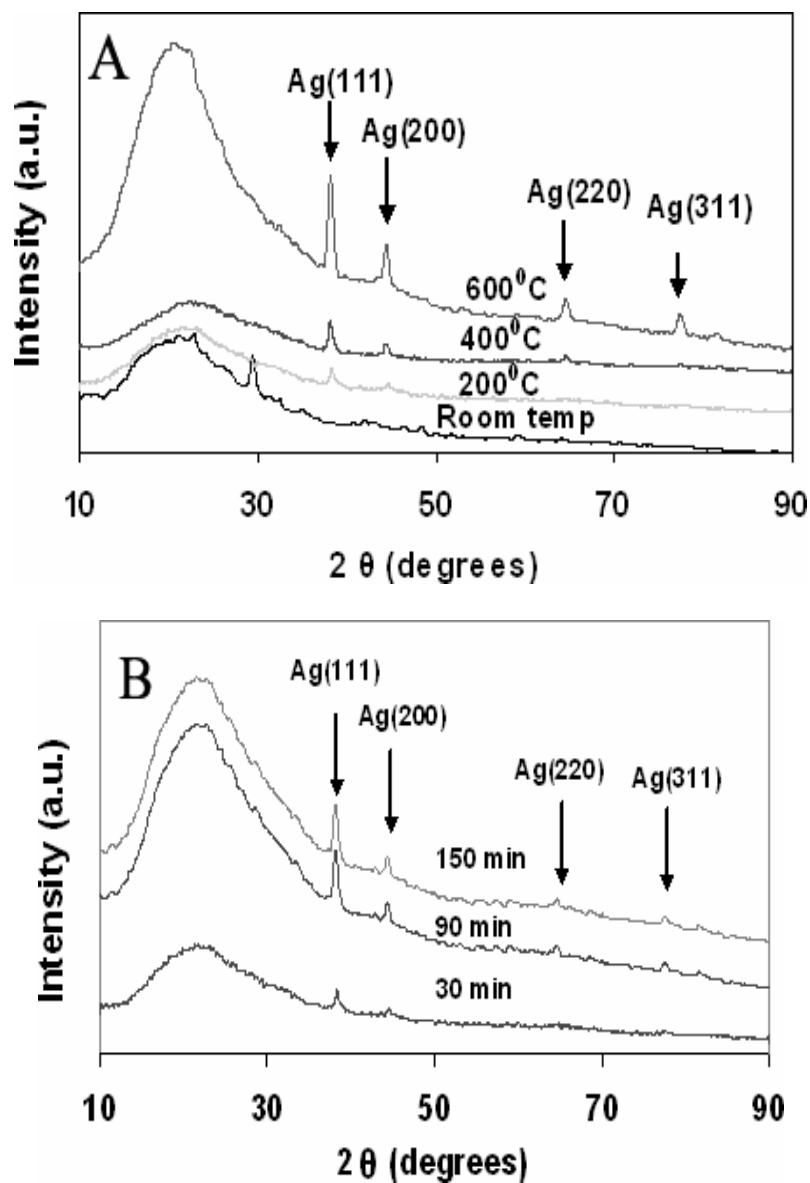


Figure 5-9. X-ray diffraction patterns for silica fibers containing 10 wt% silver nanoparticles: (a) heat-treated at various temperatures for 30 min and (b) heat-treated for various periods of time at 400 °C.

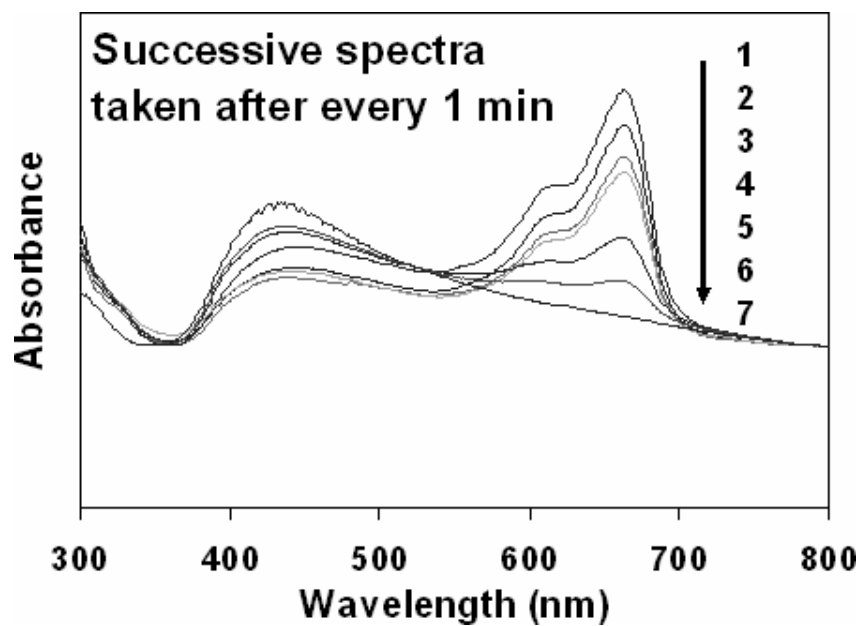


Figure 5-10. Successive UV-visible spectra (taken every 1 min) of methylene blue (MB) dye reduction, using silica nanofibers containing silver nanoparticles as the catalyst and  $\text{NaBH}_4$  as the reducing agent.

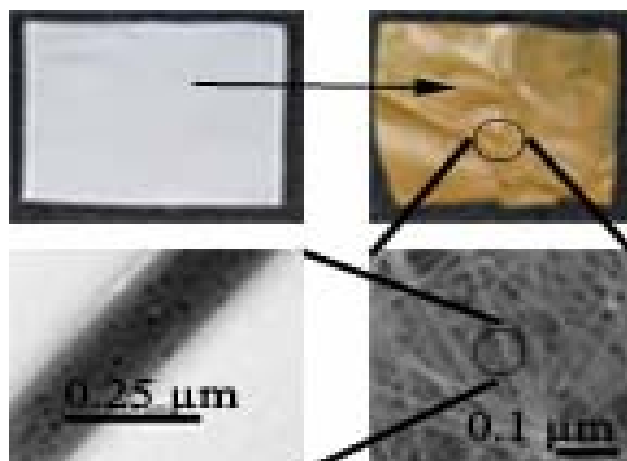
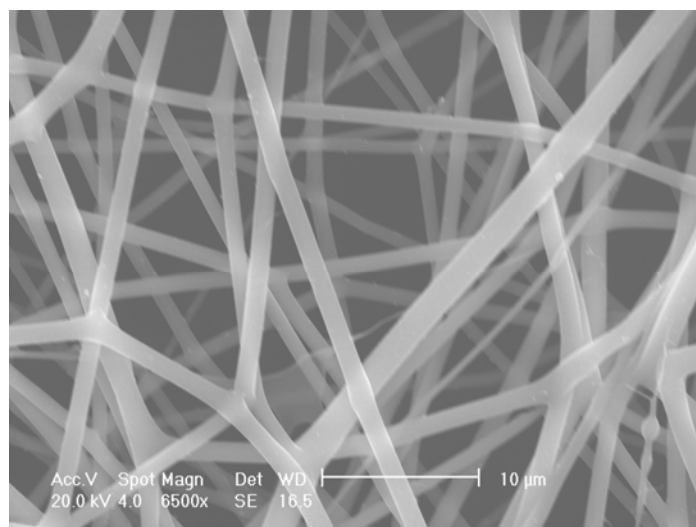
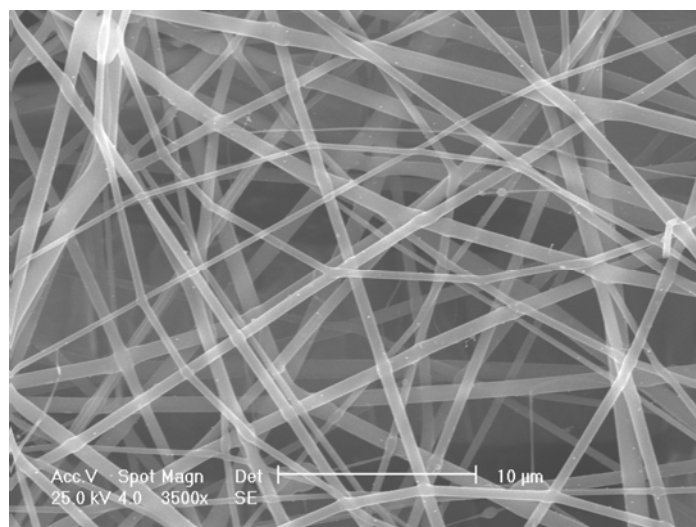


Figure 5-11. Representation of PSFSP.



(5-12a)



(5-12b)

Figure 5-12. ESEM images of non heat-treated electrospun silica/ $\text{HAuCl}_4 \cdot 4\text{H}_2\text{O}$  nanofibers containing (a) 0.06 mol/L  $\text{HAuCl}_4 \cdot 4\text{H}_2\text{O}$  (scale bar 10  $\mu\text{m}$ ) and (b) 0.1 mol/L  $\text{HAuCl}_4 \cdot 4\text{H}_2\text{O}$  (scale bar 10  $\mu\text{m}$ ).

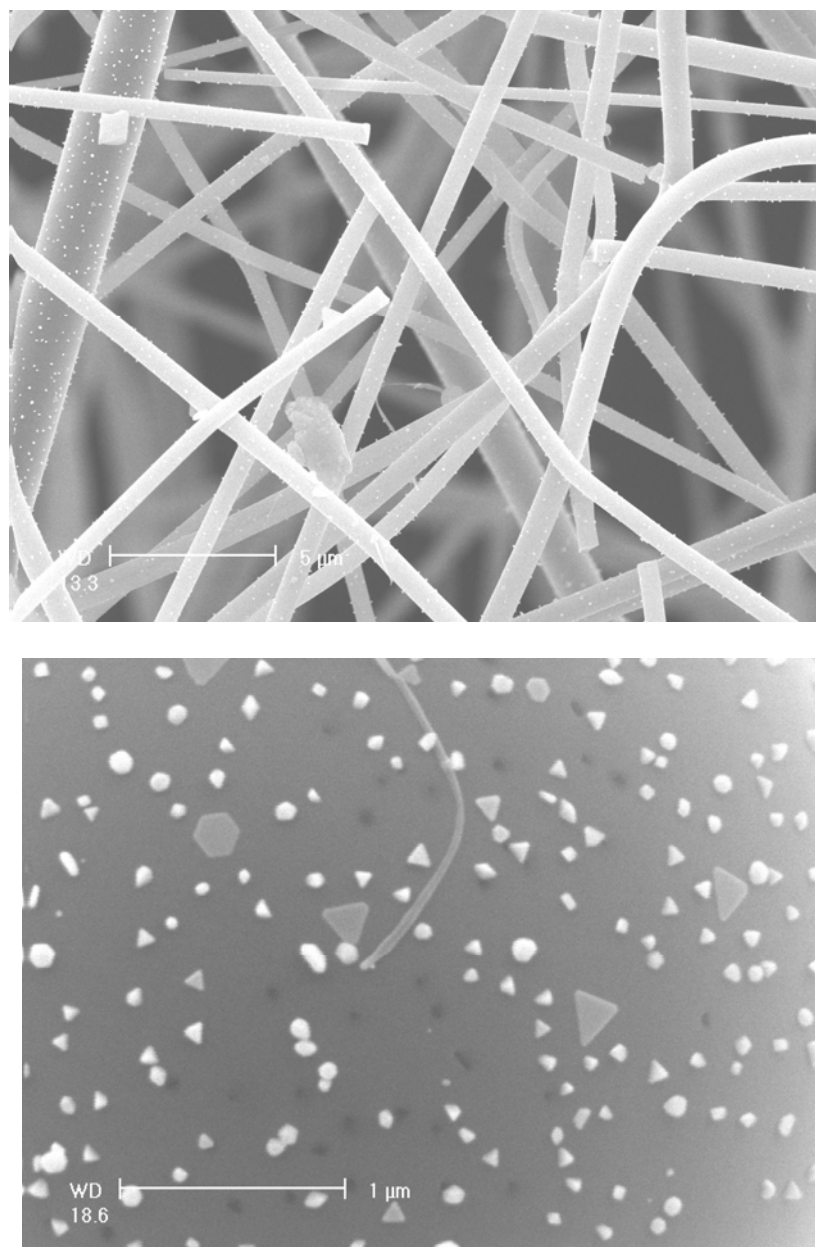


Figure 5-13. ESEM images of heat-treated electrospun silica nanofibers showing (a) precipitation of Au nanoparticles on top of silica fibers (scale bar 5  $\mu\text{m}$ ) and (b) high resolution image of Au particles on the silica fiber surface (scale bar 1  $\mu\text{m}$ ).

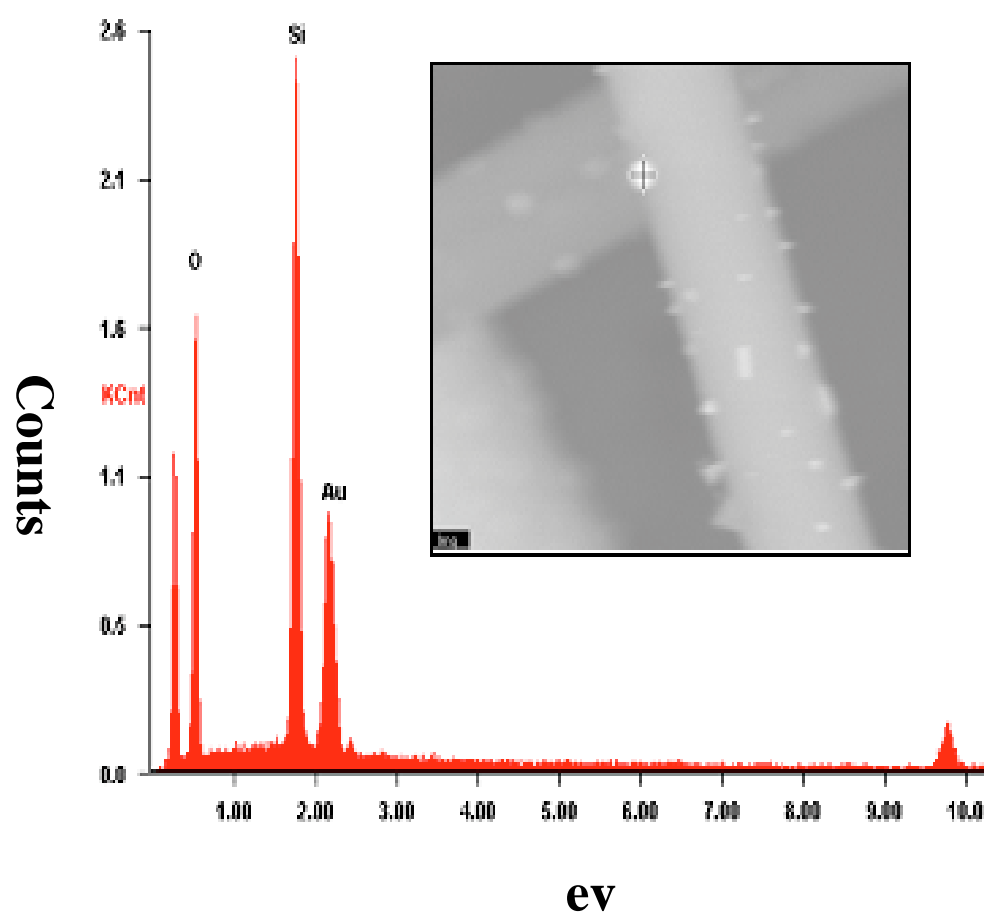


Figure 5-14. Elemental analysis (EDX) of gold nanoparticles present on the heat-treated silica fiber.



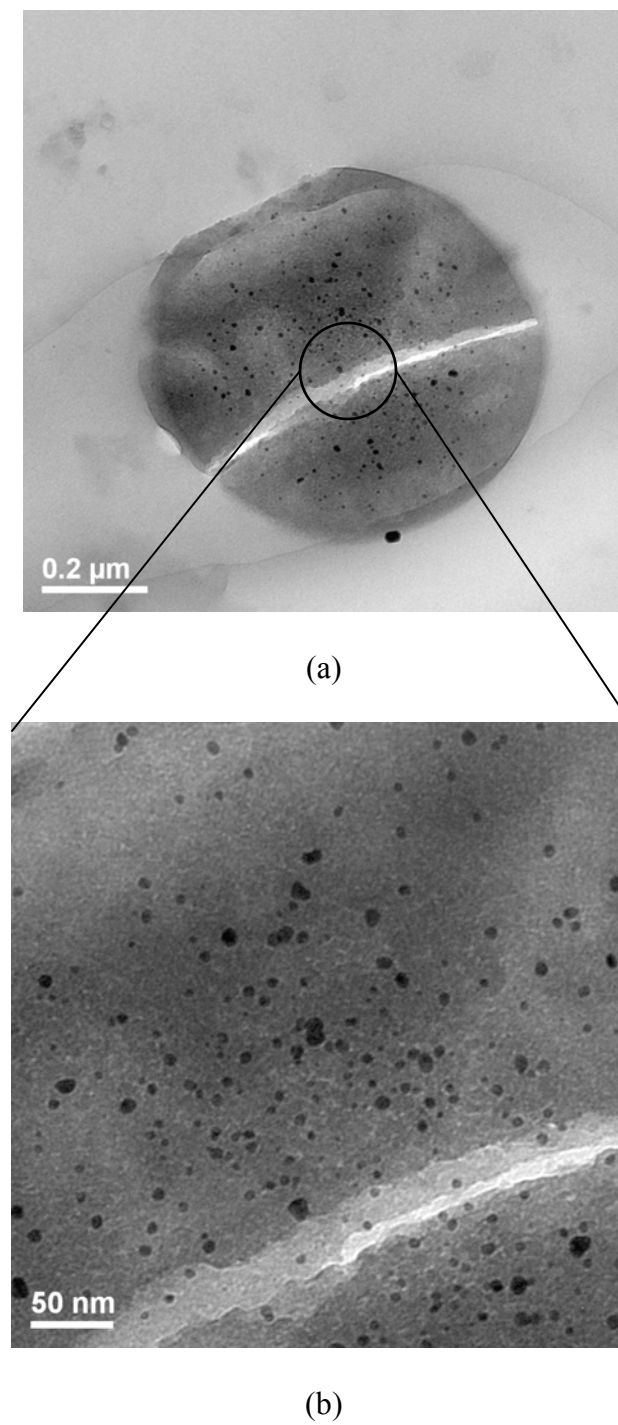


Figure 5-15. TEM cross section micrographs of heat-treated electrospun porous (light features: pores) silica nanofibers, containing gold nanoparticles (dark spherical regions). (a) Low-resolution image (scale bar 0.2 μm) and (b) high-resolution image (scale bar 50 nm).

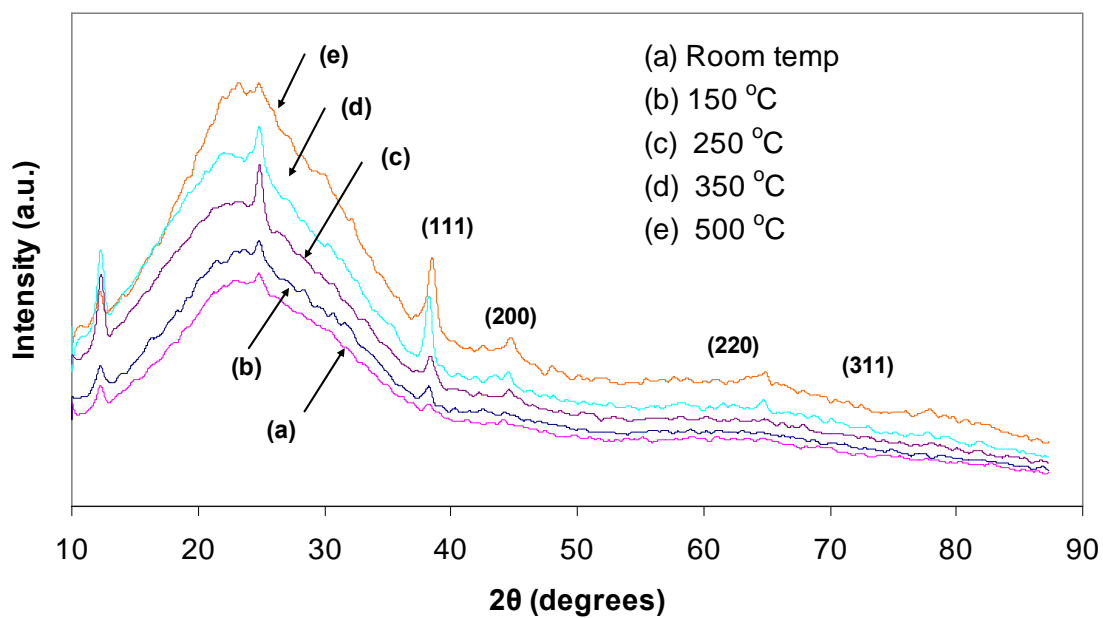


Figure 5-16. X-ray diffraction patterns for silica fibers containing gold nanoparticles heat-treated at (a) room temperature, (b) 150 °C, (c) 250 °C, (d) 350 °C and (e) 500 °C.

## **Chapter 6: In-Situ Encapsulation of Horseradish Peroxidase in Electrospun Porous Silica Fibers for Potential Biosensor Applications**

### **6.1 Introduction**

Various biotic substances are used as sensors for a wide range of applications from detecting hazardous chemicals in the atmosphere to measuring glucose in a human body.<sup>1-5</sup> Even with many successes, utilizing free enzymes for biosensor applications often encounters problems of poor stability and reusability.<sup>6</sup> To counteract these problems, polymer and sol-gel materials have been utilized to immobilize enzymes, which has proven to moderately increase the storage and thermal properties of enzymes.<sup>7,8</sup>

One of the above-mentioned methods, which has been extensively studied, is the sol-gel immobilization technique.<sup>8-12</sup> Here the enzymes are encapsulated in-situ and at room temperature using a sol-gel precursor, e.g., Tetraethylorthosilicate (TEOS) and tetramethylorthosilicate (TMOS). Upon immobilization, the entrapped biologics showed some apparent or remaining activity. The current sol-gel immobilization remains essentially a trial and error process, due to the complexity of the sol-gel reactions and the lack of control over fine structures of the final products at the molecular level. In addition to this, appropriate porosity of the sol-gel matrix is needed for containing biomolecules and for mass transport of the reactants and products of the bio-catalyzed reactions.<sup>8,11</sup> Hence, research on encapsulating enzymes in mesoporous silica and organically modified silicate sol-gel materials via various surfactant and non-surfactant templating processes has been looked at.<sup>13,14</sup> The porosity of the materials (e.g., silica sol-gel materials) has been fine-tuned further in our laboratory by using neutral, biocompatible, non-surfactant,

pore-forming agents or templates.<sup>13,15,16</sup> Advantage is taken of the fact that the increase in wt% of nonsurfactant template in the sample increases the surface area as well as the porosity of the samples (which in turn increases the catalytic activity of the sol-gel sample). The enzymes show better stability in nonsurfactant templated mesoporous silica matrices than in surfactant-templated and non-templated samples.<sup>16</sup> There are still a number of issues, however, such as time consuming multiple steps for encapsulating and drying enzyme immobilized materials, decreased enzyme activity, small surface area and finally enzyme leakage, which limit the biosensor applications of such materials.<sup>17,18</sup>

Thus an urgent need to synthesize an ideal biosensor matrix, for detecting harmful agents as well as for biocatalytic applications, has led scientists in the last couple of years to study a simple and efficient technique called electrospinning,<sup>19-22</sup> to produce polymer nanofiber mats as enzyme immobilization substrates. Some attractive features, which make electrospun nanofibers an interesting candidate for enzyme immobilization, include large surface area, reusability of the fiber mats due to easy separation from the reaction mixture and retention of catalytic activity due to evaporation of harmful solvents from fibers during electrospinning. Surface immobilization is one of the techniques studied for immobilization of enzymes via electrospinning. In this technique, only the external surface of the electrospun fibers is utilized for enzyme immobilization, while the internal surface remains as such. The limited availability of enzyme attachment sites on the surface of the fibers causes low enzyme loading. A loss of enzyme activity is noticed due to the limited mobility and direct exposure of the surface immobilized enzymes to harsh chemicals and high temperatures.<sup>23,24</sup> Direct electrospinning of enzymes along with various polymers is another method used to encapsulate and protect enzymes inside

polymer fibers.<sup>4,25,26</sup> This technique causes limited interaction of enzymes with the substrates due to the complete confinement of some of the enzymes inside the nonporous fibers. Some of these fiber mats employed for enzyme encapsulation are water soluble and hence, tend to swell and disintegrate when immersed in solvents, causing enzyme leakage, decreased thermal stability and non reusability of the fiber mats, thus requiring extra steps to protect the fibers via coating or cross linking. Attempts made to cross link the enzyme encapsulated fibers<sup>23,24</sup> causes reduced porosity of the fiber mats and conformational changes in the enzyme molecules, which in turn causes limited accessibility of substrates to the active sites of the enzymes, thus causing loss in enzyme activity.<sup>5,26-30</sup>

Keeping in mind all the obstacles faced by researchers to date as mentioned above, a novel method is presented here, in which a biosensor based on direct electrospinning of enzyme-encapsulated mesoporous silica fibers (EIMSF) has been synthesized. This biosensor is a unique combination of two nanotechnologies, i.e., the direct encapsulation of enzymes in nanoporous silica matrix<sup>31</sup> and electrostatic nanofiber spinning.<sup>32</sup> The unique features that differentiate and make EIMSF a superior candidate for biosensor applications include 1) high surface area due to the nanometer range control of mesopore formation inside the silica fibers (e.g., 2 to 10 nm or greater) facilitating substrate diffusion; 2) no deformation of the silica fibers with little or no swelling; 3) no enzyme leakage; 4) high thermal stability; 5) increased reusability and 6) the freedom to encapsulate various kinds of enzymes individually or as mixtures in a short period of time.

In this work, tetramethyl orthosilicate (TMOS) was used as a silica precursor, poly(vinyl alcohol) (PVA, Mn 30,000) was used as an extender, which assists in easy spinning of silica fibers, and  $\beta$ -D- glucose not only functions as a nonsurfactant template for controlling mesoporosity<sup>31,33</sup> of the resultant sol-gel silica fibers, but also helps in the fiber spinning by increasing viscosity. The enzyme immobilized inside the mesoporous silica fibers was horseradish peroxidase (HRP). HRP has relatively low molecular weight (39.8 kDa) and size (Stokes radius 30.3 Å).<sup>34</sup> It has high catalytic activity and stability over a wide range of temperature and pH. HRP also has the ability to catalyze the oxidation of a number of substrates by hydrogen peroxide, and finally has potential applications as biosensors (glucose sensor) and biocatalysts.<sup>33,35,36</sup> An important point that needs to be specified is that, although HRP has been previously immobilized in sol-gel materials and evaluated with amperometric, chemiluminescent, and spectrophotometric methods, these methods were in either wet gel or hydrogels instead of in fully dried gels.<sup>37</sup> An investigation focusing on the dependence of its enhanced activity on the surface area and shape of the material (electrospun nanofibers) having varied pore volumes and sizes (effect of glucose on pore size) is warranted. In this study, the encapsulated HRP was assayed with a colorimetric method using phenol, 4-aminoantipyrine and hydrogen peroxide as the dye-generating compounds. The thermal stability, pH profiles, and activity dependence of HRP on the fiber pore parameters were also reported. The apparent activity of immobilized HRP was evaluated against that of the enzyme in solution for comparison, in order to elucidate the influence of immobilization on the protein molecules. The effect of the hydrophilicity/hydrophobicity of the microenvironment on the immobilized enzyme were also studied.

## 6.2 Experimental Section

Direct immobilization of HRP in the porous nanofibers followed two main steps. One was the preparation of the enzyme containing sol-gel electrospinning solution and second was the electrospinning of the solution into enzyme-containing nanofiber mats. After the fabrication of the nanofibers, the glucose templates present inside the fibers were extracted out, leaving behind enzyme encapsulated porous nanofibers. These fibers were then tested for catalytic activity.

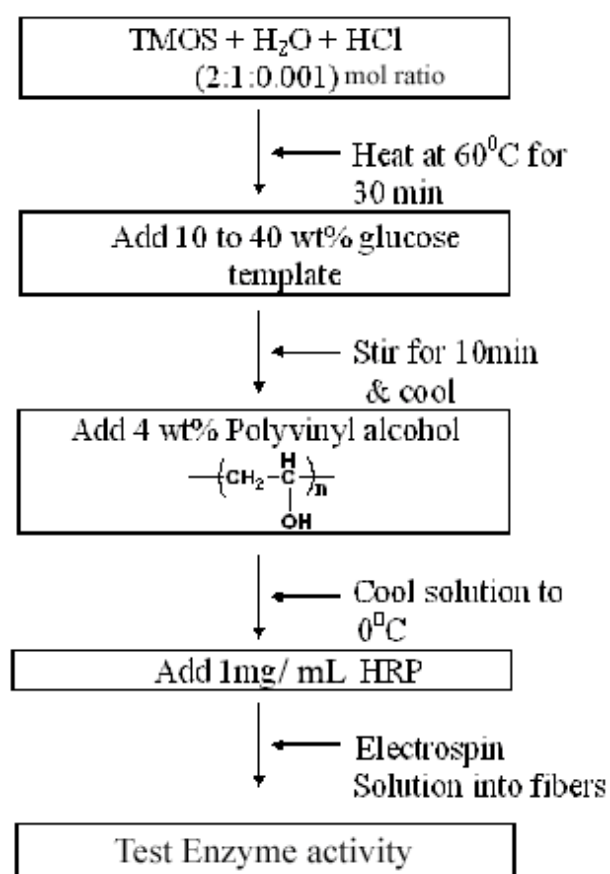
### 6.2.1 Materials and Reagents

Horseradish peroxidase (HRP, EC 1.11.1.7, Type II, 200 purpurogallin units/mg), 4-aminoantipyrine (4-AAP), phenol (PhOH),  $\beta$ -D- glucose and sodium phosphate were purchased from Sigma (St. Louis, MO). Tetramethyl orthosilicate (TMOS, 99%) and poly(vinyl alcohol) (PVA, Mn 30,000) and hydrogen peroxide ( $H_2O_2$ ) were purchased from Aldrich (Milwaukee, WI). HCl was a product of Fisher Scientific (Fair Lawn, NJ). The concentration of  $H_2O_2$  was determined by titration with potassium permanganate ( $KMnO_4$ ), which was standardized by using sodium oxalate in acidic solution. All chemicals and reagents were used as received without further purification.

### 6.2.2 Preparation of HRP Containing Sol-Gel Electrospinning Solution

Scheme 6-1 briefly explains the steps involved in the fabrication of enzyme-encapsulated nanofibers. In general, a mixture of four separate solutions of hydrolyzed silica sol, glucose solution, PVA solution and enzyme buffer solution makes up the final electrospinning solution. Hydrolyzed silica sol was prepared by mixing TMOS with water and HCl in a [2:1: 0.05] mol ratio. In an typical procedure, 0.77 g of TMOS precursor (accounts for 0.3 g of silica) was prehydrolyzed using 0.25 g of  $H_2O$  and 30  $\mu$ l

of 40 mM HCl catalyst with continuous stirring for 30 min.<sup>33</sup> Initially TMOS and water remain as separate phases and hence, the solution looks cloudy in nature during stirring. After 20 to 30 min, the entire mixture turns clear giving out some amount of heat due to the exothermic nature of the reaction. The reaction mixture was then heated to 60 °C for 30 min to evaporate off the methanol produced during hydrolysis. The sol was then cooled to 0 °C. Next 0.2 g of glucose (dissolved in water to make a 50 wt% solution), 0.01 g of PVA (dissolved in water to make a 8 wt% solution) and 1 mg of commercially available HRP in 1 ml of phosphate buffer (100 mM, pH 6.5) were added with constant stirring to yield a clear spinning solution. The temperature of the spinning solution was maintained at 0 °C until ready for electrospinning.



Scheme 6-1. Fabrication of enzyme-encapsulated mesoporous silica nanofibers.



### 6.2.3 Electrospinning of the Enzyme Containing Sol Gel Mixture

The enzyme containing solution thus produced was filled in a syringe and subjected to an electric field of 20 kV. A grounded metal plate placed at a distance of 20 cm from the tip of the syringe was used to collect the electrospun fibers. Under the electric field, a droplet suspended from the tip of the syringe acted as a feed source from which a charged jet of enzyme immobilized silica solution was ejected out, leaving behind white, flexible, dry fiber mats containing approximately 1 mg of HRP. The enzyme-encapsulated fibers thus produced were then washed with buffer solution to extract the glucose template and PVA polymer present inside the fibers. Removing the glucose template caused the fibers to become porous in nature, thus producing enzyme-encapsulated porous nanofiber mats. During template-extraction, no enzyme leakage was noticed.

### 6.2.4 Activity Assay of Free and Immobilized HRP

An adapted colorimetric method using PhOH, 4-AAP and H<sub>2</sub>O<sub>2</sub> as the dye generating compounds has been employed to estimate the initial catalytic activity of free and immobilized HRP. A schematic representation of the entire catalytic activity assay is represented in Figure 6-1. The initial activity of HRP was determined from the absorbance change at 510 nm by using a UV-vis spectrophotometer (Perkin Elmer Lambda 2, Norwalk, CT). The absorbance increase was due to the formation of a colored compound, N-antipyryl-*p*-benzoquinoneimine, which was caused by the interaction of HRP with H<sub>2</sub>O<sub>2</sub> as illustrated in Figure 6-2. For free HRP, 1.0 mL of the enzyme solution (containing  $4.0 \times 10^{-4}$  mg or nominally 0.08 units of HRP) was mixed with 2.0 mL of 4-AAP (2.46 mM)-PhOH (172 mM) solution at room temperature. After 15 min, 2.0 ml of

H<sub>2</sub>O<sub>2</sub>-phosphate (100 mM, pH 6.5) solution was added to initiate the reaction, upon which, the absorbance change with time was recorded. For immobilized HRP nanofibers, all samples were first washed thoroughly with dilute buffer solution before proceeding to activity assay according to the following procedure. The sample (3-7 mg, each containing nominally 0.50 units of HRP) was weighed into a tube, and 10 mL sodium phosphate buffer (10 mM, pH 6.5) was added to soak the sample under agitation. After 1 hour, the wash solution was separated from the solid by decantation after centrifugation. The washing procedures were repeated two more times at 1 hour intervals and the wash solutions (supernatants) were collected for enzyme activity assay (to test any enzyme, leakage into wash solution). The HRP-containing template-extracted fibers were then evaluated for the apparent activity following the same procedures as for the free enzyme except substituting the enzyme solution with 1.0 mL of distilled H<sub>2</sub>O.

The activity dependence of HRP on the bulk hydrogen peroxide concentration present in the assay solution was conducted in the range of 0.1 - 8.0 mM at a constant pH 6.5. The Lineweaver-Burk plot was used to calculate the Michaelis constant ( $K_m$ ) and the maximal velocity ( $V_m$ ). The effect of pH (in the range of 4.5-9.1) on the activity of free and immobilized HRP was studied at a fixed concentration of hydrogen peroxide,  $[H_2O_2] = 2.0$  mM. Sodium phosphate buffer (40 mM) was used to obtain all pH values. The enzyme-containing fiber samples were washed according to the above procedures prior to the assay of HRP activity.

To assess the efficiency of encapsulation or the amount of unbound, loosely trapped, leached or surface absorbed HRP in as-synthesized fibers, the wash solutions collected before the activity assay for immobilized samples, according to the above

procedures, were assayed for HRP activity in the same way as free enzyme in solution. Here an assumption was made that the HRP activity was not altered by the immobilization procedures or in the presence of minor amount of other chemicals (e.g., glucose).

Thermal stability of free and immobilized HRP was estimated from the remaining activity after a thermal treatment between 60 °C and 80 °C, in comparison with the activity of the same sample without the heat treatment. The thermal treatment was conducted as follows. After a typical washing procedure, a few milligrams of immobilized HRP sol-gel fiber were added to 1.0 mL of H<sub>2</sub>O. For free HRP, 1.0 mL of dilute HRP aqueous solution was used directly. The sample-containing tubes were sealed with paraffin film and put into a 60 °C water bath for 30 min. After removing them from the warm water bath, the tubes were replaced in a room temperature water bath. After which, both free and gel-immobilized samples were assayed for remaining activities by following the general procedures at pH 6.5 (40 mM sodium phosphate) and [H<sub>2</sub>O<sub>2</sub>] = 2.0 mM. Before proceeding to the activity assay, however, the thermal-treated fiber samples were separated from the aqueous phase in order to avoid any activity contribution from possible enzyme leaching from the fiber samples during the thermal treatment. The supernatant was collected by decantation after centrifugation and estimated for any enzyme activity.

In all the activity assay experiments, both 4-AAP-PhOH and H<sub>2</sub>O<sub>2</sub>-phosphate solutions were freshly prepared daily before the assay, the concentrations of 4-AAP and PhOH were fixed at 2.46 mM and 173 mM, respectively.

### 6.3 Characterization of Enzyme Immobilized Electrospun Nanofibers

Scanning electron microscopy (SEM, Phillips XL30) was used to measure the diameter and study the surface morphology of the electrospun fibers. About 1 x 1 cm square fiber mats were taped onto sample holders using conducting carbon tape. The fiber mats were then sputter coated with a monolayer of platinum metal. The samples were then exposed to an electron beam of 20 kV in the SEM through which high-resolution images of fibers were obtained. The diameter of the fibers was then measured from the obtained micrographs using the UTHSCSA ImageTool 3.0. The extraction of glucose template and PVA from the electrospun fibers was monitored using FTIR (Perkin-Elmer, Model-1600) and thermogravimetric analysis (TA Q50 TGA). The sample for FTIR studies was made by mixing the fibers with dry KBr and compressed into small pellets. The pellets were exposed to 50 scans, with wavelengths ranging from 400 to 4000  $\text{cm}^{-1}$ . After the complete extraction of templates from the fibers, the fibers were dried and then analyzed for surface area and mesoporosity by nitrogen adsorption-desorption at  $-196\text{ }^{\circ}\text{C}$  using Micromeritics ASAP 2010 instrument. Transmission electron microscopy (TEM, JEOL 2010F) was used to study the mesoporosity of the template-extracted fibers. The samples for TEM studies were prepared by embedding irregular clusters of template-extracted fibers in resin. The resin was then temperature-cured to a hard form and microtomed into 100 nm thick cross-sections. Due to the different mechanical properties of the fibers with that of resin, the fibers tend to stick together and lose their spherical shape during sample preparation. The microtomed samples were then placed on TEM sample holders (200 mesh, lacy carbon coated copper grids) and then evaluated for

porosity. Finally, UV-vis absorbance spectroscopy (Perkin-Elmer  $\lambda$ 2S) at 510 nm was used to study the catalytic activity of the enzyme encapsulated nanofibers.

## **6.4 Results and Discussion**

The main goal in the fabrication of HRP encapsulated porous nanofibers is to obtain high surface area nanofibers with high catalytic activity. Some important factors that need to be evaluated in order to achieve this goal are the diameter and morphology of the fibers, the porosity of the fibers, the effect of pH and concentration of  $H_2O_2$  on the catalytic activity of the fibers and thermal stability of the fibers. A detailed discussion of the above-mentioned factors follow.

### **6.4.1 Factors Affecting the Morphology and Diameter of Electrospun Nanofibers**

Three sets of fibers and three control samples (Table 6-1) were synthesized to evaluate the efficiency of enzyme encapsulation. The only difference between the three sets of samples was the varying wt% of glucose, which ranged from 0, 20 and 40 wt% glucose. This brought the silica content of the samples to 96, 76 & 56 wt%, respectively. The amount of PVA and HRP was kept at a constant of 4 wt% and 1 mg respectively. The sample ID's for the three sets were 0EIMSF, 20EIMSF and 40EIMSF respectively. Three control samples, (1) 40EIMSF2, which is similar to 40EIMSF except for the average fiber diameters, (2) 40EIMSF (NoPVA), which is similar to 40EIMSF except for the absence of PVA, and (3) 40EIMSF (NoHRP), which is similar to 40EIMSF except for the absence of HRP, were fabricated. Figure 6-3 represents scanning electron micrographs of 0EIMSF, 20EIMSF and 40EIMSF samples. To obtain uniform and more homogeneous fiber mats, the electrospinning voltage (20 kV) and the distance between the tip of the electrospinning syringe and the metal collector (20 cm) were kept constant.

As the amount of glucose in the spinning solution was increased from 0 to 40 wt%, the viscosity of the spinning solution increased from 20 to 80 cP and the diameter of the electrospun fibers decreased (Table 6-1 and Figure 6-3). The effect of wt% of glucose on the diameter of the fibers can be explained by evaluating the viscosity and molecular weight of the components present in the spinning solution. The molecular weight of the hydrolyzed TEOS sol in the spinning solution is very low and thus, droplets rather than fibers are formed when spun in its pure form.<sup>38-40</sup> With the addition of glucose and PVA polymer and further increase in the wt% of glucose in the solution, the viscosity of the solution increases to a critical value required for spinning fibers.<sup>41,42</sup> Further, a higher amount of entanglement of glucose molecules with each other as well as with PVA and hydrolyzed TEOS is predicted. All the fibers, which were spun for this study, were white flexible mats, and the individual fibers were smooth and devoid of beads and other deformities as seen in Figure 6-3.

#### **6.4.2 Infrared Spectroscopy (FT-IR) and Thermogravimetric Analysis (TGA)**

As stated in the previous section, the wt% of glucose added in the fibers was varied from 0 to 40 wt%. This increase in glucose template increased the surface area and porosity of the samples. To evaluate the porosity of the enzyme encapsulated mesoporous nanofibers, the fibers had to be first washed with buffer solution to extract out the glucose template from the fibers. FT-IR was used to monitor the complete extraction of glucose and PVA polymer from the fibers. The infrared spectra of 0, 20 and 40EIMSF before glucose extraction and 40EIMSF sample after glucose extraction are represented in Figure 6-4. All fiber samples exhibited major absorption bands associated with silica network, e.g., Si-O-Si vibrational modes at  $\sim 460$ , 790, 1080, and  $1220\text{ cm}^{-1}$ , along with

Si-OH asymmetrical stretching at  $\sim 960\text{ cm}^{-1}$  and SiO-H stretching at  $3400\text{ cm}^{-1}$ .<sup>43</sup> The intensity of the band at  $\sim 2940\text{ cm}^{-1}$  for C-H stretch of the glucose component in fibers increased slightly with glucose concentration (from 20 to 40EIMSF). This band disappeared after water extraction (washed 40EIMSF), indicating complete removal of the templates from the samples.<sup>13,16</sup> The peaks for PVA, in the as-spun fiber samples are not clearly visible. This is due to the trace amount of PVA in the fibers, as well as the overlapping of PVA and silica (O-H) peaks.

The wt% of glucose, PVA and silica in the as-spun nanofibers and the template-extracted nanofibers, can be further evaluated using the TGA analysis (Figure 6-5a). Fiber samples of 20 mg were heated in air from 60 to 800 °C in a platinum pan using the TGA instrument. The derivative TGA graphs (Figure 6-5b), show the maximum degradation temperatures for the fiber samples. Pure PVA polymer fibers when subjected to heat treatment showed complete degradation in the range of 260 to 560 °C. Glucose also degraded completely at about 600 °C. Silica (SiO<sub>2</sub>) is the only component that remains at temperatures above 800 °C. The SiO<sub>2</sub> content of fiber samples found from TGA measurements were close to the calculated values based on the compositions of the initial feed materials used during electrospinning (Table 6-1). The graphs for template-extracted fiber samples did not show any degradation peaks for glucose and PVA, suggesting complete extraction of the templates.

#### **6.4.3 Factors Affecting the Mesoporosity of the Electrospun Nanofibers**

The surface area and pore structures of the fibers were characterized using nitrogen adsorption-desorption at -196 °C. Glucose and trace amounts of PVA were extracted out of the fibers under ambient conditions to produce porous fibers, as stated

previously. The porosity and surface area of the fibers was seen to increase with increase in glucose concentration (0EIMSF, 20EIMSF and 40EIMSF). The N<sub>2</sub> adsorption-desorption isotherms of the resultant fibers, transformed gradually from reversible Type I to Type IV H2 hysteresis, indicating the transition of the porous structures in fibers, from micro to mesopores (Figure 6-6a). The presence of the H2 hysteresis loop is typical of the mesoporous silica materials prepared via the neutral nonsurfactant templating pathway as stated by Wei et al.<sup>13,33</sup> The mesopores formed in the fibers are similar to the interconnected porous networks seen in glucose-templated mesoporous silica materials previously developed in our laboratory by Dong et al.<sup>44,45</sup> The pore size distributions (PSD) were obtained by plotting differential volume against pore size, obtained from the desorption branches of the N<sub>2</sub> adsorption-desorption isotherms according to Barrett-Joyner-Halenda (BJH)<sup>45</sup> (Figure 6-6b). The diameter of the porous structures in the fibers generally increased with increasing concentration of glucose.<sup>31</sup> The non-templated HRP-containing fibers were microporous, having very small pore volume and pore size (Figure 6-6b and Table 6-1). Fibers synthesized using 40 wt% glucose (40EIMSF; Table 6-1) were mesoporous with a specific surface area of  $\sim 500 \text{ m}^2 \text{ g}^{-1}$ , pore volume of  $\sim 0.2 \text{ cm}^3 \text{ g}^{-1}$  and BET average pore diameter of  $\sim 38 \text{ \AA}$ . Moreover, control sample 40EIMSF2, which is the same as 40EIMSF with differences only in average diameter of the fibers, showed similar surface area and porosity. The surface area and porosity of the control samples 40EIMSF(NoPVA) and 40EIMSF(NoHRP) also showed similar pore parameters as that of 40EIMSF, suggesting that PVA and HRP do not influence the surface area and porosity of the fibers. When high concentrations of the template were employed



(20EIMSF to 40EIMSF), however, the template determined the final porous structures of the fiber materials.<sup>46</sup>

Both the pore-forming template (e.g., glucose) and HRP macromolecules are predicted to act as templates directing the formation of the silica cage or network. The interactions between the growing intermediate silicates and the templates include principally, hydrogen bonding and Vander Waals forces, plus possible electrostatic interaction with the charged groups on the protein surface. When both low molecular weight neutral template and enzyme are mixed into the spinning solution, the neutral template molecules not only direct the mesopore formation around their aggregates or assembly of the aggregates,<sup>47</sup> but also join the protein molecules in forming the same pores or cages in which the biomolecules reside. The co-existence of the enzyme and the template in the same cavities provided the enzyme molecules with ample space upon removing the template. The enzymes tend to uncoil or relax a little inside the pores, which further prevents enzyme leakage during template extraction. In addition, the free space around HRP was needed for the conformational changes during the enzyme-catalyzed reactions. Thus, enzyme molecules entrapped in larger pores have greater mobility (40EIMSF) than those in smaller pores (20EIMSF). The enzymes in smaller pores thus would have stronger interaction with the inner walls of the pores. In brief, adding templates in the synthesis rendered fibers with large pore diameters, resulting in easy mass transport of reactants and products through the matrix and ample free space around the encaged enzyme for conformational change. It is noted that all the HRP-containing fibers were prepared under the same conditions except for the varying amounts of glucose added in the fibers, which was completely extracted out, before the

activity assay. In many aspects, the neutral nonsurfactant templating pathway to mesoporous host sol-gel materials is advantageous over conventional sol-gel processes (which does not employ templates and hence, gives nonporous materials) for immobilizing enzymes and other biological substances. It also restricts any long-range migration of the protein macromolecules through the matrix and thus prevents their aggregation. Moreover, the matrix protects the trapped enzyme from any attack of proteases or bacteria from outside the matrix.

Transmission electron microscopy was also employed to study the internal porous structure of the fiber samples. Worm like interconnected porous structure was noticed in the TEM cross-sections (Figure 6-7), similar to the results obtained by Wei et al.,<sup>13</sup> in nonsurfactant templated sol-gel silica powders.<sup>13,33</sup> The pores thus formed open to the outside via the surface of the fibers. This helps increase the catalytic properties of the fiber samples. Not only are the encapsulated enzymes protected from the external atmosphere, they are also well connected to the outside, thus maintaining high surface area and catalytic activity.

#### **6.4.4 Factors Affecting the HRP Activity**

Enzymes in general are extremely sensitive to changes in temperature, chemicals, pH, etc. Enzymes cannot be utilized in catalytic or sensor applications in their free form. There has been extensive research done on finding ways to protect the enzyme without decreasing its catalytic efficiency. Some of the factors that affect the activity of encapsulated HRP are 1) method of sample preparation, 2) porosity of the EIMSF, 3) the concentration of H<sub>2</sub>O<sub>2</sub> used to test the enzyme activity of HRP, 4) the pH of the solution used to test the activity of HRP and 5) the effect of temperature on the activity of HRP.

One of the main advantages of using electrospinning to synthesize enzyme immobilized sol-gel fibers is the short exposure time of enzymes to harmful solvents. The time taken for the electrospinning solution to form fibers is very short; any buffer solution, water or methanol present in the spinning solution is evaporated out during the flight of the solution between the syringe and the collecting plate to obtain dry fibers. On the other hand, conventional synthesis of enzyme immobilized sol-gel material takes an average 20 to 25 days to obtain completely dry samples.<sup>34</sup> This causes an increased exposure of enzymes to harmful solvents, hence decreased enzyme activity. It has also been well studied that, HRP is most stable at neutral pH and can retain its activity for longer periods if stored below 0 °C.<sup>34</sup> Thus, during preparation of electrospinning solution, the hydrolyzed silica/glucose/PVA solution is maintained at near-neutral pH with temperatures close to 0 °C. The HRP enzyme when added to the spinning solution is protected from fluctuations in the pH by mixing it with a neutral buffer before addition. The spinning solution is immediately electrospun into fibers, thus decreasing the time of exposure of HRP to harmful solvents, such as methanol, that is present in the spinning solution.

#### **6.4.4.1 Effect of H<sub>2</sub>O<sub>2</sub> Concentration on the HRP Activity**

Figures 6-8a and 6-8b represent the dose response plots (specific activity ( $V_i$ ) Vs [H<sub>2</sub>O<sub>2</sub>]) of apparent catalytic activity of free and encapsulated enzyme fibers at room temperature, with a constant pH of 6.5 and varying H<sub>2</sub>O<sub>2</sub> concentrations of 0.1 to 10 mM. The initial activity of free HRP increased rapidly with [H<sub>2</sub>O<sub>2</sub>] until it reached a maximum at [H<sub>2</sub>O<sub>2</sub>] = 1.0 mM, it then decreased slightly as the [H<sub>2</sub>O<sub>2</sub>] increased further. The slight decrease in activity with increase in [H<sub>2</sub>O<sub>2</sub>] is due to the “inhibition effect,” which is well

known in the case of free HRP.<sup>48</sup> Similar to the free enzyme, the apparent catalytic activity of immobilized HRP was seen to depend on the concentration of H<sub>2</sub>O<sub>2</sub> in the assay solution. For immobilized HRP, the apparent activity also increased with [H<sub>2</sub>O<sub>2</sub>] until it reached a maximum at [H<sub>2</sub>O<sub>2</sub>] = 2.0 mM and then decreased slightly at higher [H<sub>2</sub>O<sub>2</sub>] (Figure 6-8b). The activity change with [H<sub>2</sub>O<sub>2</sub>] of the immobilized samples however, was not as drastic as that seen in free enzyme. The HRP activity showed strong dependence on the concentration of glucose in EIMSF. The samples synthesized in the absence of the template showed low enzyme activity at all [H<sub>2</sub>O<sub>2</sub>] and needed higher [H<sub>2</sub>O<sub>2</sub>] to reach maximum activities. Overall, with increasing concentration of glucose from 0 to 40 wt% in EIMSF, the kinetic behavior of the entrapped HRP moved closer to that of the free HRP in solution. Their corresponding Lineweaver-Burk plots, from which the kinetic parameters are derived, also displayed good linearity over a wider range of [H<sub>2</sub>O<sub>2</sub>] (Figure 6-8c).

The Michaelis-Menten equation, originally developed for the homogeneous system, has often been used to characterize the catalytic properties of immobilized enzymes in heterogeneous systems. The apparent Michaelis constant ( $K_m$ ) and maximal velocity ( $V_m$ ) for free and immobilized HRP were calculated using the initial activity data according to the Lineweaver-Burk plots (Figures 6-8c) and summarized in Table 6-1. The  $K_m$  and  $V_m$  values were derived from the experimental data at lower concentrations of H<sub>2</sub>O<sub>2</sub> by using linear regression with correlation coefficients of  $R^2 > 0.99$ . The  $K_m$  values revealed that fiber-entrapped HRP needed higher [H<sub>2</sub>O<sub>2</sub>] at 2 mM to reach the maximal activity than the free enzyme, which required 1 mM. Compared to free HRP, the lowered apparent activities of the entrapped enzyme were attributed to deactivation, diffusion

limitations, steric hindrance, or lowered accessibility associated with sol-gel immobilization.<sup>49</sup>

A few factors may account for the differences in substrate dose-response behavior between free and immobilized HRP. Most probably, the concentration of  $\text{H}_2\text{O}_2$ , as well as other reactive species participating in the enzymatic reactions within the fiber matrix, is significantly lower than that in the bulk solution due to internal diffusion limitations within the fiber matrix. Although the inhibition effect was also evident at higher  $[\text{H}_2\text{O}_2]$ , the decrease of HRP activity with increasing  $[\text{H}_2\text{O}_2]$  was slower for the immobilized sample than for the free enzyme. Previous studies indicated that the movement of relatively small molecules within the silica sol-gel matrix was slightly retarded.<sup>50,51</sup> Another possibility is that the conformational change and kinetics of the caged protein molecules in a constrained microenvironment are deviated from that of the native protein in solution,<sup>52</sup> due to possible interactions of the protein molecules with the surrounding matrix pore walls.<sup>53</sup> It should be pointed out here that the determination of the rate of formation of the colored product, quinoneimine, is slightly more complicated in encapsulated samples than with free enzymes, as the time for the substrates to enter the pores, interact with the enzymes and then release out of the fibers as products, e.g., quinoneimine, is slow.<sup>54</sup> Thus, quantitative and accurate estimation of the intrinsic activity of the immobilized HRP is very difficult, if not impossible. Nevertheless, the kinetic data still clearly displayed the dependence of the HRP activity on  $[\text{H}_2\text{O}_2]$ .

#### **6.4.4.2 Effect of Porosity on the HRP Activity**

The apparent activities of the immobilized HRP samples were closely related to the pore structures of the silica matrix, which in turn are adjustable by the content of

glucose as stated previously. The Michaelis-Menton plots of HRP-catalyzed reactions are shown in Figure 6-8c. The control sample 0EIMSF prepared in the absence of glucose exhibited extremely low activity, while the HRP-containing fibers synthesized in the presence of 20 and 40 wt% glucose (20EIMSF and 40EIMSF) exhibited drastically improved activities, up to three orders of magnitude greater than that of non-templated control (0EIMSF). The initial activity of immobilized HRP increased with increasing concentration of glucose. Under the assay conditions employed, the apparent activity of the sample 40EIMSF was  $200 \text{ unit mg}^{-1} \text{ min}^{-1}$  at  $[\text{H}_2\text{O}_2] = 2.0 \text{ mM}$ . It should be pointed out that the results reported here are to serve as an example to demonstrate the advantages of the templated bioencapsulation preparations over conventional non-templated sol-gel immobilization. Apparently, the average diameter of the EIMSF and the addition of PVA in the fibers during electrospinning do not affect the catalytic activity drastically (as seen in 40EIMSF, 40EIMSF2 and 40EIMSF/NoPVA in Table 6-1).

#### **6.4.4.3 Effect of pH on the HRP Activity**

Free HRP and EIMSF samples were examined for activity dependence on the pH in the range of 4.5 to 9 at room temperature and a constant  $[\text{H}_2\text{O}_2] = 2 \text{ mM}$ . Free HRP also was studied for comparison. Figures 6-9a and 6-9b show the change of the apparent activities with pH, along with a representation after normalization for clarity (Figure 6-9c). Free HRP had highest activity at an optimum of pH 6-7.5, which was in good agreement with the literature value of pH 6-7.<sup>55</sup> The immobilized samples vary to some extent from free enzymes as they show better pH stability and have a broader range of optimum pH from 6-9. They maintained relatively high activities over a wide pH range.

Below pH 6 however, their activities dropped as the pH decreased, similar to that seen in free enzymes. In previous research, it has been seen that with respect to free enzymes, sol-gel-immobilized enzymes often exhibit different optimal pH and pH activity profiles.<sup>2,56</sup> This could be due to a combination of a few factors, such as the degree of interactions between the guest enzyme molecules and the host sol-gel matrix. It also could be that the possible pH profile near the encaged HRP is different from the pH of the buffered assay solution as seen in the effect of  $[H_2O_2]$ . These observations were in agreement with previous work using a series of acid-base indicators to probe the local pH inside sol-gel materials. It was indicated that the pH in the pore could be up to one pH unit lower than that in the aqueous buffer solution.<sup>18</sup>

#### **6.4.5 Thermal Stability of Encapsulated HRP Enzymes**

Thermal stability of free and immobilized HRP fiber samples were studied by subjecting the samples to varying temperatures from 25 to 80 °C for 30 min. In a typical procedure, approximately 3 mL of 0.5 mg/mL of HRP/buffer solution was taken in a test tube, and heated to 80 °C for 30 min in a water bath. The test tube was then cooled to room temperature and after 20 min; the solution was tested for catalytic activity using similar method as stated previously. A similar procedure was used to test the activity of EIMSF. Approximately 5 mg of fibers (containing 0.5 mg of enzyme) were first washed in buffer to extract out the template. The fibers were then centrifuged out, immersed in fresh buffer solution, heat-treated in a water bath to the desired temperature, centrifuged again, re-suspended in fresh buffer solution and then tested for enzyme activity. The free enzymes showed a drastic drop in activity (Figure 6- 10) from 100% at 25 °C to only 10% its original value at 80 °C. On the other hand, enzyme immobilized fibers showed

retention of its original activity and a slow drop in activity with increase in temperature. Another interesting point to note was that, as the temperature was increased from 25 to 60 °C, the activity actually shot up above its original 100% value as seen in Figure 6-10. This phenomenon was also seen previously in enzymes immobilized in other sol-gel materials, which could be due to the better interaction of enzymes with the substrate.<sup>57</sup>

When comparing the activity of 0, 20 and 40EIMSF, nonporous fibers (0EIMSF) showed better stability compared to 20 and 40EIMSF. In general, a remarkably improved thermal stability of fiber-immobilized HRP may be the result of reduced deactivating or denaturing thermal motion of the protein molecules in the restrained host cages during the thermal treatment.<sup>37</sup> The restricting local environment helps the protein molecules maintain an active state when subjected to higher temperatures.<sup>58</sup>

#### **6.4.6 Enzyme Leakage and Reusability of EIMSF**

The enzymatic activity test of the wash solutions (solution used to extract out the templates from the fibers) gives the efficiency of encapsulation or the relative amount of unbound, loosely trapped, leached, or surface-absorbed HRP in fibers. The wash solutions were obtained from washing the as-synthesized 0, 20 and 40EIMSF with sodium phosphate buffer and collected by centrifugation to separate out the washed fibers. The washed solution thus obtained was tested for activity using the same procedure explained previously for free-enzymes. The results showed that there was no enzymatic activity in the wash solutions. This proved the complete entrapment of HRP in the porous fibers, including fibers containing 40% of glucose and having relatively large surface area and pore diameters (Table 6-1). Furthermore, complete entrapment of HRP within porous fibers, instead of surface adsorption, was supported by the observations



that no enzyme activity was found in the assay solution, once it was separated from HRP-containing fibers at the end of the assay. It is important to ensure that no dissolved or free enzyme is present in the assay system, while evaluating an immobilized enzyme activity; otherwise, the dissolved enzyme will give higher but false remaining activity. The results of enzyme leaching tests demonstrated that the templated sol-gel bio-encapsulation led to complete encapsulation of HRP in porous fibers without enzyme leakage. The relatively small template molecules were readily removed from the composite fibers by water extraction. The protein macromolecules could not diffuse out of the porous matrix, however, even though both the enzyme and the template were physically entrapped in the pores of the sol-gel materials without forming primary bonding with the sol-gel network. The entrapped HRP has a Stokes diameter of  $60.6 \text{ \AA}$ ,<sup>34</sup> which is larger than the pore diameter of the hybrid matrix. During the template extraction, the protein molecules tend to relax or unfold partially, causing the enzymes to be lodged inside the pores.

Another important test was to study the reusability of the enzyme-immobilized fibers (Figure 6-11). Even though enzymes and proteins have excellent catalytic and sensor properties with several potential applications, utilizing these enzymes in large scale is extremely expensive. Hence, immobilizing the enzymes and reusing these enzymes is of utmost importance. Free enzymes do not have a good potential capability of being used in catalytic applications. The EIMSF mats electrospun in this study have a very high potential of being used in biosensor applications, because of their flexible, sensitive and reusable capability. These fibers were tested for reusability by testing the enzyme activity of the same fiber sample 5 times, by washing the fiber samples with buffer solution every time an activity test was completed. The retention of activity in the

fifth cycle was found to be up to 90% of the activity in the first cycle, for all of the immobilized fiber samples as seen in Figure 6-11.

## 6.5 Conclusion

In conclusion, for the first time, mesoporous silica based nanofibers have been fabricated and employed as a matrix for the immobilization of enzymes via a simple electrospinning method. The drastically improved features and versatility of this technique represent a huge step towards the biosensor and biocatalytic applications. The HRP-containing fibers have excellent thermal stability and high apparent catalytic activity, over a wide range of pH. The apparent activity of entrapped HRP was closely associated with the concentration of glucose in as-spun fibers. The mesoporous silica fibers, with pore parameters tunable by adding varied amounts of glucose, not only effectively retained the enzyme without leaching, but also controlled the mass transfer of the reactants into and products out of the matrix. The enzyme-immobilized samples produced by electrospinning took just a few minutes to dry compared to 20 days of tedious drying procedure, which is required for conventional enzyme immobilized sol-gel materials. As a result, HRP immobilized in templated mesoporous fibers showed significant enhancement of the apparent activity, which was three orders of magnitude greater than that of the non-templated, conventional microporous silica materials synthesized without adding the template (Table 6-1) and two orders of activity greater than HRP-immobilized silica powders.<sup>57</sup> Finally, due to the nanometer dimensions, silica fiber mats were quite flexible, unlike sol-gel silica in the form of small discs, films or powders, thus contributing further towards the biocatalytic applications.

## 6.6 Reference List

1. Arnold, M. Advances in biosensors. volume 3. biosensors: A russian perspective. *Journal of the American Chemical Society*, 119, 255. 1997.
2. Braun, S., Shtelzer, S., Rappoport, S., Avnir, D., Ottolenghi, M. Biocatalysis by sol-gel entrapped enzymes. *Journal of Non-Crystalline Solids*, 147, 739-743. 1992.
3. Shriver-Lake, L. C., Breslin, K. A., Charles, P. T., Conrad, D. W., Golden, J. P., Ligler, F. S. Detection of TNT in water using an evanescent wave fiber-optic biosensor. *Analytical Chemistry*, 67, 2431-2435. 1995.
4. Al-Shehri, H., Smith, D. J., Hansen, L. M., Reneker, D. Preservation of enzymes in electrospun nanofibers. *Technical Papers - American Chemical Society, Rubber Division, Spring Technical Meeting, 163rd, San Francisco, CA, United States*, 670-698. 2003.
5. Sawicka, K., Gouma, P., Simon, S. Electrospun biocomposite nanofibers for urea biosensing. *Sensors and Actuators, B: Chemical* B108(1-2), 585-588. 2005.
6. Bornscheuer, U. T. Immobilizing enzymes: How to create more suitable biocatalysts. *Angewandte Chemie, International Edition*, 42, 3336-3337. 2003.
7. Avnir, D., Braun, S., Lev, O., Ottolenghi, M. Enzymes and other proteins entrapped in sol-gel materials. *Chemistry of Materials*, 6, 1605-1614. 1994.
8. Dave, B. C., Dunn, B., Valentine, J. S., Zink, J. I. Sol-gel encapsulation methods for biosensors. *Analytical Chemistry*, 66, 1120A-1127A. 1994.
9. Wang, Y., Caruso, F. Mesoporous silica spheres as supports for enzyme immobilization and encapsulation. *Chemistry of Materials*, 17, 953-961. 2005.
10. Gill, I., Ballesteros, A. Encapsulation of biologicals within silicate, siloxane, and hybrid sol-gel polymers: An efficient and generic approach. *Journal of the American Chemical Society*, 120, 8587-8598. 1998.
11. Wei, L., Cui, L. Progress of sol-gel application in biosensors. *Huaxue Chuanganqi*, 23, 1-7. 2003.
12. Gimon-Kinsel, M. E., Jimenez, V. L., Washmon, L., Balkus, J., Jr. Mesoporous molecular sieve immobilized enzymes. *Studies in Surface Science and Catalysis*, 117, 373-380. 1998.
13. Wei, Y., Xu, J., Dong, H., Dong, J. H., Qiu, K., Jansen-Varnum, S. A. Preparation and physisorption characterization of glucose-templated mesoporous silica sol-gel materials. *Chemistry of Materials*, 11, 2023-2029. 1999.
14. Xu, J., Dong, H., Feng, Q., Wei, Y. Use of poly(ethylene oxide) nonionic surfactants as template for enzyme-containing mesoporous sol-gel materials. *Abstracts of Papers, 220th ACS National Meeting, Washington, DC, United States*, OLY-294. 2000.
15. Wei, Y., Feng, Q., Xu, J., Dong, H., Qiu, K. Y., Jansen, S. A., Yin, R., Ong, K. K. Polymethacrylate-silica hybrid nanoporous materials: A bridge between inorganic and polymeric molecular sieves. *Advanced Materials (Weinheim, Germany)*, 12, 1448-1450. 2000.

16. Wei, Y., Dong, H., Xu, J., Feng, Q. Simultaneous immobilization of horseradish peroxidase and glucose oxidase in mesoporous sol-gel host materials. *ChemPhysChem*, 3, 802-808. 2002.
17. Huang, S., Jiang, Z., Wu, H., Xu, S. Problems and solutions of enzyme encapsulation through sol- gel process. *Gaofenzi Tongbao*, 28-35. 2003.
18. Dunn, B., Zink, J. I. Probes of pore environment and molecule-matrix interactions in sol-gel materials. *Chemistry of Materials*, 9, 2280-2291. 1997.
19. Kenawy, E. R., Bowlin, G. L., Mansfield, K., Layman, J., Simpson, D. G., Sanders, E. H., Wnek, G. E. Release of tetracycline hydrochloride from electrospun poly(ethylene-co-vinylacetate), poly(lactic acid), and a blend. *Journal of Controlled Release*, 81, 57-64. 2002.
20. Wang, X. W., Hu, Z. M., Pan, W. L., Liu, Z. F. Electrospun polymer nanofibers. *Donghua Daxue Xuebao, Ziran Kexueban*, 31, 115-119. 2005.
21. Lee, S. W., Belcher, A. M. Virus-based fabrication of micro- and nanofibers using electrospinning. *Nano Letters*, 4(3), 387-390. 2004.
22. Li, D., Wang, Y., Xia, Y. Electrospinning of polymeric and ceramic nanofibers as uniaxially aligned arrays. *Nano Letters*, 3(8), 1167-1171. 2003.
23. Jia, H., Zhu, G., Vugrinovich, B., Kataphinan, W., Reneker, D. H., Wang, P. Enzyme-carrying polymeric nanofibers prepared via electrospinning for use as unique biocatalysts. *Biotechnology Progress*, 18(5), 1027-1032. 2002.
24. Hsieh, Y. L., Wang, Y., Chen, H. Amphiphilic surface grafts for enzyme binding on ultra-high specific surface fibers. *Polymer Preprints (American Chemical Society, Division of Polymer Chemistry)*, 44(2), 565-566. 2003.
25. Al-Sheheri, H. A. The use of electrospinning technology in enzymes preservation and chemical warfare protective clothing applications. University of Akron, Akron, OH, USA, Ph.D. Dissertation, 128. 2003.
26. Herricks, T. E., Kim, S. H., Kim, J., Li, D., Kwak, J. H., Grate, J. W., Kim, S. H., Xia, Y. Direct fabrication of enzyme-carrying polymer nanofibers by electrospinning. *Journal of Materials Chemistry*, 15(31), 3241-3245. 2005.
27. Wu, L., Yuan, X., Sheng, J. Immobilization of cellulase in nanofibrous PVA membranes by electrospinning. *Journal of Membrane Science*, 250(1-2), 167-173. 2005.
28. Xie, J., Hsieh, Y. L. Ultra-high surface fibrous membranes from electrospinning of natural proteins: casein and lipase enzyme. *Journal of Materials Science*, 38(10), 2125-2133. 2003.
29. Zeng, J., Chen, X., Liang, Q., Xu, X., Jing, X. Enzymatic degradation of poly(L-lactide) and poly( $\epsilon$ -caprolactone) electrospun fibers. *Macromolecular Bioscience* 4(12), 1118-1125. 2004.
30. Zeng, J., Aigner, A., Czubyko, F., Kissel, T., Wendorff, J. H., Greiner, A. Poly(vinyl alcohol) nanofibers by electrospinning as a protein delivery system and the retardation of enzyme release by additional polymer coatings. *Biomacromolecules*, 6(3), 1484-1488. 2005.
31. Wei, Y., Xu, J., Feng, Q., Lin, M., Dong, H., Zhang, W. J., Wang, C. A novel method for enzyme immobilization: direct encapsulation of acid phosphatase in nanoporous silica host materials. *Journal of nanoscience and nanotechnology*, 1, 83-93. 2001.

32. Doshi, J., Reneker, D. H. Electrospinning process and applications of electrospun fibers. *Journal of Electrostatics*, 35, 151-160. 1995.
33. Wei, Y., Jin, D. L., Ding, T. Z., Shih, W. H., Liu, X. H., Cheng, S. Z. D., Fu, Q. A non-surfactant templating route to mesoporous silica materials. *Advanced Materials (Weinheim, Germany)*, 10, 313-316. 1998.
34. Gemeiner, P. *Enzyme engineering: immobilized biosystems*. E.Harwood, New York. 1992.
35. Yamanaka, S. A., Nishida, F., Ellerby, L. M., Nishida, C. R., Dunn, B., Valentine, J. S., Zink, J. I. Enzymatic activity of glucose oxidase encapsulated in transparent glass by the sol-gel method. *Chemistry of Materials*, 4, 495-497. 1992.
36. Navas Diaz, A., Ramos Peinado, M. C., Torijas Minguez, M. C. Sol-gel horseradish peroxidase biosensor for hydrogen peroxide detection by chemiluminescence. *Analytica Chimica Acta*, 363(2-3), 221-227. 1998.
37. Li, J., Tan, S. N., Oh, J. T. Silica sol-gel immobilized amperometric enzyme electrode for peroxide determination in the organic phase. *Journal of Electroanalytical Chemistry*, 448(1), 69-77. 1998.
38. Casper, C. L., Stephens, J. S., Tassi, N. G., Chase, D. B., Rabolt, J. F. Controlling surface morphology of electrospun polystyrene fibers: effect of humidity and molecular weight in the electrospinning process. *Macromolecules*, 37(2), 573-578. 2004.
39. Bognitzki, M., Frese, T., Steinhart, M., Greiner, A., Wendorff, J. H., Schaper, A., Hellwig, M. Preparation of fibers with nanoscaled morphologies: electrospinning of polymer blends. *Polymer Engineering and Science*, 41(6), 982-989. 2001.
40. Buer, A., Ugbohue, S. C., Warner, S. B. Electrospinning and properties of some nanofibers. *Textile Research Journal*, 71(4), 323-328. 2001.
41. McKee, M. G., Wilkes, G. L., Colby, R., Long, T. E. Correlations of solution rheology with electrospun fiber formation of linear and branched polyesters. *Macromolecules*, 37(5), 1760-1767. 2004.
42. McKee, M. G., Layman, J. M., Cashion, M. P., Long, T. E. Phospholipid nonwoven electrospun membranes. *Science (Washington, DC, United States)*, 311(5759), 353-355. 2006.
43. Inama, L., Dire, S., Carturan, G., Cavazza, A. Entrapment of viable microorganisms by silicon dioxide sol-gel layers on glass surfaces: trapping, catalytic performance and immobilization durability of *Saccharomyces cerevisiae*. *Journal of Biotechnology*, 30(2), 197-210. 1993.
44. Roux, C., Livage, J., Farhati, K., Monjour, L. Antibody-antigen reactions in porous sol-gel matrixes. *Journal of Sol-Gel Science and Technology*, 8(1/2/3), 663-666. 1997.
45. Zhang, L., Papaefthymiou, G. C., Ziolo, R. F., Ying, J. Y. Novel g-Fe<sub>2</sub>O<sub>3</sub>/SiO<sub>2</sub> magnetic nanocomposites via sol-gel matrix-mediated synthesis. *Nanostructured Materials*, 9(1-8), 185-188. 1997.
46. Xu, J. Immobilization of enzymes in mesostructured materials via the nonsurfactant-templated sol-gel chemistry. Ph.D. Dissertation. Drexel University, Philadelphia. 2000.
47. Wei, Y., Jin, D., Ding, T., Xu, J. Mesoporous materials and methods of making the same. (Drexel University, USA. 99-US1116(9936357), 79. WO. 1999.

48. Baynton, K. J., Bewtra, J. K., Biswas, N., Taylor, K. E. Inactivation of horseradish peroxidase by phenol and hydrogen peroxide: a kinetic investigation. *Biochimica et biophysica acta*, 1206, 272-278. 1994.
49. Choi, Y. J., Chae, H. J., Kim, E. Y. Steady-state oxidation model by horseradish peroxidase for the estimation of the non-inactivation zone in the enzymatic removal of pentachlorophenol. *Journal of Bioscience and Bioengineering*, 88, 368-373. 1999.
50. Koone, N., Shao, Y., Zerda, T. W. Diffusion of simple liquids in porous sol-gel glass. *Journal of Physical Chemistry*, 99(46), 16976-16981. 1995.
51. Shen, C., Kostic, N. M. Kinetics of photoinduced electron-transfer reactions within sol-gel silica glass doped with zinc cytochrome c. study of electrostatic effects in confined liquids. *Journal of the American Chemical Society*, 119(6), 1304-1312. 1997.
52. Shibayama, N., Saigo, S. Kinetics of the allosteric transition in hemoglobin within silicate sol-gels. *Journal of the American Chemical Society*, 121(2), 444-445. 1999.
53. Hench, L. L. *Sol-Gel Silica: Properties, Processing and Technology Transfer*. Noyes publications, Westwood New Jersey, US, 168. 1998.
54. Yamanaka, S. A., Nishida, F., Ellerby, L. M., Nishida, C. R., Dunn, B., Valentine, J. S., Zink, J. I. Enzymatic activity of glucose oxidase encapsulated in transparent glass by the sol-gel method. *Chemistry of Materials*, 4(3), 495-497. 1992.
55. Worthington, V., Zacka, J. A. *Comprehensive manual on enzymes and related biochemicals*. *American biotechnology laboratory*, 12(4), 72. 1994.
56. Braun, S., Rappoport, S., Zusman, R., Avnir, D., Ottolenghi, M. Biochemically active sol-gel glasses: the trapping of enzymes. *Materials Letters*, 10, 1-5. 1990.
57. Dong, H. *Organic-inorganic hybrid mesoporous silica materials and their application as host matrix for protein molecules*. Ph.D. Dissertation. Drexel University, Philadelphia. 2000.
58. Brinker, J. C., Scherer, W. G. *Sol-gel science: The physics and chemistry of sol-gel processing*. Elsevier Science, California. 1990.

Table 6-1. Material and activity parameters of free and HRP immobilized mesoporous silica fibers (EIMSF).

sample ID <sup>a</sup>	SiO <sub>2</sub> (wt%)		V <sub>m</sub> <sup>d</sup> mg <sup>-1</sup> min <sup>-1</sup>	K <sub>m</sub> <sup>d</sup> mmol L <sup>-1</sup>	TS <sup>e</sup> (%)	S <sub>BET</sub> <sup>f</sup> m <sup>2</sup> g <sup>-1</sup>	V <sub>SP</sub> <sup>g</sup> cm <sup>3</sup> g <sup>-1</sup>	D <sub>BET</sub> <sup>h</sup> Å	Av dia <sup>i</sup> nm
	calcd <sup>b</sup>	expt <sup>c</sup>							
Free HRP	----	----	500	0.65	50	----	----	----	----
0EIMSF	96	92	63	0.3	300	80	0.004	7	500
20EIMSF	76	74	163	0.56	108	224	0.1	26	350
40EIMSF	56	55	227	0.62	97	500	0.2	38	100
40EIMSF2	56	57	210	0.60	95	450	0.3	35	200
40EIMSF (NoPVA)	60	59	220	0.59	90	420	0.2	29	400
40EIMSF (NoHRP)	56	54	----	----	----	490	0.2	35	110

<sup>a</sup>0, 20 & 40EIMSFs are fibers containing 0, 20 and 40 wt% glucose; 96, 76 & 56 wt% silica, constant 4 wt% of PVA, and HRP. Control samples (1) 40EIMSF2 is similar to 40EIMSF except for the average fiber diameters; (2) 40EIMSF (NoPVA) is similar to 40EIMSF except for absence of PVA and (3) 40EIMSF (NoHRP) is similar to 40EIMSF except for absence of HRP. <sup>b</sup>Theoretical value from the composition of the electrospinning mixture. <sup>c</sup>The wt% of silica content in the EIMSF measured experimentally at 800 °C in air using thermogravimetric analysis. <sup>d</sup>V<sub>m</sub> and K<sub>m</sub> values for template-extracted EIMSF were obtained from Lineweaver-Burk plots using initial velocities at [H<sub>2</sub>O<sub>2</sub>] = 0.1-1.0 mM. <sup>e</sup>Remaining activity of HRP encapsulated fibers after heating test tubes of free and fiber immobilized enzymes in phosphate buffer (pH 6.5) at 60 °C for 30 min in a water bath. <sup>f</sup>Specific surface area values for template-extracted fibers, <sup>g</sup>Pore volume obtained at relative P/P<sub>0</sub> ≈ 1 and <sup>h</sup>Pore diameter of the mesopores in the fibers are determined from adsorption-desorption isotherms. <sup>i</sup>Average diameter of EIMSF obtained by measuring about 500 fibers of a single sample from SEM micrographs.

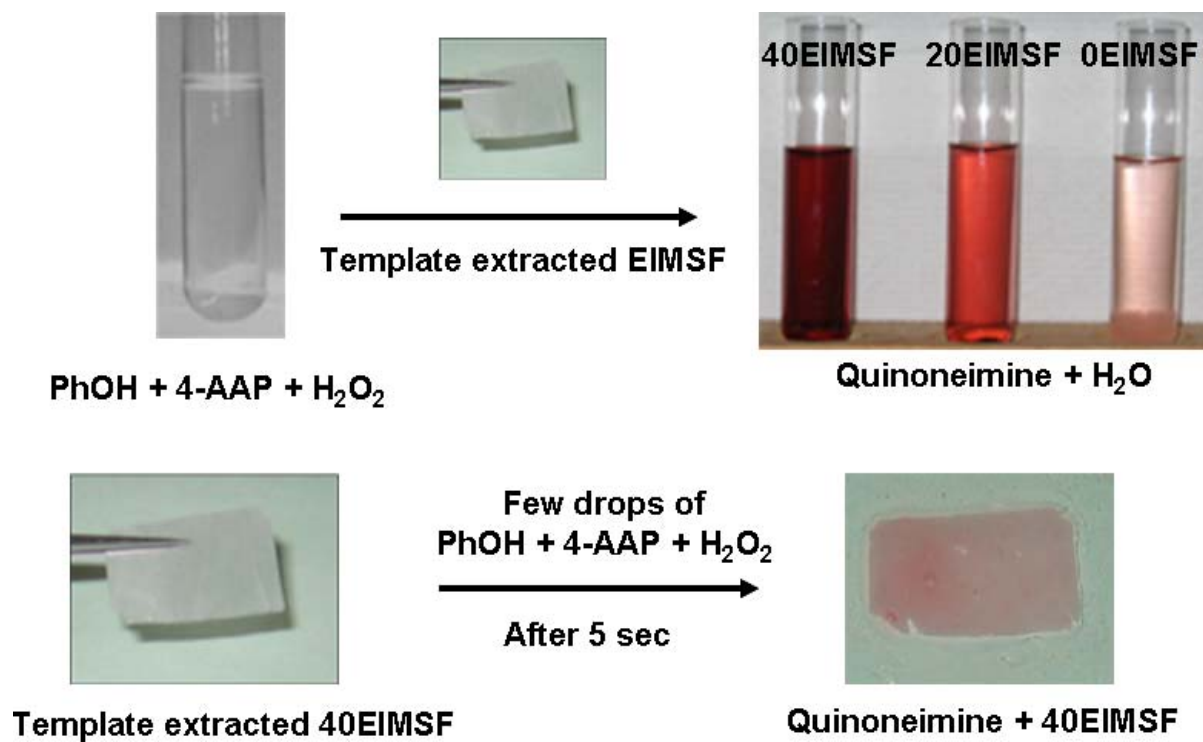


Figure 6-1. Enzyme activity assay of template-extracted EIMSF in colorless reagent mixture [phosphate buffer, phenol (PhOH), 4-aminoantipyrine (4-AAP, colorless dye) and H<sub>2</sub>O<sub>2</sub>]. The enzyme present inside the porous fibers converts H<sub>2</sub>O<sub>2</sub> to water, in the process converting 4-AAP to quinoneimine (red colored dye).



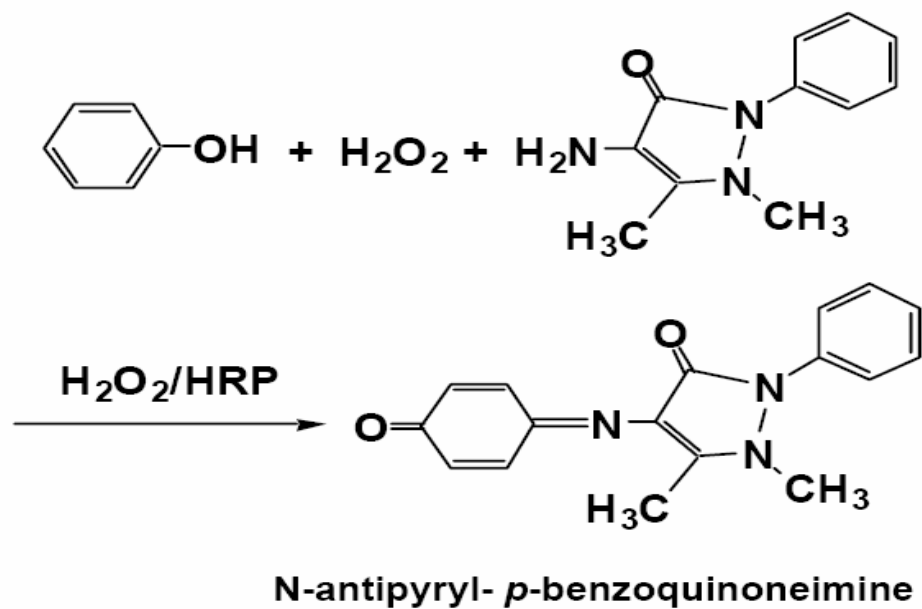


Figure 6-2. Represents the formation of a colored compound, N-antipyryl-*p*-benzoquinoneimine, during the HRP-catalyzed activity assay,  $\lambda_{\text{max}}=510\text{nm}$ .

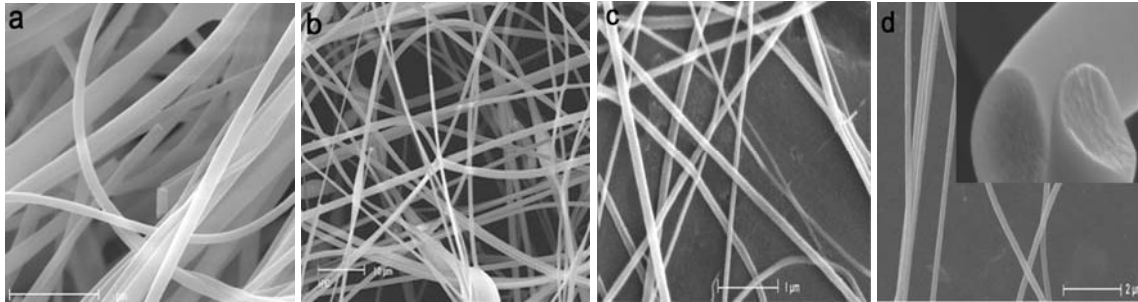


Figure 6-3. Scanning electron micrographs of EIMSF containing, a) 0 wt% glucose (scale bar: 10  $\mu\text{m}$ ); b) 20 wt% glucose (scale bar: 10  $\mu\text{m}$ ) and c) 40 wt% glucose (scale bar: 1  $\mu\text{m}$ ). d) 40 wt% glucose extracted fibers (scale bar: 2  $\mu\text{m}$ ). Inset shows the internal surface morphology of the fibers at macroscopic level.

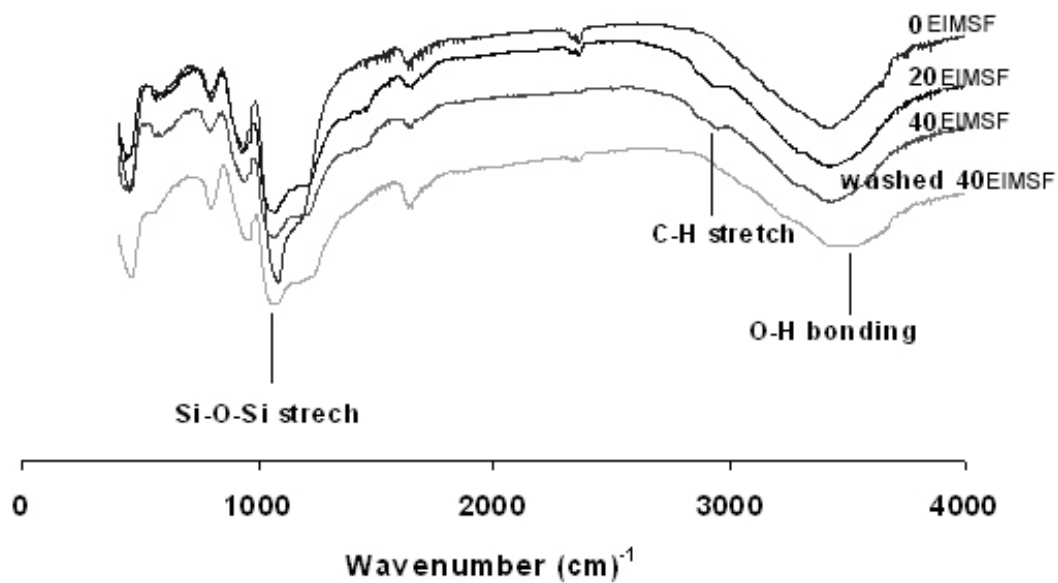


Figure 6-4. Fourier transform infrared spectroscopy (FTIR) of EIMSF containing, a) 0 wt% glucose (0EIMSF); b) 20 wt% glucose (20EIMSF) and c) 40 wt% glucose (40EIMSF). d) 40 wt% glucose extracted fibers (washed 40EIMSF).

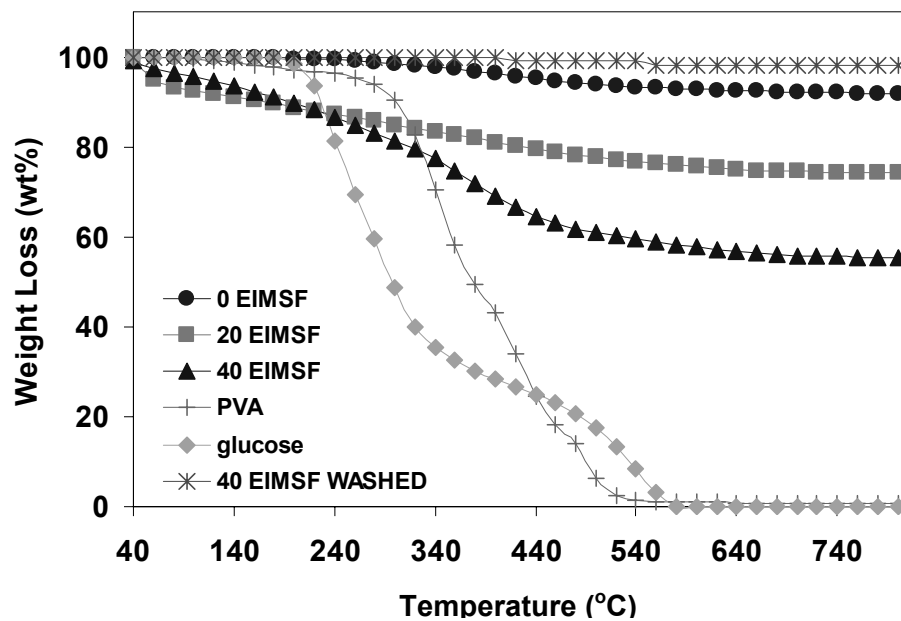


Figure 6-5a. Thermogravimetric analysis (TGA) profile for glucose, PVA, as fabricated EIMSF and template-extracted EIMSF.

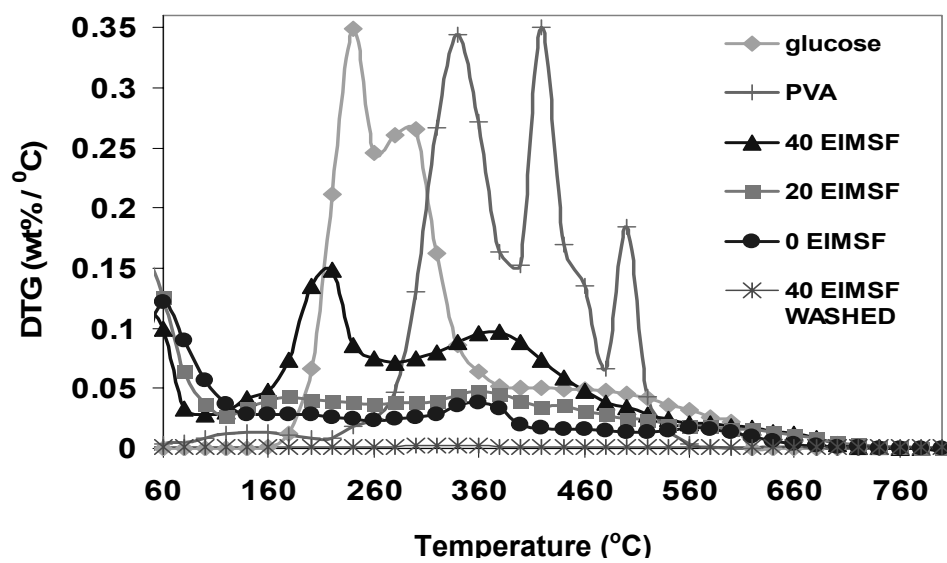


Figure 6-5b. Thermogravimetric analysis (TGA) derivative peaks showing maximum degradation temperature for glucose, PVA, as-fabricated EIMSF and template-extracted EIMSF.

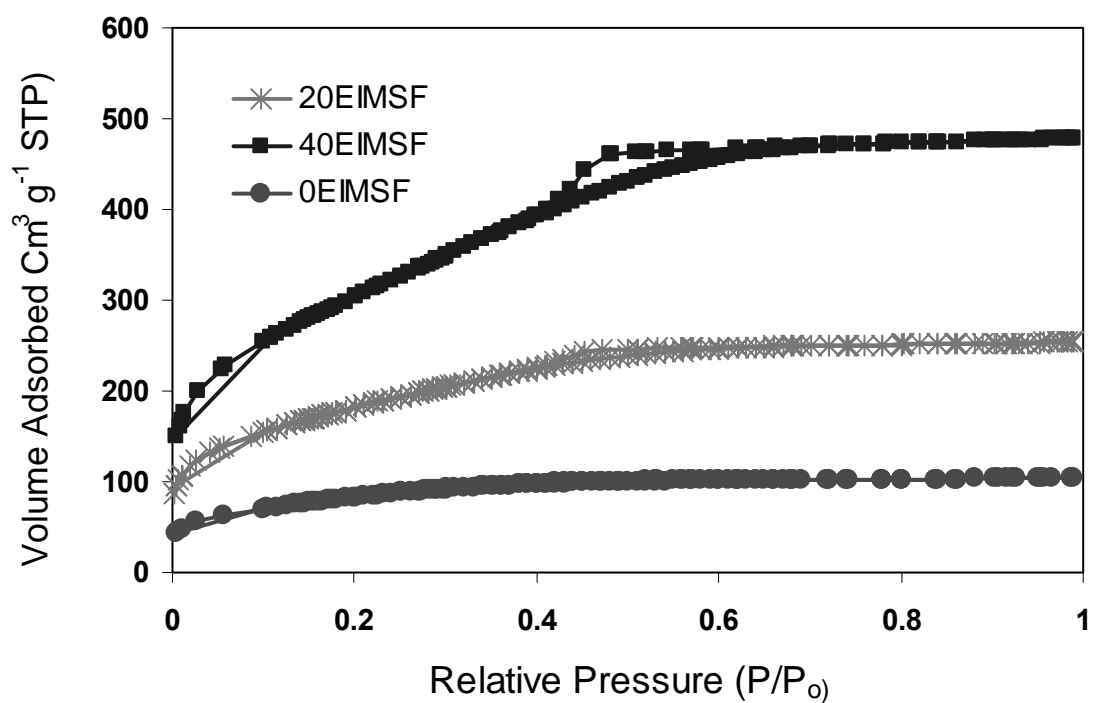


Figure 6-6a.  $\text{N}_2$  adsorption-desorption isotherms at  $-196^\circ\text{C}$  for the porous template-extracted fibers synthesized in the presence of 20 and 40 wt% glucose. Control sample is synthesized without adding the template and enzymes.

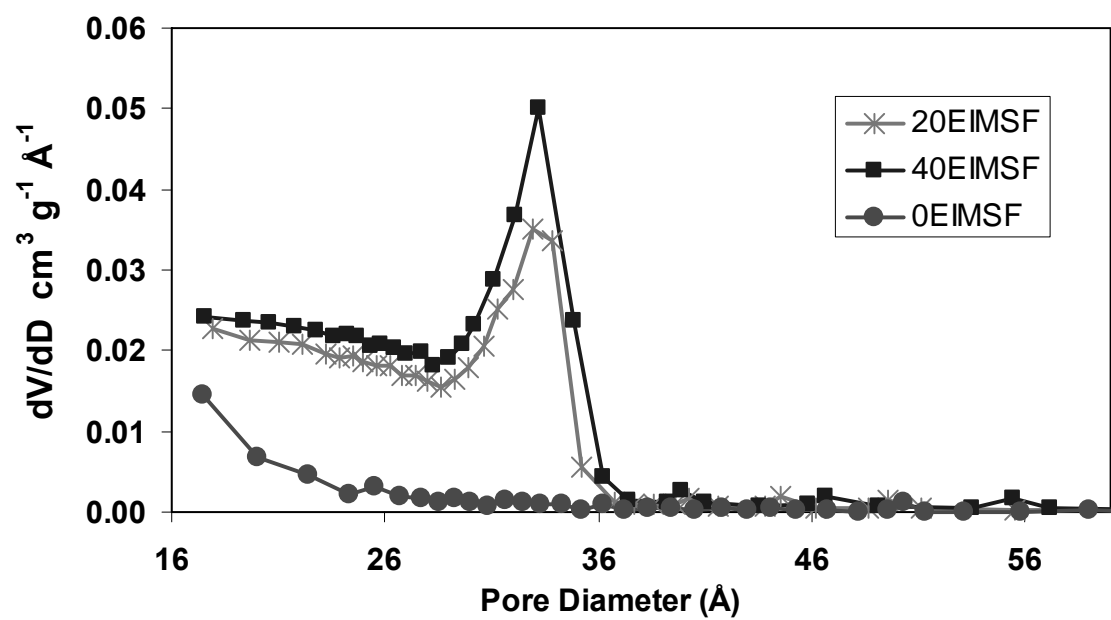


Figure 6-6b. The BJH desorption pore size distributions from the N<sub>2</sub> desorption isotherms for the HRP-containing fiber samples synthesized in the presence of 0-40 wt% glucose.

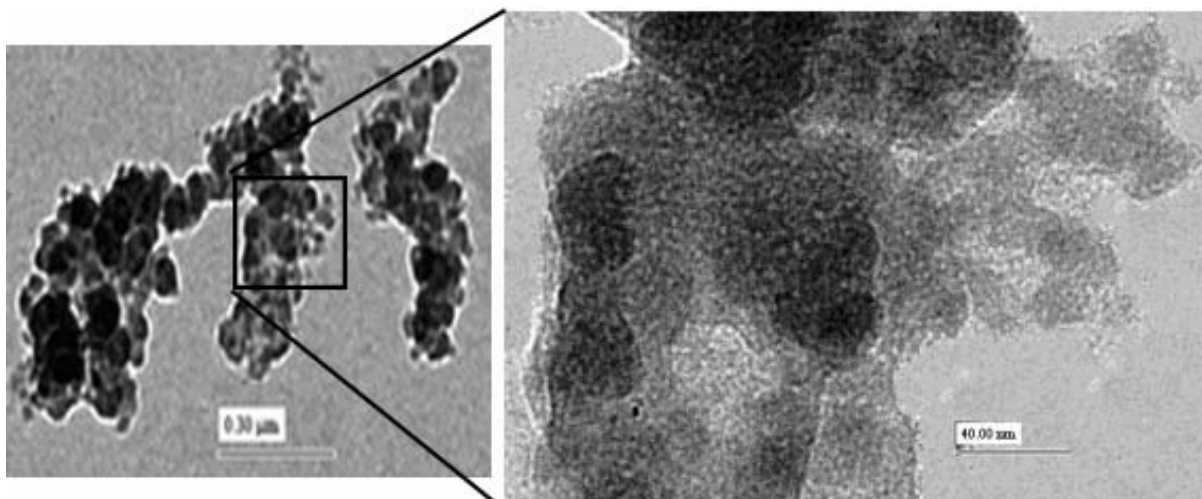


Figure 6-7. Low-resolution transmission electron micrograph (TEM) of a cluster of template-extracted cross-sectioned 40EIMSF, scale bar: 0.30  $\mu\text{m}$ . High resolution TEM of the same, scale bar; 40 nm. The light features in the micrograph represent interconnected mesopores and channels.



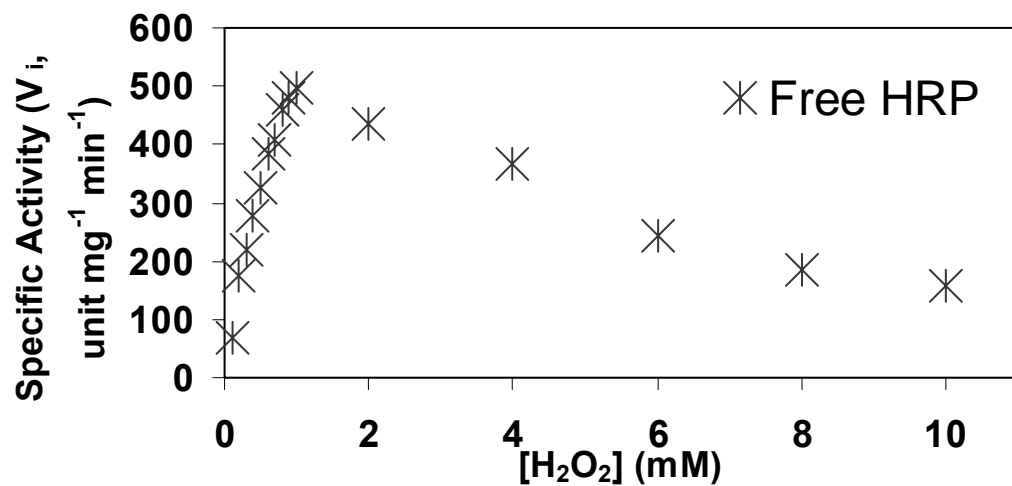


Figure 6-8a. Effect of the concentration of hydrogen peroxide,  $[\text{H}_2\text{O}_2]$ , on the activity of free HRP at pH 6.5.

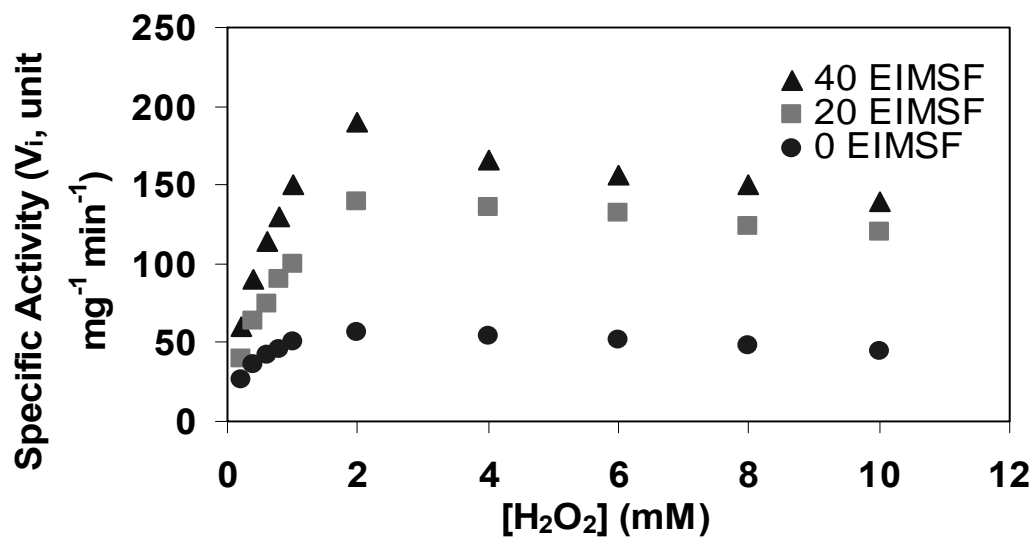


Figure 6-8b. Effect of the concentration of glucose and  $[\text{H}_2\text{O}_2]$  on the apparent activity of the porous fiber-immobilized HRP at pH 6.5.

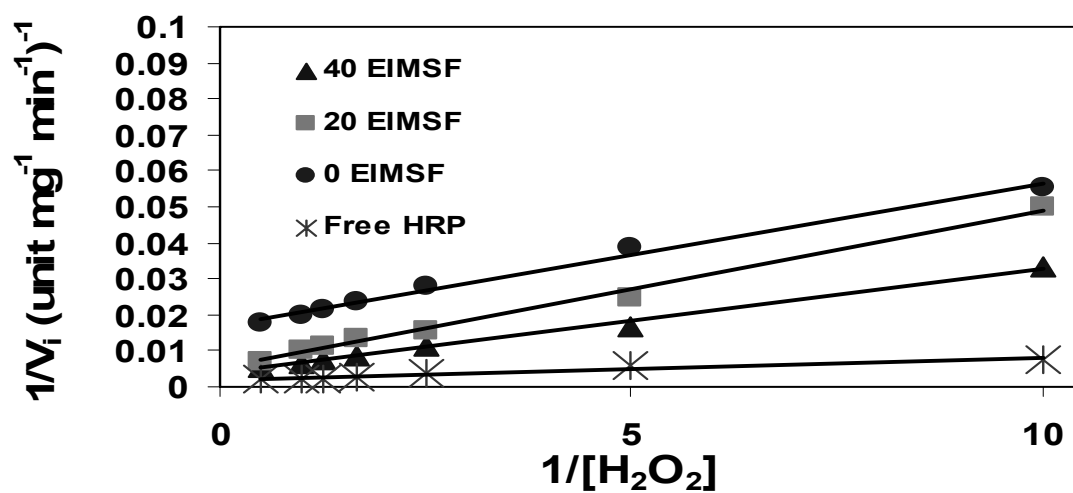


Figure 6-8c. Effect of the concentration of glucose on the apparent activity of the fiber-immobilized HRP. The straight lines on the Lineweaver-Burk plots were best-fit using linear regression, from which the  $V_m$  and  $K_m$  values were derived.

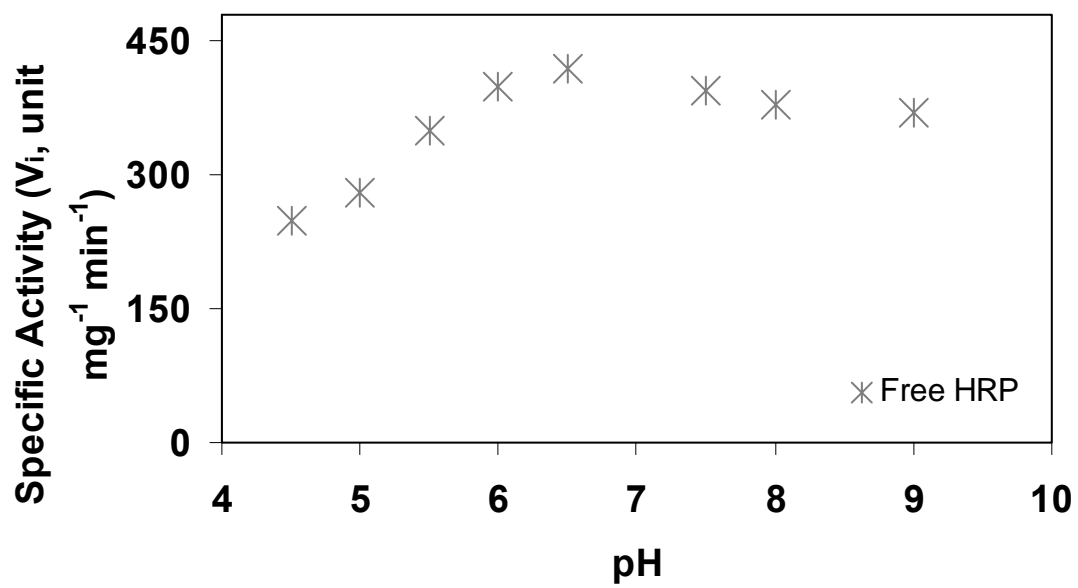


Figure 6-9a. Effect of pH on the activity of free HRP at [H<sub>2</sub>O<sub>2</sub>] of 2 mM.

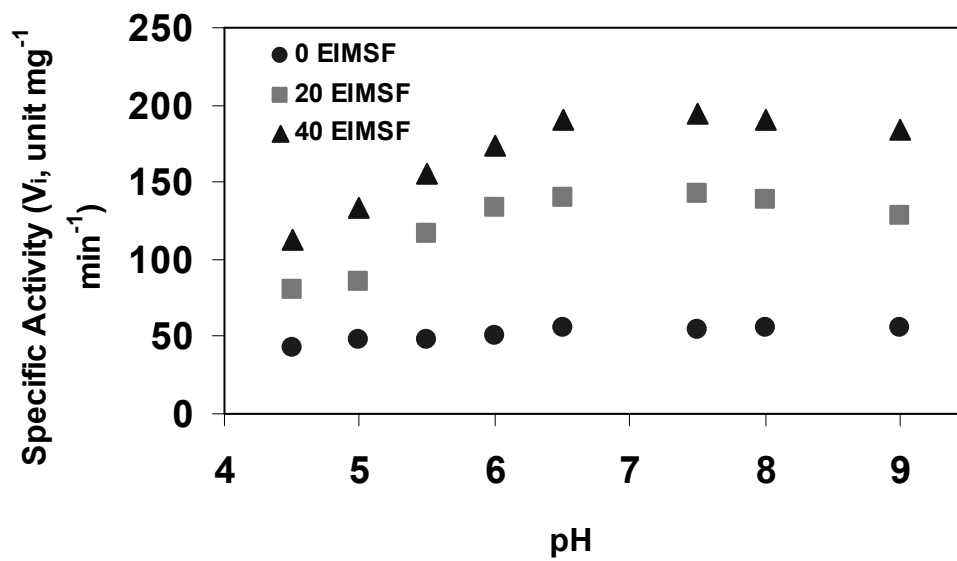


Figure 6-9b. Effect of the pH on the activity of fiber-immobilized HRP samples synthesized in the presence of 0-40 wt% glucose at  $[\text{H}_2\text{O}_2]$  of 2 mM.

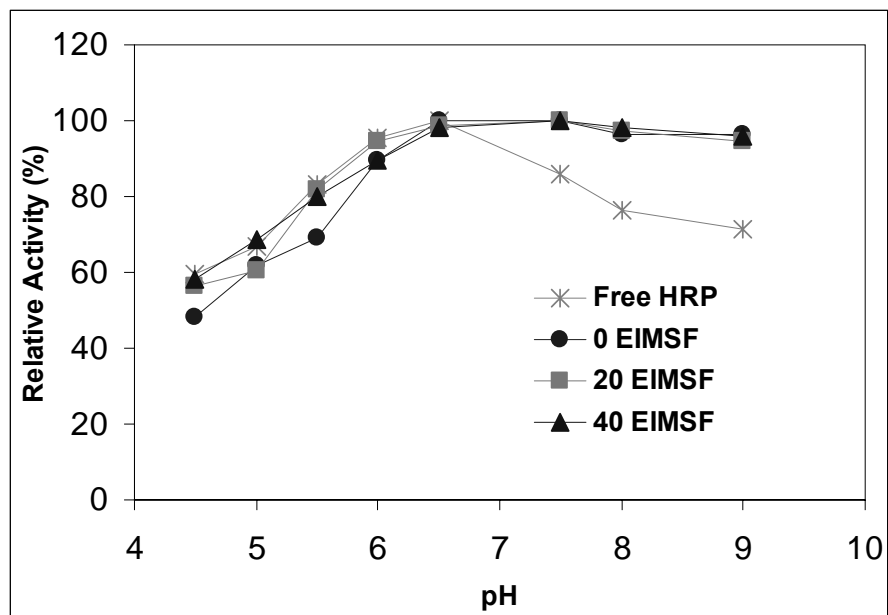


Figure 6-9c. Effect of the pH on the activity of free and fiber-immobilized HRP samples synthesized in the presence of 0-40 wt% glucose after normalization.

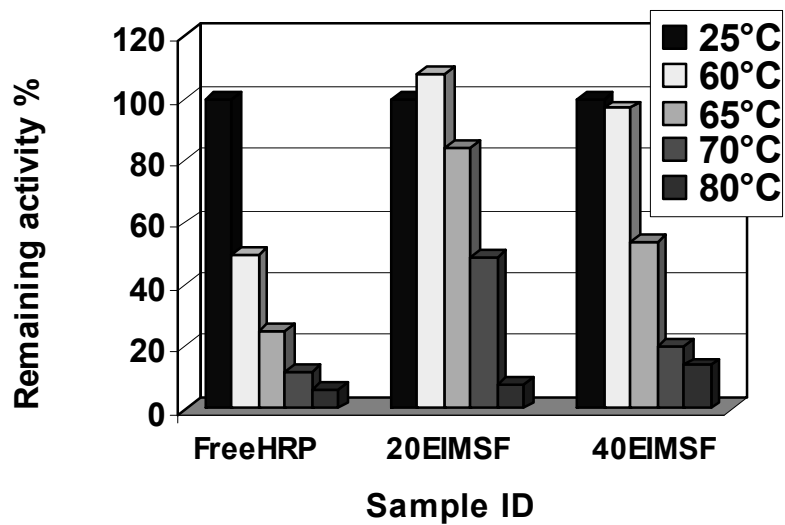


Figure 6-10. Thermal stability of free and immobilized HRP. Samples were treated under 25-80 °C for 30 min; the activity of HRP at 25°C is 100%.

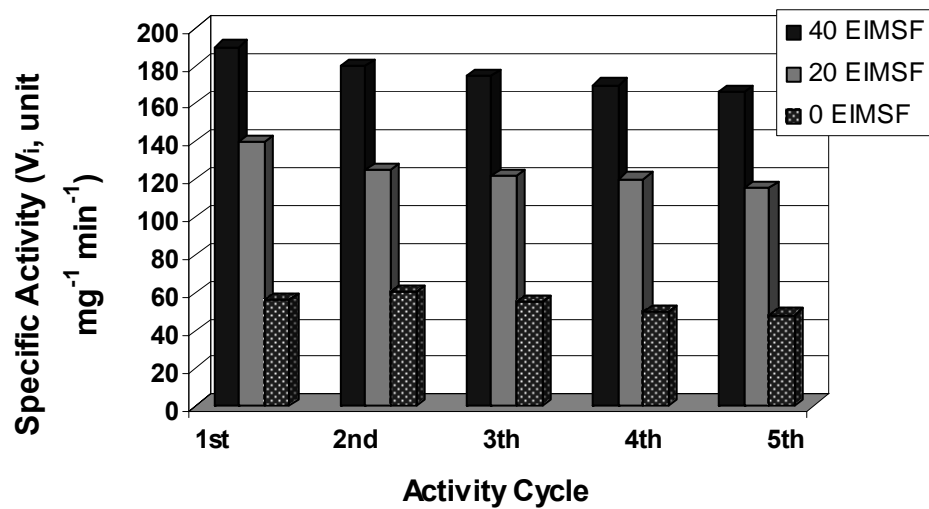


Figure 6-11. Catalytic activity cycle test to determine the efficiency of reusability of enzyme-encapsulated fiber samples.



## **Chapter 7: Electrospinning of Silica Nanofibers Containing CdSe/ZnS Quantum Dots**

### **7.1 Introduction**

An attempt is made to form linear arrays of quantum dots (QD) by encapsulating them into electrospun silica nanofibers. A detailed explanation of the research directed towards finding a compatible silica precursor and polymer additive to spin QD-encapsulated silica nanofibers is discussed. The electrospun fibers thus developed were then characterized using microscopic and spectroscopic instruments. The nanofibers contribute immensely to the extensive research being conducted in developing QD composite materials that could be utilized in optoelectronic, telecommunication, laser and optical sensor applications.<sup>1-4</sup>

#### **7.1.1 What are Quantum Dots (QD)?**

A QD, also called a semiconductor nanocrystal or artificial atom is a semiconductor nanocrystal whose size is approximately 2 to 10 nm.<sup>5,6</sup> Each QD might contain anywhere from 100 to 1000 atoms. If 10-nm-sized QD's are lined up together, about 3 million of them could easily fit within the width of a thumb. QD's have discrete energy levels, which are similar to that of atoms. The energy levels can be controlled by changing the size and shape of the QD.<sup>7-9</sup>

One unique and very interesting property of QD's is that, the same set of materials can be used to tune the optical response, absorption, and emission, within the IR to UV range specifically, with the key parameter being the size of the QD.<sup>10,11</sup> Thus, for example, 1.9 nm sized CdSe/ZnS QD's fluoresce in the blue region and the same CdSe/ZnS QD's when synthesized in the 5 nm size range will fluoresce in the red region

(Figure 7-1). Larger the QD, the redder the fluorescence, and the smaller the dots bluer in color they are.<sup>12</sup> The coloration is not related to the chemical nature of the specific material, it is directly related to the size of the QD or more specifically related to the energy levels of the QD. Quantitatively speaking, the bandgap between the energy levels is what determines the color of the fluoresced light, which is inversely proportional to the square of the size of the QD.<sup>13</sup> Hence, the QD's which are larger, have more closely spaced energy levels, allowing the QD's to absorb photons containing less energy (those closer to the red end of the spectrum). The ability to control the band gap (size of QD) provides a high degree of tenability in novel and non-traditional semiconductor applications.

### 7.1.2 Synthesis and Kinds of QD's

Epitaxy,<sup>14,15</sup> lithography,<sup>16,17</sup> and colloidal synthesis<sup>18-20</sup> are the three main methods used to synthesize QD's. Self-assembled quantum dots nucleate spontaneously on a substrate under certain conditions during molecular beam epitaxy and metallorganic vapor phase epitaxy on a material that is not lattice matched.<sup>17,21,22,23</sup> The islands can then be subsequently buried to form the quantum dot. By far the cheapest method of QD synthesis is the colloidal synthesis, due to the advantage of being able to occur under bench top conditions, and it is stated as being the least toxic of all the different forms of synthesis.

Some of the most common QD's available in the market today are the cadmium selenide (CdSe)<sup>4,10,11</sup> and core-shell cadmium selenide/zinc sulfide (CdSe/ZnS) QD's.<sup>24-26</sup> Core-shell QD's (e.g., CdSe/ZnS) are protected QD's, where a very thin (often one to two atomic layer) coating (ZnS) is present on top of the core QD, which improves the stability

and fluorescent brightness. The shell also removes defects, adding strength to the QD's and preventing natural degradation. Depending on the size of the CdSe/ZnS QD, the emission range can be anywhere between 490 to 620 nm. QD's with emissions near infrared regions, e.g., lead sulfide (PbS) or lead selenide (PbSe), are also synthesized with emission range between 850 to 2350 nm. Table 7-1 gives a more detailed description of some of the common QD's and their properties.<sup>27-31</sup>

### 7.1.3 Applications of QD's

Being quasi-zero dimensional, quantum dots have a sharper density of states than higher-dimensional structures. As a result, QD's have superior transport and optical properties, which are further being researched for use in diode lasers, amplifiers, and biological sensors.<sup>1,12,32,33</sup> QD's have quickly found their way into homes in many electronic goods. The new PlayStation 3 and high-definition DVD players (notably Blue-ray and HD-DVD) in the market recently, use a blue QD laser.<sup>34-36</sup> Another innovative application of QD's is also being researched as potential artificial fluorophore for intra-operative detection of tumors using fluorescence spectroscopy.<sup>37</sup> For all the above-mentioned applications, one important concern is to protect the QD's from degrading during use. QD's in general are very sensitive to moisture, methanol, etc. Some organic solvents that have been used to suspend these QD's as colloidal solutions are toluene, chloroform and hexane. Research on encapsulating QD's into materials (e.g., polymers, epoxy resins and silicones) for engineering QD-based materials and bridging them into macro-world applications has been pursued. Most importantly the encapsulated QD's have shown to be well protected, which then could be handled with ease.<sup>38-41</sup>

#### 7.1.4 Obtaining Linear Arrays of QD's

It has been discovered that one-dimensional chains or linear assemblies of QD's, characterized by a certain degree of spatial and energetic disorder, may give rise to interesting optical phenomena such as localization effects for electromagnetic fields.<sup>8,42</sup> The Anderson localization phenomenon is known from electron transport, which involves a disorder-induced transition from a classical diffusion behavior (Ohms law) to a localized state (insulator).<sup>43,44</sup> This effect originates from the interference of electrons subjected to multiple scattering by defects. A similar effect is expected to take place for electromagnetic waves,<sup>45</sup> that is, localized wave functions are predicted to exist. Systems that should display such effects, according to theory, are linear arrays of quantum dots or quantum films.<sup>46,47</sup> These effects are furthermore predicted to depend on the distance between the quantum structures along the chain, on their energetic disorder, related to the size distribution, as well as to the spatial disorder. A major step towards studying such phenomena and towards possible applications consists of devising preparation methods, allowing one to come up with stable arrays of quantum dots that might in addition be integrated into specific devices. The basic concept is to incorporate quantum dots into appropriate silica matrices and to prepare nanofibers (infinitely long) from such compound systems, for applications in telecommunication, sensors, low cost optical amplifiers, high speed and broadband fiber systems.<sup>48,49</sup>

There has been limited work done on encapsulating QD's in nanofibers. Recently, due to the above-mentioned applications, attempts are being made to obtain linear arrays of QD's. Chae et al.<sup>61</sup> in 2005 successfully encapsulated QD's in self-assembled silica composite fibers using porous alumina as the template. Schlecht et al.<sup>8</sup> recently

(2006) encapsulated QD's in polymer nanofibers using an electrospinning technique. There has been no research reported on encapsulating QD's in electrospun silica nanofibers. Using silica as the composite material for encapsulating nanofibers helps protect the QD's from high temperature and strong chemicals. The QD encapsulated silica nanofibers electrospun in this section are in the range of 50 to 250 nm. Stable arrays of QD's in the fibers without any aggregation were achieved. There were no adverse effects in the photoluminescence properties of encapsulated QD's. The silica fiber mats thus produced were white in color and were flexible and easy to handle.

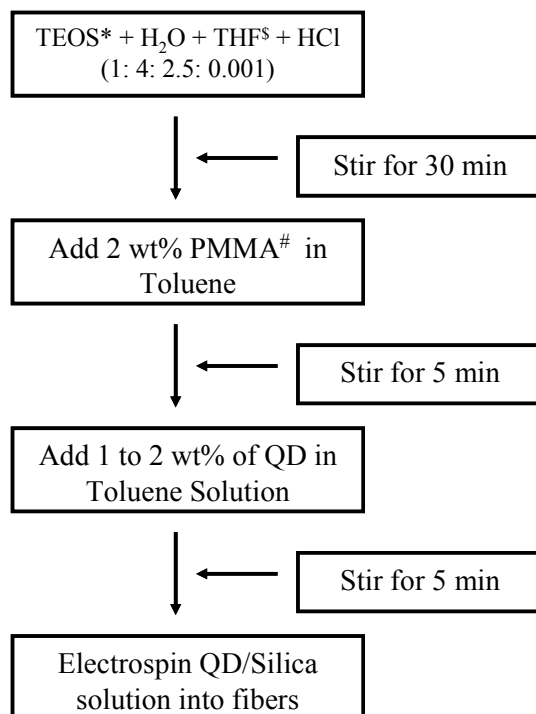
### **7.1.5 Electrospinning**

Electrospinning is one such method that could be used in producing infinitely long silica nanofibers containing QD's. Electrospinning involves the application of a strong electric current to a viscous solution collected in a glass pipette. The solution forms a droplet at the tip of the pipette, which deforms into a Taylor cone.<sup>50</sup> A charged jet of spinning solution then ejects out of the Taylor cone and is deposited in the form of fibers onto a copper plate or a rotating metal drum collector.<sup>51-53</sup>

Some of the factors that affect the distribution of QD's in the fibers include diameter of the fiber, morphology of the fiber, chemical nature of the spinning solution (including the type of silica precursor used), and the size of the QD's used. To obtain linear arrays of quantum dots in the fibers, the fiber diameter of around 10 to 100 nm have to be approached. Some of the methods that could be used to induce QD alignment in the fibers include, charge effect, rapid shear flow effect (analogues to river flow), self-elongation of the spinning solution into fibers and mechanical stretching of the fibers using rotating drum collectors.

## 7.2 Experimental Section

The two main steps involved in the fabrication of silica/QD composite nanofibers are the preparation of the spinning solution and electrospinning of silica nanofibers containing relatively ordered QD's. Scheme 7-1 represents a detailed procedure for producing silica/QD nanofibers.



Scheme 7-1. Fabrication of quantum dot encapsulated silica nanofibers. \* TEOS (tetraethyl orthosilicate), <sup>s</sup> THF (tetrahydrofuran), <sup>#</sup> PMMA (Mw 350,000).

### 7.2.1 Materials and Reagents

Tetraethylorthosilicate (TEOS, 98%), reagent grade tetrahydrofuran (THF, 99.9%), chloroform (CHCl<sub>3</sub>), toluene, hydrogen chloride (HCl, 2 M solution in water), toluene, poly-methyl methacrylate (PMMA, Mw 350,000) and poly vinyl alcohol (PVA, Mw 80,000) were all purchased from Sigma-Aldrich Chemical Co. and used as received. Two colors of CdSe/ZnS core shell quantum dots selected from opposite ends of the

available wavelength (Figure 7-1), a) Lake Placid Blue QD in toluene, with absorbance at 462 nm, emission at 484 nm, diameter of the QD around 1.9 nm and b) Maple Red-Orange QD in toluene, with absorbance at 598 nm, emission at 614 nm and diameter of approximately 5.2 nm, were purchased from Evident Technologies, NY.<sup>28</sup> Table 7-2 gives complete specifications of these QD's.

### 7.2.2 Preparation of Electrospinning Solution

Tetraethyl orthosilicate (silica precursor) was first hydrolyzed by mixing water, HCl (2 M, acid catalyst) and THF solvent in the molar ratio of 1:4:2.5:0.001. The solution was initially cloudy, but turned clear after 30 min of continuous mixing and complete hydrolysis of TEOS (Scheme 7-2). The hydrolyzed sol has low viscosity and molecular weight and hence, forms drops rather than fibers during electrospinning. A certain amount of 15 wt% PMMA/toluene solution was then added to the hydrolyzed sol with continuous mixing in a 2:8 solution mass fraction, respectively. Two sets of fibers were then spun by adding 0.1 wt% of Maple Red-Orange or 0.05 wt% of Lake Placid Blue with respect to the weight of the final fibers. In a typical procedure, 3.85 g of TEOS was mixed with 1.25 g of water, 4 g of THF and 0.001 ml of 2 M HCl with constant stirring. After the hydrolysis of TEOS, about 2 g of PMMA/toluene solution was added under constant agitation. The solution was viscous and clear in nature. About 0.4 ml of Maple Red QD's in toluene solution (180  $\mu\text{g}/\text{nmol}$ ) or 1.8 ml of Lake Placid Blue QD's in toluene solution (2.7  $\mu\text{g}/\text{nmol}$ ) were then added to the above solution and mixed for 5 min to produce the final spinning solution.

### 7.2.3 Electrospinning of Silica Nanofibers Containing QD's

The above mentioned silica sol containing the PMMA additive and QD's was then placed inside a glass pipette with a tip opening of approximately 0.5 mm. An electric field of 20 kV (Gamma High Voltage Research D-ES30) was applied by dipping a charged copper wire directly into the spinning solution. A grounded aluminum plate or rotating drum placed at a distance of 20 cm from the tip of the pipette was used as a fiber-collecting device. Under the electric field, a droplet suspended from the tip of the pipette acted as the feed source from which a charged jet of hydrolyzed TEOS/PMMA/QD sol solution was ejected out in the form of nanofibers. The small amounts of THF and toluene present in the spinning solution evaporated out during fiber formation. The two sets of silica fibers containing 0.1 and 0.05 wt% of red and blue QD's, respectively, were thus synthesized.

### 7.2.4 Metal Plate and Rotating Drum Fiber Collector

Initially, a grounded metal plate was used to collect the electrospun nanofibers. The fibers obtained by this method were irregularly distributed in the form of nonwoven mats. To induce alignment of QD in the electrospun nanofibers, a method of mechanically stretching partially dry fibers and collecting ordered fibers was used. To accomplish this, a grounded metal rotating cylinder was placed horizontally to the tip of the glass pipette so that the fibers could be collected along the circumference of the cylinder (Figure 7-2). The general rule is that to obtain aligned fibers the speed of the rotating cylinder should be at a higher speed than the speed at which the fibers jet out of the syringe.<sup>54</sup> Hence, a speed of about 4500 rpm was used, which not only aligned the fibers but also mechanically stretched them during the process of collection.



### 7.3 Instrumentation

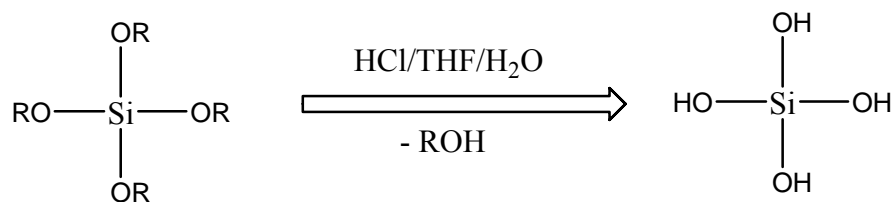
An environmental scanning electron microscope (ESEM, Phillips XL-30), equipped with an energy dispersive X-ray analyzer (EDX) was used to analyze the diameter and the surface morphology of the electrospun fibers. The average diameter of the fibers was obtained by measuring about 100 fibers from the SEM micrographs. The fluorescence emission (FE) spectra of the QD-immobilized fibers were obtained using a fluorescence spectrophotometer (Perkin-Elmer, Model-1000). The fibers to be analyzed were spun directly onto Quartz glass slides, which were used as sample holders for the FE experiments. UV-vis absorbance spectroscopy (Perkin-Elmer  $\lambda$ 2S) was used to detect the emission spectra of the QD-immobilized fibers. The pure blue and red QD/toluene solutions were used as control samples. Fluorescent images of the QD-containing electrospun nanofibers were also acquired using a Leica DMRX microscope equipped with a near UV filter cube. A transmission electron microscope (TEM, JEOL 2010F) was used to study the encapsulated QD's inside the fibers. The samples for TEM analysis were obtained by directly spinning the fibers onto a lacy carbon coated 200 mesh copper grid.

### 7.4 Results and Discussion

As stated previously, two sets of fibers containing red and blue QD's were electrospun. The distance between the tip of the pipette and the fiber collector was kept at a constant of 20 cm. The voltage applied to the spinning solution also was kept at 20 kV. Several factors affecting the morphology of the fibers, diameter of the fibers, and distribution of QD's inside the fibers were studied. An attempt to align QD's at the nanoscale level was also made.

### 7.4.1 Effect of Silica Precursor on Silica/QD Nanofibers

CdSe/ZnS nanocrystals are relatively stable QD's that can be easily suspended in organic solvents and can withstand temperatures up to 65 °C. The outer core of the QD (ZnS) acts as a protective covering, which makes the QD more stable.<sup>55,56</sup> In spite of this added advantage, encapsulating evenly distributed individual QD's in composites is a challenge, due to the aggregation of QD's in water, methanol, or at high temperature. The aggregation further causes drastic decrease in emission, fluorescence lifetime, and excitation.<sup>57,58</sup> Hence, solvents and silica precursors needed to spin QD solutions have to be carefully selected to avoid aggregation.



R = C<sub>2</sub>H<sub>5</sub> (Tetraethylorthosilicate)

R = CH<sub>3</sub> (Tetramethylorthosilicate)

Scheme 7-2. Hydrolysis of silica precursor.

Initially, TMOS was selected as the silica precursor to spin QD composite nanofibers. During hydrolysis of TMOS, methanol was formed as a byproduct (Scheme 7-2). As soon as the QD solution was added into the methanol-containing spinning solution, QD aggregation occurred. Hydrolysis of TEOS, on the other hand, produces small amounts of ethanol as byproduct. Ethanol in small amounts does not degrade or aggregate QD's, and thus can be used to spin silica fibers. Figures 7-3a and 7-3b represent the SEM micrographs of the nanofibers formed using TMOS and TEOS silica

precursors, respectively. The fibers formed using TMOS were rough, showed beaded morphology and were large, with diameters ranging from 1 to 5  $\mu\text{m}$ . All these features might be attributed to the aggregation of QD's in the fiber. On the other hand, fibers formed using TEOS were relatively smooth and devoid of beads. The diameter of the fibers ranged from 50 to 250 nm.

#### **7.4.2 Effect of Polymer Additive on Silica/QD Nanofibers**

Hydrolyzed TEOS sol has a very low viscosity, which is too low to spin fibers. Individual hydrolyzed TEOS sol molecules are relatively small and cannot entangle with each other to extend into a fiber during spinning. Attempts made to spin the pure hydrolyzed silica with QD's formed drops rather than fibers. Thus, a polymer additive (e.g., PMMA) was added to the hydrolyzed sol to increase the viscosity of the solution. Polymer additives usually interact with the hydrolyzed sol via hydrogen bonding. The polymer chains also tend to entangle with each other causing an increase in the viscosity of the spinning solution, and hence assist in easy spinning of fibers.<sup>54</sup> Search for a polymer additive that would assist in spinning silica fibers without causing QD aggregation was conducted. Figure 7-4 gives a detailed list of polymer solutions added at different ratios to the silica precursor, with SEM micrographs that were studied in the pursuit of finding the ideal polymer additive.

15 wt% of poly (vinyl alcohol) (PVA) dissolved in various solvents were added dropwise into hydrolyzed TEOS solution in 1:9, 2:8 and 3:7 mass fractions (Figure 7-4). PVA was found to be less compatible with hydrolyzed sol solution, causing the polymer to precipitate out of the spinning solution. Next a more compatible and easy spinning polymer PMMA was tested. PMMA polymer is easily soluble in THF, toluene, or

chloroform. 15 wt% PMMA polymer solutions prepared using the above mentioned solvents were then added to the hydrolyzed silica sol in 1:9, 2:8 and 3:7 mass ratios. As the amount of PMMA was increased from 1 to 3 mass fractions, the viscosity of the spinning solution also increased, causing the fibers to become thicker. In the end 15 wt% PMMA/toluene (at the ratio of 2:8) was found to be the most compatible polymer additive. The fibers formed were smooth in texture (Figure 7-4), with fiber diameters of 50 to 250 nm.

#### **7.4.3 Effect of QD Size on Silica/QD Nanofibers**

Two sets of silica/QD fibers were spun using 0.1 wt% of Maple Red-Orange and 0.05 wt% of Lake Placid Blue QD's, with respect to the final wt% of fibers. An important point that needs to be kept in mind is that even though the volume/mass ratio of fibers is very large, the actual amount of QD needed to obtain good fluorescence emission from encapsulated QD fiber composites is very small. The average diameter of the red and the blue QD's purchased from Evident Tech. is around 5.2 nm (0.0027 g of QD's/mL of toluene) and 1.9 nm (0.00036 g of QD's/mL of toluene), respectively. On average, the weight of QD's present in 1 ml of red QD/toluene solution is much higher than the weight of blue QD's. Initially an attempt to obtain 0.1 wt% of blue QD's, with respect to the final weight of fibers, was made by adding a higher volume of blue QD/toluene mixture into the spinning (hydrolyzed TEOS/PMMA) solution. This caused the electrospun fibers to be rough and beaded in morphology (Figure 7-5). When the wt% of blue QD's was dropped down to 0.05 wt%, much smoother and cylindrical fibers were obtained (average diameter of 250 to 400 nm). The loading of red QD's on the other hand could easily be pushed up to 0.1 wt% with respect to the final weight of the fibers,

obtaining smooth cylindrical nanofibers with average nanofiber diameter of 50 to 250 nm (Figure 7-5).

#### **7.4.4 Attempts to Obtain Linear Arrays of QD in Silica Fibers**

In recent years, research on obtaining composite fibers containing metal nanoparticles, magnetic nanoparticles, carbon nanotubes (CNT), minerals, enzymes, etc., has been actively pursued.<sup>59,60</sup> Work on obtaining aligned CNT and polymer crystals inside the electrospun fibers has also been extensively studied by Ko et al.<sup>60</sup> (Figure 7-6). Three main factors that contribute to the alignment of nanomaterials inside fibers are: 1) the applied electric field present between the tip of the pipette and the collecting plate, which produces charge effects in the spinning solution and the fibers; 2) the shear flow rate of the spinning solution jetting out of the pipette (analogues to river flow and confinement effect that cause alignment of nanomaterials in the spinning solution); and 3) mechanical pulling of the fibers using a high speed rotating drum collector, causing the fibers to stretch and induce alignment of the fibers and QD's present inside the fibers.

Initially, a grounded metal plate was used to collect electrospun nanofibers. The fibers obtained by this method were irregularly distributed in the form of a nonwoven mat. On the other hand, nanofibers obtained using a metal drum collector were relatively aligned (Figure 7-7). The average diameter of the fibers collected on a flat metal plate was greater than 500 nm. When the fibers were spun using the rotating drum at 1000 rpm, the fiber diameter dropped to 400 nm. With further increase in the speed of the rotating drum to 4500 rpm, the fibers were mechanically stretched giving rise to aligned fibers of smaller diameter (less than 200 nm) with a more uniform distribution of QD's. The number of irregularities and beads on the fibers also decreased drastically.

## **7.5 Characterization of Silica/QD Nanofibers**

The QD-immobilized nanofibers thus obtained were characterized to study the distribution of QD's and to compare the efficiency of free and immobilized QD's.

### **7.5.1 Environmental Scanning Electron Microscopy (ESEM) and Electron Diffraction Spectroscopy (EDX)**

ESEM was used to study the external morphology and the diameter of the fibers. The electrospun nanofibers were placed on sample holders, with the help of a conducting carbon tape. The fibers were then sputter coated with a monolayer of platinum metal. The samples thus prepared were then subjected to a 20 kV electron beam to obtain ESEM micrographs. Elemental analysis of the fibers was also performed using EDX. Pure QD/toluene solution was used as a control sample that showed sharp and specific elemental peaks for Cd, Se, Zn and S. Elemental spectra for pure silica fibers shows sharp peaks for silica (Si) and oxygen (O). The QD encapsulated fibers showed peaks for Si, O, Cd, Se, Zn and S as seen in Figure 7-8.

### **7.5.2 Fluorescence Emission (FE)**

Maple Red-Orange (red) and Lake Placid Blue (blue) QD immobilized silica nanofibers, pure silica fibers without QD, and pure QD/toluene solution were all subjected to UV-irradiation, and the emitted fluorescence was determined. Figures 7-9 shows the fluorescence emission spectra (FE) of red QD/toluene solution and the red QD composite fibers respectively. An excitation wavelength of 300 nm was used. The red QD/toluene solution showed a sharp emission peak at 620 nm.<sup>27,28</sup> The red QD-composite fibers also showed a sharp peak at around 616 nm. Fluorescence peaks for pure blue QD/toluene solution and blue QD-composite fibers are also shown in Figure 7-9. There is

a sharp emission peak at 490 nm for pure blue QD,<sup>27,28</sup> and another at 486 nm for blue QD-composite fibers was noticed. The quantum yield of pure QD in solution was around 30 to 50%, which decreased to 20 to 30% when encapsulated in silica fibers. Pure silica fibers without QD, when excited at 300 nm, did not show any prominent emission peak between 400 and 700 nm. The above results imply that encapsulation of QD in the silica/PMMA fibers does not affect the photoluminescence properties of CdSe/ZnS quantum dots, which is a requirement for the target applications.

### **7.5.3 Fluorescence Microscopy (FM)**

Fluorescence microscopy technique was used to obtain fluorescence images of QD encapsulated silica nanofibers. The composite nanofibers were spun directly onto quartz glass slides. Visible and UV light were used to obtain these images, as seen in Figure 7-10. The fibers fluoresced very strongly when exposed to UV light. The images were taken at 150x magnification.

### **7.5.4 Absorption Spectroscopy**

The red and blue QD encapsulated silica fibers, pure red and blue QD/toluene solution and pure silica fibers were all subjected to absorbance from 400 to 700 nm wavelength. Figure 7-11 shows the absorption spectra for all the above-mentioned samples and controls. A sharp absorption peak at 610 nm was seen for both the free and immobilized red QD's. An absorption peak at 470 and 468 nm for pure blue QD/toluene<sup>28</sup> and blue QD composite fibers was observed. No absorption peak for pure silica fibers was observed within 400 to 700 nm wavelength. There is no change in the absorption values going from pure to encapsulated QD's, which again proves that the silica/PMMA fiber does not decrease the efficiency of the immobilized QD's.

### 7.5.5 Transmission Electron Microscopy

The samples for obtaining TEM images were prepared by directly spinning QD encapsulated nanofibers on a 200 mesh copper grid. One of the difficulties in obtaining TEM images of encapsulated QD's is the very small size of the dot, ranging from 1.9 to 5.2 nm. Another disadvantage is the thick layer of silica/PMMA fiber, which hinders the electron beam from penetrating the fibers, which is required to obtain an image. Thus to obtain high-resolution images, the TEM needs to be operated at an high accelerating voltage of 300 kV, which causes the fibers to degrade if exposed for longer time periods. Figure 7-12 represents a TEM image of red QD-encapsulated silica fiber. The inset shows a high-resolution image showing arrays of QD's obtained during electrospinning.

### 7.6 Conclusion

The main aim of this research was to encapsulate QD's and attempt to obtain linear arrays of QD's in silica nanofibers. Two types of ZnS-coated CdSe QD's, fluorescing in two opposite regions of the spectrum (blue and red) were selected for encapsulation. Electrospinning was used to encapsulate these QD's into silica nanofibers. A trail and error method was used to prepare a suitable spinning solution made up of a silica precursor, polymer additive and QD's. Care was taken to avoid aggregation of QD's in the fibers. Electrospun nanofibers were collected on metal cylindrical drums to induce mechanical alignment of fibers and encapsulated QD's. The QD-encapsulated fibers were in the form of flexible white fiber mats that produced sharp emission in the 400 to 700 nm wavelength region. These fibers not only protect the QD's from moisture and temperature but also act as an excellent medium to link the nano world to the micron



world for potential applications in sensors, low cost optical amplifiers, high speed and broadband telecommunication, etc.

## 7.7 Reference List

1. Dabbousi, B. O., Bawendi, M. G., Onitsuka, O., Rubner, M. F. Electroluminescence from CdSe quantum-dot/polymer composites. *Applied Physics Letters*, 66(11), 1316-1318. 1995.
2. Gao, M., Lesser, C., Kirstein, S., Mohwald, H., Rogach, A. L., Weller, H. Electroluminescence of different colors from polycation/CdTe nanocrystal self-assembled films. *Journal of Applied Physics*, 87(5), 2297-2302. 2000.
3. Gaponik, N., Radtchenko, I. L., Sukhorukov, G. B., Weller, H., Rogach, A. L. Toward encoding combinatorial libraries: charge-driven microencapsulation of semiconductor nanocrystals luminescing in the visible and near IR. *Advanced Materials (Weinheim, Germany)*, 14(12), 879-882. 2002.
4. Kershaw, S. V., Harrison, M., Rogach, A. L., Kornowski, A. Development of IR-emitting colloidal II-VI quantum-dot materials. *IEEE Journal of Selected Topics in Quantum Electronics*, 6(3), 534-543. 2000.
5. Ashoori, R. C. Electrons in artificial atoms. *Nature (London)*, 380(6574), 559. 1996.
6. Kastner, M. A. Artificial atoms. *Physics Today*, 46(1), 24-31. 1993.
7. Granqvist, C. G. Electrochromic tungsten oxide films: Review of progress 1993-1998. *Solar Energy Materials and Solar Cells*, 60(3), 201-262. 2000.
8. Schlecht, S., Tan, S., Yosef, M., Dersch, R., Wendorff, J. H., Jia, Z., Schaper, A. Toward linear arrays of quantum dots via polymer nanofibers and nanorods. *Chemistry of Materials*, 17(4), 809-814. 2005.
9. Yamase, T. Photo- and electrochromism of polyoxometalates and related materials. *Chemical Reviews (Washington, D.C.)*, 98(1), 307-325. 1998.
10. Murray, C. B., Norris, D. J., Bawendi, M. G. Synthesis and characterization of nearly monodisperse CdE (E = sulfur, selenium, tellurium) semiconductor nanocrystallites. *Journal of the American Chemical Society*, 115(19), 8706-8715. 1993.
11. Rogach, A. L., Kornowski, A., Gao, M., Eychmueller, A., Weller, H. Synthesis and characterization of a size series of extremely small thiol-stabilized CdSe nanocrystals. *Journal of Physical Chemistry B*, 103(16), 3065-3069. 1999.
12. Colvin, V. L., Schlamp, M. C., Allvisatos, A. P. Light-emitting diodes made from cadmium selenide nanocrystals and a semiconducting polymer. *Nature (London, United Kingdom)*, 370(6488), 354-357. 1994.
13. Eichmann, R. Linear optical characteristics dielectrically structured semiconductor. Ph.D. Dissertation, Philipps University, Marburg. 2002.
14. Jiang, C., Sakaki, H. Controlling anisotropy of GaSb(As)/GaAs quantum dots by self-assembled molecular beam epitaxy. *Physica E: Low-Dimensional Systems & Nanostructures (Amsterdam, Netherlands)*, 32(1-2), 17-20. 2006.
15. Prieto, J. E., Markov, I. Quantum-dot nucleation in strained-layer epitaxy. Minimum-energy pathway in the stress-driven two-dimensional to three-dimensional transformation. *Physical Review B: Condensed Matter and Materials Physics*, 72(20), 205412-1-205412/8. 2005.

16. Crozier, P. A., Tolle, J., Kouvetakis, J., Ritter, C. Synthesis of uniform GaN quantum dot arrays via electron nanolithography of D<sub>2</sub>GaN<sub>3</sub>. *Applied Physics Letters*, 84(18), 3441-3443. 2004.
17. Nguyen, Lam H., LeThanh, V., Debarre, D., Yam, V., Halbwax, M., El Kurdi, M., Bouchier, D., Rosner, P., Becker, M., Benamara, M., Strunk, H. P. Selective epitaxial growth of Ge quantum dots on patterned SiO<sub>2</sub>/Si(0 0 1) surfaces. *Applied Surface Science*, 224(1-4), 134-138. 2004.
18. Canizal, G., Schabes-Retchkiman, P. S., Pal, U., Liu, H. B., Ascencio, J. A. Controlled synthesis of ZnO nanoparticles by bioreduction. *Materials Chemistry and Physics*, 97(2-3), 321-329. 2006.
19. Greenberg, M. R., Smolyakov, G. A., Jiang, Y. B., Boyle, T. J., Osinski, M. Synthesis and characterization of in-containing colloidal quantum dots. *Proceedings of SPIE-The International Society for Optical Engineering*, 6096(Colloidal Quantum Dots for Biomedical Applications), 60960D-1-60960D/13. 2006.
20. Xie, R., Zhong, X., Basche, T. Synthesis, characterization, and spectroscopy of type-II core/shell semiconductor nanocrystals with ZnTe cores. *Advanced Materials (Weinheim, Germany)*, 17(22), 2741-2745. 2005.
21. Neves, Marcia C., Pereira, Angela S., Peres, Marco., Kholkin, Andrei., Monteiro, Teresa., Trindade, Tito. Layer-by-layer deposition of organically capped quantum dots. *Materials Science Forum* 514-516(Pt. 2, Advanced Materials Forum III), 1111-1115. 2006.
22. Joyce, B. A., Vvedensky, D. D. Quantum dots in the InAs/GaAs system. An overview of their formation. *NATO Science Series, II: Mathematics, Physics and Chemistry*, 190(Quantum Dots: Fundamentals, Applications, and Frontiers), 1-26. 2005.
23. Simeonov, D., Feltin, E., Carlin, J. F., Butte, R., Ilegems, M., Grandjean, N. Stranski-Krastanov GaN/AlN quantum dots grown by metal organic vapor phase epitaxy. *Journal of Applied Physics*, 99(8, Pt. 1), 083509-1-083509/6. 2006.
24. Liu, W., Liang, J. G., Zhu, Y. L., Xu, H. B., He, Z. K., Yang, X. L. CdSe/ZnS quantum dots loaded solid lipid nanoparticles: novel luminescent nanocomposite particles. *Materials Science Forum*, 510-511(Eco-Materials Processing & Design VII), 170-173. 2006.
25. Zhang, K., Chang, H., Fu, A., Alivisatos, A. P., Yang, H. Continuous distribution of emission states from single CdSe/ZnS quantum dots. *Nano Letters*, 6(4), 843-847. 2006.
26. Zhao, K., Choi, J., Lo, Y. H. Engineering of quantum dot emission wavelength using conductive layer coating. *Applied Physics Letters*, 88(24), 243104-1-243104/3. 2006.
27. Bhattacharjee, B., Hsu, C. H., Lu, C. H., Chang, W. H. Colloidal CdSe-ZnS core-shell nanoparticles: Dependence of physical properties on initial Cd to Se concentration. *Physica E: Low-Dimensional Systems & Nanostructures (Amsterdam, Netherlands)*, 33(2), 388-393. 2006.
28. Evident Technologies.  
<http://www.evidenttech.com/nanomaterials/evidots/quantum-dot-introduction.php>. Quantum Dots. 2006.

29. Jin, T., Fujii, F., Yamada, E., Nodasaka, Y., Kinjo, M. Control of the optical properties of quantum dots by surface coating with calix[n]arene carboxylic acids. *Journal of the American Chemical Society*, 128(29), 9288-9289. 2006.
30. Murcia, M. J., Shaw, D. L., Woodruff, H., Naumann, C. A., Young, B. A., Long, E. C. Facile sonochemical synthesis of highly luminescent ZnS-shelled CdSe quantum dots. *Chemistry of Materials*, 18(9), 2219-2225. 2006.
31. Wang, S., Zou, J., Jarrett, B. R., Cho, S., Louie, A. Y., Kauzlarich, S. M. High quality ZnS and core/shell CdSe/ZnS nanoparticles from air-stable precursors. *Proceedings of SPIE-The International Society for Optical Engineering*, 6096(Colloidal Quantum Dots for Biomedical Applications), 60960U-1-60960U/8. 2006.
32. Michalet, X., Pinaud, F. F., Bentolila, L. A., Tsay, J. M., Doose, S., Li, J. J., Sundaresan, G., Wu, A. M., Gambhir, S. S., Weiss, S. Quantum dots for live cells, in vivo imaging, and diagnostics. *Science (Washington, DC, United States)*, 307(5709), 538-544. 2005.
33. O'Regan, B., Graetzel, M. A low-cost, high-efficiency solar cell based on dye-sensitized colloidal titanium dioxide films. *Nature (London, United Kingdom)*, 353(6346), 737-740. 1991.
34. Arakawa, Y., Someya, T. Prospect of blue light emitting VCSELs and quantum dot lasers. *Optronics*, 241, 127-132. 2002.
35. Arakawa, Y. Prospect of nanophotonic devices: quantum dot lasers and related devices. *Optronics*, 260, 92-99. 2003.
36. Someya, T., Tachibana, K., Arakawa, Y. Blue vertical cavity surface emitting lasers and InGaN quantum dot lasers. *Optoelectronic Properties of Semiconductors and Superlattices*, 16(III-V Nitride Semiconductors), 503-524. 2003.
37. Zhang, C. Y., Ma, H., Ding, Y., Jin, L., Chen, D. Y., Miao, Q., Nie, S. M. Studies on quantum dots-labeled trichosanthin. *Gaodeng Xuexiao Huaxue Xuebao*, 22(1), 34-37. 2001.
38. Chu, M. Method for preparing fluorescent spectrum adjustable quantum dot composite nanoparticles. (Shanghai Jiao Tong University, Peop. Rep. China. 1008-9298(1616342), 10. CN. 2004.
39. Rodriguez-Viejo, J., Babbousi, B. O., Bawendi, M. G., Jensen, K. F. Synthesis of CdSe/ZnS quantum dot composites for electroluminescent devices. *Materials Research Society Symposium Proceedings*, 424(Flat Panel Display Materials II), 477-482. 1997.
40. Shen, Y., Pang, L., Tetz, K. A., Fainman, Y. Characterization of PMMA quantum dot composite fabricated by pre-polymerizing method. *Proceedings of SPIE-The International Society for Optical Engineering*, 5510(Monophotonic Materials), 33-40. 2004.
41. Tian, H. Y., He, R., Gu, H. C. The preparation and properties of polymer beads and quantum dots composites. *Shanghai Jiaotong Daxue Xuebao*, 39(11), 1807-1810, 1815. 2005.
42. Eichmann, R., Pasenow, B., Meier, T., Stroucken, T., Thomas, P., Koch, S. W. Semiconductor absorption in photonic crystals, *Applied Physics Letters*, 82(3), 355-357. 2003.

43. Anderson, P. W. Absence of diffusion in certain random lattices. *Physical Review*, 109, 1492-1505. 1958.
44. Anderson, P. W., Abrahams, E. & Ramakrishnan, T. V. Possible explanation of nonlinear conductivity in thin-film metal wires. *Physical Review Letters*, 43(10), 718-720. 1979.
45. Wiersma, D. S., Bartolini, P., Lagendijk, A. & Righini, R. Localization of light in a disordered medium. *Nature (London)*, 390(6661), 671-673. 1997.
46. Golub, J.E., Eichmann, R., Strasser, G., Bernatz, G., Nau, S., Stolz, W., Thomas, P. Observations of interaction-assisted hopping transport in GaAs/Ga<sub>1-x</sub>Al<sub>x</sub>As quantum wells. *Journal of Luminescence*, 91(1&2), 7-12. 2000.
47. Thomas, P., Moller, M., Eichmann, R., Meier, T., Stroucken, T., Knorr, A. Microscopic foundation of the Forster excitonic energy transfer process. *Physica Status Solidi B: Basic Research*, 230(1), 25-29. 2002.
48. Bowers, M. J., II, McBride, J. R., Rosenthal, S. J. White-Light Emission from Magic-Sized Cadmium Selenide Nanocrystals. *Journal of the American Chemical Society*, 127(44), 15378-15379. 2005.
49. El-Taher, A. E., Tsang, Y. H., Binks, D. J. Three color operation of a diode-pumped broadband Yb-doped fibre laser. *Proceedings of SPIE-The International Society for Optical Engineering*, 6190(Solid State Lasers and Amplifiers II), 61900G-1-61900G/7. 2006.
50. Reneker, D. H., Hou, H. Electrospinning. *Encyclopedia of Biomaterials and Biomedical Engineering*, 1, 543-550. 2004.
51. Doshi, J., Reneker, D. H. Electrospinning process and applications of electrospun fibers. *Journal of Electrostatics*, 35(2&3), 151-160. 1995.
52. Patel, A. C., Li, S., Wei, Y., Wang, C., Zhang, W. Electrospinning of porous silica micro/nanofibers containing silver nanoparticles. *PMSE Preprints*, 91, 690-691. 2004.
53. Patel, A. C., Wei, Y. Electrospinning of silica nanofibers containing quantum dots. *Abstracts of Papers*, 230th ACS National Meeting, Washington, DC, United States, INOR-158. 2005.
54. Ramakrishna. S. An introduction to electrospinning and nanofibers. World Scientific Publishing Company. Singapore. 2005.
55. Wu, S. M., Zhao, X., Zhang, Z. L., Xie, H. Y., Tian, Z. Q., Peng, J., Lu, Z. X., Pang, D. W., Xie, Z. X. Quantum-dot-labeled DNA probes for fluorescence in situ hybridization (FISH) in the microorganism *Escherichia coli*. *ChemPhysChem*, 7(5), 1062-1067. 2006.
56. Lasne, D., Cognet, L., Berciaud, S., Blab, G. A., Groc, L., Heine, M., Choquet, D., Lounis, B. Single molecule CdSe/ZnS quantum dot and gold nanoparticle detection in live neurons. *Proceedings of SPIE-The International Society for Optical Engineering*, 6096(Colloidal Quantum Dots for Biomedical Applications), 609616-1-609616/9. 2006.
57. Raffaele, R. P., Cress, C. D., Wilt, D. M., Bailey, S. G. Radiation degradation of nanomaterials. *Materials Research Society Symposium Proceedings*, 887(Degradation Processes in Nanostructured Materials), 147-157. 2006.
58. Nadeau, J. L., Clarke, S. J., Khatchadourian, R. K., Bahcheli, D. M., Suffern, D., Bradforth, S. E. Mechanisms of quantum dot interactions with biological cells.

- Proceedings of SPIE-The International Society for Optical Engineering, 5969(Photonic Applications in Biosensing and Imaging), 596907-1-596907/13. 2005.
59. Amekura, H., Kono, K., Kishimoto, N., Buchal, C. Formation of zinc-oxide nanoparticles in SiO<sub>2</sub> by ion implantation combined with thermal oxidation. Nuclear Instruments & Methods in Physics Research, Section B: Beam Interactions with Materials and Atoms, 242, 96-99. 2006.
  60. Lam, H., Titchenal, N., Ye, H., Gogotsi, Y., Ko, F. Structure and properties of aligned carbon nanotubes reinforced nanocomposite fibrils. Proceedings of the American Society for Composites, Technical Conference 19th, NT10-1-NT10/11. 2004.
  61. Chae, W. S., Lee, S. W., An, M. J., Choi, K. H., Moon, S., W., Zin, W. C., Jung, J. S., Kim, Y. R. Nanostructures and optical properties of mesoporous composite nanofibers containing CdS quantum dots. Chemistry of Materials, 17(23), 5651-5657. 2005.

Table 7-1. Common types of quantum dots and their important applications.<sup>28</sup>

type of QD	emission range nm	QD diameter range Nm	QD system	Standard solvent	example application
CdSe	465 – 640	1.9 – 6.7	core	toluene	solar cells, LED's
CdSe/ZnS	490 – 620	2.9 – 6.1	core-shell	toluene	visible fluorescence applications, electroluminescence, telecommunication
CdTe/CdS	620 – 680	3.7 – 4.8	core-shell	toluene	deep red fluorescence applications
ZnSe	440 – 500	3 – 7	core	dichloromethane	telecommunication, sensors
PbS	850 – 950	4.5 – 9	core	toluene	near infrared applications, security inks, solar cells
PbSe	1200 – 2340	4.5 – 9	core	hexane	opto-electronics, optical switching, non-linear applications

Table 7-2. Complete specification of quantum dots used for encapsulation in silica nanofibers.<sup>28</sup>

material system	type	color	emission peak nm	suggested excitation Nm	1 <sup>st</sup> excitation peak nm	crystal diameter nm	molecular weight $\mu\text{g/nmol}$
CdSe/ZnS	core-shell	Lake Placid Blue	490	<400	470	1.9	2.7
CdSe/ZnS	core-shell	Maple Red-Orange	620	<400	610	5.2	180



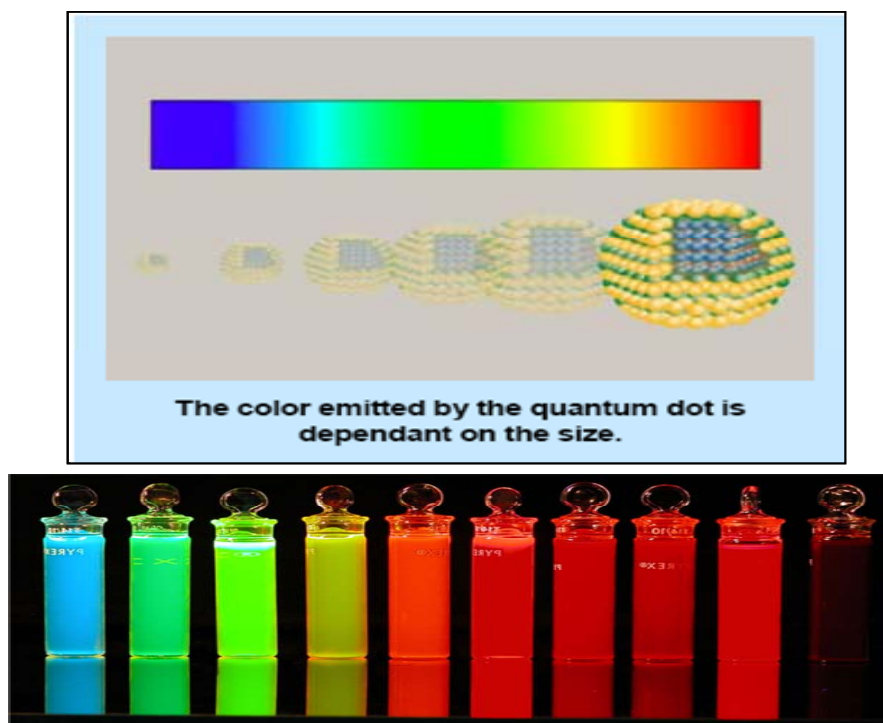


Figure 7-1. Different sized CdSe/ZnS quantum dots suspended in toluene solution. The same set of materials (CdSe/ZnS) can be used to tune the optical properties of the QD depending on the size of the QD. The blue (Lake Placid Blue) QD's have an average diameter of 1.9 nm and the red (Maple Red-Orange) QD's have an average diameter of 5.2 nm. (<http://www.evidenttech.com/qdot-definition/quantum-dot-introduction.php>).

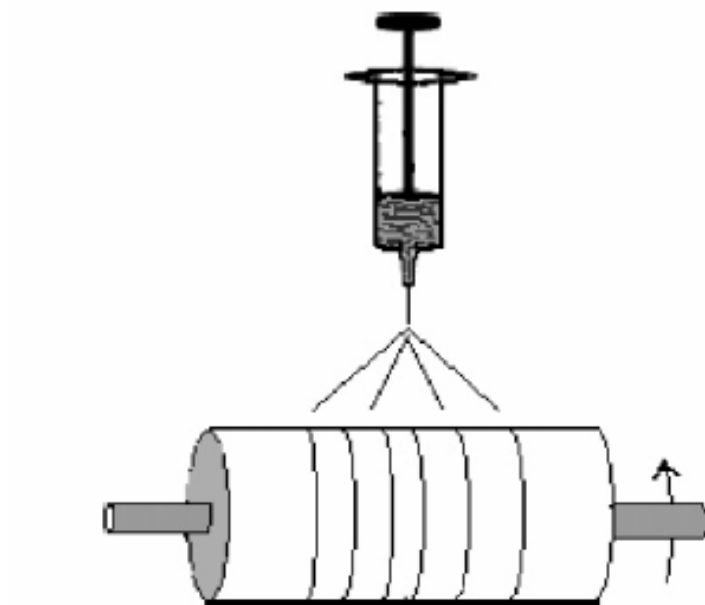
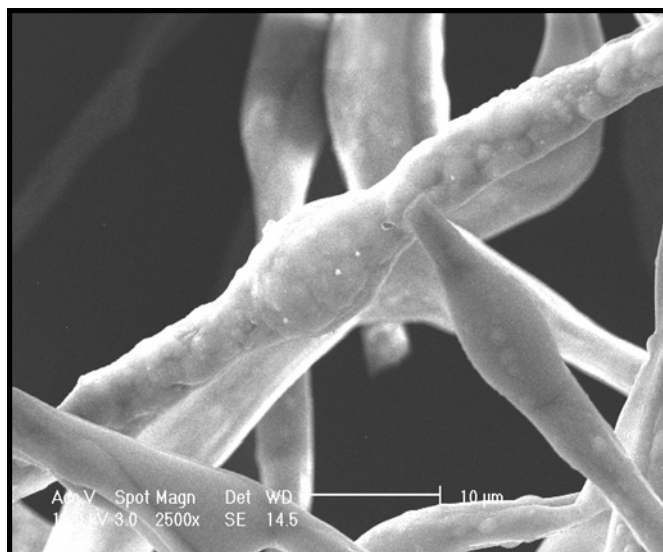
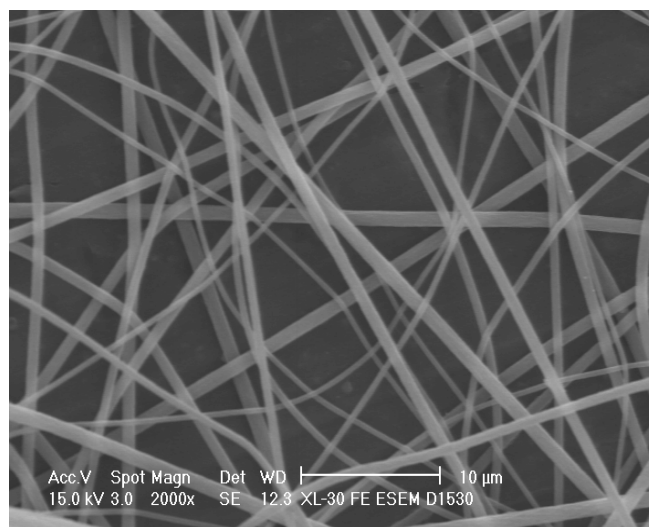


Figure 7-2. A schematic diagram of the grounded rotating metal cylinder for collecting electrospun nanofibers.



(7-3a)



(7-3b)

Figure 7-3. Scanning electron microscopy images of QD-encapsulated silica nanofibers fabricated using (a) tetramethyl orthosilicate as the silica precursor (scale bar: 10  $\mu\text{m}$ ) and (b) tetraethyl orthosilicate as the silica precursor (scale bar: 10  $\mu\text{m}$ ).

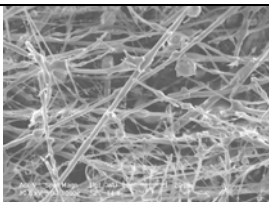
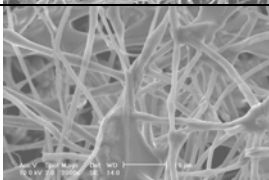
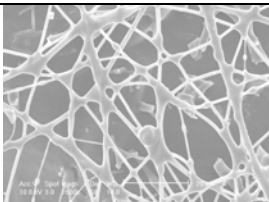
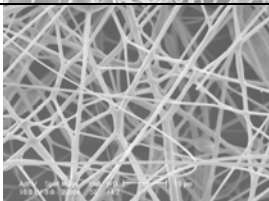
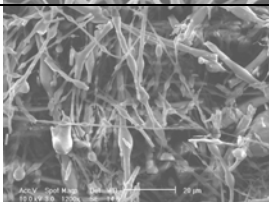
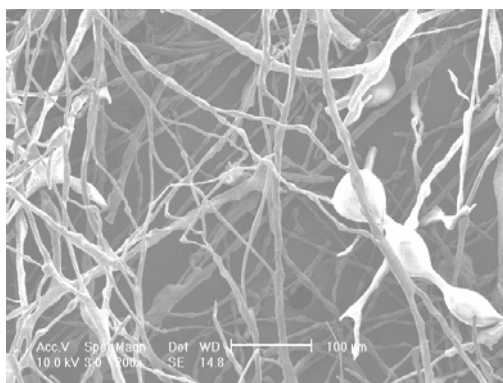
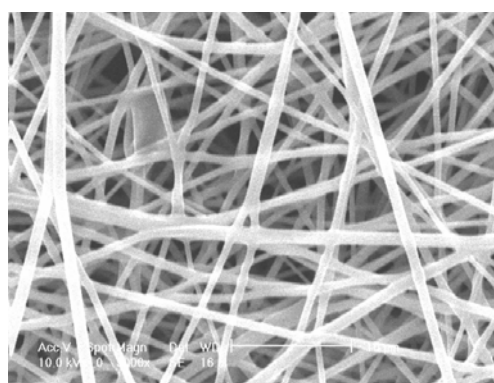
type of polymer additive	solvent <sup>a</sup>	wt% of PS <sup>b</sup>	ratio of PS : sol <sup>c</sup>	observation	ESEM image
PVA	water	15	1:9	polymer precipitation	
PVA	THF	15	1:9	polymer precipitation	
PVA	CHCl <sub>3</sub>	15	1:9	spinning solution gels	
PMMA	CHCl <sub>3</sub>	15	1:9	solution dilute	
PMMA	CHCl <sub>3</sub>	15	2:8	forms fibers with beaded morphology	
PMMA	CHCl <sub>3</sub>	15	3:7	thick fibers	
PMMA	THF	15	1:9	solution too dilute	
PMMA	toluene	15	1:9	spins fibers with some beads	
PMMA	toluene	15	2:8	spins smooth fibers, fewer beads	
PMMA	toluene	15	3:7	very thick fibers with lots of beads	

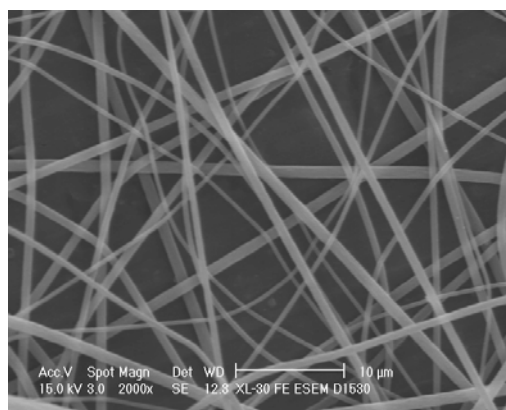
Figure 7-4. A detailed list of the polymer additives and the concentration used to spin silica fibers. <sup>a</sup>The solvent used to dissolve the polymer additive (tetrahydrofuran (THF) and chloroform (CHCl<sub>3</sub>)), <sup>b</sup>wt% of polymer solution additive and <sup>c</sup>the mass fraction of 15 wt% polymer additive solution to that of hydrolyzed silica sol (silica precursor used is TEOS). For this study, red QD's (0.1 wt% with respect to the final weight of fiber) is added to the silica/PMMA solution before electrospinning.



(7-5a)

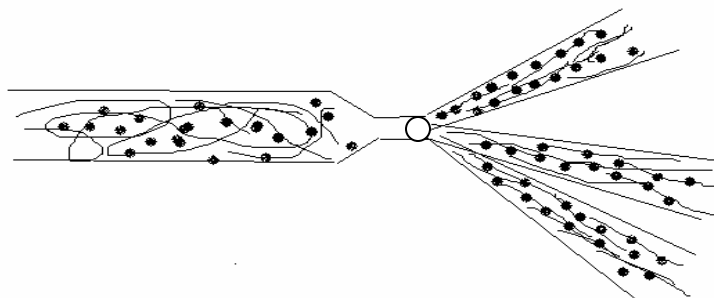


(7-5b)

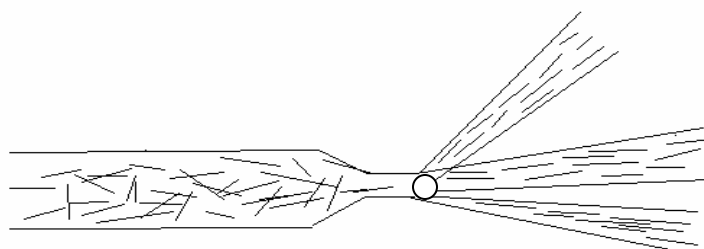


(7-5c)

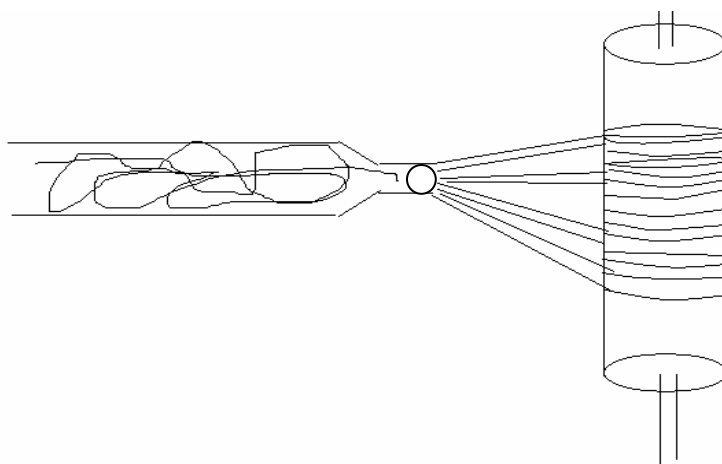
Figure 7-5. Scanning electron microscope images of QD encapsulated silica nanofibers fabricated using (a) 0.1 wt% of Lake Placid Blue QD's (scale bar: 10 μm), (b) 0.05 wt% of Lake Placid Blue QD's (scale bar: 20 μm) and (c) 0.1% of Maple Red-Orange QD's with respect to the final weight of the fiber (scale bar: 10 μm).



7-6a

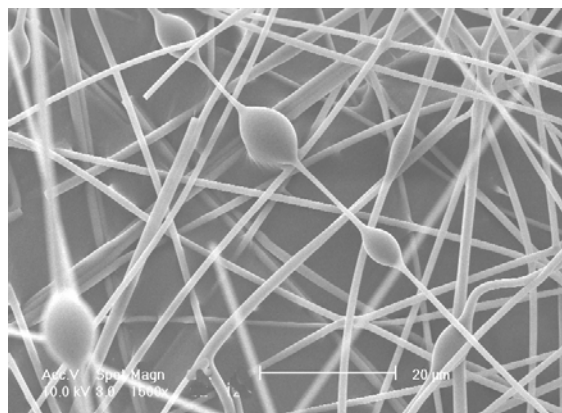


7-6b

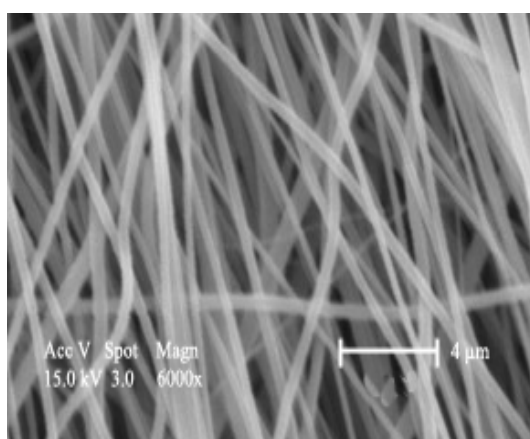


7-6c

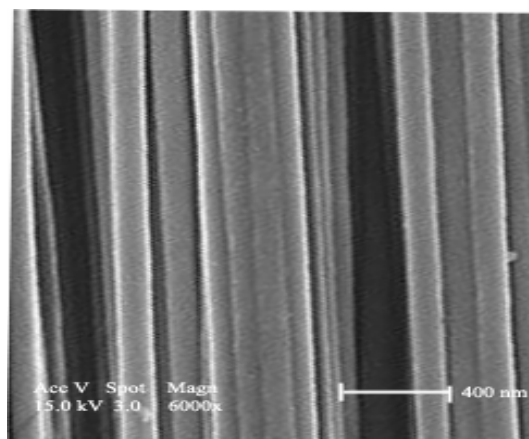
Figure 7-6. Alignment of a) nanoparticles and b) carbon nanotubes during electrospinning and c) mechanical alignment of nanofibers using a rotating metal drum.



(7-7a)

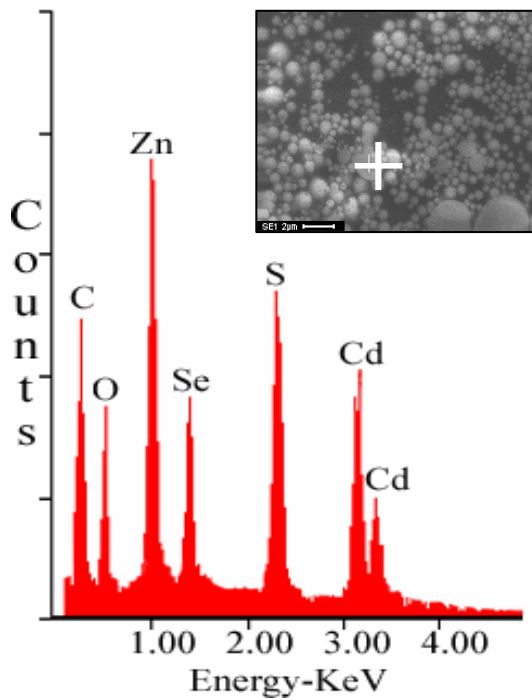


(7-7b)

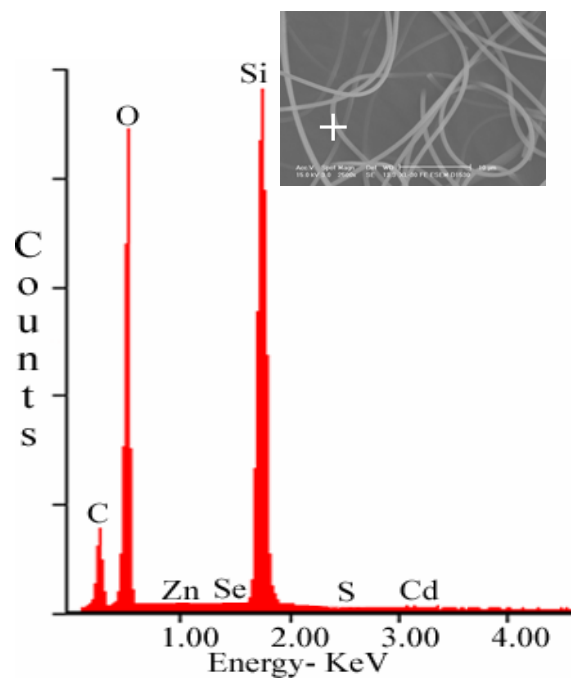


(7-7c)

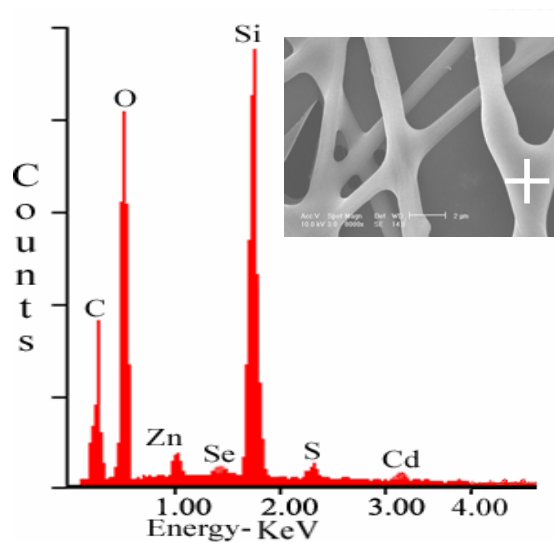
Figure 7-7. a) Irregular, nonwoven fiber mats obtained by collecting the electrospun fibers on grounded flat metal plate (scale bar 10 μm), b) aligned nanofibers collected using a grounded metal cylinder rotating at 1000 rpm (scale bar 4 μm) and c) 4500 rpm (scale bar 400 nm).



(7-8a)



(7-8b)



(7-8c)

Figure 7-8. Elemental analysis (EDX) of (a) pure CdSe/ZnS quantum dots, (b) pure silica fibers without any QD's and (c) silica fibers containing encapsulated QD's.



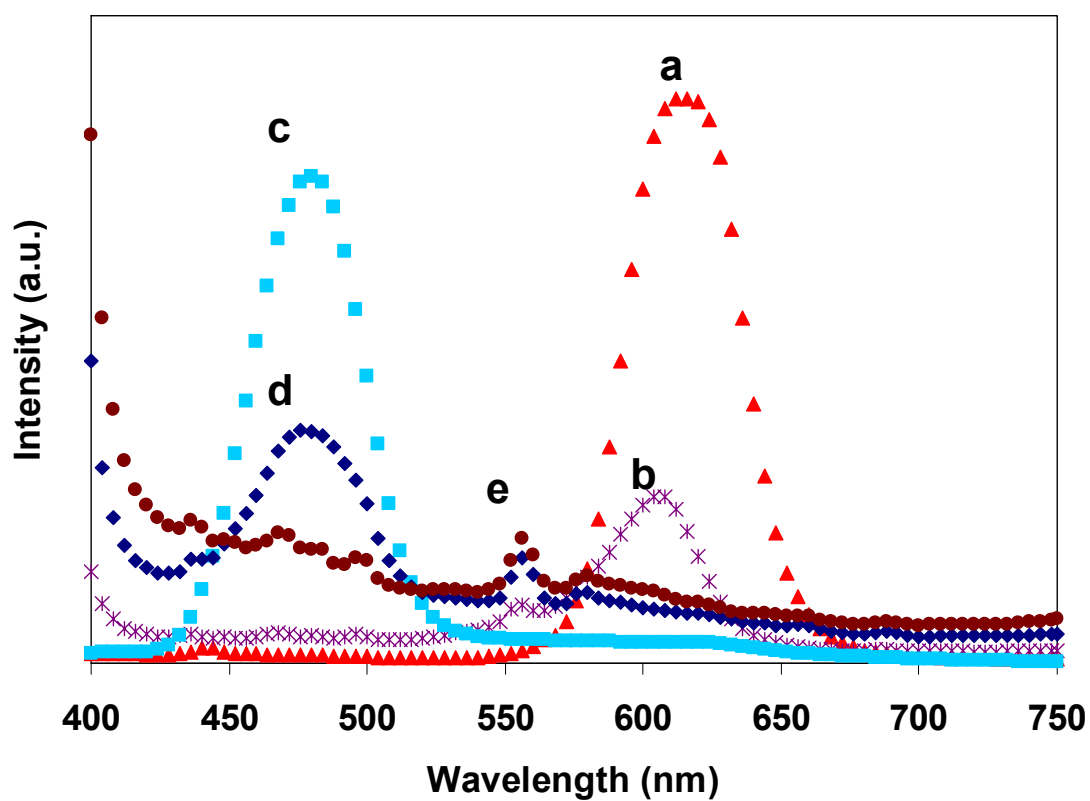
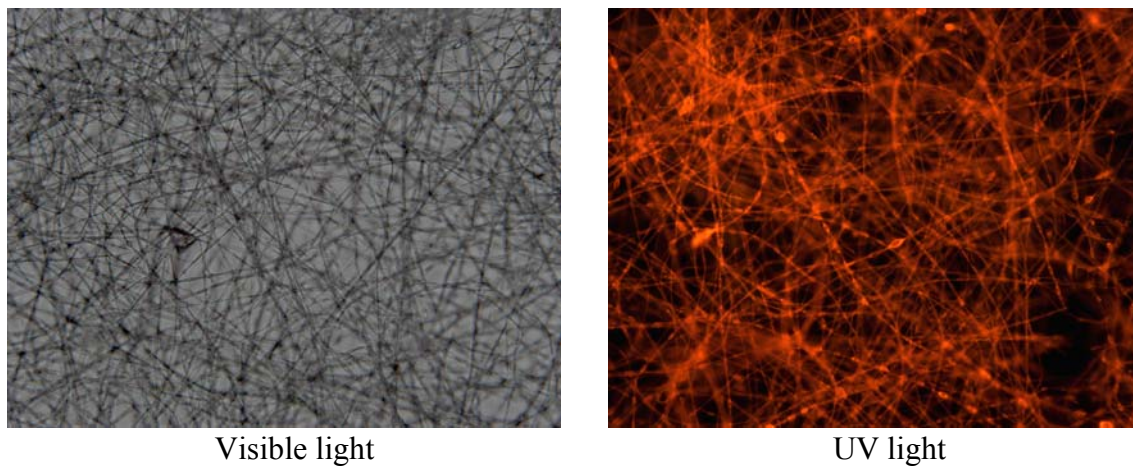
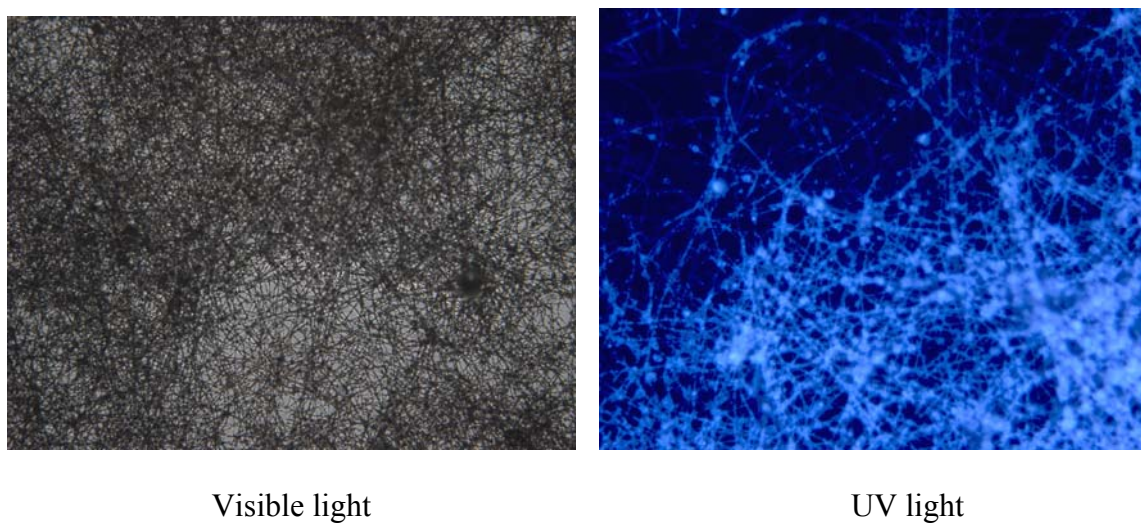


Figure 7-9. Fluorescence emission spectra of (a) pure Maple Red-Orange QD's (620 nm), (b) silica nanofibers containing red QD's (616 nm), (c) pure Lake Placid Blue QD's (490 nm), (d) silica nanofibers containing blue QD's (486 nm), and (e) pure silica fibers without QD's.



(7- 10a)



(7-10b)

Figure 7-10. Fluorescence microscopic images of silica nanofibers containing a) Maple Red-Orange QD's and b) Lake Placid Blue QD's (using visible light and UV light at 150x magnification).

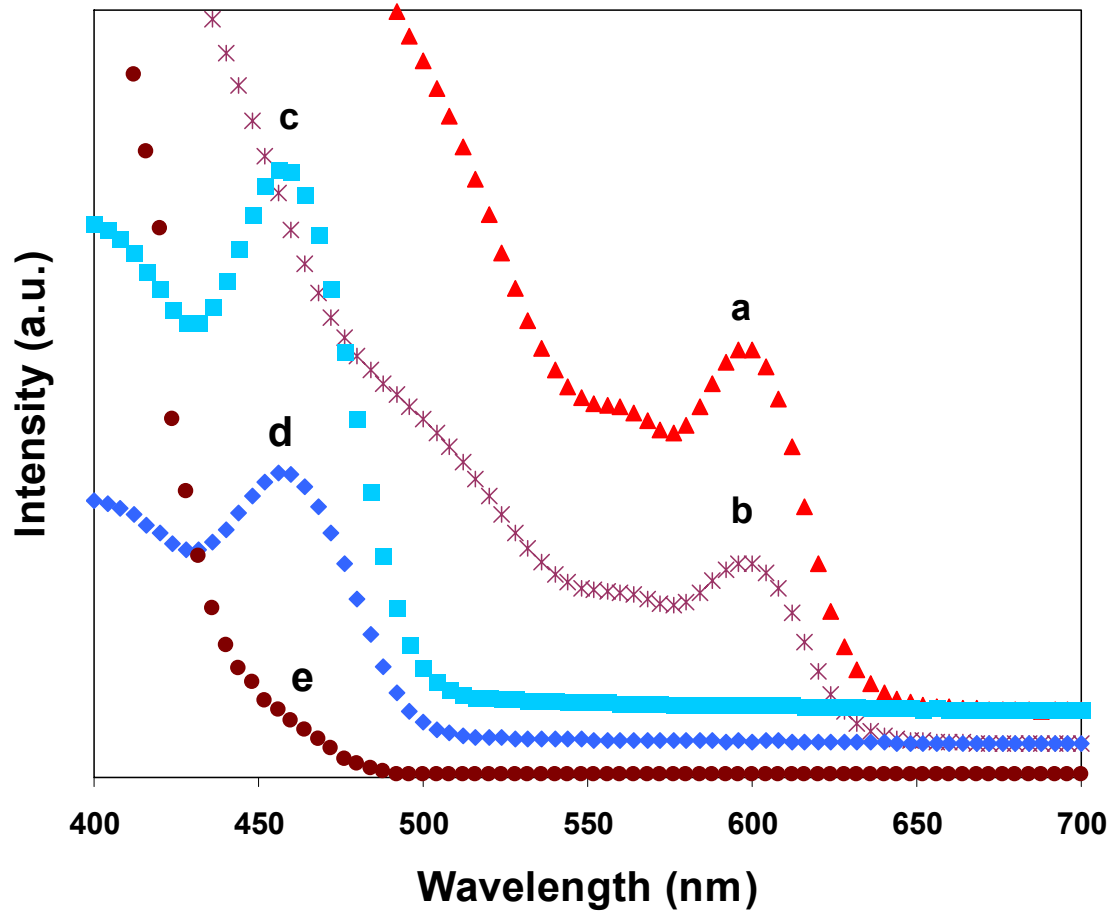


Figure 7-11. Absorbance spectra of (a) pure Maple Red-Orange QD's (610 nm), (b) silica nanofibers containing red QD's (610 nm), (c) pure Lake Placid Blue QD's (470 nm), (d) silica nanofibers containing blue QD's (468 nm) and (e) pure silica fibers without QD's.

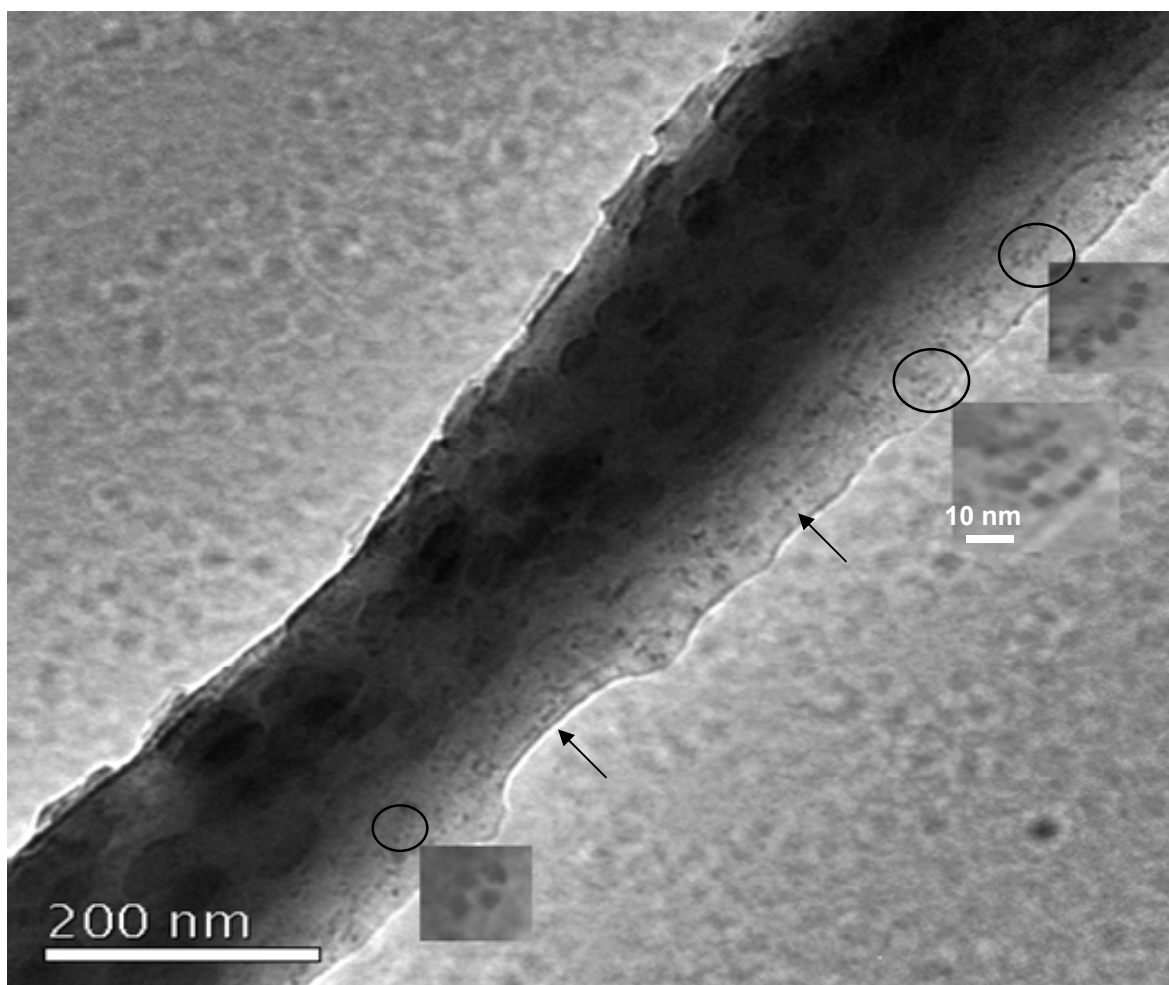


Figure 7-12. Transmission electron microscopic image of (a) red QD's (size 5.2 nm) in silica fibers collected using a rotating metal cylinder. The arrows point to many more such arrays of QD's. Scale bar: 200 nm. Insets show a linear array of QD's, scale bar: 10 nm.

## **Chapter 8: Conclusion and Future Work**

The focus of this research work has been to synthesize nanostructured materials for sensor, catalytic and reinforcement applications. The two elegant technologies that formed the foundation of this research work were 1) formation of pores in nanomaterials using a nonsurfactant templated technology and 2) electrospinning of nanofiber mats. Applying these two technologies separately or together, unique, commercially viable, and versatile products have been developed. Both the technologies worked in (symbiosis with each other and the products developed were tested for use in several potential applications. The research conducted in this dissertation strikes a fine balance between both developing technologies that would form the basis for fabricating highly efficient sensors and catalysts, and developing techniques to make these catalysts and sensors commercially viable. A short description of the technologies, their important features and drawbacks are stated. The goals that were accomplished by combining the technologies and the products that were developed are explained. Finally, the future direction of the research that would be required is explained.

### **8.1 Formation of Porous Structures in Nanomaterials**

An innovative technology developed in our lab deals with the formation of mesoporous metal oxide (e.g., silica) materials using nonsurfactant templates as pore forming agents. Numerous nonsurfactants, such as glucose, fructose, and urea, have been used as templates and the effect of templates on the porosity and surface area has been studied. This technology took a huge step forward when the nonsurfactant templated silica materials were utilized to encapsulate biomolecules, such as enzymes and proteins. The materials thus produced showed great potential as catalysts and sensors. Further

research was conducted on testing the catalytic efficiency of the developed products. A patent on encapsulating biomolecules in the porous materials was issued in 2004. This technology was also used to study the folding and unfolding phenomena of proteins in a confined space (e.g., porous silica material) that contributes to the study of molecular interaction or behavior of biomolecules in various environmental conditions (e.g., when exposed to varying pH, chemicals, temperature).

Some important features of this technology are

- Versatility: this technology can be used to encapsulate virtually any biomolecule, metal nanoparticles and pharmaceutical products.
- Efficiency: the biomolecules that are encapsulated using this technology maintain their viability and show high product efficiency.
- Commercially viable: only few steps are involved in the development of the products and the raw materials used are not expensive.

Even with such excellent features, this technology was still new, and a lot of work had to be done to understand its potential in the catalytic and sensor applications. Its adaptability to different applications has also been explored as seen in appendix A (hydraulic cracking, detergents, water purifications, etc.). Taking this technology from the research arena to the commercial realm is a huge step and extensive collaboration was needed. Some aspects of this technology, such as efficiency, number of steps involved in obtaining the final products, and the time required for drying the products, morphological compatibility of the samples to various applications, had to be drastically improved. A simple solution to all the above-mentioned challenges was sought. This led to the research conducted in this dissertation, where the nonsurfactant-templated method of

pore formation was combined with another technology called electrospinning to form commercially viable sensors, catalysts and reinforcement material.

## **8.2 Electrospinning**

Electrospinning is a technology used to create nanofiber mats. Several polymer and metal oxides fibers have been spun using this technology. Even though electrospinning was invented many years ago, the potential use of electrospinning in various applications was only realized recently. Some important features of this technology are:

- Rapid formation of nanofibers with large surface area;
- Room temperature nanofiber synthesis;
- Versatile method, can be used to spin several polymer and metal oxide fibers;
- Flexible fiber mats with high potential for reinforcement applications.

Some fields in which these fibers were proposed to make a huge impact are health care (e.g., biodegradable bandages, patches for drug delivery and scaffolds for cell growth and implants), defense (e.g., sensors, wound or blood adsorbents and decontaminating materials) and as reinforcement material (fillers for dental materials, for glass panels and bullet shields). Electrospinning was thus combined with the sol-gel pore forming technology to obtain porous nanofibers for several catalytic and sensor applications.

## **8.3 Products Developed**

A simple method of producing a highly efficient silver catalyst was accomplished, using the glucose-templated mesoporous silica material. A single step of soaking the

silica/glucose material in silver nitrate solution caused the reduction of silver nitrate to silver nanoparticles that were deposited inside the pores of silica material. The catalyst thus produced was economical and efficient.

Organic/inorganic hybrid polymer was synthesized and spun into fiber mats. The factors affecting the diameter and morphology of the fibers were extensively studied. The fibers thus obtained were then used as reinforcements to increase the mechanical properties of dental materials.

Silver and gold nanoparticle/silica composite nanofibers were produced by electrospinning polymer/silica fibers containing metal salts. The fibers thus produced were heat-treated, which caused the degradation of polymer and reduction of metal salt into nanoparticles, finally giving rise to porous silica/metal composite fibers. These fibers proved to have high catalytic activity and reusability.

Enzyme-encapsulated porous nanofibers with excellent sensor and catalytic capabilities were developed. Here the nonsurfactant technology was used to form pores and electrospinning was used to spin fibers. The product showed high surface area and excellent enzyme activity. The fibers proved to have high chemical detection limits making it a good chemical sensor.

An effort was made to align CdSe/ZnS quantum dots (2 to 5 nm) into silica nanofibers via electrospinning for applications in telecommunication, sensors and low cost optical amplifiers.

Finally, several enzyme-immobilized porous composites were developed for companies to test the efficiency of these products and utilize in several interesting applications. Significant improvements were made on the basic sol-gel nonsurfactant



templated pore forming technology to obtain high efficiency products, catering to the specific applications required by our collaborators.

#### **8.4 Unique Goals Achieved**

The unique and important features that are accomplished by utilizing the nonsurfactant templated pore forming technology and electrospinning technology are:

- High surface area samples obtained by pore formation using the nonsurfactant template method, plus electrospinning;
- Increased enzyme viability and activity in nanofibers due to the rapid formation of nanofibers and solvent evaporation;
- Rapid detection of hazardous chemicals and increased catalytic reactions (in a few seconds) achieved by easy interaction of enzymes and nanoparticles present inside the samples to the external reagents;
- High stability of the encapsulated enzymes and nanoparticles to external changes in pH, temperature or chemicals;
- Increased flexibility in product morphology from fine micron sized powders to nanofiber mats;
- Economical due to the inexpensive raw materials and reusability of the products;
- Easy scale up due to the simple steps involved in the sample formation.

#### **8.5 Future Direction**

There is still some work that needs to be done in terms of bridging the two technologies with the aim of developing useful products:

- Immobilizing specific enzymes into porous silica nanofibers that could detect and decontaminate hazardous chemicals and nerve gas agents present in the atmosphere. The products thus developed could contribute to the increased safety in chemical plants, airplanes, etc.
- Better control over the diameter of the nanofibers and bringing down the size of the fibers to nanometer levels ( $\sim 50$  nm), thus increasing the surface area of the fibers, which in turn increases the efficiency of the nanofibers for catalytic and sensor applications.
- Increased alignment of quantum dots with smaller diameter of fibers
- Further, increase in the mechanical properties of the dental materials by increasing the wt% of silica and fiber loading in the dental resin.

## **Appendix A: Work In Collaboration with Universities and Companies**

### **A.1 Abstract**

Research work conducted in collaboration with universities and companies is explained in this appendix. A brief introduction on each project along with an explanation on development of products is given. A part of the work stated in this section deals with the development of products for companies. Due to the confidential constraints, some of the work explained below is intentionally brief. The collaborative work explained below was based on a patented technology developed in our group.<sup>1,2</sup> Using this technology nanoparticles and biomolecules were encapsulated in nonsurfactant templated mesoporous silica materials.

The work explained in this section can be divided into two main sections

- **A.2** Encapsulation of manganese dioxide ( $\text{MnO}_2$ ) in nonsurfactant templated mesoporous silica materials (In collaboration with Princeton University)
- **A.3** Encapsulation of enzymes in nonsurfactant templated mesoporous silica materials (In collaboration with University of Pennsylvania and companies A, B and C).

### **A.2 Encapsulation of $\text{MnO}_2$ in Nonsurfactant Templated Mesoporous Silica**

#### **Materials**

##### **A.2.1 Introduction**

The aim of this project was to synthesize porous silica materials containing  $\text{MnO}_2$  nanoparticles, which would oxidize atrazine (AT) (a harmful herbicide present in nature)

to less toxic byproducts. The samples thus synthesized were then sent to Princeton University for further tests.

AT (2-chloro-4-ethylamino-6-isopropylamino-*s*-triazine) is the most common herbicide used for weed control on agricultural and non-agricultural lands.<sup>3</sup> Such widespread use has resulted in frequent detection of AT in surface and groundwater's of USA.<sup>4</sup> The presence of AT in water is particularly disturbing given recent findings that AT have potentially carcinogenic effects.<sup>5</sup> Frogs were reported to become hermaphroditic after being exposed at low ecologically relevant doses of the herbicide in the laboratory. Biological degradation of AT is well documented.<sup>6,7</sup> Until recently,<sup>8</sup> however, studies on the abiotic interactions of soil components with AT were generally limited to clay mineral catalyzed hydrolysis,<sup>9,10</sup> and sorption reactions on clays,<sup>11,12</sup> activated carbon,<sup>13</sup> and organic matter.<sup>14</sup> Reactions such as these decrease the mobility of AT but do not necessarily degrade the herbicide to potentially less toxic forms to wildlife and humans. Manganese dioxide minerals, although generally present in small amounts (up to 1%), are common components of soils. Synthetic forms of such oxides are known to oxidize a number of organic compounds, e.g., phenols and aniline.<sup>15-17</sup> The herbicides 2,4-D-(2,4-dichlorophenoxyacetic acid) and AT are known to be oxidized by synthetic forms of the common soil component oxide mineral birnessite ( $\delta$ -MnO<sub>2</sub>).<sup>8,18</sup> The main interaction of AT with MnO<sub>2</sub> takes place at the surface of MnO<sub>2</sub> particles. Work on degradation of atrazine by MnO<sub>2</sub> minerals other than birnessite has also been studied extensively by Shin et al.<sup>8,19</sup> They tested the effects of MnO<sub>2</sub> mineral type and surface area on atrazine transformation and reaction products. In this study, they observed partial degradation of AT in all four synthetic manganese oxides ( $\delta$ -MnO<sub>2</sub>,  $\beta$ -MnO<sub>2</sub>, and two types of  $\alpha$ -MnO<sub>2</sub>).

They also found that the surface area of  $\text{MnO}_2$  played a very important role in degradation of AT. Realizing the potential of  $\text{MnO}_2$  to degrade AT in the ground water and soil systems (without itself being toxic), research and methods have been proposed to synthesize and use synthetic  $\text{MnO}_2$  as a key decontaminating agent in regular ground and water basins.<sup>19</sup>

The four important forms of  $\text{MnO}_2$  available in the market at present are pyrolusite ( $\beta$ -  $\text{MnO}_2$ ), birnessite ( $\delta$ -  $\text{MnO}_2$ ), and cryptomelane type I and II ( $\alpha$ -  $\text{MnO}_2$ ). The building block of all the types of  $\text{MnO}_2$  consists of  $\text{MnO}_6$  octahedra forming layers and channels. The main difference in all the different forms of  $\text{MnO}_2$  are the intercalated metal ions (e.g.,  $\text{Li}^+$ ,  $\text{Na}^+$  and  $\text{K}^+$ ) present between the layers of these octahedral sheets of  $\text{MnO}_2$ .<sup>20</sup> Many procedures have been developed for the synthesis of  $\text{MnO}_2$  using precipitation, ion exchange, hydrothermal routes, high temperature solid-state routes, etc.<sup>20-24</sup> A classical method used for making sodium-birnessite is the oxidation of a Mn(II) salt, usually  $\text{MnCl}_2$  or  $\text{MnSO}_4$ , with air, oxygen, or  $\text{H}_2\text{O}_2$  in aqueous NaOH solution. The other common approach is the reduction of  $\text{NaMnO}_4$  or  $\text{KMnO}_4$  with fumaric acid or a reducing sugar (glucose) in an acid or neutral solution.<sup>22</sup> Even though all these methods stated above are capable of producing relatively large amount of  $\text{MnO}_2$ , the tendency of the  $\text{MnO}_2$  to aggregate extensively in the presence of high moisture content causes a drastic decrease in its efficiency as a catalysts.

As stated previously the main oxidization and chemical reactions of AT and  $\text{MnO}_2$  take place at the surface of  $\text{MnO}_2$  particles. The surface area of the commercially available  $\text{MnO}_2$  was tested to be around  $183 \text{ m}^2 \text{ g}^{-1}$  for cryptomelane type II ( $\alpha$ -  $\text{MnO}_2$ ),  $39 \text{ m}^2 \text{ g}^{-1}$  for birnessite ( $\beta$ -  $\text{MnO}_2$ ),  $32 \text{ m}^2 \text{ g}^{-1}$  for cryptomelane type I ( $\alpha$ -  $\text{MnO}_2$ ) and  $0.2$

$\text{m}^2 \text{g}^{-1}$  for pyrolusite ( $\beta\text{-MnO}_2$ ). Thus the surface area of most of the commercially available  $\text{MnO}_2$  is too low to be used as a catalyst for the degradation of AT.<sup>8,18</sup>

Some work by Imperor-Clerc et al.,<sup>25</sup> and Aronson et al.,<sup>26</sup> directed toward synthesizing  $\text{MnO}_2$  in porous materials has been conducted towards increasing the surface area and protecting the  $\text{MnO}_2$  particles from aggregation. Continuing further on this direction research was conducted towards synthesizing  $\text{MnO}_2$  particles in porous silica materials. Two different approaches were taken for producing  $\text{MnO}_2$  silica composites. The samples thus produced were then sent to our collaborators for further characterizations and for testing the efficiency of the samples as catalyst for the reduction of AT to less harmful byproducts.

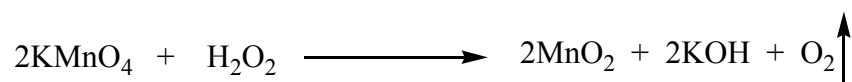
## A.2.2 Experimental Section and Observation

The nonsurfactant templated method of synthesizing porous silica materials is a patented technology developed in our lab by Wei et al.<sup>2,27,28</sup> It is a simple, bio-friendly and versatile method used to develop porous metal oxide (e.g., silica) materials using nonsurfactants such as glucose, fructose, urea, etc. Using the above stated technology two different approaches were attempted in synthesizing the final  $\text{MnO}_2$ /silica composite.

### A.2.2.1 Materials and Reagents

Tetraethyl orthosilicate (TEOS, 99%), hydrochloric acid (HCl, 1 M),  $\beta\text{-D-glucose}$ , potassium permanganate ( $\text{KMnO}_4$ ), aqueous hydrogen peroxide ( $\text{H}_2\text{O}_2$ , 10 wt%), urea (98%) were purchased from Sigma Aldrich (Milwaukee, WI).

### A.2.2.2 Reduction of $\text{KMnO}_4$ to $\text{MnO}_2$ using $\text{H}_2\text{O}_2$



Scheme A.2-1. Reduction of potassium permanganate to manganese dioxide.

An attempt was made to synthesis  $\text{MnO}_2$  inside porous silica material by reducing  $\text{KMnO}_4$  to  $\text{MnO}_2$  using  $\text{H}_2\text{O}_2$  as the reducing agent (Scheme A.2-1). Nonsurfactant templated silica samples were prepared using TEOS as the silica precursor in which water and small amounts of HCl catalyst was added to facilitate the hydrolysis of TEOS to form a sol. To the resultant TEOS sol were added various amounts of a 50 wt% aqueous urea solution. The urea-containing sol was homogeneous and the sol-gel reactions (i.e., further hydrolysis and polycondensation) proceeded at room temperature. Various amounts of  $\text{KMnO}_4$  were then added to the silica sol. The samples were allowed to gel and dry at room temperature for a few days until dry-semi-transparent, dark purple and monolithic urea and  $\text{KMnO}_4$ -containing silica gels were obtained. A control sample containing 0 wt% of urea template was also synthesized (transparent in nature).

In a typical procedure to make 30 wt% urea templated and  $\text{KMnO}_4$  doped material, 9.64 g of TEOS was mixed with 1.6 g of water and 0.1 g of HCl (1 M) for 30 min. TEOS hydrolyzed to give a clear solution. 2.4 g of (50 wt%) urea solution was then added with constant mixing for 5 min. Various amounts of 1 N aqueous  $\text{KMnO}_4$  solutions were then added to the sol with constant mixing (Table A.2-1). The solution is then allowed to gel and dry at room temperature for 10 days. The samples thus produced were immersed in 10 wt%  $\text{H}_2\text{O}_2$  solution for 1 hour.

#### **A.2.2.2.1 Observation**

The urea templated samples were dark purple in color due to the presence of  $\text{KMnO}_4$  inside the silica matrix. When these silica samples were immersed in 10 wt%  $\text{H}_2\text{O}_2$ , the  $\text{KMnO}_4$  present inside the samples reacted instantly with  $\text{H}_2\text{O}_2$  to produce  $\text{MnO}_2$  and oxygen. A large number of bubbles in and around the immersed silica sample

was noticed.  $\text{KMnO}_4$  leaked out of the silica matrix, causing the samples to become colorless. This further caused the reduction of  $\text{KMnO}_4$  outside the silica particles. This phenomenon was seen in all the silica samples synthesized (Table A.2-1). The control samples containing 0 wt% urea and 1 wt%  $\text{KMnO}_4$  also showed leakage of  $\text{KMnO}_4$  from the silica samples with formation of bubbles. The control sample containing 30 wt% urea and no  $\text{KMnO}_4$  (transparent samples) when immersed in  $\text{H}_2\text{O}_2$  did not show any color change nor did they form any bubbles. The distribution of  $\text{KMnO}_4$  in the silica material was at the molecular level hence, causing  $\text{KMnO}_4$  to leak out of the samples easily. Another approach of using glucose templated silica materials to reduce  $\text{KMnO}_4$  into  $\text{MnO}_2$  was studied.

#### **A.2.2.3 Reduction of $\text{KMnO}_4$ Using Glucose Templated Silica Materials**

0, 10, 30 and 60 wt% glucose templated silica samples were synthesized using the previously reported procedure by Wei et al.,<sup>2,27,28</sup> and as explained in the experimental section of chapter 2. The samples were then immersed in aqueous 1 M  $\text{KMnO}_4$  solutions for 4 hours. The glucose present inside the silica samples reduced  $\text{KMnO}_4$  to  $\text{MnO}_2$ . The samples turned a dark brown to black color. The samples were then washed with water thoroughly, filtered and finally dried in the oven at 110 °C over night.

##### **A.2.2.3.1 Observation**

10, 30 and 60 wt% glucose templated samples changed to a dark brown color due to the reduction of  $\text{KMnO}_4$  to  $\text{MnO}_2$  in the presence of glucose. Glucose not only acts as a reducing agent, but also assists in forming pores in the silica material. The 60 wt% samples, unlike other samples, showed some precipitation of  $\text{MnO}_2$  outside the silica samples. This might be caused due to the higher wt% of glucose in the samples that tend



to leak out of the samples and reduce  $\text{KMnO}_4$  outside the silica pores. Another reason could be the fact that the pores in the 60 wt% samples are larger and hence, the  $\text{MnO}_2$  present inside the silica tends to leak out of the samples. In addition, when the samples were washed with water after the initial reduction reaction, further leakage of  $\text{MnO}_2$  was seen in 60 wt% samples. The 10 and 30 wt% glucose templated samples did not show any leakage. The control sample containing 0 wt% glucose templated samples when immersed in  $\text{KMnO}_4$  changed only slightly to a pale yellow color suggesting that no reduction of  $\text{KMnO}_4$  occurred in the absence of glucose. The samples thus produced were then sent to our collaborators for further characterizations and for testing the efficiency of the samples as catalyst for the reduction of AT to less harmful byproducts.

### **A.3 Encapsulation of Biomolecules in Nonsurfactant Templated Mesoporous Silica**

#### **Materials**

##### **A.3.1 Introduction**

Biomolecules such as enzymes and proteins have been utilized for several catalytic and sensor applications.<sup>23-26</sup> Enzymes have found a place in many day to day house hold products, e.g., cosmetics, skin care products, detergents, etc.<sup>29-34</sup> Less obvious but extremely useful applications under the defense sector, e.g., detecting and decontaminating hazardous materials in air and water is also an area of importance.<sup>35-37</sup> Work on utilizing enzymes to produce biofuels (using readily available plant and animal products),<sup>38-40</sup> and health care products is another important application.<sup>41-43</sup> Even though the enzymes are extremely useful they are also very expensive, sensitive to changes in temperatures and pH. Thus, a method needs to be developed to protect the enzymes and make them available for reuse.

Several methods have been developed to protect these enzymes using surfactants, polymer and metal oxide substrates, etc.<sup>26,44,45</sup> At present, companies all over the world are investing heavily in developing enzyme encapsulating materials that could replace free enzymes as additives in detergents, cosmetics, hydraulic cracking and water purification applications. This move would cut down the cost of household products and increase the profit margins drastically. Obtaining highly efficient immobilized enzymes could also mean better defense products and improvement in health care products. Last but not the least; the enzyme material could also be used in place of strong and harmful chemicals, further increasing the quality of living. Some companies and university research groups that have developed enzyme materials, potential for commercialization are, Unilever Home & Personal Care USA Division of Conopco Inc.'s, Proctor & Gamble's, Sandia National Laboratory's and Pacific Northwest National Laboratory's.<sup>46,47</sup>

Even with such extensive work on developing enzyme materials, only a few technologies have found their way into commercial products. The main criteria for a technology to be successful in developing enzyme materials for commercialization are, 1) high efficiency and performance, 2) reusability, 3) extremely cheap raw materials, 4) maximum of one to two steps to obtain final products, 5) environmentally friendly synthesis procedure and, 6) versatility in immobilizing several different enzymes.

The technology developed in our group for encapsulating enzymes in nonsurfactant templated mesoporous silica materials deals successfully with all the above-mentioned criteria.<sup>2</sup> Extensive work has been done in our group for many years to test and study the technology for developing efficient enzyme materials. Several

enzymes, for e.g., lipase, protease, peroxidase, etc., have been successfully immobilized in to porous silica materials.<sup>2,28,48</sup> The effect of various reagents, solvents, temperature, surface area, porosity, etc., on the efficiency of these materials has also been tested. The technology is based on the concept of immobilizing enzymes in porous metal oxide materials using nonsurfactant templates. Further details on the significant features of this technology and its efficiency can be found in the US Patent. 6,696,258 B1 issued on Feb. 24, 2004.

Figure A-1 represents the steps involved in the formation of the enzyme-encapsulated material. A metal oxide precursor (e.g., Tetraethylorthosilicate (TEOS)) is hydrolyzed using water and HCl as a catalyst. The solution is mixed at room temperature for 30 min. Any byproduct produced during this reaction (e.g., ethanol) is extracted out using a simple vacuum pump. Desired amounts of aqueous solutions of nonsurfactant template (e.g., glucose, fructose, etc.) are then added to the hydrolyzed solution with constant stirring. Next, depending on the type of enzyme needed to be encapsulated (green fluorescence protein, protease, cellulase, lipase, etc.), either the pH of the hydrolyzed sol is adjusted before enzyme addition or an enzyme/buffer solution is added into the hydrolyzed sol with constant mixing. This is done to protect the enzymes from pH fluctuations during encapsulation. The solution thus obtained is then left to gel at the desired temperature (10 to 0 °C) and finally dried using either a lyophilizer or a low temperature vacuum drying method. The samples thus produced can be broken down into small particles or powder before use (Figure A-2). The nonsurfactant template (e.g., glucose) can be easily washed out of the samples by water extraction leaving behind porous silica materials containing enzymes. During template extraction, no enzyme

leakage is noticed. The samples are then sent to our collaborators for testing the efficiency of the enzyme materials for the desired applications. Further adjustments and changes in the sample are made, depending on requirements from companies for specific applications.

### **A.3.2 Enzyme Materials Developed**

Depending on the above stated technology, four types of enzymes were separately encapsulated in nonsurfactant templated mesoporous silica materials. A brief description on the type of enzyme, the purpose of encapsulation and the method of encapsulation is given below.

#### **A.3.2.1 Encapsulation of Green Fluorescence Protein (GFP) in Glucose Templated Mesoporous Silica Material**

The aim of this project was to study the distribution of the encapsulated protein inside the silica matrix. As noticed in Figure A-1, the enzymes are immobilized simultaneously along with the formation of the silica matrix. The template e.g., glucose tends to aggregate into 3 to 10 nm sized particles and the hydrolyzed silica sol tends to condense on top of these template aggregates. The template aggregates can then be washed out leaving behind interconnected porous structures. The enzymes are predicted to interact with the template aggregates and immobilize along with the aggregates inside the silica matrix. The mechanism involved in the encapsulation of enzymes and the final distribution of enzymes in the porous silica matrix has yet to be clearly determined. Visualizing the distribution of individual protein molecules (with diameter of 2 to 60 Å) inside the silica matrix is difficult. Until recently, there were no known microscopes that could capture images of individually, encapsulated enzymes. A detailed study on the

distribution of the encapsulated enzyme in the porous silica matrix would further help in increasing the catalytic efficiency of the samples.

The green fluorescent protein (GFP) was discovered in the early 1960s.<sup>49</sup> The chromophore that confers the typical green color and fluorescent properties to the protein is a p-hydroxybenzylideneimidazole, originated from an internal cyclization at residues Ser65, Tyr66, and Gly67 in the protein structure.<sup>50</sup> The spectroscopic properties of GFP have been intensively investigated in the recent years,<sup>51,52</sup> using the newly developed confocal microscope that is extremely powerful and has the capability of detecting the fluorescence emissions from single GFP's. Using this technology, our collaborators at University of Pennsylvania further aim to study the distribution of GFP in nonsurfactant templated silica materials. This study would thus help us determine the factors effecting the distribution of enzymes in silica matrix and improve the catalytic efficiency of the enzyme/silica materials.

#### **A.3.2.1.1 Materials and Synthesis**

Tetraethyl orthosilicate (TEOS, 99%), hydrochloric acid (HCl, 1 M),  $\beta$ -D-glucose, tris (hydroxymethyl) aminomethane (Tris), ethylenediaminetetraacetic acid (EDTA) were purchased from Sigma Aldrich (Milwaukee, WI). Recombinant green fluorescence protein (rGFP, 27-KDa monomer with 238 amino acid) was purchased from Bio Vision Incorporated, California. The initial steps of hydrolyzed silica sol preparation follow the same procedure explained under the introduction section. In a typical procedure to make 30 wt% glucose templated and rGFP encapsulated materials, 9.64 g of TEOS was mixed with 1.6 g of water and 0.1 g of HCl (1 M) for 30 min. TEOS hydrolyzed to give a clear solution. Ethanol was produced as the byproduct, which was extracted out of the solution

using a vacuum pump. 2.4 g of (50 wt%) aqueous glucose solution was then added with constant mixing for 5 min. The solution was cooled to 0 °C. 0.5 ml of rGFP/buffer solution (0.5 µg pure rGFP in 0.5 ml of 10mM tris-HCl/10 mM EDTA buffer, pH = 8 solution) was added into the sol with constant mixing. The final mixture was allowed to gel in a beaker (while it was left in the refrigerator, 6 °C) for 2 days. It was further dried for 10 days at 0 °C in vacuum. Four sets of sample varying only in wt% of glucose were produced (0, 10, 30 and 60 wt% glucose). The sample thus formed were sent to our collaborators for single molecular spectroscopy studies using confocal microscope and stored in a -20 °C freezer until use.

#### **A.3.2.2 Encapsulation of Protease in Glucose Templated Mesoporous Silica Material**

The aim of this project was to encapsulate a protease enzyme in glucose templated mesoporous silica materials for detergent applications. Enzymes play an important role in increasing the efficiency of detergents for removing dirt, stains, grease, etc., from laundry.<sup>53,54</sup> At present most of the detergents available in the market use strong chemicals and high pH (11 to 13) to increase the efficiency of detergents. Strong chemicals present in the detergents are toxic in nature and also decrease the lifespan of the washing machines and laundry.<sup>55-58</sup> In the last few years, companies have actively researched substituting strong chemicals with enzymes in detergents. Enzymes are biofriendly, required in small amounts and are highly efficient in breaking down stains, oils, etc.<sup>59-61</sup> Some of the most commonly used enzymes are: proteases to digest protein based stains,  $\alpha$ -amylase to digest starch based stains, and lipases to digest fat or oil based stains. Even though enzymes have proven to be very useful in detergent applications, they are not economical. This is because, enzymes are

sensitive to high temperatures and pH and cannot be used in their free state.<sup>62</sup> The shelf life of free enzymes in detergents is very short. Thus, a simple and inexpensive method is needed to protect the enzymes, yet maintain their efficiency in detergent applications. Keeping these points in mind a product was developed using the nonsurfactant template technology to encapsulate a particular protease enzyme provided by our collaborators in mesoporous silica materials for detergent applications.

#### **A.3.2.2.1 Materials and Synthesis**

Tetraethyl orthosilicate (TEOS, 99%), hydrochloric acid (HCl, 1 M),  $\beta$ -D-glucose, tris (hydroxymethyl) aminomethane (Tris) were purchased from Sigma Aldrich (Milwaukee, WI) and used without further purification. The protease enzyme to be encapsulated was provided by our collaborators (company A).

The initial steps of hydrolyzed silica sol preparation follow the same procedure explained under the introduction section. In a typical procedure to make 30 wt% glucose templated and enzyme encapsulated materials, 9.64 g of TEOS was mixed with 1.6 g of water and 0.1 g of HCl (1 M) for 30 min. TEOS hydrolyzed to give a clear solution. Ethanol was produced as the byproduct, which was extracted out of the solution using a vacuum pump. 2.4 g of (50 wt%) glucose solution was then added with constant mixing for 5 min. The solution was cooled to 0 °C. 20 wt% protease enzyme (with respect to silica) in tris buffer solution (0.1 M, pH = 10) was added into the sol with constant mixing. The final mixture was allowed to gel in a beaker (while it was left in the refrigerator at 6 °C) for 2 days. It was further dried for 10 days at 0 °C in vacuum. Three sets of sample varying only in wt% of glucose were produced (0, 30 and 60 wt%

glucose). The samples thus formed were sent to our collaborators for testing the efficiency of the samples as laundry detergent additives.

The samples thus produced proved to have good thermal stability, high efficiency compared to free enzymes and other enzyme-encapsulated products. The silica/enzyme samples that were produced also proved to have much better shelf life in detergents, compared to free enzymes. Our collaborators were also assisted with product scale up experiments.

### **A.3.2.3 Encapsulation of Cellulase in Glucose Templated Mesoporous Silica**

#### **Material**

The aim of this project was to encapsulate a cellulase enzyme in glucose templated mesoporous silica material for hydraulic fracturing of fuel and gas.

Hydraulic fracturing<sup>63,64</sup> is a half century-old technology that is used in oil and natural gas production. This technique allows oil or natural gas to move more freely from the rock pores where they are trapped to a producing well that can bring the oil or gas to the surface. After a well is drilled into a reservoir rock that contains oil, natural gas, and water, every effort is made to maximize the production of oil and gas. One way to improve or maximize the flow of oils from the rock bottom to the well is to connect many pre-existing fractures and flow pathways in the reservoir rock with a larger fracture. This larger, man-made fracture starts at the well and extends out into the reservoir rock for as much as several hundred feet. The fracturing process begins with the injection of water into a sealed borehole until the pressure of the water exceeds the overburden pressure and a fracture is created. Slurry composed of coarse-grained sand and a viscous fluid containing enzyme is then injected as the fracture grows away from the well. After



pumping, the sand grains hold the fracture open while an enzyme additive breaks down the viscous fluid.<sup>65,66</sup> The thinned fluid is pumped from the fracture, forming a permeable subsurface channel suitable for delivery or recovery of a vapor or liquid.

Enzyme additives play a very important role in the formation and maintenance of the fracture. It is important that the enzymes remain viable until the time when the enzymes are required to break down the viscous fluid. Fracturing takes place at elevated temperatures and in the presence of chemicals, gas, etc. Maintaining the fracture helps increase the yield of fuel and gas. Using free enzymes for this procedure is not viable as the enzymes tend to deactivate in harsh conditions of drilling and fracturing.<sup>66</sup> Hence, an encapsulated enzyme product is required where the enzymes can be protected before use. Enzyme products available in the market at present for fracturing applications are developed using an adsorption or spray dry technology on support materials. These products have proven to be less successful in fracturing applications due to the inability of the support materials to protect the enzymes from harsh environment.<sup>66</sup> Keeping these points in mind a product was developed using the nonsurfactant templated technology to encapsulate a particular enzyme provided by our collaborators (company B) in mesoporous silica materials for hydraulic fracture applications.

#### **A.3.2.3.1 Materials and Synthesis**

Tetraethyl orthosilicate (TEOS, 99%), hydrochloric acid (HCl, 1 M),  $\beta$ -D-glucose, glacial acetic acid, sodium hydroxide (5N, NaOH) were all purchased from Sigma Aldrich (Milwaukee, WI) and used without further purification. The cellulase enzyme to be encapsulated was provided by our collaborators.

The initial steps of hydrolyzed silica sol preparation follow the same procedure explained under the introduction section. In a typical procedure to make 30 wt% glucose templated and enzyme encapsulated materials, 9.64 g of TEOS was mixed with 1.6 g of water and 0.1 g of HCl (1 M) for 30 min. TEOS hydrolyzed to give a clear solution. Ethanol was produced as the byproduct, which was extracted out of the solution using a vacuum pump. 2.4 g of (50 wt%) glucose solution was then added with constant mixing for 5 min. The solution was cooled to 0 °C. 5 wt% cellulase enzyme (with respect to silica) in 1 M acetate buffer (pH = 4) solution was then added. The final mixture was allowed to gel in a beaker (while it was left in the refrigerator at 6 °C) for 2 days. It was further dried for 10 days at 0 °C in vacuum. Three sets of sample varying only in wt% of glucose were produced (0, 30 and 60 wt% glucose). The samples thus formed were sent to our collaborators for testing the efficiency of the samples as additives in the hydraulic fracturing application.

#### **A.3.2.4 Encapsulation of Lipase in Glucose Templated Mesoporous Silica Material**

The aim of this project was to encapsulate lipase enzyme in glucose templated mesoporous silica material for water purification purposes. A column packed with porous lipase encapsulated silica granules was proposed. Water containing hydrogen peroxide, (H<sub>2</sub>O<sub>2</sub>) contaminant, would then be passed through the column. The lipase present in the column would interact with the H<sub>2</sub>O<sub>2</sub>, eliminating it to produce purified water via a simple continuous flow method.

##### **A.3.2.4.2 Materials and Synthesis**

Tetraethyl orthosilicate (TEOS, 99%), hydrochloric acid (HCl, 1 M), β-D-glucose, sodium hydroxide (0.25N, NaOH) were all purchased from Sigma Aldrich (Milwaukee,

WI) and used without further purification. The lipase enzyme to be encapsulated was provided by our collaborators (company C).

The initial steps of hydrolyzed silica sol preparation follow the same procedure explained under the introduction section. In a typical procedure to make 30 wt% glucose templated and enzyme encapsulated materials, 9.64 g of TEOS was mixed with 1.6 g of water and 0.1 g of HCl (1 M) for 30 min. TEOS hydrolyzed to give a clear solution. Ethanol was produced as the byproduct, which was extracted out of the solution using a vacuum pump. 2.4 g of (50 wt%) aqueous glucose solution and 1 g of water was then added with constant mixing for 5 min. The solution was cooled to 0 °C and then 0.25 N NaOH solution was added drop wise, with constant stirring, till the hydrolyzed sol reached a pH of 6. 10 wt% lipase enzyme (with respect to silica) solution, obtained by our collaborators was added with continuous mixing. The final mixture was allowed to gel in a beaker (while it was left in the refrigerator at 6 °C) for 2 days. It was further dried for 10 days at 0 °C in vacuum. Three sets of sample varying only in wt% of glucose were produced (0, 30 and 60 wt% glucose). The samples thus formed were sent to our collaborators for testing the efficiency of the samples as additives in the water purification application.

#### **A.4 Conclusion**

The work explained in this chapter focuses on the development of products in collaboration with universities and companies utilizing a versatile sol-gel technology developed in our lab by Wei et al., and patented in 2004. The technology was fine-tuned and adapted further, depending on the type of enzyme required to be encapsulated. All the developed products utilize nanoparticles or enzymes as catalyst in various different

environments and conditions. The products are economical, highly efficient and versatile. At present, the products are at various stages of collaboration and commercialization.

## A.5 Reference List

1. Wei, Y., Jin, D., Ding, T., Xu, J. Mesoporous materials and methods of making the same. (Drexel University, USA. 99-US1116(9936357), 79. 2004. WO. 1999.
2. Wei, Y., Xu, J., Dong, H., Feng, Q. Direct encapsulation of biomacromolecules in surfactant templated mesoporous and nanoporous materials. (Drexel University, USA. 2001-US23979(2002010218), 15. WO. 2001.
3. Sposito, G., Martin-Neto, L., Yang, A. Atrazine complexation by soil humic acids. *Journal of Environmental Quality*, 25(6), 1203-1209. 1996.
4. Seybold, C. A., Mersie, W. Adsorption and desorption of atrazine, deethylatrazine, deisopropylatrazine, hydroxyatrazine, and metolachlor in two soils from Virginia. *Journal of Environmental Quality*, 25(6), 1179-1185. 1996.
5. Biradar, D. P., Rayburn, A. L. Chromosomal damage induced by herbicide contamination at concentrations observed in public water supplies. *Journal of Environmental Quality*, 24(6), 1222-1225. 1995.
6. Esser, H. O., Dupuis, G., Ebert, E., Marco, G. J., Vogel, C. s-Triazines. *Herbic.: Chemistry, Degradation Mode Action*, 1, 129-208. 1975.
7. Kruger, E. L., Coats, J. R. Fate of atrazine and atrazine degradates in soils of Iowa. *ACS Symposium Series*, 630(Herbicide Metabolites in Surface Water and Groundwater), 140-150. 1996.
8. Cheney, M. A., Shin, J. Y., Crowley, D. E., Alvey, S., Malengreau, N., Sposito, G. Atrazine dealkylation on a manganese oxide surface. *Colloids and Surfaces, A: Physicochemical and Engineering Aspects*, 137(1-3), 267-273. 1998.
9. Jordan, L. S., Farmer, W. J., Goodin, J. R., Day, B. E. Nonbiological detoxication of the s-triazine herbicides. *Residue reviews*, 32, 267-286. 1970.
10. Russell, J. D., Cruz, M., White, J. L., Bailey, G. W., Payne, W. R. Jr., Pope, J. D. Jr., Teasley, J. I. Mode of chemical degradation of s-triazines by montmorillonite. *Science (Washington, DC, United States)*, 160(3834), 1340-1342. 1968.
11. Laird, D. A., Barriuso, E., Dowdy, R. H., Koskinen, W. C. Adsorption of atrazine on smectites. *Soil Science Society of America Journal*, 56(1), 62-67. 1992.
12. Laird, D. A., Yen, P. Y., Koskinen, W. C., Steinheimer, T. R., Dowdy, R. H. Sorption of atrazine on soil clay components. *Environmental Science and Technology*, 28(6), 1054-1061. 1994.
13. Knappe, D. R. U., Snoeyink, V. L., Roche, P., Prados, M. J., Bourbigot, M. M. The effect of preloading on rapid small-scale column test predictions of atrazine removal by GAC adsorbers. *Water Research*, 31(11), 2899-2909. 1997.
14. Hayes, M. H. B. Adsorption of triazine herbicides on soil organic matter, including a short review on soil organic matter chemistry. *Residue Reviews*, 32, 131-174. 1970.
15. Stone, A. T. Reductive dissolution of manganese(III/IV) oxides by substituted phenols. *Environmental Science and Technology*, 21(10), 979-988. 1987.
16. Stone, A. T., Morgan, J. J. Reduction and dissolution of manganese(III) and manganese(IV) oxides by organics: 2. Survey of the reactivity of organics. *Environmental Science and Technology*, 18(8), 617-624. 1984.

17. Stone, A. T., Morgan, J. J. Reduction and dissolution of manganese(III) and manganese(IV) oxides by organics. 1. Reaction with hydroquinone. *Environmental Science and Technology*, 18(6), 450-456. 1984.
18. Cheney, M. A., Sposito, G., McGrath, A. E., Criddle, R. S. Abiotic degradation of 2,4-D (dichlorophenoxyacetic acid) on synthetic birnessite: a calorimetric method. *Colloids and Surfaces, A: Physicochemical and Engineering Aspects*, 107, 131-140. 1996.
19. Shin, J. Y., Buzgo, C. M., Cheney, M. A. Mechanochemical degradation of atrazine adsorbed on four synthetic manganese oxides. *Colloids and Surfaces, A: Physicochemical and Engineering Aspects*, 172(1-3), 113-123. 2000.
20. Brock, S. L., Duan, N., Tian, Z. R., Giraldo, O., Zhou, H., Suib, S. L. A Review of porous manganese oxide materials. *Chemistry of Materials*, 10(10), 2619-2628. 1998.
21. Le Goff, P., Baffier, N., Bach, S., Pereira-Ramos, J. P. Chemical lithium insertion into sol-gel lamellar manganese dioxide  $\text{MnO}_{1.85} \cdot n\text{H}_2\text{O}$ . *Journal of Materials Chemistry*, 4(1), 133-137. 1994.
22. Ching, S., Petrovay, D. J., Jorgensen, M. L., Suib, S. L. Sol-gel synthesis of layered birnessite-type manganese oxides. *Inorganic Chemistry*, 36(5), 883-890. 1997.
23. Bach, S., Pereira-Ramos, J. P., Baffier, N., Messina, R. Birnessite manganese dioxide synthesized via a sol-gel process: a new rechargeable cathodic material for lithium batteries. *Electrochimica Acta*, 36(10), 1595-1603. 1991.
24. Fritsch, S., Post, J. E., Suib, S. L., Navrotsky, A. Thermochemistry of framework and layer manganese dioxide related phases. *Chemistry of Materials*, 10(2), 474-479. 1998.
25. Imperor-Clerc, M., Bazin, D., Appay, M. D., Beaunier, P., Davidson, A. Crystallization of b-MnO<sub>2</sub> nanowires in the pores of SBA-15 silicas: in situ investigation using synchrotron radiation. *Chemistry of Materials*, 16(9), 1813-1821. 2004.
26. Aronson, B. J., Kinser, A. K., Passerini, S., Smyrl, W. H., Stein, A. Synthesis, Characterization, and Electrochemical Properties of Magnesium Birnessite and Zinc Chalcophanite Prepared by a Low-Temperature Route. *Chemistry of Materials* 11(4), 949-957. 1999.
27. Wei, Y., Jin, D. L., Ding, T. Z., Shih, W. H., Liu, X. H., Cheng, S. Z. D., Fu, Q. A non-surfactant templating route to mesoporous silica materials. *Advanced Materials (Weinheim, Germany)*, 10, 313-316. 1998.
28. Wei, Y., Dong, H., Xu, J., Feng, Q. Simultaneous immobilization of horseradish peroxidase and glucose oxidase in mesoporous sol-gel host materials. *ChemPhysChem*, 3, 802-808. 2002.
29. Shinohara, A. Deodorant-containing products. (Takasago Perfumery Co., Ltd. Japan and Novozymes A/S). 2003-209140(2005065750), 99. JP. 2003.
30. Ness, J., Simonsen, O., Symes, K. Microcapsules for household products. *Microspheres, Microcapsules & Liposomes*, 6, 199-234. 2003.
31. Yamamoto, M. Cleaning and deodorizing agents containing enzyme-producing microorganisms. (Monsieur K.K., Japan. 2000-370127(2002173699), 4. JP. 2000.

32. Olsen, A. A., Hansen, L. B. Enzyme-polymer conjugates with reduced allergenicity for household detergent, toiletry, cosmetic, pharmaceutical, food, textile, and agrochemical industry applications. (Novo Nordisk A/s, Den. 95-DK497(9617929), 88. WO. 1995.
33. Kohara, T. Enzyme-containing cleaning compositions. (Himetsubaki K.K., Japan. 88-202694(02051599), 2. JP. 1988.
34. Wang, D. I. C., Humphrey, A. E. Enzyme detergents, already a multimillion-dollar industry, are but one concrete result from . . . biochemical engineering. *Chemical Engineering* (New York, NY, United States), 86(27), 108-120. 1969.
35. Gordon, R. K. Rapid method to make OP detoxifying sponges composed of multiple immobilized enzymes of cholinesterases and op hydrolases and oximes as reactivators. (The United States of America as represented by the Secretary of the Army, USA. 2000-558512(2003113902), 31. US. 2000.
36. Gordon, R. K. Preparation of differentially acting organophosphorus- and/or organosulfur-detoxifying sponges comprising enzyme immobilized polyurethane foam. (U.S.Army Medical Research and Material Command, USA. 2000-US11072(2000064957), 61. WO. 2000.
37. Vanderberg, L. A., Foreman, T. M., Attrep, M., Jr., Brainard, J. R., Sauer, N. N. Treatment of heterogeneous mixed wastes: enzyme degradation of cellulosic materials contaminated with hazardous organics and toxic and radioactive metals. *Environmental Science and Technology* 33(8), 1256-1262. 1999.
38. Barriere, F., Kavanagh, P., Leech, D. A laccase-glucose oxidase biofuel cell prototype operating in a physiological buffer. *Electrochimica Acta*, 51(24), 5187-5192. 2006.
39. Sticklen, M. Plant genetic engineering to improve biomass characteristics for biofuels. *Current Opinion in Biotechnology*, 17(3), 315-319. 2006.
40. Zhu, Z., Momeu, C., Zakhartsev, M., Schwaneberg, U. Making glucose oxidase fit for biofuel cell applications by directed protein evolution. *Biosensors & Bioelectronics*, 21(11), 2046-2051. 2006.
41. Zhang, A. Method for manufacturing cow placenta extract by hydrolysis with different enzymes, and health-care composition containing this extract. (First Institute of Oceanography, State Oceanic Administration Peop. Rep. China. 1004-2139(1683551), 4. CN. 2005.
42. Schedel, M. Industrial biotechnology in Bayer Health Care Product Supply: more than 30 years of experience. *Chemie Ingenieur Technik*, 78(4), 485-489. 2006.
43. Wang, Z. Health care diet therapy preparation of ultrafine broad spectrum immune olyrhachis ants and the preparation method thereof. (Peop.Rep.China), 2003-105376(1524545). CN. 2003.
44. Avnir, D., Braun, S., Lev, O., Ottolenghi, M. Enzymes and other proteins entrapped in sol-gel materials. *Chemistry of Materials*, 6, 1605-1614. 1994.
45. Arnold, M. Advances in biosensors. volume 3. biosensors: a Russian perspective. *Journal of the American Chemical Society*, 119, 255. 1997.
46. Chemical and Engineering News.  
<http://pubs.acs.org/cen/coverstory/8003/8003soaps.html>. Enzyme Products. 2006.

47. Now Foods.  
[http://www.nowfoods.com/index.php?action=itemdetail&item\\_id=73882](http://www.nowfoods.com/index.php?action=itemdetail&item_id=73882).  
Enzyme Products. 2006.
48. Wei, Y., Xu, J., Feng, Q., Lin, M., Dong, H., Zhang, W. J., Wang, C. A novel method for enzyme immobilization: direct encapsulation of acid phosphatase in nanoporous silica host materials. *Journal of Nanoscience and Nanotechnology*, 1, 83-93. 2001.
49. Shimomura, O., Johnson, F. H., Saiga, Y. Extraction, purification, and properties of aequorin, a bioluminescent protein from the luminous hydromedusan, *Aequorea*. *Journal of Cellular and Comparative Physiology* 59, 223-239. 1962.
50. Cubitt, A. B., Heim, R., Adams, S. R., Boyd, A. E., Gross, L. A., Tsien, R. Y. Understanding, improving and using green fluorescent proteins. *Trends in Biochemical Sciences*, 20(11), 448-455. 1995.
51. Tsien, R. Y. The green fluorescent protein. *Annual Review of Biochemistry*, 67, 509-544. 1998.
52. Volkmer, A., Subramaniam, V., Birch, D. J. S., Jovin, T. M. One- and two-photon excited fluorescence lifetimes and anisotropy decays of green fluorescent proteins. *Biophysical Journal*, 78(3), 1589-1598. 2000.
53. Baillely, G. M., Hartshorn, R. T., Vermote, C. L. M. Detergent composition comprising source of hydrogen peroxide and protease enzyme. (Procter and Gamble Company, USA. 96-US2337(9628534), 57. WO. 1996.
54. Christensen, P. N., Gormsen, E. Detergent enzymes. *Chimica Oggi*, 11(10), 15-17. 1993.
55. Jong, G. S. Powder cleaning composition and its manufacturing method. (Jong, Geun-Sik S. Korea. 97-52778(236374), No. KR. 1997.
56. Sirisattha, S., Momose, Y., Kitagawa, E., Iwahashi, H. Toxicity of anionic detergents determined by *saccharomyces cerevisiae* microarray analysis. *Water Research*, 38(1), 61-70. 2003.
57. Almarza, E., Martinez, M. A., Sanchez de la Torre, C. Chemical analysis performed in cases of poisonings due to detergents and cleansers. *Revista de Toxicologia (Alicante, Spain)*, 19(2), 79-84. 2002.
58. Nielsen, G. D., Nielsen, J. B., Andersen, K. E., Grandjean, P. Effects of industrial detergents on the barrier function of human skin. *International Journal of Occupational and Environmental Health*, 6(2), 138-142. 2000.
59. Nagata, S., Kobayashi, H., Okuma, Y. Granular or solid bleaching detergent compositions showing good detergency and efficient stain removal in hard water. (Lion Corp., Japan. 2002-379553(2004210862), 17. JP. 2002.
60. Ryom, N. M. Detergents using enzymes. *Tinctoria*, 100(12), 50-54. 2003.
61. Wu, W., Zhang, L., Zhou, M. Aqueous laundry pre-treatment detergent containing multiple enzymes. (Shanghai White Cat Co., Ltd. Peop. Rep. China. 2000-127485(1354245), 13. CN. 2000.
62. Bornscheuer, U. T. Immobilizing enzymes: How to create more suitable biocatalysts. *Angewandte Chemie, International Edition*, 42, 3336-3337. 2003.
63. Castro Dantas, T. N., Santanna, V. C., Ntas Neto, A. A., Encar Moura, M. C. P. Hydraulic gel fracturing. *Journal of Dispersion Science and Technology*, 26(1), 1-4. 2005.



64. Schlager, B. Hydraulic fracturing: recent advances in technology have doubled the success rate in Austria. *Erdoel, Erdgas, Kohle*, 120(1), 22-25. 2004.
65. Malone, M. R., Nelson, S. G., Jackson, R. Enzyme breaker technology increases production. *JPT, Journal of Petroleum Technology*, 52(10), 36-37. 2000.
66. Miller, M., Dismuke, K. Hydraulic fracture and the development of encapsulated fracturing agents. *Rossiiskii Khimicheskii Zhurnal*, 47(4), 78-91. 2003.

Table A-1 Represent the samples produced using various wt% of urea as the nonsurfactant template and various wt% of  $\text{KMnO}_4$  as an additive.

wt% of urea <sup>b</sup> →					
wt% of $\text{KMnO}_4$ <sup>a</sup>		0	10	30	60
↓	0.5	0M0.5	10M0.5	30M0.5	60M0.5
	1	0M1	10M1	30M1	60M1
	5	0M5	10M5	30M5	60M5

<sup>a</sup>wt% of nonsurfactant template (urea) in the silica samples, <sup>b</sup>wt% of  $\text{KMnO}_4$  present in the silica sample.



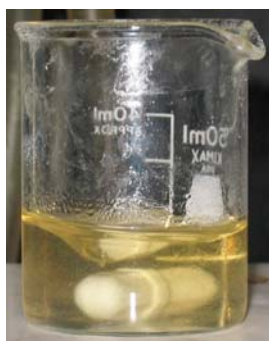
Step I



Step II



Step III



Step IV



Step V

Figure A-1. Pictorial representation of synthesis of enzyme immobilized nonsurfactant templated mesoporous silica samples. The yellow tint comes from the enzyme encapsulated.

Step I. Hydrolysis of TEOS using water and HCl to obtain a clean solution containing ethanol as the by product

Step II. Vacuum extraction of byproducts

Step III. Addition of 50 wt% glucose water solution

Step IV. Addition of enzyme solution

Step V. Gelation and drying



Figure A-2. The final enzyme immobilized sol-gel samples can be used either in the form of discs, particles or powder. The yellow ting seen in the samples is form the encapsulated enzyme.

## **Appendix B: Microfabrication of Carbon Nanopipettes for Imaging and Manipulating Live Cells**

(An Independent Research Proposal Defended and Passed On November 1<sup>st</sup>, 2004 in Partial Fulfillment of the Requirement for the Ph.D. Candidacy)

### **B.1 Proposal Statement**

Microfabrication of AFM cantilevers, containing individual, hollow multi walled carbon nanotubes, which image individual cancer cells at nanometer resolution and acts as nanopipettes for injecting and extracting minute amounts of cytoplasmic fluid from the cancer cells at short intervals of time, without causing cell death.

### **B.2 Abstract**

Recently it has been realized that, individual cells from the same region in the body behave differently to external physical and chemical stimuli. The study of the mRNA (one of the strands of the double helix DNA present inside the nucleus is replicated in large number to form the mRNA, which is then released from the nucleus membrane into the cytoplasm of the cell), produced by these cells for extended periods, contributes to the better understanding of juvenile research areas of cloning, gene therapy, cancer and tumor diagnostics, etc. At present, the only method available to extract mRNA from the cytoplasmic fluid of the cell is cell lysis. More recently, glass Micropipettes with tip diameters of 1  $\mu\text{m}$  to 100 nm are being used to manually inject or extract samples from individual cells. This technique is time consuming, harmful to the cells and sometimes causes cell death. In order to manipulate single cells without affecting their viability, it is important to use minuet cellular probes, which are easy to handle and manufacture. Carbon nanotubes are excellent cellular probe candidates as they

are hollow in nature, have high aspect ratio and good mechanical characteristics. Instruments such as optical and electron microscopes are being used to study the morphological changes of cells to external stimuli. These methods are harsh and usually cause cell death. Recently, AFM has been the instrument of choice for characterizing delicate biological live samples because of its ability to preserve the viability of the cells and produce high-resolution images. Thus combining the two important aspects, using AFM cantilevers as a source to handle individual hollow multi walled CNT for injecting and extracting minute amounts of cytoplasmic at precise locations of live cells, would bridge the gap between the nano and the micro world. This would allow us to probe and study the behavior of cancer cells to drugs in minuet details.

### **B.3 Introduction**

#### **B.3.1 Atomic Force Microscopy (AFM)**

##### **B.3.1.1 Basics of AFM**

A key element of the AFM is its microscopic force sensor or cantilever (Figure B-1). The cantilever is usually formed by one or more beams of silicon or silicon nitride.<sup>1</sup> Mounted on the end of the cantilever is a sharp tip that is used to sense a repulsion or attraction force between the sample and tip. For normal topographic imaging, the probe tip is brought into continuous or intermittent contact with the sample and raster-scanned over the surface. Fine motion piezoelectric scanners (Figure B-1,  $x$ ,  $y$ , and  $z$  axes) are used to generate the precision motion of the sample holder needed to generate topographic images and force measurements.<sup>2</sup> A well-built piezoelectric scanner can generate stable motion on a scale below 1 Angstrom.<sup>2</sup> Three-dimensional topographical maps of the surface are then constructed by plotting the local sample height versus horizontal

probe tip position.<sup>3</sup> Recently AFM is being used extensively to study biological samples because of its ability to image live biological samples at atomic resolutions, causing minimal damage to the delicate biological samples under study.<sup>4-6</sup>

### **B.3.1.2 Force Curve Measurement**

In addition to the basic imaging mode, the AFM instruments are usually equipped with a force (curve) mode,<sup>7</sup> that records the deflection of the cantilever as a function of the voltage applied to the *z*-piezo without raster scanning in the *x* and the *y* direction. The force curve measurement is a very important feature for the proposed study, as it helps in moving the AFM cantilever containing the CNT pipette in the *z* direction at precise nanometer fractions, required for injecting the CNT pipette into the cell as seen in Figure B-2.

### **B.3.1.3 Key Role of the Tip**

In order to image the samples, at sub nanometer levels, the uncertainties in the detailed nature of the probe tip must be addressed. Pyramidal or needle shaped silicon (Si) and silicon nitride ( $\text{Si}_3\text{N}_4$ ) are the two main tips used in AFM. Variation in tip-to-tip properties,<sup>8</sup> severally harming biological samples<sup>9</sup> and most importantly wearing of tips during scanning<sup>10</sup> were some of the disadvantages they poses. Carbon nanotubes are the only known materials that can overcome the above stated limitations and thus have the potential to form ideal probes for AFM imaging and injecting live bio samples.<sup>11</sup>

## **B.3.2 Carbon Nanotubes (CNT)**

### **B.3.2.1 Basics of CNT**

Carbon nanotubes consist of a honeycomb  $\text{sp}^2$  hybridized carbon network that is rolled up into a seamless cylinder<sup>12</sup> (Figure B-3), which can be a few microns in length.

There are two basic structural classes of carbon nanotubes: single-walled nanotubes (SWNTs) and multiwalled nanotubes (MWNTs). SWNTs consist of a single seamless cylinder (Figure B-3) with radii ranging from 0.35 to 2.5 nm, while MWNTs consist of multiple concentric graphene cylinders with radii ranging from 3 to 70 nm<sup>13</sup> (Figure B-4). To bring the cost of CNTs into perspective, the estimate market price of the SWNTs is \$30 to \$750/gm and that of MWNTs is low as \$10 which can range widely depending on the purity of the product.<sup>14</sup> CNTs can either have an armchair ( $n = m$ ), zigzag ( $n = 0, m = 0$ ) or chiral (any other  $n$  &  $m$  value) geometry depending of their chiral vectors ( $n, m$ ).<sup>15</sup>

### **B.3.2.2 Mechanical Property of CNTs**

The application of CNTs rely on their electrical, optical and mechanical properties.<sup>16</sup> The main property, which governs the application of the MWNTs in the proposed study, is the mechanical property. The small diameter and high aspect ratio, makes MWNTs uniquely suited as a high-resolution probe tip. The characteristics relevant to the use of nanotubes as AFM tips depend on the stiffness or Young's modulus and the ability to buckle elastically rather than break under large loads.<sup>17</sup> The extremely high Young's modulus of nanotubes is critical to the creation of high aspect ratio, sub-nanometer radius tips with high resolution<sup>18</sup> and cell injection capabilities.<sup>19</sup>

### **B.3.2.3 Growth of CNTs on AFM Cantilever**

Realizing the unique advantages of CNT, many efforts have been made to fabricate CNT-based imaging probes. Most reported work so far has relied on a "pick and stick" approach to manually attach MWNTs on silicon pyramid tips under an optical microscope.<sup>19</sup> Direct catalytic growth of CNTs on silicon pyramid tips using thermal chemical vapor deposition (CVD) methods have also been looked into.<sup>20</sup> However, the



methods mentioned above have many disadvantages: 1) they have little control over the CNT location, density, length, orientation and number. 2) It becomes extremely difficult to obtain individual freestanding and well-oriented MWNTs using thermal CVD. 3) Readily usable tip yields are very low. 4) In addition, these processes all depend on commercially available silicon tips or prefabricated commercial silicon probe wafers.<sup>21</sup> Recently plasma enhanced chemical vapor deposition (PECVD) is being used to grow aligned CNTs.<sup>22</sup> In this method, an electric field is applied in a plasma discharge to direct the nanotubes to grow and align parallel to the field. The CNTs thus grown are always aligned and Multi walled in nature. Depending on the temperature of growth, type of carbon source used, and the position of the catalyst on the growing CNTs (catalysts particle remains either on top or bottom of the CNT), the CNTs can be completely hollow or bamboo shaped<sup>22</sup> (Figure B-5). Selecting the right growth characteristic, one can use PECVD to grow single hollow CNTs on silicon wafers which then can be micromechanically modified to fabricate AFM cantilevers containing hollow CNT.

### **B.3.3 Microfabrication Techniques**

The main hurdle in nanoscience and nanotechnology is the integration of nanoscale materials with micron scale structures to form workable devices. Although there are, numerous works discussing the synthesis, structure and properties of nanomaterials, studies related to nano-micro integration for device and sensor fabrication are very limited. In the proposed project a simple method of integrating a nanostructure, i.e., MWNT with a systematically fabricated microdevice i.e., a modified AFM cantilever has brought forth an integrated device, which acts as a sensor as well as a nanopipette. Microfabrication is simply the science of miniaturization (Figure B-6), which is accom-

plished by using steps such as: 1) lithography which is a method used to transfer copies of a master pattern onto the surface of a solid material, with the help of a photoresist and also to fabricate microchannels and nanopores for catalyst deposition using electron beams or X-rays, 2) spin coating and spray coating which helps in deposition of polymer materials, which form the bulk of the nanopipette, 3) mechanical and chemical polishing which is used to planarize rough and uneven surfaces and finally, 4) wet and dry etching which uses concentrated acids and dry gases respectively to shape and bring microstructures to desired form.<sup>23</sup>

## **B.4 Design Concept and Theoretical Consideration**

### **B.4.1 AFM Cantilever Nanopipette Design**

Before the actual fabrication of the AFM cantilever containing the carbon nanopipette, there are several theoretical concepts, which need to be evaluated in detail. The Figure B-7 series represents the various steps for the fabrication of the microstructure whose experimental details will be explained under the experimental section. In this section, each step in turn is analyzed theoretically and narrowed down to the best workable route. The entire fabrication section is divided into two major parts, one deal with the fabrication of the nanopipette and other deals with the fabrication of the main cantilever head.

#### **B.4.1.1 Substrate Used to Grow CNT and to Fabricate the Body of the AFM**

##### **Cantilever**

In the proposed study a simple 4 mm diameter silicon wafer can be used to grow CNTs,<sup>21</sup> which at the end of the fabrication steps will represent the head of the AFM cantilever (Figure B-7).

#### **B.4.1.2 Sketching Repeated Alignment Marks on the Silicon Wafers for Multi Fabrication of the Nanopipette**

((Figure B-7, Top View) as the proposed design consists of various micro and nanofabrication steps, the allowed error in marking and aligning various individual fabrication steps with respect to the other, is in the nanometer range. The two types of alignment marks, which are required, are the **Wafer Marks**: The wafer marks (or called global marks) are used to help find the center of the wafer. **Chip Marks**: The chip marks help determine position, rotation, magnification, and trapezoidal corrections for each repeating unit in a silicon wafer. The above mentioned alignment marks can be easily written using the software available in all e-beam lithographical instruments (e.g. Hitachi HL-700F).<sup>25</sup>

#### **B.4.1.3 Theoretical Evaluation of Growth of CNT on Silicon Wafer**

Types of metal catalysts used to grow CNTs are Nickel (Ni), Cobalt (Co), Iron (Fe) and molybdenum (Mo).<sup>21</sup> The three main methods by which these catalysts can be deposited on silicon wafer are Spin coating, metal vapor deposition, and e-beam sputtering. Methods used to grow CNTs are thermal vapor deposition (TVD), chemical vapor deposition (CVD),<sup>23</sup> microwave plasma vapor deposition,<sup>26</sup> plasma enhance chemical vapor deposition (PECVD), etc. Gases used as carbon sources for growth of CNTs are, a mixture of ammonia (NH<sub>3</sub>) and acetylene (C<sub>2</sub>H<sub>2</sub>) or Hydrogen (H<sub>2</sub>).<sup>22</sup> There are several combinations of the above-mentioned methods, which have been used to grown CNT. In the proposed study: The catalyst selected is Ni, as it can be easily deposited on the silicon wafer and most importantly, the CNT can be directed to grow as a well aligned hollow CNT. E-beam lithography (e.g. Hitachi HL-700F) can be selected

to make nanoscale markings (50nm) on the silicon wafer for the vapor deposition of Ni catalyst thus ensuring the growth of individual MWNTs. PECVD can be used to grow the CNTs as it gives aligned growth.

#### **B.4.1.4 Deposition of Support Layer**

After the CNTs are grown on the surface of a silicon wafer, silicon dioxide is then deposited on individual CNTs and silicon wafer, using a chemical-vapor deposition method.<sup>27</sup> The purpose of depositing silicon dioxide on the substrate and CNT is to attach the CNT to the silicon wafer and to make them robust enough for nanopipette applications (Figure B-7.7).

#### **B.4.1.5 Filler Used to Embed CNTs**

Filler is deposited on the CNTs and substrate for surface planarization purposes. Some important properties a filler should possess in case of the proposed study are, they should be compatible with the silicon wafer, good gap filling properties, easily deposited onto the wafer and most importantly the filler should have an etch rate 4 to 5 times faster than SiO<sub>2</sub>. Silicon nitride (Si<sub>3</sub>N<sub>4</sub>) is one such filler, which has all the above mentioned properties (Figure B-8).

#### **B.4.1.6 Fabrication of the Body of the AFM Cantilever**

After filler deposition, the silicon wafer is turned over and the bottom part of the wafer is then fabricated to produce the body of the AFM cantilever. The AFM body of the cantilever has three unique features, **1)** a reservoir at the head of the cantilever which is dry etched gradually until it hits the silicon dioxide layer present at the upper side of the silicon wafer, **2)** a hollow fluid flow channel which can be etched and connected to the reservoir, **3)** a high reflectance “Pyrex glass slide which is used to seal the reservoir

and the fluid flow channel, present on top of the AFM cantilever head Figure B-7.9 & 7.10.

#### **B.4.1.7 Opening the CNTs to Form Nanopipettes**

After the fabrication of AFM cantilever (Figure B-7), the silicon wafer is tuned back up to complete the final work on nanopipette production. Manual paper polishing, chemical mechanical planarization<sup>28</sup> and dry reactive ion etching (RIE)<sup>29</sup> are three main polishing methods which could be used to open the tips of CNTs. The 1<sup>st</sup> two methods are wet methods which require concentrated acid slurries, which could block the hollow CNTs while polishing. The last method RIE method uses a dry polishing method, produces a relatively smooth surface, and most importantly does not block the CNTs. Thus, RIE and ion milling can be used to polish the filler material and remove any catalytic nickel particles blocking the tip of the CNT. Next, a chemical reactive ion etching is used to completely etch away  $\text{Si}_2\text{N}_3$  and partially etch  $\text{SiO}_2$  to expose approximately 3  $\mu\text{m}$  length of free CNT, leaving the rest of the CNT base covered with  $\text{SiO}_2$  for mechanical support.

#### **B.4.2 Penetration of Cell Membrane Using AFM Cantilever Nanopipette**

A successful injection is determined mainly by the applied force on the cell membrane, injection speed and trajectory. Manual and micromanipulator assisted injections cannot record the force applied on a cell membrane nor can they monitor the speed and trajectory accurately. AFM cantilever for that matter can be moved in the z direction in sub-nanometer range using piezo-electric transducers, which helps monitor force as well as speed. The important points, which need to be evaluated before successful cell injection using MWNT, are as follows, as seen in Figure B-8.

#### **B.4.2.1 Cell Membrane**

The cell membrane serves as a gateway, which helps to control materials going in and out of the cell. Structurally, the membrane is made of phospholipids in which are embedded different kinds of protein molecules, glycolipids and glycerol.<sup>30</sup> Phospholipids make the major constituents of the cell membrane and give way easily to sharp objects or needles with minimal resistance of forces as small as few Pico Newton.

#### **B.4.2.2 Role of AFM Probe Tip**

It was noted that sharp tips made of silicon nitride caused cell damage when used to scan cell surfaces. Among CNTs, SWNT was shown to give very high resolution images but buckled when brought too close to the cell membrane.<sup>31</sup> Instead MWNT for that matter were ridged enough not to buckle but flexible enough not to cause any harm to the cell membrane while scanning its surface,<sup>32</sup> thus MWNT can be used as AFM probe tips as well as cell injectors.

#### **B.4.3 Study of Interaction Force Curves and Young's Modulus**

Previous studies have investigated the force interactions between living cells and the AFM tips by constructing force-distance curves and have suggested that blunt tips (1 micrometer to 200 nm diameters) deform the cells and sharp tips penetrate the cells. To further test this hypothesis, two force-distance curves which compare the piezo-induced movement of the tip in the  $z$  axis with the displacement of the tip by the cell on a glass slide were compared<sup>33</sup> as seen in Figure B-9.

#### **B.4.4 Theorization of the Movement of Fluids in and out of the MWNT**

Before evaluating different experimental methods for injecting samples into live cells, actual basic concept of movement of fluids in the MWNT has to be considered. The

inner diameter of the MWNTs used in the proposed study is around 20-30nm. Fullerenes, metal nanoparticles, radioactive elements and dyes have been successfully encapsulated<sup>34,35</sup> inside single and multiwalled CNTs using high temperatures, pressures and super critical fluids. The methods mentioned above use harsh conditions, and hence, are not compatible for encapsulating, and transporting bio samples. There have also been some successful attempts of encapsulating fluids<sup>36</sup> and partial encapsulation of DNA inside the carbon tubes.<sup>37</sup> An evaluation of some simple methods to transport bio-fluids through MWNTs has been discussed below.

#### **B.4.4.1 Capillarity Action**

The ability of CNTs to encapsulate and transport fluids depends on two main characteristics: fluids must 'wet' the capillaries and have surface tensions below a threshold value<sup>38</sup> (depending on the diameter of the CNT) and the fluid should not chemically interact with the CNTs. Thus simply by immersing open ended MWNTs (5nm inner diameter) in silver nitrate ( $\text{AgNO}_3$ ) and gold chloride ( $\text{AuCl}_3$ ) solutions, Chu et al.,<sup>39</sup> were able to transport the metal salts inside the CNTs.

#### **B.4.4.2 Transport of DNA Through a Membrane Embedded with MWNT (20-30 nm)**

On one side of a synthetic cell membrane, a buffer solution is placed and on the other side a DNA solution. When potential is applied to this set up, DNA transport through the CNT takes place.

#### **B.4.4.3 DNA Injection and Extraction Through a Glass Pipette**

DNA solution and other bio-fluids have also been studied extensively by using glass pipettes with diameters as small as 100 nm.<sup>40</sup> Here the nanopipette is manipulated

by applying an ion current that flows between electrode in a solution containing DNA and the electrode in the nanopipette. Thus, a high electric field causes a pulsating delivery of DNA solution into or out of the pipette. Considering the 3 main methods stated above transport through the AFM cantilever nanopipette can be further enhanced by connecting a micro pump and an electrode directly in to the fluid channel, which in turn could be connected to the reservoir on the AFM cantilever. Thus, a simple method of capillary action combined with pressure suction and or voltage application can be used to inject or extract bio-fluids without causing any harm to the live cell.

### **B.5 Experimental Conditions**

Below a simple step wise procedure for the fabrication of the AFM cantilevers nanopipette is listed (Figure B-7 series).

- 1) The silicon wafer 100mm (2-in) diameter and 20 micrometer thick can be selected as a substrate for growing CNT and AFM cantilever.
- 2) A sensitive bilayer resist made of low and high molecular weight poly (methyl methacrylate) (PMMA) in methyl isobutyl ketone and isopropyl alcohol (3:1), 100nm thick can then be applied onto the silicon wafer via spinning at 1000-5000 rpm for 60 sec and then prebaked at 170<sup>0</sup>C for 30 min
- 3) Using Hitachi HL-700F Electron Beam Lithography Machine (HL-700F) instrument for local and global alignments on both sides of the wafer are made and 50 nm diameter spots for catalyst deposition on the top side of the wafer.
- 4) The surface of the silicon wafer can then be cleaned off all the debris using a short O<sub>2</sub> plasma descum and a thin layer of Ni (approx 20nm thick) can be deposited on the top side of the wafer using the same e-beam instrument.



- 5) The resist from step 2 can then be lifted off the silicon wafer using acetone, thus (leaving behind 20 nm spots of nickel catalyst) taking with it all the unwanted the nickel metal present on it.
- 6) The patterned wafer can then be loaded into a plasma-enhanced-hot-filament CVD system for the growth of CNTs (6-7 $\mu$ m long).
- 7) Conformal chemical vapor deposition of silicon dioxide around the CNTs and on the substrate can then be carried out
- 8) Deposition of filler ( $\text{Si}_3\text{N}_4$ ) is performed by spin method.
- 9) A photoresist of 1 to 2  $\mu$ m thick is deposited on the bottom side of the wafer.
- 10) A fluid channel and a reservoir are then etched using dry silicon etch method exactly on the alignment marks deposited on the wafer in step 3 and a Pyrex glass with the same dimensions of the cantilever is then used to seal the top of the AFM cantilever head.
- 11) Surface polishing on the top side of the wafer is then done using reactive ion etching (RIE) which uses  $\text{CF}_4/\text{O}_2$  gases at a certain watt power followed by Argon (Ar) ion milling to polish, equalize and open the tips of CNTs.
- 12) Approximately 3 $\mu$ m of silicon dioxide and all of  $\text{Si}_3\text{N}_4$  is etched away by chemical RIE using combination of gasses ( $\text{CF}_3/\text{O}_2/\text{N}_2$ )

Thus (hollow CNTs partially covered with  $\text{SiO}_2$ ) nanopipettes can be fabricated as mentioned above using an automated large scale method or manual one on one base.

## **B.6 Application**

### **B.6.1 Application of the AFM Cantilever Nanopipette With Regard to Influence of Cancer Drugs on Individual Cancer Cells**

The properties of indivisible cells depend on molecules that constitute them<sup>41</sup>. Depending on the applications and external stimuli, individual cells in the body produce different kinds of mRNA, the mRNA in-turn produces proteins.<sup>42</sup> Thus any change caused by the cell or on the cell is an indirect effect of the production of different kinds of mRNA. The cells which are exposed to carcinogenic (cancerous) agents produce specific and large quantities of mRNA (which in-turn produce proteins) not produced in normal cells.<sup>43</sup> The proteins in-turn directs the cells to replicate in large numbers causing tumors. Cancer fighting drugs attack cancer causing proteins present in the cytoplasm, which in-turn destroys the cancer cell. It is very important to test the reaction of individual cells to drugs, as each individual cancer cell even if present in the same cancer patient react differently to the same drug.<sup>44</sup> The study of change in cell surface properties, quantity and type of mRNA produced or destroyed in an individual cell during various drug exposure sessions, helps in deciding on the specific type of drug, which would be most compatible for a cancer patient. Cancer cells which were exposed to different drugs till date were studied by rupturing the cells<sup>45</sup> and extracting the mRNA from the cytoplasmic fluid. Recently micropipettes are being used to extract small amounts of cytoplasmic fluid from the cells which are then analyzed for mRNA.<sup>46</sup> The two main disadvantages of using cell rupture and micropipette methods are 1) as the exposure time of drugs to cancer cells increases, the quantity and type of mRNA produced also changes. Understating this fluctuation of mRNA in the cytoplasm is very essential for efficient drug use. In the

above two mentioned methods the cancer cells are destroyed after just one extraction session of cytoplasm and thus lack the criteria for further tests, 2) there are many surface changes, which also take place due to drug exposure or other external stimuli that can not be studied using the above mentioned methods. Using AFM cantilever nanopipette devices, not only can the surface of a live cancer cell be studied at nanometer resolution, the nanopipette can also be used to extract nanoliters of cytoplasmic fluids several times from the same cell for a long period without causing cell death.

## **B.7 Characterization**

To test and prove the working condition of the AFM cantilever nanopipette some basic characterization steps can be conducted.

### **B.7.1 TEM**

Transmission electron microscope can be used to study the morphology of the CNTs (diameter, hollow nature, etc.).

### **B.7.2 Gas and Fluid Flow Test**

CNT as a whole along with the filler intact can be easily lifted of the silicon wafer as a porous membrane. The membrane is then checked for any blockages present in the CNTs by placing the CNT membrane between two ends of a tube. The membrane is then exposed to  $N_2$  gas or ion solution on one side of the tube and on the other end a detector is placed to test the permeability of the gas or solution through the CNT membrane.<sup>47</sup>

### **B.7.3 Test the Workability of Single Nanopipettes**

The amount of sample collected by individual MWNT from inside the cells can also be tested by ejecting out the solution from within a CNT onto a flat slide and measuring the spot size as well as the chemical content of the solution released.

## B.8 Possible Experimental Out Comes

There could be four main possible out comes of using the AFM cantilever as a nanopipette. 1) Successful microfabrication, high resolution images of live cells along with easy suction and release of sample from within the CNT. Goal achieved and no further action required. 2) Unsuccessful microfabrication: Two to three different possible paths of microfabrication can be designed and studied and the most successful design can be chosen. The CNT nanopipette and the cantilever head can be fabricated in one major set as proposed in this paper or they can be fabricated separately and then combined together using an adhesive. 3) Unsuccessful penetration of the CNT into a live cell: buckling of CNT can be one reason for unsuccessful injection of the CNT. The outer wall of the CNT protruding out of the silicon dioxide layer can be covered with a layer of polymer to enhance the mechanical properties of the tube. As the amount of force required to penetrate a cell depends on the elasticity of the cell membrane, different force curves can also be studied to decide on the accurate force finally required. 4) Unsuccessful movement of bio-fluids in and out of the CNT: If blockage of the CNT is one reason for unsuccessful movement, then different catalyst, ratio of carbon source, temperature and voltage parameters, etc., can be studied to get completely hollow CNTs. If a simple capillary action is not enough for the suction of the bio-fluids inside the CNT, then pressure using micro pumps or voltage can be applied to suck or force fluids out of the CNT. The tip of the CNT can be modified using polymer to attract the Bio fluids inside the tubes. Individual CNTs can be also grown using a template method, which gives tubes with similar outer diameter as that of catalyst grown nanotubes but larger inner diameter for easy flow of fluids inside the tube.

## B.9 Conclusion

The proposed fabrication of an AFM cantilever nanopipette is a means of experimentally proving the feasibility of using a CNT as a nanopipette for testing single live cells. The fabrication of such micro-devices is easily achievable, because of the vast knowledge collected over the years in micro-fabrication areas. Complicated devices smaller than the diameter of hair have also been fabricated. The proposed nanopipette provides a good example of a device, which incorporates the nano and the micro device in few simple steps. In addition, the proposed AFM cantilever nanopipette offers the following advantages: 1) the extremely difficult task of handling individual CNTs is made easy by incorporating a micro device. 2) The device not only acts as a sensor for studying the structural details of a sample at sub-nanoscale resolution, but at the same time it also acts as a nanopipette for injecting and extracting minute samples from within cells. 3) Multiple sample injections to a single cell can be conducted without harming the cell. 4) Batch fabrication process of AFM cantilever nanopipettes could produce as many as 200 devices using a 300 mm silicon wafer. Even though the numbers of fabrication steps required to build the device are many, the actual amount of time required for each step ranges from 2 sec to 60 min. Except for silicon wafer all other materials required for the fabrication of the device are in minute quantities. Silicon wafers are also very easy to process and the raw materials required for the production of the wafer are found abundantly in nature. Thus, the final cost of a single AFM cantilever nanopipette could range from 20 cents to a few dollars depending on the quality of the raw materials used. Finally, this device could help shine light and contribute immensely to the study of single organisms, which in turn would help us answer unanswered questions about the behavior

of indivisible cells to various chemical and physical stimuli such as toxins, drugs, temperature, pressure, etc.

## B.10 Reference List

1. DeRose, J. A. Revel, J. P. Examination of atomic (scanning) force microscopy probe tips with the transmission electron microscope. *Microscopy and Microanalysis*, 3(3), 203-213. 1997.
2. Rangelow, I. W., Shi, F., Hudek, P., Gotszalk, T., Grabiec, P. B., Dumania, P. Fabrication of piezoresistive sensed AFM cantilever probe with integrated tip. *Proceedings of SPIE-The International Society for Optical Engineering*, 2879(Micromachining and Microfabrication Process Technology II), 56-64. 1996.
3. Satoh, N., Kobayashi, K., Watanabe, S., Fujii, T., Horiuchi, T., Yamada, H., Matsushige, K. Dynamic-mode AFM using the piezoelectric cantilever: investigations of local optical and electrical properties. *Applied Surface Science*, 188(3-4), 425-429. 2002.
4. Stobinski, L., Tomasik, P., Lii, C. Y., Chan, H. H., Lin, H. M., Liu, H. L., Kao, C. T., Lu, K. S. Single-walled carbon nanotube-amylopectin complexes. *Carbohydrate Polymers*, 51(3), 311-316. 2002.
5. Lehenkari, P. P., Charras, G. T., Nykanen, A., Horton, M. A. Adapting atomic force microscopy for cell biology. *Ultramicroscopy*, 82(1-4), 289-295. 2000.
6. Jimenez-Garcia, L. F., Frago-so-Soriano, R. Atomic force microscopy of the cell nucleus. *Journal of Structural Biology*, 129(2/3), 218-222. 2000.
7. Kawai, A. Adsorption force variation due to wearing of micro tip apex on cleaved mica surface. *Nippon Setchaku Gakkaishi*, 36(5), 172-175. 2000.
8. Zou, J., Wang, X., Bullen, D., Ryu, K., Liu, C., Mirkin, C. A. A mould and-transfer technology for fabricating scanning probe microscopy probes. *Journal of Micromechanics and Microengineering*, 14(2), 204-211. 2004.
9. Woolley, A. T., Li Cheung, C., Hafner, J. H., Lieber, C. M. Structural biology with carbon nanotube AFM probes. *Chemistry & Biology*, 7(11), R193-R204. 2000.
10. Mannelquist, A., Almqvist, N., Fredriksson, S. Influence of tip geometry on fractal analysis of atomic force microscopy images. *Applied Physics A: Materials Science & Processing A66(Suppl., Pt. 2, Scanning Tunneling Microscopy/Spectroscopy and Related Techniques)*, S891-S895. 1998.
11. Guo, L., Liang, J., Dong, S., Xu, Z., Zhao, Q. Property of carbon nanotube tip for surface topography characterization. *Applied Surface Science*, 228(1-4), 53-56. 2004.
12. Souza Filho, A.G., Fagan, S.B., Mendes Filho, J. Carbon nanotubes as a model system for discussing nanoscience. 2004.
13. Yu, M. F., Lourie, O., Dyer, M. J., Moloni, K., Kelly, T. F., Ruoff, R. S. Strength and breaking mechanism of multiwalled carbon nanotubes under tensile load. *Science (Washington, D.C.)*, 287(5453), 637-640. 2000.
14. Ouellette, J. Building the nanofuture with carbon tubes. *The Industrial Physicist*, 22(30). 2003.
15. Baughman, B. R., Zakhidov, A. A., Heer, W. Carbon nanotubes—the route toward applications. *Science*, 297. 2002.

16. Dresselhaus, M. S., Dai, H. G. E. Carbon nanotubes: continued innovations. *Materials Research Symposium Bulletin*, 26. 2004.
17. Ye, Q., Cassell, M. A., Liu, H., Chao, K-J., Han, J., Meyyappan, M. Integrating carbon nanotubes for atomic force microscopy imaging applications. *Materials Research Society Symposium Proceeding*, 820. 2004.
18. Poncharal, P., Wang, Z. L., Ugarte, D., De Heer, D. Electrostatic deflections and electromechanical resonances of carbon nanotubes. *Science*, 283, 1513-1516. 1999.
19. Dai, H., Hafner, J. H., Rinzler, A. G., Colbert, D. T., Smalley, R. E. Nanotubes as nanoprobe in scanning probe microscopy. *Nature (London)*, 384(6605), 147-150. 1996.
20. Liu, J., Fan, S., Dai, H. Recent advances in methods of forming carbon nanotubes. *Materials Research Symposium Bulletin*, 29(4), 244-250. 2004.
21. Ye, Q., Cassell, M. A., Liu, H., Chao, K-J., Han, J., Meyyappan, M. Large-scale fabrication of carbon nanotube probe tips for atomic force microscopy critical dimension imaging applications. *Nanoletters*, 0, 20. 2004.
22. Meyyappan, M., Delzeit, L., Cassell, A., Hash, D. Carbon nanotube growth by PECVD. *Plasma Sources Science and Technology*, 12, 205-216. 2003.
23. Madou, J. M. *Fundamentals of microfabrication*. CRC-Press, London. 2002.
24. Cohn, M. B., Bohringer, K. F., Noworolski, J. M., Singh, A., Keller, C. G., Goldberg, K. Y., Howe, R. T. *Microassembly technologies for MEMS*. Proceedings of SPIE-The international society for optical engineering, *Micromachined Devices and Components IV*, 2-16, 3514. 1998.
25. Stanford Nanofabrication Facility. <http://snf.stanford.edu/Process/Process.html>. Nanofabrication. 2004.
26. Maschmann, M. R., Goyal, A., Iqbal, Z., Fisher, T. S. Gat, R. Growth and characterization of single-walled carbon nanotubes by microwave plasma-enhanced chemical vapor deposition. *Applied Physics Letters*, 30, 1574. 2004.
27. Rai-Choudhury, P. *Microolithography. Micromachining. Microfabrication*. SPIE Press monograph, PM39-PM40 IEE materials & devices series, 12A-12B. 1998.
28. Li, J., Ye, J., Cassell, A., Hou, T. N., Stevens, R., Han, J., Meyyappan, M. Bottom-up approach for carbon nanotube interconnects. *Applied Physics Letters*, 82. 2003.
29. Holt, J. K., Noy, A. T., Huser, D. E., Bakajin, O. Fabrication of a carbon nanotube-embedded silicon nitride membrane for studies of nanometer-scale mass transport. *Nanoletters*, 0, a-f. 2004.
30. Huskey J. R. <http://wsrv.clas.virginia.edu/~rjh9u/humbiol.html>. Human Biology Web Site. 1996.
31. Lee, S. I., Howell, S. W., Raman, A., Reifenberger, R., Nguyen, C. V., Meyyappan, M. Nonlinear tapping dynamics of multi-walled carbon nanotube tipped atomic force microcantilevers. *Nanotechnology*, 15(5), 416-421. 2004.
32. Nguyen, C. V., So, C., Ramsey, R. M., You, L. Lance, D., Philippe, S., Meyyappan, M. High lateral resolution imaging with sharpened tip of multi-walled carbon nanotube scanning probe. *Journal of Physical Chemistry B*, 108(9), 2816-2821. 2004.



33. Philippe, P., Wang, Z. L., Ugarte, D., De Heer, W. Membrane deformation of living glial cells using atomic force microscopy. *Journal of Microscopy*, 182, 114-120. 1996.
34. Britz, D. A., Khlobystov, A. D., Wang, J. B., O'Neil, S. A., Poliakoff, A., Ardavanc, A., Briggs, A. Selective host-guest interaction of single-walled carbon nanotubes with functionalised fullerenes. *Chemical Communications*, 176-177. 2004.
35. Takenobu, T., Takano, T., Shiraishi, M., Murakami, Y., Ata, M., Kataura, H., Achiba, Y. Iwasa, Y. Stable and controlled amphoteric doping by encapsulation of organic molecules inside carbon nanotubes. *Nature Materials*, 2, 683-688. 2003.
36. Rossi, M. R., Ye, H., Gogotsi, Y., Babu, S., Ndungu, P., Bradley, J-C. Environmental scanning electron microscopy study of water in carbon nanopipes. *Nanoletters*, 0, a-e. 2004.
37. Cui, D., Ozkan, C. S., Kong, Y., Gao, H. Experimental study of filling carbon nanotubes with nucleic acids. *Materials Research Society Symposium Proceedings 820(Nanoengineered Assemblies and Advanced Micro/Nanosystems)*, 89-99. 2004.
38. Dujardin, D., Ebbesen, T. W., Hiura, H., Tanigaki, K. Capillarity and wetting of carbon nanotubes. *Science*, 265, 1850-1852. 1994.
39. Chu, A., Cook, J., Heesom, J. R., Hutchison, L. H., Green, G. L., Sloan, J. Filling of carbon nanotubes with silver, gold, and gold chloride. *Chemistry Materials*, 8, 2751-2754. 1996.
40. Ying, L., White, S. S., Bruckbauer, A., Meadows, L., Korchevz, Y. H., Klenerman, D. Frequency and voltage dependence of the dielectrophoretic trapping of short lengths of DNA and dCTP in a nanopipette. *Biophysical Journal*, 82, 1018-1027. 2004.
41. Jain, S. Cell mechanisms key to disease. *The daily online Californian* . 2004.
42. Osada, T., Uehara, H., Kim, H., Ika, T. mRNA analysis of single living cells. *Journal of Nanobiotechnology*, 26, 156-159. 2003.
43. Church, J. G., Stapleton, E. A., Reilly, B. D. Isolation of high quality mRNA from a discrete cell cycle population identified using a nonvital dye and fluorescence activated sorting. *Cytometry*, 14(3), 271-275. 1993.
44. BCCA information database. *Chemotherapy Side Effects*. 2004.
45. Hukkanen, J. Xenobiotic-metabolizing cytochrome P450 enzymes in human lung. *Materials and methods*. University of Oulu, Oulun Yliopisto. 2001.
46. Lambolez, B., Audinat, E., Bochet, P., Crepel, F., Rossier, J. AMPA receptor subunits expressed by single Purkinje cells. *Neuron*, 9, 247-258. 1992.
47. Hinds, B. J., Chopra, N., Rantell, T., Andrews, R., Gavalas, V., Bachas, L. Aligned multiwalled carbon nanotube membranes. *Science*, 303, 62-65. 2004.

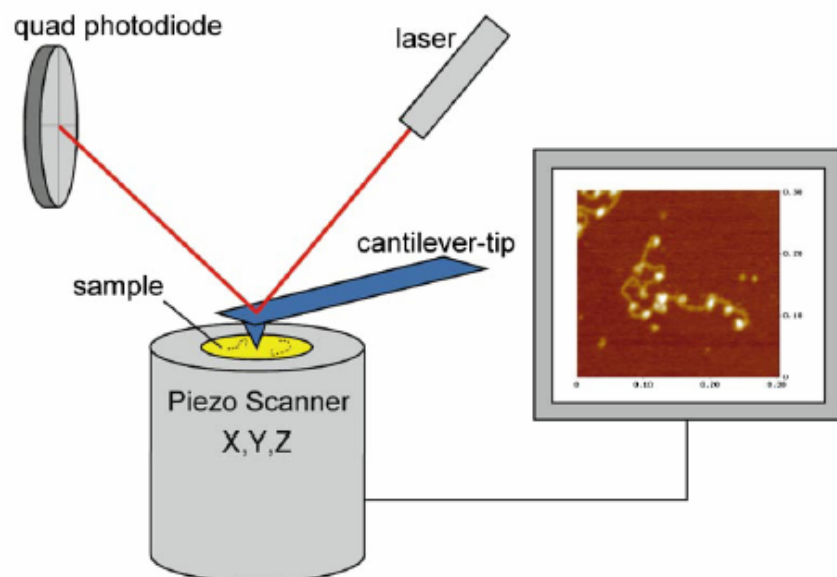


Figure B-1. Schematics of atomic force microscopy.

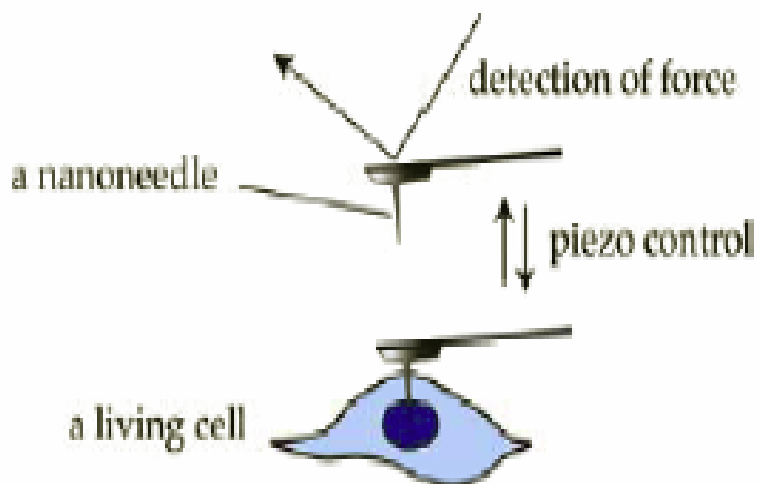


Figure B-2: Movement of cantilever in the z direction. <http://www.nano-lab.com/imagegallery.html>.

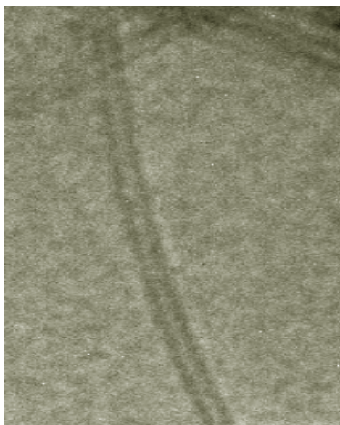


Figure B-3. Single walled CNT. <http://www.veeco.com/default.asp>.

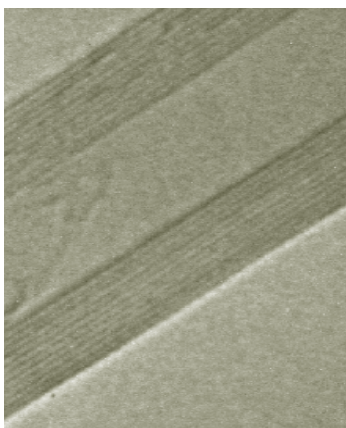


Figure B-4. Multiwalled CNT. <http://www.veeco.com/default.asp>.

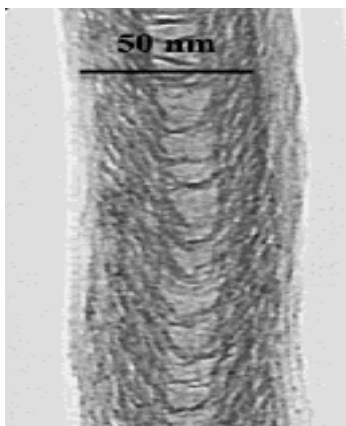


Figure B-5. Bamboo shaped CNT. <http://www.veeco.com/default.asp>.

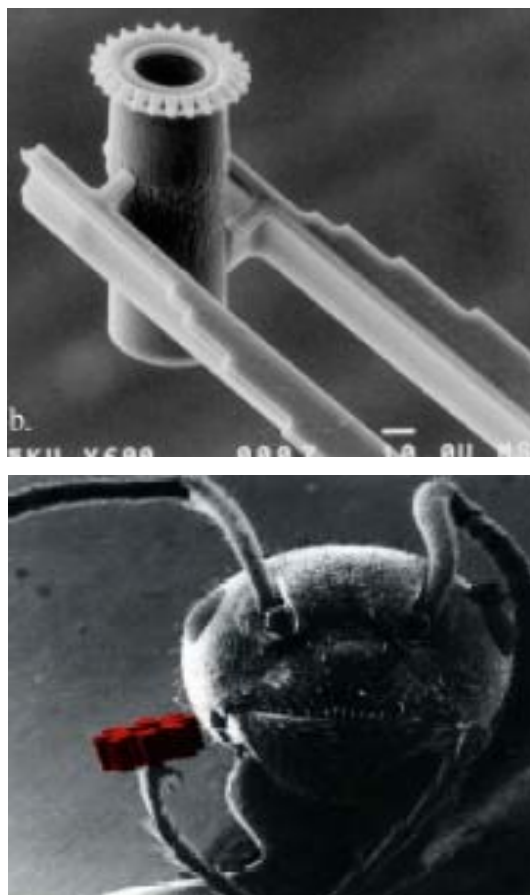
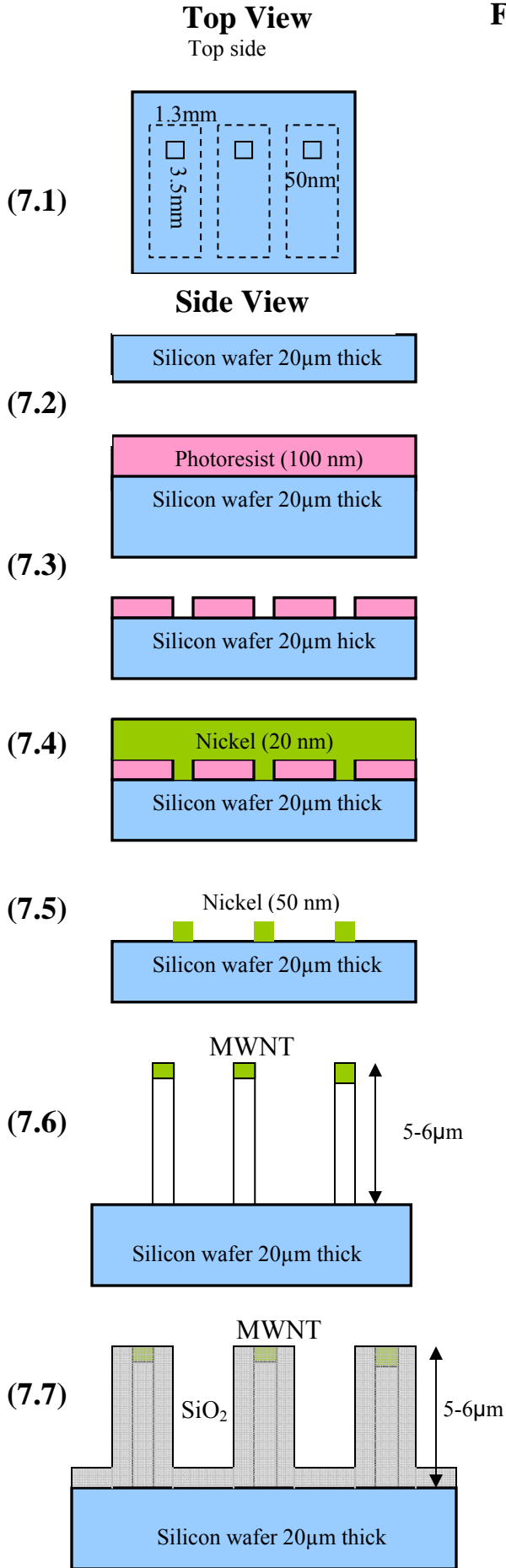
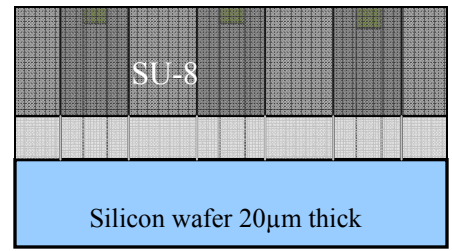


Figure B-6a&b. Miertweezers by Si etching<sup>24</sup> & microsized nut compared to an ant<sup>23</sup>

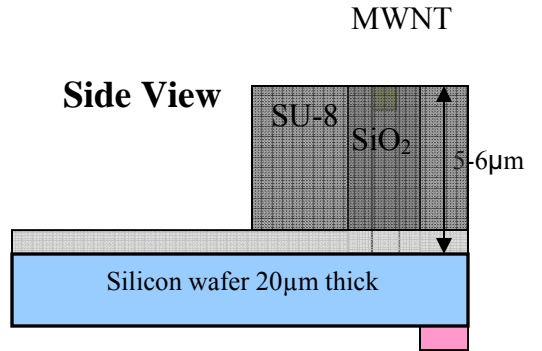
**Figure 7 Series**



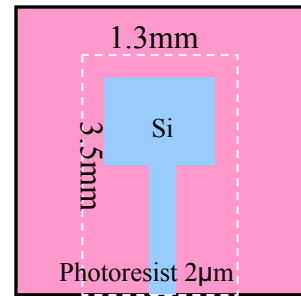
**(7.8)**



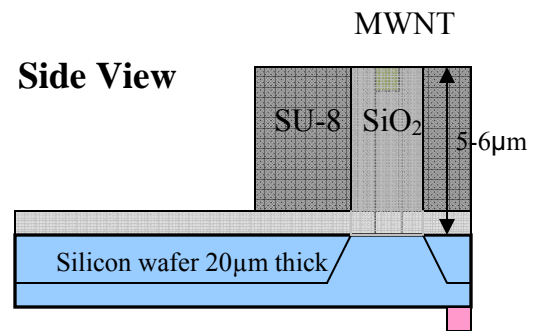
**(7.9)**



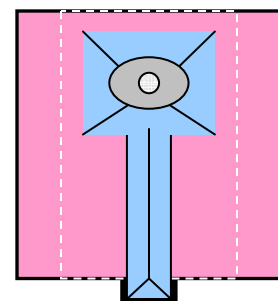
**Top View**



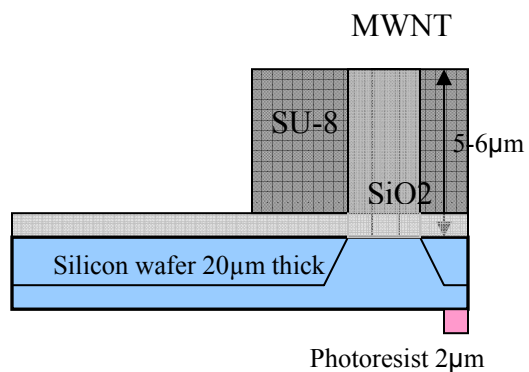
**(7.10)**



**Top View**



(7.11)

**Side View**

(7.13)

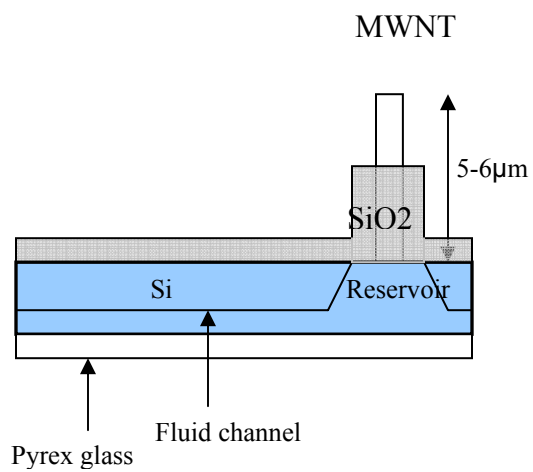
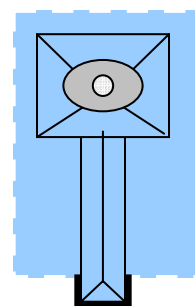
**Top View**

Figure B-7. Steps involved in the microfabrication of AFM cantilever.

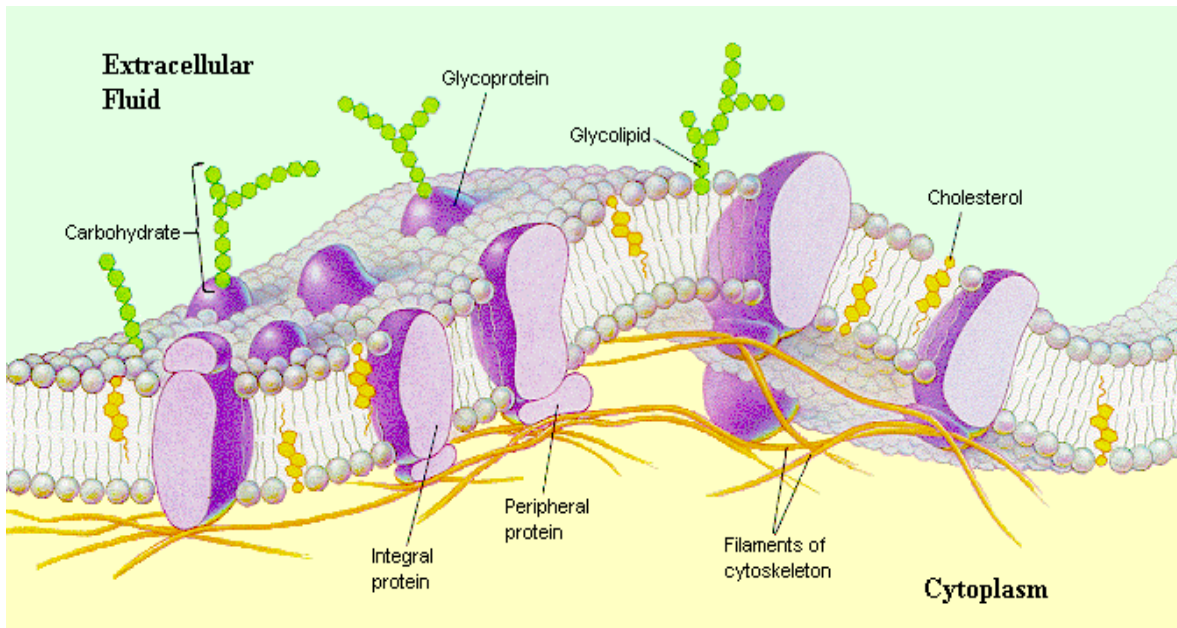
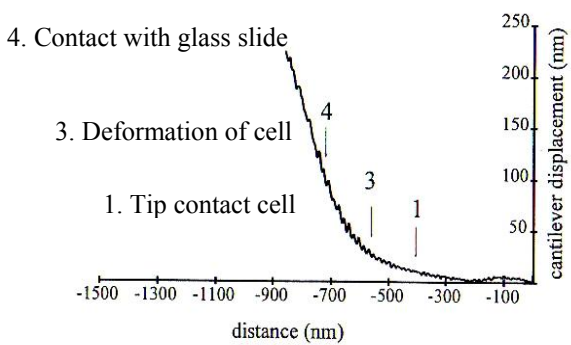


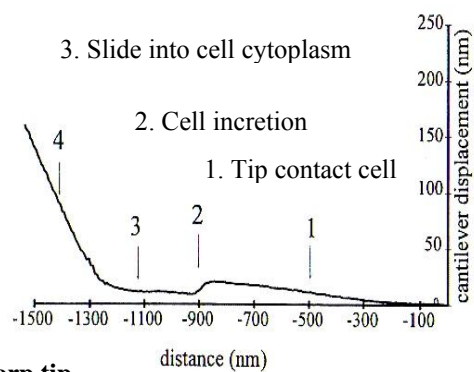
Figure B-8. Schematic representation of the cell membrane.

<http://wsrv.clas.virginia.edu/~rjh9u/humbiol.html>.



**Blunt tip**

4. Contact with glass slide

**Sharp tip**Figure B-9a & b. Cantilever displacement- piezo distance curve<sup>33</sup>

### Vita

Alpa Patel was born in the town of Motimarad, state of Gujarat, India on February 28<sup>th</sup>, 1978. She received her Bachelors of Science degree in Chemistry, Microbiology and Zoology from Mangalore University, Karnataka, India, in 1999. She joined Drexel University, Philadelphia, PA in 2001 and received her Masters of Science degree in Chemistry from Drexel University, Philadelphia, PA in 2003. From then on, she has been pursuing a Ph.D. degree under the supervision of Dr. Yen Wei from the Center of Advanced Polymers and Materials Chemistry and Department of Chemistry, Drexel University. Her research interests include a wide range of fields in polymer and materials chemistry, especially novel sol-gel materials for catalytic and biosensor applications. She has developed two products for two multibillion-dollar companies, which are at various stages of commercialization. While at Drexel, Alpa won six awards at the Drexel University research day and American Chemical Society poster sessions. In 2006, she was awarded the American Institute of Chemists Graduate Achievement Award and the Graduate Student Excellence Award for research/service towards Drexel's research.

#### Selected Publications:

- S. Praveen, A. Patel, Z. Sun, J. Xu, R. Ranade, G. Baran and Y. Wei. Compression and aging properties of experimental dental composites containing mesoporous silica as fillers. *Mol. Cryst. Liq. Cryst Journal*, 448, 825-833. 2006.
- A. Patel, S. Li, J. M. Yuan and Y. Wei. In situ encapsulation of horseradish peroxidase in electrospun porous silica fibers for potential biosensor applications. *Nano Letters*, 6(5), 1042-1046. 2006.
- O. E. Ansong, S. Li, A. C. Patel, G. Pomrink, S. Jansen, Y. Wei. Acid catalyzed free radical polymerization of methacrylates by stabilized nitroxide unimolecular initiators. *Polymer Materials*, 2006 (in revision)
- A. C. Patel, S. Li, Y. Wei, Ce Wang, W. Zhang. Electrospinning of porous silica nanofibers containing silver nanoparticles for catalytic applications. *Chemistry of Materials*, 2006 (in revision)

